DISSERTATION

VERTICALLY RESOLVED WEAK TEMPERATURE GRADIENT ANALYSIS OF THE MADDEN-JULIAN OSCILLATION

Submitted by

Brandon Wolding

Department of Atmospheric Science

In partial fulfillment of the requirements

For the Degree of Doctor of Philosophy

Colorado State University

Fort Collins, Colorado

Spring 2017

Doctoral Committee:

Advisor: Eric Maloney

David Randall
Susan van den Heever
George Kiladis
Jay Ham

ABSTRACT

VERTICALLY RESOLVED WEAK TEMPERATURE GRADIENT ANALYSIS OF THE MADDEN-JULIAN OSCILLATION

Interactions between moisture, convection, and large-scale circulations are thought to play an important role in destabilizing the Madden-Julian Oscillation (MJO). A simplified framework for understanding such interactions is developed, building upon the work of Chikira (2014). Tropical weak temperature gradient (WTG) balance is used to diagnose intraseasonal variations in large-scale vertical velocity from variations in apparent heating, allowing intraseasonal variations in large-scale vertical moisture advection to be decomposed into contributions from various apparent heating processes (e.g. radiative heating, microphysical processes). The WTG diagnosis captures the vertical structure and magnitude of large-scale vertical velocity and vertical moisture advection with exceptional accuracy throughout the free troposphere.

Moisture and moisture variance budgets are used to investigate the MJO in ERA-interim (ERAi) reanalysis and the Superparameterized Community Earth System Model (SP-CESM). Moisture budgets indicate that, during the enhanced phase of the MJO, anomalous moistening by large-scale vertical moisture advection exceeds anomalous drying by microphysical processes and sub-grid scale (SGS) eddy fluxes, such that the net effect of these large and opposing processes (hereafter the column process) is to further moisten regions that are anomalously moist. Moisture variance budgets indicate that the column process helps grow moisture variance, acting to destabilize the MJO. Horizontal advective damping of

moisture variance, associated with the modulation of higher frequency convective variability on intraseasonal timescales, acts to stabilize the MJO.

The vertically resolved WTG balance framework is used to assess the contribution various apparent heating processes make to the column process, and its ability to destabilize the MJO. Intraseasonal variations in longwave radiative heating enhance variations in large-scale vertical moisture advection at low and mid levels, strongly supporting destabilization of the MJO in both ERAi and SP-CESM. The effect of convection alone (i.e. without radiative and surface flux feedbacks) is to weakly grow moisture variance in SP-CESM, and weakly damp moisture variance in ERAi, suggesting that the MJO is unrealistically unstable in the former. Surface flux feedbacks appear to play a more important role in destabilizing the real world MJO. Moisture variance budget analysis of periods of weak, moderate, and strong MJO activity suggests that changes in the vertical structure of apparent heating do not play a dominant role in limiting the amplitude of the MJO in SP-CESM in the current climate.

WTG balance provides a useful framework for investigating how the MJO, and its impacts, may change as the climate system warms. Two simulations of SP-CESM, one at pre-industrial levels of CO_2 (280 ppm, hereafter PI) and one where CO_2 levels have been quadrupled (1120 ppm, hereafter 4xCO2), were analyzed. MJO convective variability increases considerably in the 4xCO2 simulation, a consequence of more favorable mean state moist thermodynamic conditions. A steepened mean state vertical moisture gradient allows MJO convective heating to drive stronger variations in large-scale vertical moisture advection, helping to support enhanced MJO convective variability in the 4xCO2 simulation. The dynamical response to MJO convective heating weakens in the warmer climate, a result of

increased tropical static stability. One consequence of this weakened dynamical response is that the MJO's ability to influence the extratopics, which is closely tied to the strength of its associated divergence, is reduced considerably in the 4xCO2 simulation.

ACKNOWLEDGMENTS

My acceptance into the CSU atmospheric science graduate program has already proven to be a watershed event in my life, and I will forever be indebted to Bill Cotton, Sue van den Heever, and Eric Maloney for the roles they played in bringing me to CSU. The students, faculty, and staff of the Atmospheric Science Department at CSU have come to feel more like friends and family than colleagues. While I have benefited from great conversations with nearly everyone here, a few people deserve special mention for allowing me to stretch their "open-door" policy beyond reasonable expectations. Eric Maloney, Wayne Schubert, Thomas Birner, Jim Benedict, Charlotte DeMott, Mark Branson, and Richard Johnson, thank you for your time and patience, and for the great conversations. I remember many of these conversations as vividly as the greatest climbing adventures of my life. It has been a privilege to work with the fun and talented members of the Maloney group, past and present. My apologies to the members of the BBMT group meetings for my over-enthusiastic and under-prepared talks on subjects outside of my expertise. Eric, thank you for having so much faith in me, for allowing me the freedom that I desired, and for providing the guidance that I required. I don't think that I would have thrived in this program under any other guidance. Many thanks to the members of my Ph.D. committee for your contributions to this work, for your counsel, and for being so generous with your time. I really do appreciate it. Special thanks to George Kiladis and Jay Ham for making the journey to the foothills campus so many times. Last but not least, to my family, thank you for your unwavering support.

TABLE OF CONTENTS

CHAPTER 1

Introduction

1.1. Purpose

The Madden-Julian Oscillation (Madden and Julian 1971, 1972) is the leading mode of tropical intraseasonal variability, and is characterized by broad envelopes of enhanced and suppressed convection that propagate slowly eastward from the Indian Ocean to the western Pacific Ocean (Zhang 2005). The broad envelopes of enhanced and suppressed convection are coupled to large-scale circulations that, directly or indirectly, extend the MJO's influence over the globe. Briefly, the MJO directly impacts tropical precipitation and winds (Zhang 2005), strongly modulates tropical cyclone activity in all basins (Maloney and Hartmann 2000a,b; Hall et al. 2001; Slade and Maloney 2013), interacts with ENSO (McPhaden 1999; Takayabu et al. 1999), influences extratropical modes of variability (Zhou and Miller 2005; Carvalho et al. 2005; Cassou 2008; Lin et al. 2009), and impacts North American regional surface temperature (Vecchi and Bond 2004; Zhou et al. 2012), winter blocking (Hamill and Kiladis 2014; Henderson et al. 2016) and atmospheric river events (Mundhenk et al. 2016). The MJO's intraseasonal timescale and global influence combine to make it an important source of predictability on weekly to monthly timescales.

More than four decades of research have made great strides in understanding this immensely important phenomenon. Numerous theories, summarized by Zhang (2005) and Wang (2012) and discussed in detail in sections 2.1 and 3.1 of this study, have been put forward to explain the existence and characteristics of the MJO. Several of these theories posit that interactions between moisture, convection, and large-scale circulations are important to the MJO (Bladé and Hartmann 1993; Sobel et al. 2001; Raymond 2001; Benedict and

Randall 2007; Sobel and Maloney 2012; Chikira 2014; Arnold and Randall 2015; Adames and Kim 2016). The purpose of this study is to better understand these interactions, and how they may change as the climate system warms.

1.2. Study Outline

Building off of the work of Chikira (2014), Chapter 2 uses tropical weak temperature gradient (WTG) balance to develop a simplified framework for understanding the interactions between moisture, convection, and large-scale circulations. ERA-interim (ERAi) re-analysis is used to calculate moisture and moist static energy (MSE) budgets of the MJO, and the WTG framework is used to investigate the importance of radiative feedbacks to the MJO. Chapter 2 has been published as in the Journal of Climate as Wolding and Maloney (2015a). In Chapter 3, moisture and moisture variance budgets of the MJO in the Superparameterized Community Earth System Model (SP-CESM) are used to further investigate the role that interactions between moisture, convection, and large-scale circulations play in destabilizing and propagating the MJO. Chapter 3 has been published in the Journal of Advances in Modeling Earth Systems as Wolding et al. (2016). Chapter 4 uses SP-CESM to examine how the changing moist thermodynamic structure of the tropics may impact the MJO, and its global influence, as the climate system warms. Chapter 4 has been published in the Journal of Advances in Modeling Earth Systems as Wolding et al. (2017). A summary of the primary findings of this study are presented in Chapter 5.

CHAPTER 2

Objective Diagnostics and the Madden-Julian Oscillation: Application to Moist Static Energy and Moisture Budgets

In this chapter, WTG balance is used to further develop a simplified framework for understanding slow variations in large-scale vertical motion in the tropics. This simplified framework is applied to ERAi data and used to examine the importance of radiative feedbacks to the MJO. This chapter has been published as in the Journal of Climate as Wolding and Maloney (2015a).

2.1. Introduction

Variability in the tropical atmosphere on timescales less than a season is strongly influenced by the Madden-Julian Oscillation (MJO), a phenomena traditionally described as a large-scale coupling of deep convection and tropospheric circulation anomalies that propagates eastward at $\sim 5\ \mathrm{m\,s^{-1}}$. Since its discovery over four decades ago (Madden and Julian 1971), tremendous effort has been put into explaining the existence of the MJO and improving its representation in models. This effort is warranted by the MJOs far reaching societal impacts, which result from its direct impacts as well as its interactions with phenomena such as tropical cyclone activity (Maloney and Hartmann 2000a,b; Hall et al. 2001; Slade and Maloney 2013) and interannual variability (McPhaden 1999; Takayabu et al. 1999). Despite continual advancement in the understanding of the MJO, various observed features remain insufficiently explained by the physical mechanisms proposed to be responsible for the MJOs existence. Zhang (2005) and Wang (2012) provide a good overview of this body of work.

This chapter is published in the Journal of Climate as Wolding and Maloney (2015a).

The development of large-scale regions of anomalous free-tropospheric humidity has played a central role in several recent theories of the MJO, including discharge-recharge theory (Bladé and Hartmann 1993; Hu and Randall 1994; Benedict and Randall 2007), multi-scale theories (Majda and Stechmann 2009, 2011), and moisture mode theory (Sobel et al. 2001; Raymond and Fuchs 2009; Sobel and Maloney 2012, 2013). A moist free troposphere can promote convection by reducing the diminishment of buoyancy that occurs as a rising plume entrains environmental air, and by reducing penetrative downdrafts that lower boundary layer theta-e and potentially inhibit further convection (Raymond 1995). The former is particularly important to convection over tropical oceans, where observations indicate that large dilution of updrafts occurs below 500 hPa (Lucas et al. 1994; Zipser 2003). The influence of moisture on tropical convection is enhanced by the small Coriolis parameter of the tropics, which allows gravity waves to quickly disperse buoyancy anomalies over large horizontal distances, making the realization of free tropospheric temperature anomalies on larger spatiotemporal scales difficult (Charney 1963; Maloney and Sobel 2007; Yano and Bonazzola 2009). Peters and Neelin (2006) used observations to show that the transition to deep convection occurs at a critical column water vapor (CWV), and Neelin et al. (2009) showed that precipitation statistics for different temperature regimes collapse to a simple dependence on CWV and critical CWV when vertically averaged tropospheric temperature is taken into account. Sahany et al. (2012) found that lower free tropospheric moisture was particularly important, highlighting potential "choke points" where dry air entrainment could prevent a plume from undergoing deep convection. While the interaction between free tropospheric humidity and convection is fundamental to both discharge-recharge theory and moisture mode theory, these theories differ significantly in their view of the mechanisms

controlling free tropospheric humidity and the manner in which anomalous convection and moisture interact.

Although not originally conceptualized in terms of free tropospheric humidity (Hu and Randall 1994), the discharge-recharge framework has been applied by studies that have observed an extended "recharge" period of gradual tropospheric moistening preceding MJO convective events, which subsequently "discharge" moisture during periods of enhanced convection (Bladé and Hartmann 1993; Kemball-Cook and Weare 2001; Kiladis et al. 2005; Benedict and Randall 2007; Thayer-Calder and Randall 2009). In this view, processes act to moisten the lower free troposphere during convectively quiescent periods, reducing the effects of dry air entrainment and eventually making the environment favorable for the onset of deep convection. The onset of deep convection is responsible for the discharge of free tropospheric moisture and return to quiescent conditions. In other words, suppressed convective conditions push the system towards enhanced convective conditions, and vice versa. The processes that recharge moisture must be favored east of the regions that discharge moisture in order to drive propagation, and the time period required for processes to discharge and recharge free tropospheric moisture determines the overall period of the oscillation.

Moisture mode theory (Sobel et al. 2001; Raymond 2001) seeks to explain the MJO using a simplified set of equations, whereby horizontal temperature gradients and temperature tendency are neglected under weak temperature gradient (WTG) balance. The distribution of convection is diagnosed from that of moisture, which is prognostically determined. Instability of the moisture mode occurs if a feedback exists such that convection, acting through various processes, results in a further enhancement of moisture anomalies. Of particular relevance to this study is the work of Chikira (2014), who showed the net effect of vertical

advection and cloud processes (termed the "column process") worked as a positive feedback to positive moisture anomalies in the enhanced phase of the MJO in both model results and European Center for Medium-Range Weather Forecasts Re-Analysis (ERAi). Using a novel method of assessing the moisture budget of the model MJO, Chikira (2014) provided unique insight as to what mechanisms may be responsible for this instability. Invoking WTG balance, the prognostic equations of potential temperature and free-tropospheric moisture were linked, allowing diabatic processes to be directly related to environmental vertical motion. The large-scale vertical motion associated with various diabatic processes was assessed, and the resulting vertical moisture advection quantified. The reduction of radiative cooling (which is associated with a reduction in large-scale subsidence under WTG balance) in the enhanced phase of the model MJO was shown to be the primary driver of anomalous lower free tropospheric moistening. Janiga and Zhang (2016) applied a similar theoretical framework to a cloud-permitting model simulation of an MJO event that occurred during the Dynamics of the MJO (DYNAMO) field campaign, and also found that the reduction of longwave radiative cooling helped to maintain moisture anomalies during the enhanced phase. While moisture-mode theory and discharge-recharge theory are compatible in many ways, the results of Chikira (2014) and Janiga and Zhang (2016) suggest that instead of acting to "discharge" moisture anomalies and stabilize the atmosphere, the ensemble cloud population present during the enhanced phase of the MJO helps support moisture anomalies against the drying effect of horizontal advection, thereby helping maintain atmospheric instability.

Many other attempts have been made to understand the mechanisms controlling moisture variations associated with the MJO (Benedict and Randall 2007; Maloney 2009; Maloney

et al. 2010; Kiranmayi and Maloney 2011; Andersen and Kuang 2012; Wu and Deng 2013; Kim et al. 2014a). Efforts using moisture budgets (Kiranmayi and Maloney 2011), particularly in the enhanced phase of the MJO, are often stymied by the difficult task of quantifying the small moisture tendency that results from large anomalous moistening due to vertical moisture advection and large anomalous drying due to processes associated with deep convection (e.g. precipitation). The small moisture tendency that results from these large processes is key to understanding moisture variations associated with MJO, and distinguishing between a discharge-recharge mechanism and certain moisture-mode mechanisms for the MJO. An alternative approach to assessing the small residual moistening tendency is the use of a vertically integrated moist static energy (MSE) budget (Maloney 2009; Maloney et al. 2010; Kiranmayi and Maloney 2011; Andersen and Kuang 2012; Wu and Deng 2013; Kim et al. 2014a; Sobel et al. 2014). In addition to providing insight into the role of various diabatic processes (e.g. radiative heating) whose importance has been highlighted in recent studies (Chikira 2014; Janiga and Zhang 2016; Yokoi 2015), use of the column MSE budget has the benefit of allowing the net effect of large-scale vertical moisture advection and precipitation on column moisture content to be assessed without having to directly quantify precipitation. Note that while MSE remains unchanged by latent heat release associated with vapor-liquid transitions, MSE is not conserved during liquid-ice transitions. While use of a column-integrated approach makes the assessment of moisture and MSE budgets of the MJO more tractable, it is worth highlighting that important information about the vertical structure of the physical processes at work can not be determined using this approach alone (Matthews 2008; Ling et al. 2013; Chikira 2014).

While these studies have provided a great deal of insight into systematic variations of moisture associated with the MJO, documentation of the mechanisms responsible for these variations remains relatively incomplete. The limited geographical scope of many of these studies, and their focus on the enhanced phase of the MJO, brings into question how "systematic" of a role various mechanisms play. This study compares anomalous column moisture and MSE budgets of the MJO, and uses methods introduced in part I (Wolding and Maloney 2015b) to assess the geographical variability of their various terms. The residual of each budget is presented, and implications for the interpretation of mechanisms responsible for moisture variations associated with the MJO discussed. A theoretical framework similar to that implemented by Chikira (2014) and Janiga and Zhang (2016) is applied to ERAi reanalysis for the first time. Processes responsible for intraseasonal variations in large-scale vertical moisture advection are investigated using vertical profiles of various apparent heating (Yanai et al. 1973) processes. Finally, the column moisture budget is used to examine the role of various processes in destabilizing the MJO.

Section 2 discusses the various datasets utilized in this study, calculation of the anomalous MSE and moisture budgets, and methods used in composite analysis. Results and discussion of both budgets are presented in section 3, as well as further interpretation of the MSE budget in the context of WTG balance. Summary and conclusions of this study are presented in section 4.

2.2. Data and Methodology

Moisture and MSE budgets are calculated using ERAi reanalysis (Dee et al. 2011), provided by the European Center for Medium-Range Weather Forecasts (ECMWF). This data

was obtained at 6-hour $1.5^\circ \times 1.5^\circ$ resolution for the years 1979-2012. Unless otherwise indicated, the various terms of the budget (e.g. tendencies, horizontal advection, etc.) were calculated from the 6-hourly data, vertically integrated from the surface to 100 hPa, and then averaged to daily. ERAi apparent and radiative heating rates were obtained directly from the ECMWF. Please note that ERAi precipitation was used in the calculation of the moisture budget. Daily $2.5^\circ \times 2.5^\circ$ NOAA interpolated OLR (Liebmann and Smith 1996) was similarly obtained for the years 1979-2012. Both aforementioned datasets were either lowpass or bandpass filtered to various timescales as indicated in text and figures, and then limited to boreal winter months (October-April) from October 1 1980 to April 30 2011 before compositing. In all figures presented in this study, terms that have been lowpass filtered to 20 days or 100 days are indicated by subscripts of $LP20$ and $LP100$ respectively, while terms that have been bandpass filters to 20-100 days are indicated by the subscript MJO. TRMM 3B42 daily precipitation was obtained at 3-hour $0.25^\circ \times 0.25^\circ$ resolution, averaged to daily resolution, bandpass filtered to 20-100 days, and then limited to boreal winter months from October 1 1999 to April 30 2011.

Composite analysis is performed using the Filtered MJO OLR (FMO) index (Kiladis et al. 2014). The FMO index and the EOFs used in its calculation can be obtained from http://www.esrl.noaa.gov/psd/mjo/mjoindex/. In order to match the phase convention of the Realtime Multivariate MJO (RMM) index (Wheeler and Hendon 2004), EOF1 and PC1 were multiplied by -1, and then the order of the first two EOFs and PCs were reversed. This was motivated by the widespread use of the RMM index, its potential familiarity to the reader, and because this convention was also adopted by Kiladis et al. (2014). Composites are made using relative phase, a diagnostic developed in Part I of this study. Relative

phase objectively identifies the index phase where the largest MJO-related anomalies in a given field are likely to be observed for a given geographical location. Figure 2.1a illustrates a traditional phase composite of latitudinally averaged NOAA OLR anomalies, where the bold numbers adjacent to the brackets indicate the "phase" as defined by Wheeler and Hendon (2004). The black line in (a) indicates the objectively determined phase at which positive OLR anomalies are the largest at each longitude. Block arrows indicate the manner in which data is shifted in the transition from (a) to (b), such that maximum OLR anomalies are now centered in (b). Subsequent plots are shifted such that the enhanced phase of the MJO is located in the center of the figure. Further details of the relative phase, and its calculation, are given in part I.

Data are composited as a function of relative phase of OLR for the FMO index. This is done by first restricting dates to periods when the magnitude of the respective index exceeded a value of 1. Data at each point are then binned by relative phase, with bins spanning 30 degrees of relative phase made every 15 degrees. The minimum number of days included in any single bin is 225 for composites spanning 1980-2011, and 60 for composites spanning 1999-2011. Vertical profiles presented in Figures 2.6, 2.7, 2.8, and 2.9 were composited in similar fashion, except spatially averaging was performed over the region $5°\text{N} - 10°\text{S}, 75°\text{E} - 85°\text{E}$. These figures will be discussed in the following section.

Composite "snapshots" presented in Figure 2.2 were produced by selecting days when the relative phase of OLR at 80°E was within 10° of $\pm 180°$. This corresponds to maximum negative OLR anomalies at 80°E, as seen half way down the vertical axis at 80°E in each plot of Figure 2.3. These days were then limited to those when the FMO magnitude exceeded 1. Figures 2.2 and 2.3 will be discussed in the following section.

2.3. Results and Discussion

2.3.1. A moisture budget perspective of the MJO

2.3.1.1. Moisture budget framework

Neglecting $-\nabla \cdot \overline{q'\mathbf{V}'_{\mathbf{h}}}$, the apparent moisture sink (Q_2) is

$$Q_2 \equiv -\mathrm{L_v}\left(\frac{\partial \overline{q}}{\partial t} + \overline{\mathbf{V}}_{\mathbf{h}} \cdot \nabla \overline{q} + \overline{\omega}\frac{\partial \overline{q}}{\partial p}\right) = -\mathrm{L_v}\left(\overline{M} - \frac{\partial \overline{\omega' q'}}{\partial p}\right) \tag{2.1}$$

where the overbar and prime indicate the large-scale average of a quantity and deviations from the area average respectively, $\vec{V}_h$ and ω are the horizontal and vertical winds respectively, q is specific humidity, $\mathrm{L_v}$ is the latent heat of vaporization, and M is the moisture tendency due to microphysical processes. Vertical eddy fluxes of moisture ($-\frac{\overline{\partial \omega' q'}}{\partial p}$) primarily represent moistening by subgrid-scale cumulus convection (Yanai and Johnson 1993). Decomposing M into contributions from various microphysical processes gives

$$M = -\frac{1}{\mathrm{L_v}}Q_{ce} - \frac{1}{\mathrm{L_s}}Q_{ds} \tag{2.2}$$

where Q_{ce} and Q_{ds} are the dry static energy (DSE) tendency due to condensation minus evaporation (hereafter net condensation) and deposition minus sublimation (hereafter net deposition) respectively, and $\mathrm{L_s}$ is the latent heat of sublimation. The Eulerian moisture tendency is obtained by re-arranging equation 2.1, giving

$$\begin{aligned} \frac{\partial \overline{q}}{\partial t} &= -\overline{\mathbf{V}}_{\mathbf{h}} \cdot \nabla \overline{q} - \overline{\omega}\frac{\partial \overline{q}}{\partial p} - \frac{1}{\mathrm{L_v}}Q_2 \\ &= -\overline{\mathbf{V}}_{\mathbf{h}} \cdot \nabla \overline{q} + C \end{aligned} \tag{2.3}$$

where C is the column process introduced by Chikira (2014), which quantifies the moisture tendency resulting from large-scale vertical moisture advection, microphysical processes, and vertical eddy fluxes of moisture. In other words, C quantifies the moisture tendency resulting from all processes occurring within a vertical column with the exception of horizontal moisture advection. Integrating equation 2.3 through the depth of the troposphere gives

$$\left\langle \frac{\partial \overline{q}}{\partial t} \right\rangle = -\left\langle \overline{\mathbf{V}}_h \cdot \nabla \overline{q} \right\rangle + \langle C \rangle \tag{2.4}$$

where

$$\langle C \rangle = C_{free} + BL + \frac{1}{\mathrm{L}_v} \overline{SLHF} \tag{2.5}$$

$$C_{free} = -\left\langle \overline{\omega} \frac{\partial \overline{q}}{\partial p} \right\rangle_{900} + \left\langle \overline{M} \right\rangle_{900} \tag{2.6}$$

$$BL = -\left\langle \overline{\omega} \frac{\partial \overline{q}}{\partial p} \right\rangle_{1000}^{900} + \left\langle \overline{M} \right\rangle_{1000}^{900} \tag{2.7}$$

and the angled brackets indicate the column integral from 1000 to 100 hPa, subscripts and superscripts on the angled brackets indicate differing lower and upper levels of integration respectively, and SLHF is the surface flux of latent heat. C_{free} and BL quantify the moisture tendency resulting from large-scale vertical moisture advection and microphysical processes within the free troposphere and boundary layer respectively. In other words, the sum of C_{free} and BL quantifies the moisture tendency resulting from all processes occurring within a vertical column with the exception of fluxes of moisture from the surface and horizontal moisture advection. The distinction between C_{free} and BL is made because WTG balance, which is used in subsequent sections, is not applicable within the boundary layer, and because C_{free} is closely related to the aggregate effect an ensemble of clouds has on moisture (Janiga

and Zhang 2016). A detailed discussion of the physical processes controlling intraseasonal variations in C_{free} will be provided in a later section.

Please note that ERAi does not provide the fields necessary to calculate $\overline{M}$, and that the approximation $\langle \overline{M} \rangle = \overline{P}$, where P is precipitation, was used in the actual calculation of the moisture budget. This approximation neglects the moisture tendency associated with net deposition and net condensation that does not result in precipitation. As will be discussed in subsequent sections, the inability to close the column moisture budget motivated the choice to calculate C as the residual of the moisture tendency and horizontal advection, and to calculate the sum of C_{free} and BL as the residual of the moisture tendency, horizontal advection, and $SLHF$. This choice was made because the moisture tendency, horizontal advection, and $SLHF$ are likely better constrained within ERAi than the remaining budget terms (e.g. precipitation). Calculated in this manner, C and the sum of C_{free} and BL should include representation of all process included in $\langle \overline{M} \rangle$.

2.3.1.2. The MJO in the eastern Indian Ocean

Before analyzing the geographical variability of processes affecting column moisture, we begin by looking at a composite "snapshot" of various processes when anomalous OLR is at a minimum at 80°E. Composite anomalies of column latent heat and the various terms in equation 2.4 are presented in Figure 2.2. Please note that the subscript notation used in Figure 2.2, as well as all subsequent figures, is defined in section 2 and within figure captions. Maximum column latent heat anomalies (Fig. 2.2a) of $\sim 1 \times 10^7\,\mathrm{J\,m^{-2}}$ ($\sim 4\,\mathrm{mm}$) are approximately co-located with minimum OLR anomalies. Maximum TRMM precipitation anomalies (Fig. 2.2b) of $\sim 200\,\mathrm{W\,m^{-2}}$ ($\sim 7\,\mathrm{mm\,day^{-1}}$) are also approximately co-located with minimum OLR anomalies. The distribution of TRMM precipitation anomalies closely

matches the overall distribution of column latent heat anomalies, but has a clear maximum near the equator in comparison to the broader maximum of column latent heat anomalies. It is worth highlighting that, in the absence of anomalous moisture sources, anomalous precipitation in this region could remove the enhanced column moisture content (presumably built up over the previous 10-15 days) in less than a day. Yet the moisture tendency (Fig. 2.2c) over much of the eastern Indian Ocean is near zero or weakly negative, particularly in regions where the precipitation anomalies are largest. This collocation of maximum precipitation anomalies with near zero column moisture tendency is consistent with previous work (Benedict and Randall 2007; Kiranmayi and Maloney 2011), and indicates that some other process or processes are acting to maintain enhanced column moisture content against dissipation by anomalous precipitation. These processes will now be identified.

The pattern of anomalous horizontal moisture advection (Fig. 2.2d) is very similar to that of the moisture tendency and is typically of larger magnitude, acting as an anomalous moisture source over a broad region east of the convective maximum, and as an anomalous moisture sink to the west where strong westerly U850 anomalies are evident. Worth noting is the extent to which anomalous horizontal advective drying extends through the region of minimum OLR anomalies, acting as an additional moisture sink in regions of strong precipitation and enhanced column moisture content. In contrast, C anomalies (Fig. 2.2e) have a distribution similar to both moisture and precipitation anomalies, helping to maintain column moisture anomalies against dissipation by enhanced precipitation. In other words, the net effect of anomalous SLHF, large-scale vertical moisture advection, and microphysical processes during the mature stage of the MJO is to further moisten the column. SLHF (Fig. 2.2f) is enhanced along a narrow strip of strong westerly U850 anomalies in the Indian

Ocean, and suppressed over oceanic regions of the Maritime Continent where easterly U850 anomalies are present. While the enhancement of SLHF does contribute substantially to C anomalies, they only provide $5-10\%$ of the moisture removed by anomalous precipitation in the eastern Indian Ocean. This is consistent with results obtained from buoy observations in the Indian Ocean by Riley Dellaripa and Maloney (2015), and indicates that the vast majority of moisture removed by enhanced precipitation during the enhanced phase of the MJO is supplied by anomalous large-scale vertical moisture advection (i.e. horizontal convergence and divergence acting throughout the column). In fact, Figure 2.2g shows that the sum of C_{free} and BL anomalies is near zero or weakly positive in the region of enhanced precipitation, suggesting that the moisture supplied by anomalous large-scale vertical moisture advection may actually exceed that removed by microphysical processes. The net effect of C_{free} and BL anomalies also appears to play an important role in moistening over the oceanic regions of the Maritime Continent to the east.

Taken together, the various processes presented in Figure 2.2 are consistent with the findings of Chikira (2014) and Sobel et al. (2014), in that C anomalies are clearly acting to enhance column moisture anomalies. The role of anomalous horizontal moisture advection in both propagating column moisture anomalies eastward, as well as damping their further growth in the regions where precipitation anomalies are largest is qualitatively consistent with many previous studies (Benedict and Randall 2007; Kiranmayi and Maloney 2011; Sobel et al. 2014; Chikira 2014; Kim et al. 2014a). In considering the results of Figure 2.2 presented above, it is important to remember that this is only a "snapshot" of the processes occurring when the MJO is at a given location. The extent to which these processes play

an important role in other parts of the eastern hemisphere remains to be seen, as does the extent to which these processes are mirrored in the suppressed phase of the MJO.

2.3.1.3. The MJO in the Eastern Hemisphere

In order to assess how the processes affecting anomalous moisture change as the MJO moves across the eastern hemisphere, relative phase composites of the various column moisture budget terms (equation 2.4) are now examined. Figure 2.3a shows latitudinally averaged moisture (color shading), OLR (contours), and U850 (arrows) anomalies throughout a composite convective lifecycle of the MJO. Moving downwards from the top of the figure corresponds with the transition from suppressed convection (top of figure, positive OLR anomalies) to enhanced convection (center of the figure, negative OLR anomalies) and back to suppressed convection (bottom of figure, positive OLR anomalies) at each longitude. The transition from suppressed to enhanced convection is accompanied by easterly U850 anomalies, and the transition back to suppressed conditions is accompanied by westerly U850 anomalies. These basic features are consistent with the well documented structure of the MJO (Madden and Julian 1972; Wheeler and Hendon 2004; Kiladis et al. 2005). Column moisture anomalies and TRMM precipitation anomalies (Fig.2.3b) tend to peak between 15 and 30 degrees of phase prior to OLR anomalies, which is $\sim$ 1.5 to 3 days for a MJO event of typical duration. The tendency for OLR to be disproportionately influenced by widespread anvil decks that persist for considerable times (Morita et al. 2006) may explain this slight offset. While OLR is used as a convenient proxy for convection in this study, the interaction of various processes with column moisture is of real interest. Therefore, the slight lag should be kept in mind during subsequent discussion.

Comparing Figures 2.3a-g with Figures 2.2a-g largely supports generalizing the results of the previous section to the rest of the Indian Ocean and Maritime Continent region. Irrespective of geographical location, and during both the enhanced and suppressed phase, the moisture tendency (Fig. 2.3c) is near zero when precipitation anomalies are largest. Please note that the colorbar values in Figure 2.3b are an order larger than those in Figures 2.3c-g. Anomalous horizontal advective moistening (Fig. 2.3d) contributes to the buildup of enhanced moisture anomalies, while anomalous horizontal advective drying contributes to their depletion, consistent with previous studies (Benedict and Randall 2007; Kiranmayi and Maloney 2011; Chikira 2014; Kim et al. 2014a; Pritchard and Bretherton 2014). During both enhanced and suppressed periods, C acts to enhance moisture anomalies (Fig. 2.3a), lagging moisture anomalies slightly in the central Indian Ocean and being approximately in phase with moisture anomalies in the Maritime Continent region. There is a notable "gap" in C between $100° - 105°$E, where the Malay Peninsula and Sumatra span much of the latitude range considered here. As C is often positive when the total tendency is zero, this implies that horizontal advection plays a role in damping the further growth of moisture anomalies when they are largest.

Both SLHF and the net effect of C_{free} and BL anomalies (Figs. 2.3f,g) make substantial contributions to C anomalies discussed above, with the former acting as an anomalous moisture source predominantly in the late stages of enhanced convection and the latter in the early stages of enhanced convection. Most importantly, Figure 2.3g suggests that intraseasonal variations in the net effect of large-scale vertical moisture advection and microphysical processes (i.e. the sum of C_{free} and BL) play no role in the "discharge" of column moisture anomalies during the enhanced phase of the MJO, which appears to result entirely from

the enhancement of horizontal advective drying. From the Indian Ocean to the eastern side of the Maritime Continent, latitudinally average SLHF is reduced during periods of easterly wind anomalies (when moisture anomalies are growing), and enhanced during period of westerly wind anomalies (when moisture anomalies are dissipating). The distribution of SLHF largely reflects the distribution of boreal winter mean low level westerly winds (Fig. 2.4), which determines where wind anomalies associated with the MJO add constructively or destructively to mean winds (Shinoda et al. 1998; Riley Dellaripa and Maloney 2015). The change in mean state winds that occurs east of the Maritime Continent explains the change in the SLHF anomalies that occurs in this region in Figure 2.3f.

To summarize, the results of Figure 2.3 suggest that the processes controlling column moisture variations associated with the MJO do not change as a function of geographical location throughout much of the eastern hemisphere. Figure 2.3 also shows that the processes controlling column moisture content in the enhanced phase are approximately mirrored in the suppressed phase. Column moisture content "recharged" in the weeks leading up to the onset of enhanced convection is insufficient to support prolonged enhanced precipitation during the enhanced phase of the MJO. To first order, prolonged enhanced precipitation is supported by the moisture supplied by anomalous large-scale vertical advection, which appears to actually exceed moisture removal by anomalous precipitation, resulting in a net moistening. At no point does the net effect of these processes appear to "discharge" column moisture anomalies.

2.3.1.4. A role for the MSE budget

The results of this section have demonstrated that changes in horizontal advection and SLHF during the enhanced phase of the MJO are relatively modest, being a full order of

magnitude smaller than changes in precipitation and large-scale vertical moisture advection, with the latter experiencing a three-fold increase relative to climatological values in this region (not shown). Unfortunately, a moisture budget perspective alone does not provide much insight to the physical mechanisms that could be responsible for this dramatic change in large-scale vertical moisture advection. An even larger disadvantage of using a moisture budget alone to investigate the MJO is that the budget residual (i.e. the difference between the left and right hand sides of equation 2.3) (Fig. 2.5a) is larger than the individual terms from which conclusions are often drawn. Accurate assessment of the small difference between the two large terms in C_{free} is important for distinguishing the role of various processes in destabilizing the MJO, as well as evaluating various theories of the MJO such as discharge-recharge theory and moisture mode theory.

Fortunately the MSE budget offers solutions to both of these problems. Not only can the MSE budget be approximately closed, but recent studies (Chikira 2014; Janiga and Zhang 2016) have begun developing a framework for using the MSE budget to understand the dramatic changes in large-scale vertical moisture advection. The next section will introduce the MSE budget, highlight the physical mechanisms that can drive changes in large-scale vertical moisture advection and C_{free}, and demonstrate that the conclusions drawn in this section are robust. Discussion of both the moisture budget and MSE budget residuals will be provided.

2.3.2. A MSE perspective of the MJO

2.3.2.1. MSE budget framework

Moist static energy (h;MSE), DSE (s), and moisture are related by

$$h = s + \mathrm{L}_v q \tag{2.8}$$

Neglecting $-\nabla \cdot \overline{s' \mathbf{V}'_{\mathbf{h}}}$, the apparent heat source (Q_1) (Yanai et al. 1973) is

$$Q_1 \equiv \frac{\partial \overline{s}}{\partial t} + \overline{\mathbf{V}}_{\mathbf{h}} \cdot \nabla \overline{s} + \overline{\omega} \frac{\partial \overline{s}}{\partial p} = \overline{Q}_s - \frac{\partial \overline{\omega' s'}}{\partial p} \tag{2.9}$$

where Q_s is the DSE tendency due to diabatic processes. Vertical eddy fluxes of dry static energy ($-\frac{\overline{\partial \omega' s'}}{\partial p}$) primarily represent heating by subgrid-scale cumulus convection (Yanai and Johnson 1993). The DSE tendency due to diabatic processes results from latent heating associated with microphysical processes as well as radiative heating, such that

$$Q_s = Q_M + Q_R \tag{2.10}$$

where Q_M and Q_R are the DSE tendency due to microphysics and radiation respectively. Decomposing Q_M into contributions from various microphysical processes gives

$$Q_M = Q_{ce} + Q_{fm} + Q_{ds} \tag{2.11}$$

where Q_{fm} is the DSE tendency due to net freezing minus melting.

Combining equations 3.3 and 2.1 to arrive at the Eulerian MSE tendency gives

$$\begin{aligned}\frac{\partial \overline{h}}{\partial t} &= -\overline{\mathbf{V}}_{\mathbf{h}} \cdot \nabla \overline{h} - \overline{\omega}\frac{\partial \overline{h}}{\partial p} + Q_1 + Q_2 \\ &= -\overline{\mathbf{V}}_{\mathbf{h}} \cdot \nabla \overline{h} - \overline{\omega}\frac{\partial \overline{h}}{\partial p} + \overline{Q}_s + \mathrm{L_v}\overline{M} - \frac{\partial \overline{\omega' s'}}{\partial p} - \mathrm{L_v}\frac{\partial \overline{\omega' q'}}{\partial p}\end{aligned} \tag{2.12}$$

This equation is our jumping off point for understanding variations in large-scale vertical moisture advection and C_{free} associated with the MJO.

2.3.2.2. MSE in WTG balance

In this section, WTG balance is used to understand variations in large-scale vertical moisture advection and C_{free}. The Eulerian tendency and horizontal advection of $\overline{s}$ (see equation 3.3) are neglected under WTG balance (Sobel et al. 2001), such that

$$\overline{\omega} = \frac{\overline{Q}_s - \frac{\overline{\partial \omega' s'}}{\partial p}}{\frac{\partial \overline{s}}{\partial p}} \tag{2.13}$$

$$\frac{\partial \overline{h}}{\partial t} = \mathrm{L_v}\frac{\partial \overline{q}}{\partial t} \tag{2.14}$$

$$\overline{\mathbf{V}}_{\mathbf{h}} \cdot \nabla \overline{h} = \mathrm{L_v}\overline{\mathbf{V}}_{\mathbf{h}} \cdot \nabla \overline{q} \tag{2.15}$$

One method of assessing the applicability of WTG balance is to compare vertical velocity anomalies to those diagnosed using the right hand side of equation 2.13. Figure 2.6a shows anomalous vertical velocity (color shading) and specific humidity (contours) throughout a composite convective lifecycle of the MJO in the eastern Indian Ocean (5°N – 10°S,75°E – 85°E). Moving from the right side to the left side of the figure corresponds with the transition from suppressed convection to enhanced convection and back to suppressed convection, as indicated at the bottom of the figure. The largest specific humidity anomalies occur at 750

hPa and 500 hPa, while the largest vertical velocity anomalies occurring at around 400 hPa. Figure 2.6b shows the vertical velocity diagnosed using the right hand side of equation 2.13, and Figure 2.6c shows the difference between the actual and diagnosed vertical velocity. Please note that Q_1, which is used in the right hand side of equation 2.13, was obtained directly from the ECMWF, not calculated as the sum of the Eulerian tendency and large-scale advective terms. While the right hand side of equation 2.13 slightly underestimates vertical velocity anomalies below 200 hPa, and overestimates vertical velocity anomalies above 200 hPa, the evolution, vertical structure, and magnitude of the vertical velocity anomalies are well captured to first order. This suggests that a WTG balance framework is applicable to the MJO, consistent with the findings of previous studies (Chikira 2014; Janiga and Zhang 2016). We wish to emphasize that this framework is not applicable within the boundary layer.

Assuming WTG balance and using equations 2.13, 2.14, and 2.15, equation 2.12 becomes

$$\begin{aligned}\frac{\partial \overline{h}}{\partial t} = \mathrm{L_v}\frac{\partial \overline{q}}{\partial t} &= -\mathrm{L_v}\overline{\mathbf{V}}_{\mathbf{h}} \cdot \nabla \overline{q} + \overline{\alpha}\left(\overline{Q}_s - \overline{\frac{\partial \omega' s'}{\partial p}}\right) + \mathrm{L_v}\overline{M} - \mathrm{L_v}\overline{\frac{\partial \omega' q'}{\partial p}} \\ &= -\mathrm{L_v}\overline{\mathbf{V}}_{\mathbf{h}} \cdot \nabla \overline{q} + \overline{\alpha} Q_1 - Q_2\end{aligned} \tag{2.16}$$

where

$$\overline{\alpha} = -\mathrm{L_v}\left(\frac{\frac{\partial \overline{q}}{\partial p}}{\frac{\partial \overline{s}}{\partial p}}\right) \tag{2.17}$$

Note that $\overline{\alpha}$ (Chikira 2014) is essentially a measure of moisture sensitivity to apparent heating (Q_1). $\overline{\alpha}$ is the quotient of the vertical moisture gradient and a measure of the static stability, with the latter determining the amount of vertical motion required to balance an apparent heating and the former determining the amount of moistening that results from the required vertical motion. The vertical structure of α and anomalous α throughout a

composite convective lifecycle is shown Figures 2.7a,b respectively. The lower troposphere has a particularly high moisture sensitivity to apparent heating, while the upper troposphere is relatively insensitive. Moistening of the lower and middle troposphere during the enhanced phase results in a reduction of α below 800 hPa and an increase of α above 400 hPa, consistent with the findings of Chikira (2014). The opposite is true during the suppressed phase.

To first order, moisture variations associated with intraseasonal variations in $\overline{\alpha}Q_1$ (Fig. 2.8b) result from intraseasonal variations in Q_1 (Fig. 2.8a) acting on the mean state $\overline{\alpha}$ profile (Fig. 2.9a). The mean state Q_1 profile acting on intraseasonal variations in $\overline{\alpha}$ (Fig. 2.9b) results in a much smaller moisture tendency, while intraseasonal variations in the Q_1 profile acting on intraseasonal variations in $\overline{\alpha}$ result in a negligible moisture tendency (not shown). Intraseasonal variations in Q_1 have a distinct peak in the upper troposphere, but the much larger values of $\overline{\alpha}$ in the lower troposphere result in a $\overline{\alpha}Q_1$ profile that is substantially more bottom-heavy, with secondary peaks in moistening evident at 600 and 825 hPa. Intraseasonal variations in $Q_1 - \overline{Q}_R$ (Fig. 2.8c), which represents the apparent heating effect an ensemble cloud population has on its environment with the exclusion of radiative impacts (i.e. the net effect of microphysical processes and vertical eddy fluxes of DSE), account for much of the variation in Q_1. This heating drives moistening (Fig. 2.8d) which begins at the lowest levels of the troposphere during the suppressed phase, gradually increases in height during the transition to enhanced convection, and then makes an abrupt jump to mid and finally upper levels during the enhanced phase. This stepwise pattern of moistening is reminiscent of that observed in the DYNAMO field campaign (Johnson and Ciesielski 2013). Note that the peak in mid-tropospheric moistening occurs prior to the largest mid-tropospheric moisture anomalies, and that drying is observed below 800

hPa throughout the enhanced phase. Intraseasonal variations in radiative heating (Fig. 2.8e), while smaller than intraseasonal variations in $Q_1 - \overline{Q}_R$, play an important role in determining the structure and magnitude of intraseasonal variations in apparent heating. The intraseasonal moisture tendency associated with radiative heating (Fig. 2.8f) is more bottom-heavy than that which results from $Q_1 - \overline{Q}_R$, and is strongest slightly after the peak in mid-tropospheric moisture anomalies. This moistening, which counteracts the lower tropospheric drying effects of $Q_1 - \overline{Q}_R$, may play a particularly important role in prolonging convection during the enhanced phase, as tropical convection is particularly sensitive to dry air entrainment below the freezing level (Lucas et al. 1994; Zipser 2003; Sahany et al. 2012).

Intraseasonal variations in both longwave and shortwave radiative heating (Figs. 2.10a,c) play an important role in determining the vertical structure and magnitude of $\overline{Q}_R$, though the longwave component is clearly dominant. Both longwave and shortwave radiative heating anomalies have vertical dipole structures that largely oppose each other, with the former being centered near 400 hPa with anomalous heating below this level during the enhanced phase, and the latter being centered near 550 hPa with anomalous cooling below this level during the enhanced phase. The vertical structure and magnitude of both longwave and shortwave radiative heating anomalies are comparable to those derived from CloudSat observations (Ma and Kuang 2011; Del Genio and Chen 2015), as is the phasing between radiative heating anomalies and moisture anomalies. Again, the vertical structure of $\overline{\alpha}$ is such that the profiles of the intraseasonal moisture tendencies associated with longwave and shortwave radiative heating (Figs. 2.10b,d) are substantially more bottom-heavy than the anomalous radiative heating profiles, with the largest moisture tendencies occurring in the lower troposphere. During the enhanced phase, reduced longwave radiative cooling results

in strong anomalous moistening in the lower and mid troposphere, while reduced shortwave heating results in anomalous drying, particularly below 750 hPa. When vertically integrated from 500-900 hPa (not shown), the latter is comparable with other moisture budget terms such as SLHF. While the effects of longwave radiative heating clearly dominate those of shortwave radiative heating, this result suggests the potential exists for interactions between the diurnal cycle and the MJO via radiative feedbacks. Further examination of this is beyond the scope of this study, and is left for future work.

Diagnosing variations in C_{free}, which represents the net effects of large-scale vertical moisture advection and microphysical processes within the free troposphere, is more complicated. Equation 2.16 can be re-arranged and combined with equation 2.4 to give

$$\begin{aligned} C_{free} &= \left\langle \frac{\overline{\alpha}}{\mathrm{L_v}} \left(\overline{Q}_{fm} + \overline{Q}_R - \overline{\frac{\partial \omega' s'}{\partial p}} \right) \right\rangle_{900} + \left\langle \frac{\left(\overline{\alpha} - \frac{\mathrm{L_v}}{\mathrm{L_s}} \right)}{\mathrm{L_v}} \overline{Q}_{ds} \right\rangle_{900} + \left\langle \frac{(\overline{\alpha} - 1)}{\mathrm{L_v}} \overline{Q}_{ce} \right\rangle_{900} \\ &= \left\langle \frac{\overline{\alpha}}{\mathrm{L_v}} Q_1 \right\rangle_{900} + \langle \overline{M} \rangle_{900} \end{aligned} \tag{2.18}$$

Examination of equation 2.18 indicates that many different processes could potentially lead to an increase in C_{free}. An increase in net freezing, radiative heating, or vertical eddy fluxes of DSE would result in an increase in C_{free}. Net deposition and net condensation occurring where $\overline{\alpha}$ exceeds 0.8 and 1.0 respectively would also result in an increase in C_{free}. In addition, the redistribution of any of these terms such that their vertical profiles became more bottom-heavy would result in an increase in C_{free}. Unfortunately the limited output available from the ECMWF does not allow for the analysis of many of the individual terms in equation 2.18. Yet, as will be shown in a subsequent section, careful examination of the available terms allows important conclusions to be drawn about the changing character of C_{free} throughout the MJO lifecycle.

In summary, application of a WTG balance framework to the MJO in the eastern Indian Ocean has allowed variations in large-scale vertical moisture advection within the free troposphere to be diagnosed from variations in apparent heating. Intraseasonal variations in large-scale vertical moisture advection within the free troposphere can, to first order, be understood as resulting from intraseasonal variations in apparent heating occurring in the mean state moist thermodynamic environment of the region. Anomalous radiative heating plays a dominant role in driving anomalous large-scale vertical advective moistening in the lower free troposphere during the enhanced phase, while the remaining apparent heating processes are the dominant drivers of anomalous large-scale vertical advective moistening in the mid and upper free troposphere. A reduction in shortwave radiative heating in the lower free troposphere during the enhanced phase results in anomalous large-scale vertical advective drying, partially opposing the anomalous large-scale vertical advective moistening that results from the reduction of longwave radiative cooling below 400 hPa. The vertically integrated MSE and moisture budgets will now be used to investigate variations in C and C_{free}.

2.3.2.3. Column MSE in WTG balance

In this section, the column MSE budget is used to assess the robustness of conclusions drawn in previous sections. Applying WTG balance (i.e. equations 2.13 - 2.15) above the boundary layer, and vertically integrating equation 2.12 through the depth of the troposphere gives

$$\begin{aligned}\frac{1}{\mathrm{L_v}}\left(\left\langle\frac{\partial\overline{h}}{\partial t}\right\rangle-\left\langle\frac{\partial\overline{s}}{\partial t}\right\rangle_{1000}^{900}\right)=\left\langle\frac{\partial\overline{q}}{\partial t}\right\rangle&=-\left\langle\overline{\mathbf{V}}_{\mathbf{h}}\cdot\nabla\overline{q}\right\rangle+\langle C\rangle\\&=-\left\langle\overline{\mathbf{V}}_{\mathbf{h}}\cdot\nabla\overline{q}\right\rangle+C_{free}+BL+\frac{1}{\mathrm{L}_v}\overline{SLHF}\end{aligned}\tag{2.19}$$

As intraseasonal variations in the boundary layer DSE tendency are less than $1\frac{\mathrm{W}}{\mathrm{m}^2}$ (not shown), negligible in comparison to other budget terms, Equation 2.19 shows that under WTG balance the column MSE budget closely approximates the column moisture budget (equation 2.4).

One benefit of the column moisture budget is that it offers a clean separation between moisture variations driven by surface fluxes of moisture (i.e. SLHF) and those driven by processes occurring within the atmospheric column. One benefit of deriving the column moisture budget from the MSE budget using a WTG balance framework is that it leads to equation 2.18, which provides insight to the physical mechanisms that can drive changes in C_{free}. A considerable disadvantage of using the moisture budget alone to investigate the MJO is the substantial budget residual (Fig. 2.5a) which, being larger than several of the terms being investigated, brings into question the robustness of conclusions drawn from such an analysis. The residual appears to be due to the tendency of ERAi to underestimate precipitation anomalies associated with the MJO when compared to observations, as recently observed during the DYNAMO field campaign (Sobel et al. 2014). Estimates of precipitation anomalies associated with the MJO based on ERAi are systematically much less than those based on either TRMM or GPCP, which tend to agree fairly well (Morita et al. 2006; Benedict and Randall 2007; Lau and Wu 2010; Kiranmayi and Maloney 2011; Sobel et al. 2014; Kim et al. 2014b). This motivated the choice to calculate C as the residual of the moisture tendency and horizontal advection (Figures 2.2e, 2.3e), and to calculate the sum of C_{free} and BL as the residual of the moisture tendency, horizontal advection, and $SLHF$ (Figures 2.2g, 2.3g). As MSE is conserved during condensation and evaporation, the MSE budget benefits from not needing to accurately quantify net condensation. This allows for approximate

closure of the MSE budget, such that the MSE budget residual (Fig. 2.5b) is smaller than any term from which conclusions are drawn in this study.

The various terms of the MSE budget are presented in Figure 2.11. Comparison of Figure 2.3 and Figure 2.11 shows that moisture anomalies account for $\sim 90\%$ of MSE anomalies, and that WTG balance assumptions made in equations 2.14 and 2.15 approximately hold. Under WTG balance, both the moisture budget and the MSE budget provide a similar assessment of the role of anomalous horizontal moisture advection and C anomalies (Figs. 2.3d,e and 2.11c,d respectively) in the propagation and maintenance of moisture anomalies, providing confidence in conclusions drawn in earlier sections. Figures 2.11e,f show the sum of C_{free} and BL anomalies as assessed by the MSE budget, with and without inclusion of the budget residual respectively. While the moisture budget suggests that the net effect of C_{free} and BL anomalies is to further grow moisture anomalies early in the enhanced phase (Fig. 2.3g), the MSE budget assessments provided in Figures 2.11e,f suggest that the net effect of C_{free} and BL anomalies is to further enhance moisture anomalies later in the enhanced phase. It therefore remains uncertain whether the net effect of C_{free} and BL anomalies is to aid the growth of column moisture anomalies, support column moisture anomalies when they are largest, or slow the reduction of column moisture anomalies. However, the moisture budget and MSE budget assessments are similar in that they suggest that the net effect of C_{free} and BL anomalies plays no role in "discharging" moisture anomalies during the enhanced phase, providing confidence that anomalous large-scale vertical moisture advection meets or exceeds anomalous moisture removal by microphysical processes throughout the enhanced phase.

In summary, it has been shown that, when interpreted using a WTG balance framework, the MSE budget supports the conclusions drawn in previous sections using the moisture budget. Foremost among these conclusions is that anomalous moistening by large-scale vertical moisture advection meets or exceeds anomalous drying by microphysical processes in the enhanced phase, and that anomalous drying by large-scale vertical moisture advection meets or exceeds the anomalous moistening by microphysical processes in the suppressed phase. The approximate closure of the MSE budget provides confidence that this conclusion is robust.

2.3.2.4. Variations in the column process and the importance of radiative feedbacks

Results presented in previous sections have shown that C anomalies act to enhance moisture anomalies where they are largest. C anomalies result from variations in surface moisture fluxes, as well as large-scale vertical moisture advection and microphysical processes within both the boundary layer and free troposphere, given by the terms BL and C_{free} respectively. As it is not possible to quantify C_{free} and BL individually given the data available from the ECMWF, their relative importances in destabilizing the MJO can not be addressed. Yet careful examination of the available fields allows the effect of the changing ensemble cloud population on large-scale moisture to be assessed, and the importance of radiative feedbacks to destabilizing the MJO to be addressed.

Examination of fields where only high frequency variability (< 20 days) has been removed provides insight to the effect of the changing ensemble cloud population on large-scale moisture, and how the ensemble cloud population may respond to an anomalous moisture source, such as enhanced SLHF or boundary layer moisture convergence. Before discussing Figure 2.12, please note that each term has been vertically integrated from 900-100 hPa, the levels

where WTG balance is applicable, and that only a 20-day low-pass filter has been applied. The numerators of the terms plotted in Figures 2.12a,b,c are the latent heat variations associated with $\left\langle \overline{\alpha}\left(Q_1 - \overline{Q}_R\right)\right\rangle$, $\left\langle \overline{\alpha}\overline{Q}_R\right\rangle$, and $\left\langle \overline{\alpha}Q_1\right\rangle$ respectively. In order to determine the amount of moisture re-supplied by each of these terms per unit microphysical moisture loss, each term plotted in Figure 2.12 has been normalized by $\left\langle Q_1 - \overline{Q}_R\right\rangle$. Intraseasonal variations in the Lagrangian tendency of specific ice water content were calculated (not shown) and found to be a negligible part of the MSE budget. Assuming little precipitation reaches the surface in the form of ice, this implies that $\left\langle Q_1 - \overline{Q}_R\right\rangle$ is approximately equal to net condensational heating of the column. In other words, each term in Figure 2.12 is approximately normalized by net condensational heating of the column. Therefore Figure 2.12 can be interpreted as the amount of moisture supplied by each of these respective processes via large-scale vertical moisture advection per unit moisture loss due to net condensation.

Figure 2.12a shows the large-scale vertical moisture advection associated with apparent heating by microphysical processes and sub-grid scale DSE fluxes normalized by moisture loss due to net condensation, therefore values less than one reflect a net drying of the column. Figure 2.12a shows that the net effect of $Q_1 - \overline{Q}_R$ is always to discharge moisture from the column, but to do so with surprising inefficiency. Remember that $Q_1 - \overline{Q}_R$ represents the apparent heating effect an ensemble cloud population has on its environment with the exclusion of radiative impacts. During the suppressed phase, more than 95% of the moisture lost by net condensation is resupplied by large-scale vertical moisture advection associated with $\left\langle \overline{\alpha}\left(Q_1 - \overline{Q}_R\right)\right\rangle$, while slightly less than 90% is resupplied during the enhanced phase. In other words, excluding its radiative impacts, the ensemble cloud population does become more efficient at discharging moisture from the environment during the enhanced phase, and

less efficient at discharging moisture from the column during the suppressed phase, but these changes are relatively modest. The change in efficiency is driven by the progression from a bottom-heavy to top-heavy heating profile that occurs in the transition from suppressed to enhanced conditions. The remarkable inefficiency with which the net effects of an ensemble cloud population, excluding radiative impacts, remove moisture from the environment has important implications for the response of the cloud population to anomalous moisture sources. A disproportionately large increase in the net condensation produced by an ensemble cloud population would be required for the net effects of the ensemble cloud population, excluding radiative impacts, to remove an anomalous moisture source (e.g. enhanced SLHF). In other words, relatively small anomalous moisture sources could sustain relatively large increases in precipitation. Similar characteristics of the warm pool climatology were discussed by Sobel (2003).

This disproportionate response is exacerbated by the reduction of the large-scale vertical advective drying associated with radiative cooling that occurs when net condensation increases. Figure 2.12b shows that large-scale vertical advective drying associated with radiative cooling is always acting to dry the column more than the net effect of $Q_1 - \overline{Q}_R$ (Fig. 2.12a), even during the enhanced phase when radiative cooling is reduced and the $Q_1 - \overline{Q}_R$ profile becomes top-heavy. In the mean state, the net effect an ensemble cloud population has on the large-scale environment (i.e. microphysical processes, radiative effects, and associated large-scale vertical advection) is always to remove moisture. Net condensation and the large-scale vertical advective drying associated with radiative cooling act together to remove moisture from the environment. But on intraseasonal timescales, an increase in net condensation is accompanied by a reduction in radiative cooling and associated large-scale

vertical advective drying. The amount of drying associated with radiative cooling that occurs per unit net condensation changes dramatically throughout the MJO lifecycle, varying from $\sim 70\%$ during the suppressed phase to $\sim 20\%$ during the enhanced phase (Fig. 2.12b). The result is that, per unit net condensation, approximately three times more moisture is re-supplied by the large-scale vertical moisture advection associated with the total apparent heating of an ensemble cloud population and its radiative impacts during the enhanced phase than during the suppressed phase (Fig. 2.12c). The importance of these radiative feedbacks for destabilizing the MJO is now quantified.

Figure 2.13a shows intraseasonal variations in the column latent heat tendency associated with radiative heating anomalies above the boundary layer, which act as a strong positive feedback to moisture anomalies throughout the MJO lifecycle. As shown in the previous section, these variations are largely the result of reduced longwave radiative cooling during the enhanced phase, and increased longwave radiative cooling during the suppressed phase. When these variations are subtracted from intraseasonal variations in the sum of C_{free} and BL (Fig. 2.13b), the net effect of microphysical processes, boundary layer moisture convergence, and the large-scale free tropospheric vertical moisture advection associated with apparent heating by microphysical processes and sub-grid scale DSE fluxes is obtained. In other words, Figure 2.13b shows the net effect boundary layer processes and the ensemble cloud population, excluding radiative impacts, have on large-scale moisture throughout the MJO lifecycle. The effect is considerable drying during the later stages of the enhanced phase when stratiform precipitation is enhanced, and considerable moistening in the later stages of the suppressed phase when the proportion of shallow and congestus clouds are enhanced (Morita et al. 2006; Lau and Wu 2010; Riley et al. 2011). This is likely explained by the

progression from a bottom-heavy to top-heavy heating profile that occurs in the transition from suppressed to enhanced conditions (Figs. 2.8c,d), and the relatively small values of $\overline{\alpha}$ in the upper troposphere. Figure 2.13b suggests that the net effect of C_{free} and BL would act to stabilize, not destabilize, the MJO if radiative feedbacks were not present. In fact, Figure 2.13c suggests that the enhancement of SLHF during the enhanced phase would not be sufficient to overcome the anomalous drying effect that would result from the sum of C_{free} and BL if radiative feedbacks were not present. Given the small anomalous drying tendency observed during the enhanced phase in Figure 2.13c, it seems plausible that the MJO could still be destabilized in an environment with relatively weak radiative feedbacks or relatively large variations in SLHF or boundary layer moisture convergence.

In summary, intraseasonal variations in radiative heating appear to play a crucial role in destabilizing the MJO, and have been shown to be essential in preventing the net effects of C_{free} and BL from reducing moisture anomalies. Throughout the MJO lifecycle, apparent heating due to microphysical processes and sub-grid scale eddy fluxes of DSE is associated with large-scale vertical moisture advection that replaces most of the moisture removed by net condensation, suggesting that a disproportionately large convective response could be maintained by an anomalous moisture source or sink. While the apparent heating profile of the ensemble cloud population becomes more top-heavy during the enhanced phase, and therefore produces less large-scale vertical moisture advection per unit apparent heating, the reduction of radiative cooling results in an increase in the ratio of apparent heating to net condensation. The net effect is that approximately three times more large-scale vertical moisture advection associated with the apparent heating of an ensemble cloud population is

realized per unit net condensation during the enhanced phase than during the suppressed phase.

2.4. Conclusions

The anomalous MSE and moisture budgets of the MJO were investigated using 31 years of ERA Interim Reanalysis data. WTG balance is approximately satisfied, allowing the mechanisms controlling moisture variations associated with the MJO to be assessed using both MSE and moisture budgets. To first order, precipitation anomalies are maintained by anomalous large-scale vertical moisture advection associated with the changing ensemble cloud population and its radiative effects. Composite analysis of the MJO in the eastern Indian Ocean clearly demonstrates that column process anomalies (i.e. the net effect of large-scale vertical moisture advection, microphysical processes, and SLHF) act to enhance column moisture anomalies in regions of increased precipitation. This enhancement of moisture anomalies results from an increase in SLHF, as well anomalous large-scale vertical moisture advection meeting or slightly exceeding the anomalous removal of moisture by microphysical processes. Increased SLHF appears to be insufficient to destabilize the MJO in the absence of radiative feedbacks, which play a crucial role in driving a positive feedback between column moisture anomalies and the net effects of anomalous large-scale vertical moisture advection and anomalous microphysical processes. The further enhancement of column moisture anomalies by column process anomalies is damped by anomalous horizontal moisture advection, which also acts to propagate the region of enhanced column moisture eastwards. The geographical variability of these processes was investigated using objective methods developed in Part I of this study. The processes controlling moisture variations associated with the MJO in the eastern Indian Ocean are fairly representative of

those occurring across the rest of the Indian Ocean, as well as oceanic regions of the Maritime Continent. The role of the various processes becomes less clear around the dateline.

Application of a WTG balance framework to the MSE budget of the MJO has been used to provide insight into the physical mechanisms responsible for intraseasonal variations in large-scale vertical moisture advection within the free troposphere. To first order, intraseasonal variations in the magnitude and vertical structure of vertical velocity can be diagnosed from apparent heating. Intraseasonal variations in large-scale vertical moisture advection are largely explained by intraseasonal variations of apparent heating occurring in the mean state moist thermodynamic environment of a region. Anomalous apparent heating by microphysical processes and sub-grid scale eddy fluxes of DSE is associated with a stepwise pattern of moistening that begins in the lower troposphere during the suppressed phase, then transitions to the mid and finally upper troposphere in the enhanced phase, during which time anomalous drying is observed below 800 hPa. Anomalous moistening associated with anomalous radiative heating offsets this anomalous lower tropospheric drying, and re-enforces the moistening of the mid-troposphere during the enhanced phase. In the column integral, this effect is strong enough to offset the anomalous drying by the net effect of microphysical processes and their associated large-scale vertical moisture advection.

Examination of vertical profiles of longwave and shortwave radiative heating anomalies provides a rich depiction of their respective roles in driving anomalous moisture tendencies, which can not be gained by examining their column integrated counterparts. During the enhanced phase, substantial lower and mid tropospheric moistening results from a reduction in longwave cooling below 400 hPa. This reduction of longwave radiative cooling plays a crucial role in the MJO, allowing anomalous large-scale vertical moisture advection to

meet or exceed anomalous removal of moisture by microphysical processes, thereby driving a positive feedback between the net effect of these processes and moisture anomalies. Near zero column shortwave heating anomalies result from a vertical dipole structure of anomalous heating and cooling that is centered near 550 hPa. Due to the high moisture sensitivity of the lower troposphere to apparent heating, the reduction of shortwave heating below 550 hPa during the enhanced phase is associated with anomalous drying that is comparable in magnitude to anomalous SLHF. While beyond the scope of this study, the importance of intraseasonal variations in shortwave radiative heating motivates further investigation into potential interactions between the diurnal cycle and the MJO via radiative feedbacks.

Changes in SLHF and horizontal moisture advection accompany changes in the ensemble cloud population. The results of this study suggest that disproportionately large changes in net condensation could be expected to result from changes in SLHF or horizontal moisture advection, as more than 85% of the moisture removed by net condensation during the enhanced phase is resupplied by the large-scale vertical moisture advection associated with microphysical processes and sub-grid scale eddy fluxes of DSE. It is worth reiterating that this disproportionate response would act to remove moisture anomalies in the absence of radiative feedbacks, which appear to play an essential role in destabilizing the MJO. The increase of horizontal advective drying appears to be the only process damping the further growth of moisture anomalies during the latter portions of the enhanced phase.

2.4.1. Discharge-recharge theory, moisture mode theory, and destabilization of the MJO

Discharge-recharge theory and moisture mode theory are compatible in many ways. Yet it is generally understood, if not explicitly stated, that suppressed convective conditions

play a destabilizing role, and enhanced convective conditions a stabilizing role, in discharge-recharge theory, while both conditions play a destabilizing role in moisture mode theory. The results of this study highlight that the distinction between the two can be incredibly fine.

It has been shown that when radiative feedbacks are excluded, column process anomalies have a weak stabilizing effect on the MJO. This result suggests that MJO-like variability with the characteristics of a "discharge-recharge" phenomena may be produced in an environment with relatively weak radiative feedbacks or relatively strong SLHF anomalies. This may be how MJO-like variability is maintained in some model simulations (Maloney et al. 2010), and help explain the wide-ranging results of mechanism denial experiments. Yet the results of this study, as well as the results of Chikira (2014) and Janiga and Zhang (2016), suggest that strong radiative feedbacks are a fundamental feature of the MJO, and that the characteristics of the MJO are those of a moisture-mode phenomena. What criteria should be considered when assessing how "MJO-like" model variability is? Is it sufficient to have a large-scale coupling of deep convection and tropospheric circulation anomalies that propagates eastward at $\sim 5\ \mathrm{m\,s^{-1}}$? Or should a realistic destabilization mechanism also be a prerequisite to be considered MJO-like variability?

The results of this study paint a picture of the MJO as a persistent, but somewhat glass-jaw phenomenon. Persistent in that a positive feedback between column moisture anomalies and the net effects of an ensemble cloud population appear to systematically push environmental conditions in the Indian Ocean and oceanic regions of the Maritime Continent towards extremes of enhanced or suppressed convection during periods of MJO activity. Glassjaw in that this positive feedback appears to be fairly modest, easily overcome by transient events

such as dry air intrusions from the subtropics. Foremost among the shortcomings of this paper is the inability to systematically address the role of boundary layer processes, which have been shown to be important on intraseasonal timescales (DeMott et al. 2014). Further investigation into the role various microphysical processes play in modifying the vertical structure and magnitude of apparent heating throughout the MJO lifecycle is needed. As only a single reanalysis product was implemented in this study, the robustness of conclusions presented here should be tested using other observational, reanalysis, and modeling products.

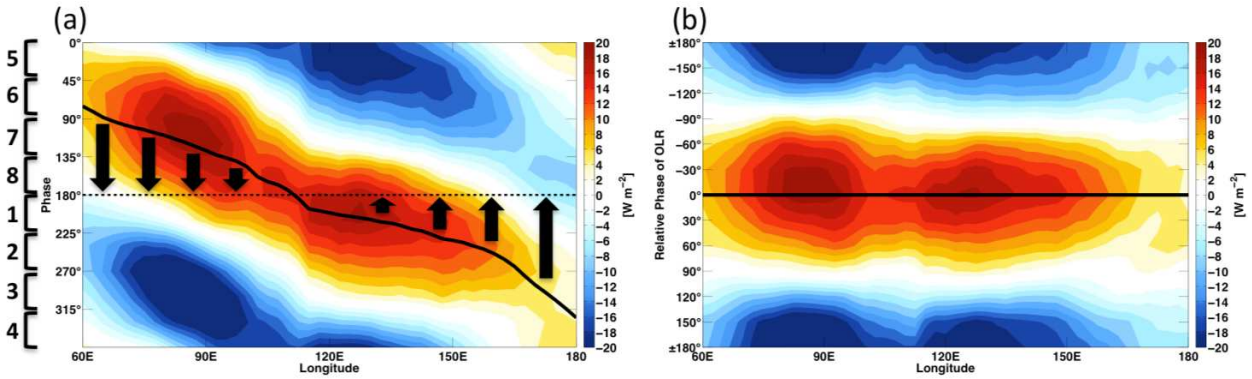

FIG. 2.1. Figure 7 from Part I. Composite of latitudinally averaged (15°N – 15°S) NOAA OLR anomalies (shading) as a function of (a) phase of the FMO index and (b) relative phase of OLR in the FMO index. Days when the magnitude of the FMO index did not exceed a value of 1 were excluded. Latitudinally averaged OLR anomalies were binned by (a) phase and (b) relative phase, with bins spanning 60° calculated every 30°. The solid black line is the grid point phase of OLR in the FMO index. The bold number adjacent to the brackets in (a) indicate the corresponding Realtime Multivariate MJO (RMM) phase, as defined by Wheeler and Hendon (2004). The block arrows indicate how the data is "shifted" in the transition from (a) to (b). In (b), moving downwards from the top of the figure corresponds with the transition from enhanced convection (top of figure, negative OLR anomalies) to suppressed convection (center of the figure, positive OLR anomalies) and back to enhanced convection (bottom of figure, negative OLR anomalies) at each longitude. Please note that subsequent plots are shifted such that the enhanced phase of the MJO is located in the center of the figure

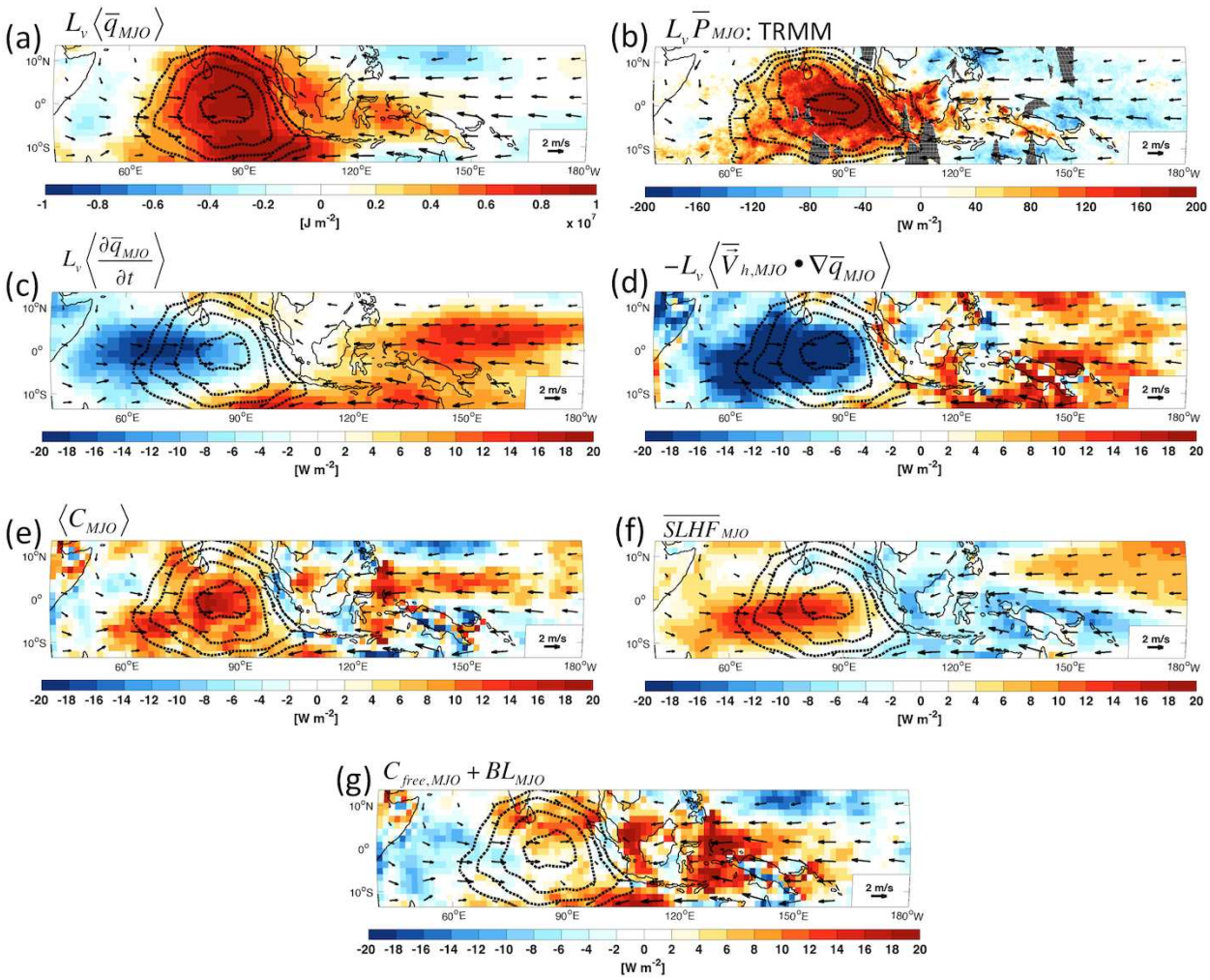

FIG. 2.2. Composite anomalies of column specific humidity (a), TRMM precipitation (b), moisture tendency (c), horizontal moisture advection (d), column process (e), surface latent heat flux (SLHF) (f), and the sum of C_{free} and BL (g). Terms (a)-(e),(g) have been multiplied by the latent heat of vaporization. Solid (dashed) contours correspond to positive (negative) NOAA OLR anomalies every 5 $\frac{\mathrm{W}}{\mathrm{m}^2}$ beginning at 15 $\frac{\mathrm{W}}{\mathrm{m}^2}$. Arrows indicate ERAi 850 hPa horizontal wind anomalies, and a reference arrow is provided in the lower right corner. Please note that composites (a) and (c)-(h) result from 75 independent events from 1980-2011, while composite (b) results from 28 events from 1999-2011, and that the colorbar in (b) spans -200 to 200 $\frac{\mathrm{W}}{\mathrm{m}^2}$. Stippling in (b) indicates missing TRMM data. The subscript $_{MJO}$ indicates bandpass filtering to 20-100 days. See text for description of compositing technique.

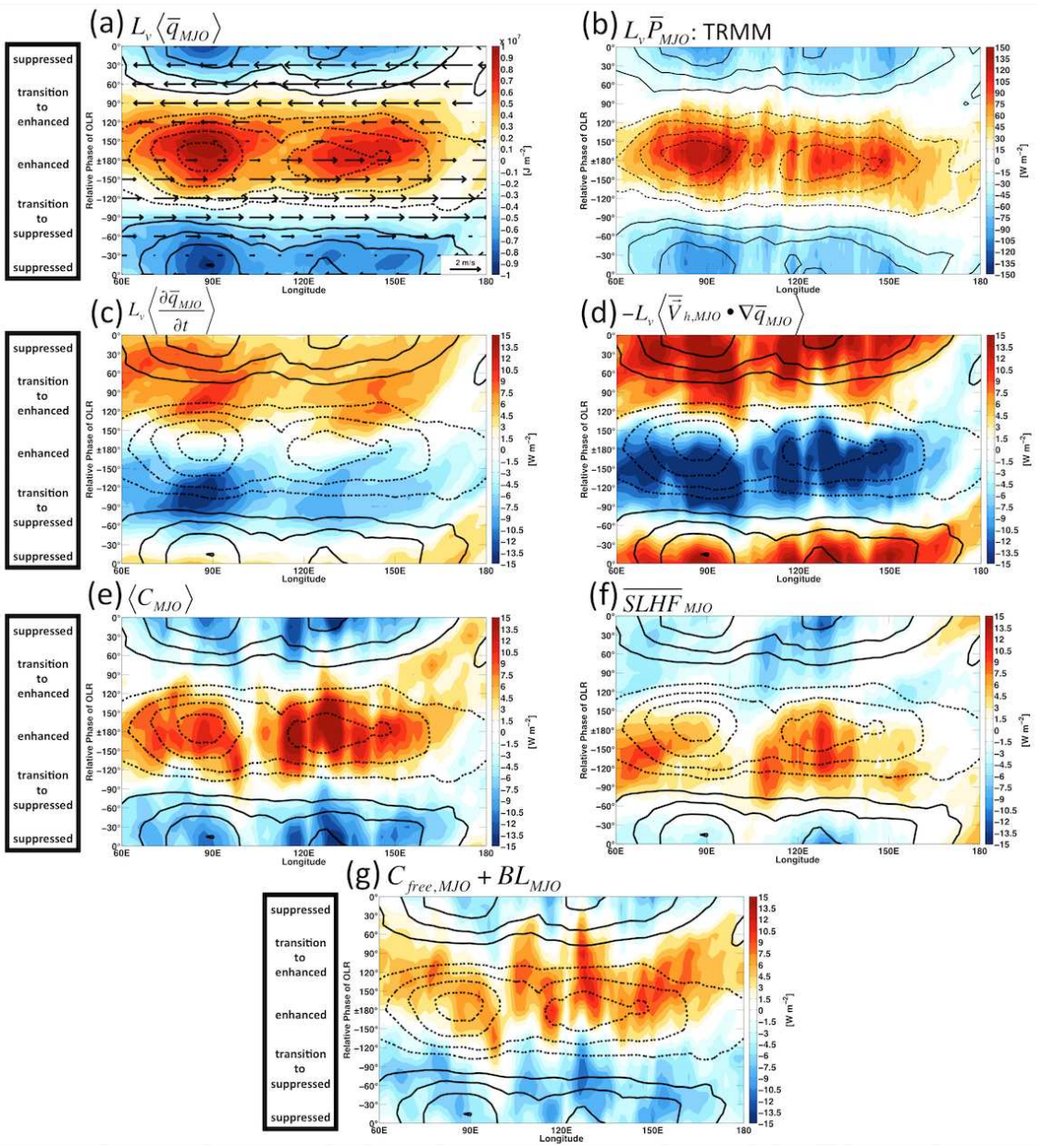

FIG. 2.3. Composite of latitudinally averaged (13.5°N – 13.5°S) ERAi column latent heat (a), TRMM precipitation (b), column latent heat tendency (c), column horizontal advection of latent heat (d), column process (e), SLHF (f), and the sum of C_{free} and BL(g) as a function of relative phase of OLR. Solid (dashed) contours correspond to positive (negative) NOAA OLR anomalies every 6 $\frac{\mathrm{W}}{\mathrm{m}^2}$ beginning at 6 $\frac{\mathrm{W}}{\mathrm{m}^2}$. Arrows in (a) and (b) indicate ERAi U850 anomalies, and a reference arrow is provided in the lower right corner. Moving downwards from the top of the figure corresponds with the transition from suppressed convection (top of figure, positive OLR anomalies) to enhanced convection (center of the figure, negative OLR anomalies) and back to suppressed convection (bottom of figure, positive OLR anomalies) at each longitude. The subscript $_{MJO}$ indicates bandpass filtering to 20-100 days. See text for description of compositing technique.

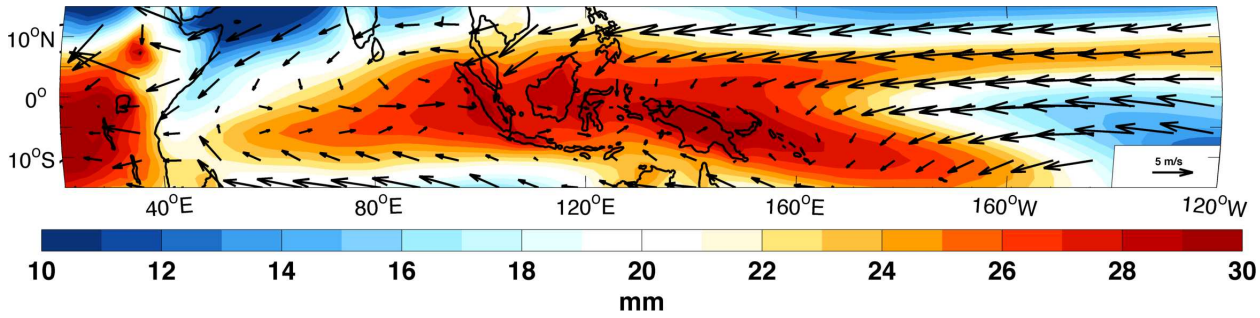

FIG. 2.4. ERAi mean specific humidity integrated from 850 to 500 hPa (color contours) and 850 hPa horizontal wind for 1980-2011 winters (October 1 - April 30). Reference wind vectors are provided in the lower right corner of both panels.

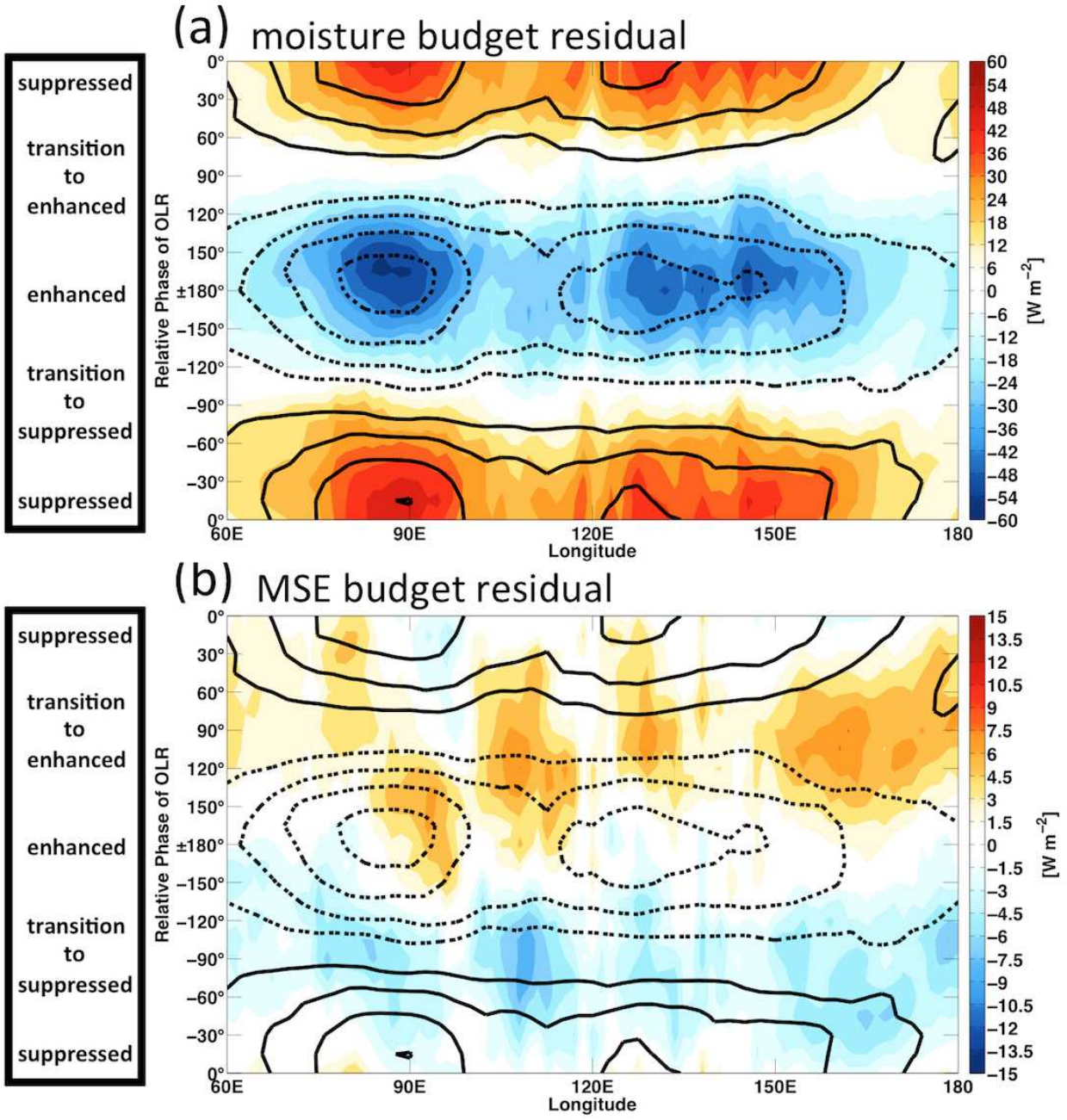

FIG. 2.5. As in Figure 2.3, except color shading is the moisture budget residual (a) and the MSE budget residual (b).

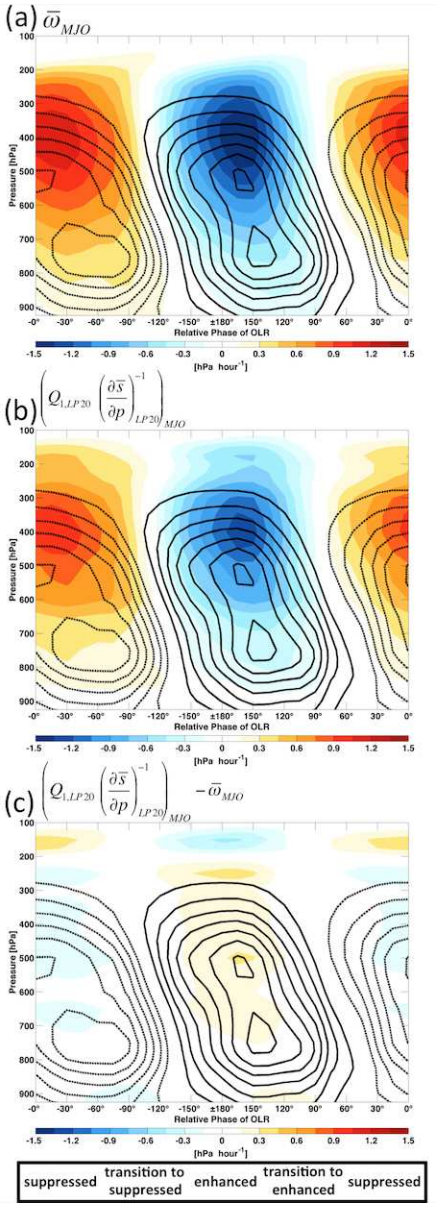

FIG. 2.6. Composite anomalies of vertical velocity (color shading) and specific humidity (contours) throughout a composite convective lifecycle of the MJO in the eastern Indian Ocean (5°N − 10°S,75°E − 85°E). Solid (dashed) contours correspond to positive (negative) specific humidity anomalies every 0.1 $\frac{\text{g}}{\text{kg}}$ beginning at 0.1 $\frac{\text{g}}{\text{kg}}$. Moving from the right side to the left side of the figure corresponds with the transition from suppressed convection to enhanced convection and back to suppressed convection, as indicated at the bottom of the figure. The subscripts $_{LP20}$ and $_{MJO}$ indicate application of 20-day lowpass and 20-100 day bandpass filtering respectively. See text for description of compositing technique.

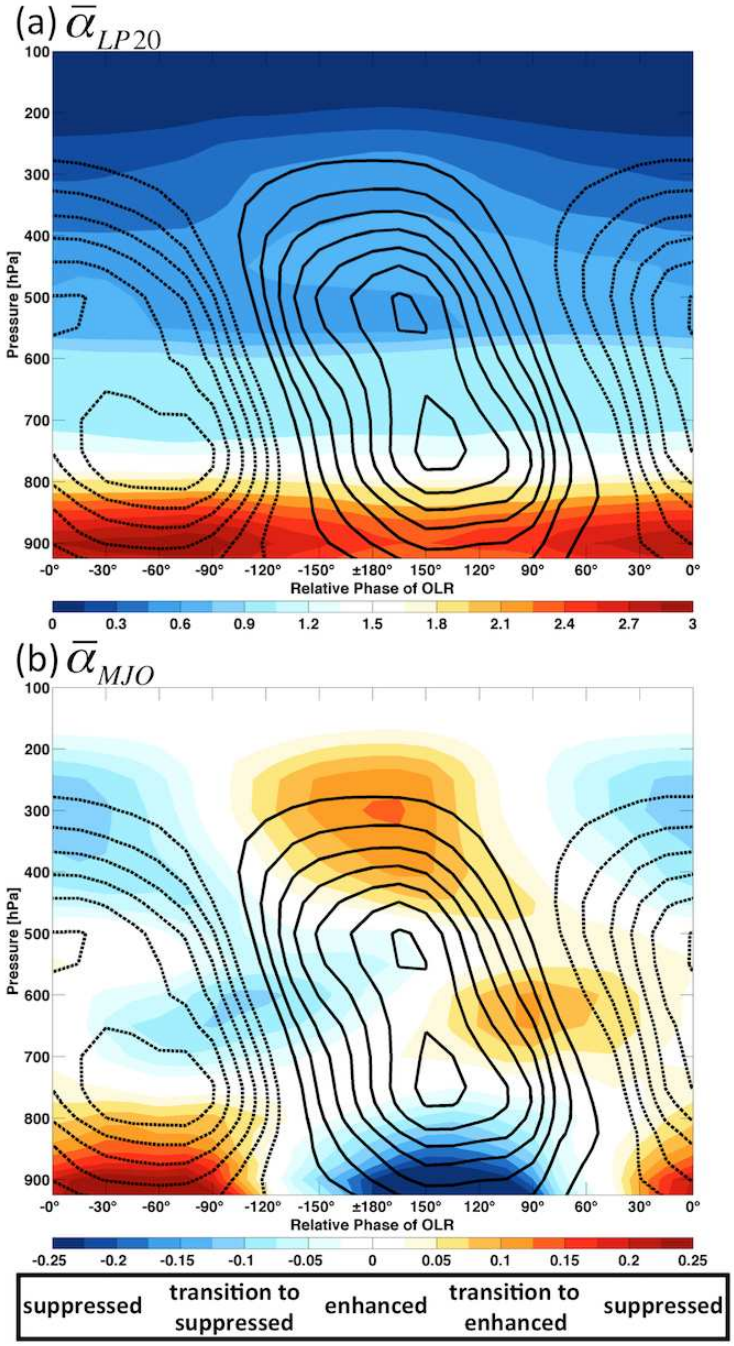

FIG. 2.7. As in Figure 2.6, except color shading is $\overline{\alpha}$. The subscripts $_{LP20}$ and $_{MJO}$ indicate application of 20-day lowpass and 20-100 day bandpass filtering respectively.

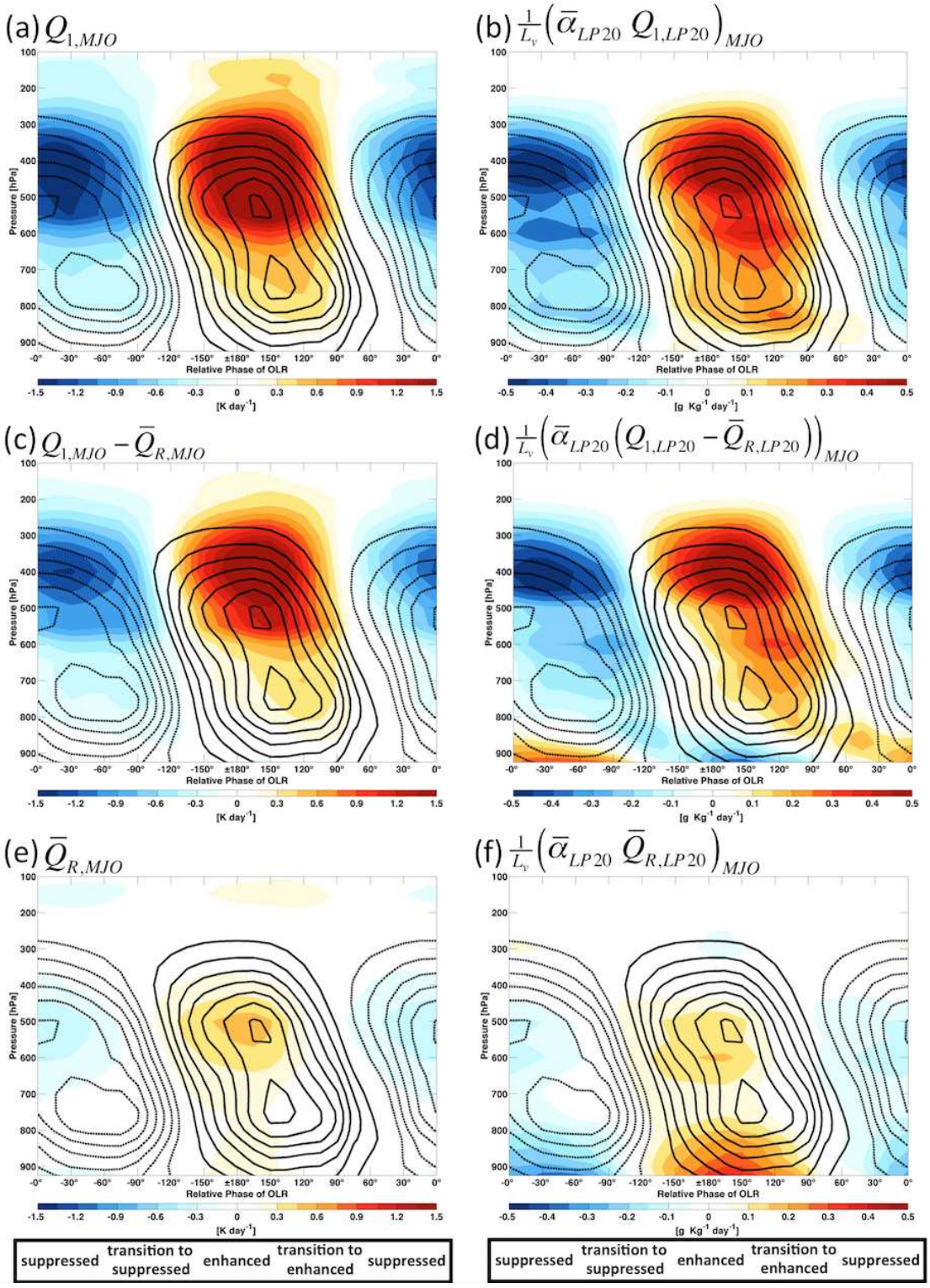

FIG. 2.8. As in Figure 2.6, except color shading is various apparent heating terms and their associated moisture tendencies under weak temperature gradient balance. The subscripts $_{LP20}$ and $_{MJO}$ indicate application of 20-day lowpass and 20-100 day bandpass filtering respectively.

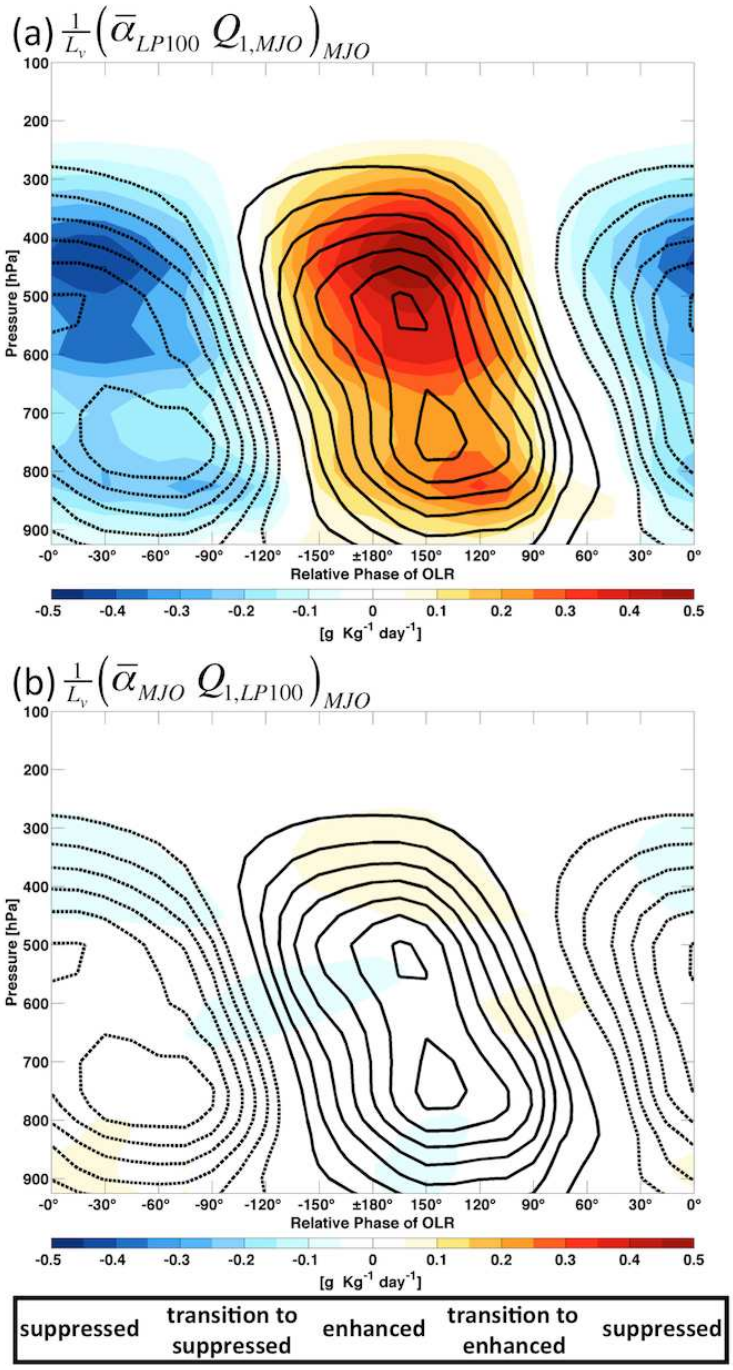

FIG. 2.9. As in Figure 2.6, except color shading is the moisture tendency associated with various apparent heating terms under weak temperature gradient balance. The subscripts $_{LP20}$, $_{LP100}$, and $_{MJO}$ indicate application of 20-day lowpass, 100-day lowpass, and 20-100 day bandpass filtering respectively.

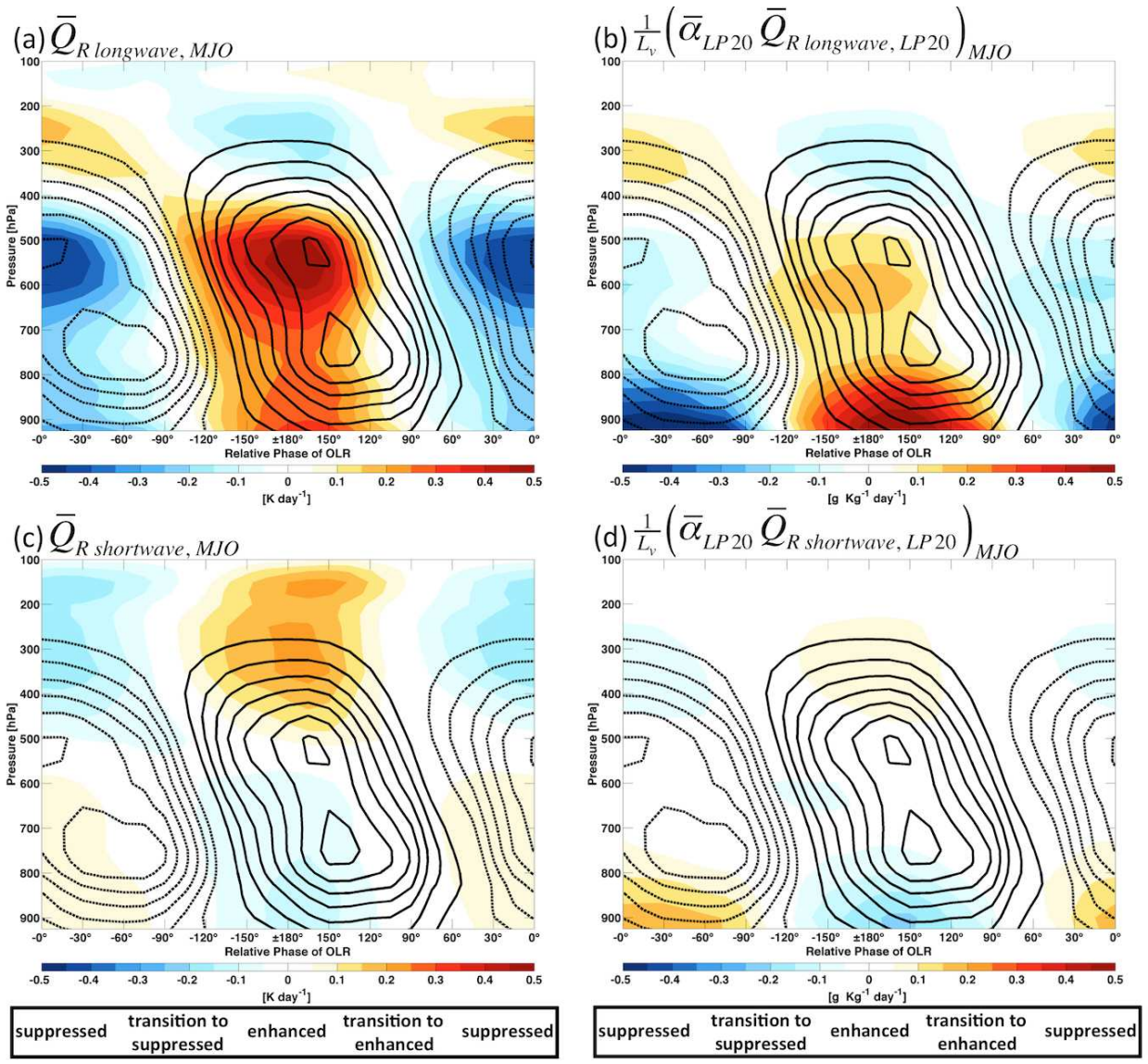

FIG. 2.10. As in Figure 2.6, except color shading is longwave (a) and shortwave (c) radiative heating, and the associated moisture tendencies (b) and (d) under weak temperature gradient balance. The subscripts $_{LP20}$ and $_{MJO}$ indicate application of 20-day lowpass and 20-100 day bandpass filtering respectively.

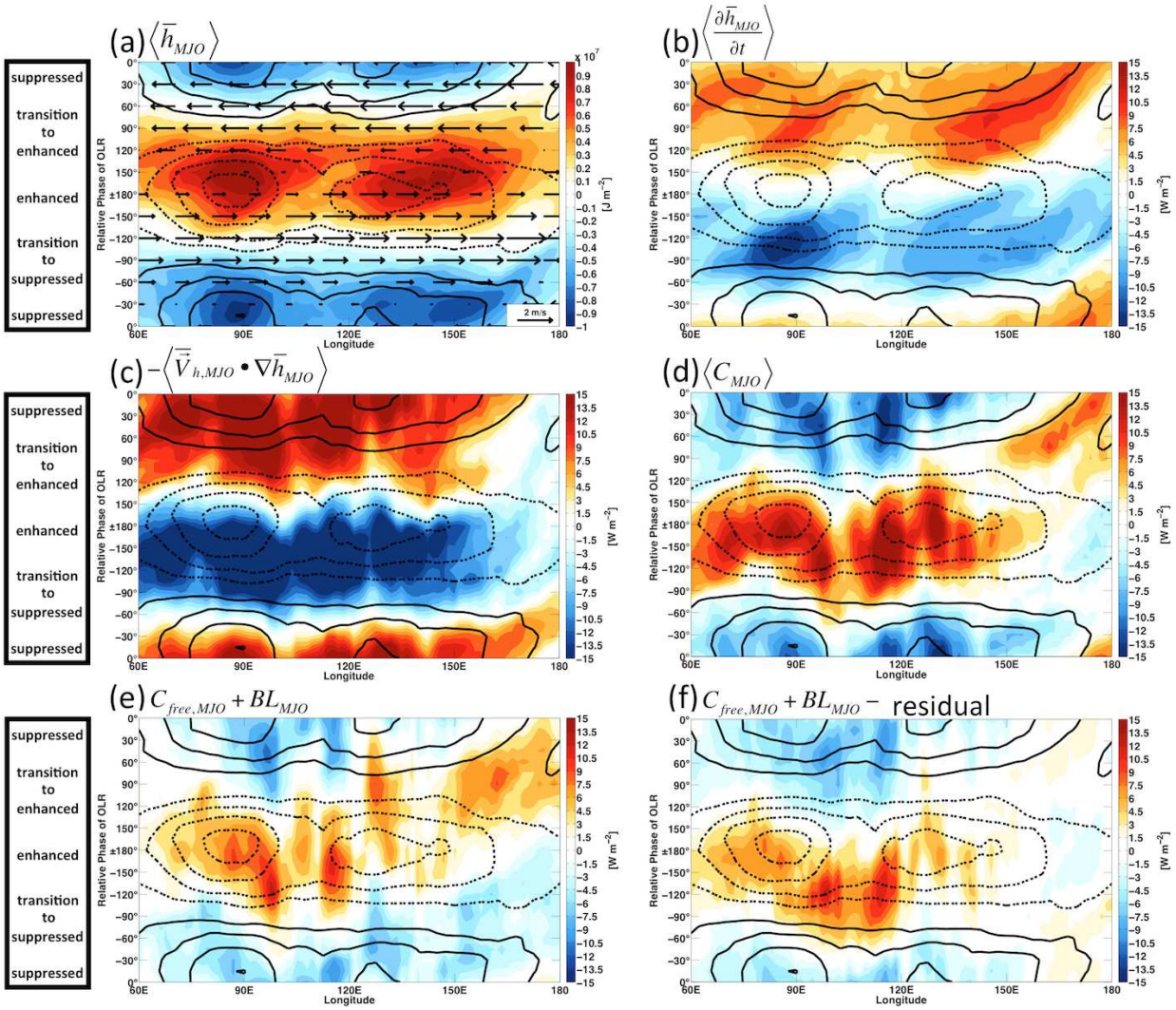

FIG. 2.11. As in Figure 2.3, except color shading is anomalies of column MSE (a), column MSE tendency (b), column horizontal advection of MSE (c), column process (d), the sum of C_{free} and BL (e), and the sum of C_{free} and BL minus the MSE budget residual (f). The subscript $_{MJO}$ indicates bandpass filtering to 20-100 days.

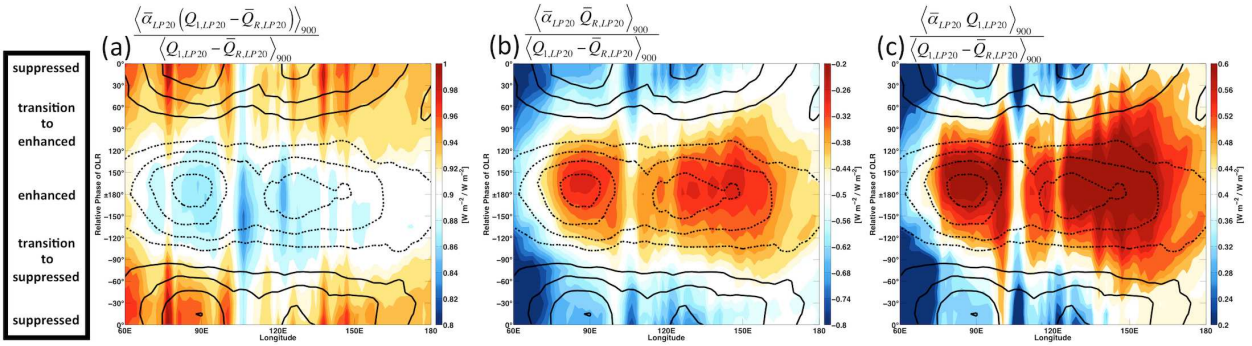

FIG. 2.12. As in Figure 2.3, except color shading is the moisture tendency associated with various apparent heating terms under weak temperature gradient balance approximately normalized by net condensation. Please note that the vertical integral was only taken from 900-100 hPa with each of these terms, as weak temperature gradient balance is not applicable in the boundary layer. The subscripts $_{LP20}$ and $_{MJO}$ indicate application of 20-day lowpass and 20-100 day bandpass filtering respectively.

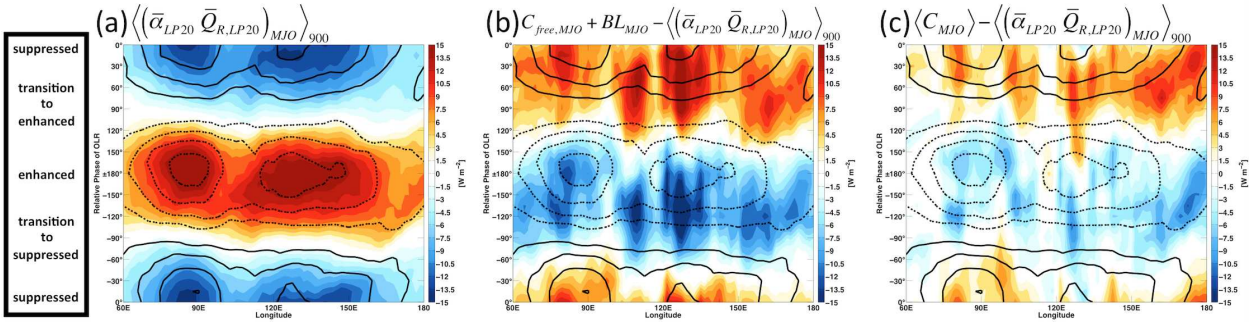

FIG. 2.13. As in Figure 2.3, except color shading is the intraseasonal moisture tendency associated with radiative heating (a), the sum of C_{free} and BL minus the intraseasonal moisture tendency associated with radiative heating (b), and the column process minus the intraseasonal moisture tendency associated with radiative heating. Please note that the vertical integral of the intraseasonal moisture tendency associated with radiative heating was only taken from 900-100 hPa, as weak temperature gradient balance is not applicable in the boundary layer. The subscripts $_{LP20}$ and $_{MJO}$ indicate application of 20-day lowpass and 20-100 day bandpass filtering respectively.

CHAPTER 3

Vertically Resolved Weak Temperature Gradient Analysis of the Madden-Julian Oscillation in SP-CESM

In this chapter, the role that interactions between moisture, convection, and large-scale circulations play in destabilizing and propagating the MJO is investigated using moisture and moisture variance budgets of the MJO in SP-CESM. This chapter is published in the Journal of Advances in Modeling Earth Systems as Wolding et al. (2016).

3.1. Introduction

The organization of clouds spans a wide range of spatial and temporal scales, from phenomena directly observable by individuals within a few hours or less, to those observable only given the perspective provided by modern satellites. Such organization not only manifests itself through variations in weather, but also influences fundamental features of our climate, including the Earth's energy balance, and remains a substantial source of uncertainty in projections of future climate (Stocker et al. 2014; Bony et al. 2015). Large-scale circulations often play an important role in driving the organization of clouds. In turn, the aggregate effect of individual clouds and cloud systems, which broker radiative transfer and redistribute heat, moisture, and momentum, can influence large-scale circulations. This scale interaction provides the potential for feedbacks to develop between clouds and large-scale circulations.

Convective aggregation, a special form of organization that may potentially be driven by such a feedback, has been documented in cloud-system-resolving-model (CSRM) simulations in radiative-convective equilibrium (Bretherton et al. 2005; Wing and Emanuel 2014) and, more recently, in near global (Bretherton and Khairoutdinov 2015) and global scale (Arnold

This chapter is published in the Journal of Advances in Modeling Earth Systems as Wolding et al. (2016).

and Randall 2015) aquaplanet simulations. Under certain conditions, these simulations exhibit the rapid development of dry regions that expand until convection, initially randomly distributed, had self-aggregated into isolated regions. When Earth-like rotation was included in the simulation of Arnold and Randall (2015), the model produced a robust Madden-Julian Oscillation (MJO) that appeared to be destabilized by processes similar to those driving convective aggregation in the non-rotating simulations. Such findings suggest that the processes responsible for convective aggregation in these idealized studies may also play a fundamental role in the real world MJO. Understanding these processes has been posed as one of the "grand challenges" (Bony et al. 2015) to atmospheric science, not only because of their importance for understanding the MJO, but also because of their potential role in climate sensitivity and feedbacks.

Interactions between moisture and convection, both at the convective scale and the large-scale, appear to play a fundamental role in both the MJO and convective aggregation. At the convective-scale, the large lower tropospheric entrainment that occurs in tropical oceanic convection (Lucas et al. 1994; Zipser 2003) allows free tropospheric moisture content to modulate convective activity. Convection can redistribute moisture locally, conditioning the environment in ways that can favor or suppress subsequent convection (Tompkins 2001). At the large-scale, the aggregate effect of a convective population can modify large-scale circulations that, in turn, affect the large-scale moisture content. If regions of enhanced or suppressed convection impact large-scale circulations in such a way that further moistening or drying of those regions occurs respectively, a modal instability, as proposed by moisture mode theory (Sobel et al. 2001; Raymond 2001), may occur (Fuchs and Raymond 2005; Raymond and Fuchs 2009; Sobel and Maloney 2012; Arnold and Randall 2015; Adames

and Kim 2016). Increasing column moisture variance and a progressively more bi-modal distribution of column water vapor may signal the development of such an instability, and are observed in simulations of convective aggregation as well as during periods of enhanced MJO activity. Understanding the processes that act to increase column moisture variance (i.e. promote the development of anomalously moist and dry patches) is an important component of understanding the processes responsible for such modal instability.

Budgets analyses of column moist static energy (MSE) and column MSE variance, commonly used in studies of both the MJO (Maloney 2009; Kiranmayi and Maloney 2011; Andersen and Kuang 2012; Wu and Deng 2013; Kim et al. 2014a; Sobel et al. 2014; Arnold et al. 2015; Wolding and Maloney 2015a) and convective aggregation (Bretherton et al. 2005; Wing and Emanuel 2014; Bretherton and Khairoutdinov 2015; Arnold and Randall 2015; Muller and Bony 2015), have provided great insight to the processes controlling column moisture and column moisture variance. Budget analyses of changes in column MSE, which closely reflect changes in column moisture under weak temperature gradient (WTG) balance, have the desirable attribute of accounting for the coupled nature of apparent heating and moisture convergence driven by that heating, thereby allowing the effect of radiative heating on column moisture to be estimated. While the MJO differs from the convective aggregation produced in modeling studies in important ways, most notably the larger zonal scale and zonal asymmetry of the former, the aforementioned MSE analyses highlight fundamental similarities between these phenomena. These studies generally agree that, when established, both forms of instability are maintained by diabatic feedbacks that transfer MSE up gradient, and that longwave radiative feedbacks play a critical role in this transfer. General agreement also exists that horizontal advection plays an important role in limiting

the further growth of these instabilities once they are established. The role of surface flux feedbacks remains less clear, appearing to play a destabilizing role in observational studies of the MJO (Kiranmayi and Maloney 2011; Kim et al. 2014a; Sobel et al. 2014; Wolding and Maloney 2015a; Riley Dellaripa and Maloney 2015) and being necessary for aggregation in some RCE simulations (Bretherton et al. 2005), while acting to stabilize the MJO in some model simulations (Arnold et al. 2015) and not being critical to aggregation in other RCE studies (Muller and Held 2012).

Another approach to understanding the processes controlling column moisture and column moisture variance, whereby WTG balance is used to diagnose vertical motion from apparent heating (Sobel et al. 2001; Raymond 2001), has been implemented in recent analyses of the MJO (Chikira 2014; Janiga and Zhang 2016; Wolding and Maloney 2015a). This approach is consistent with the column MSE budget approach, and has the added benefit of allowing the vertical advection term of the column MSE budget to be quantitatively partitioned into contributions from various processes including radiative heating, microphysical processes, and sub-grid scale (SGS) eddy transports. This approach is described briefly here, and in more detail in subsequent sections. The tropics are characterized by weak horizontal gradients of pressure and temperature, a consequence of effective gravity wave adjustment that occurs due to the relatively weak influence of planetary rotation near the equator. If variations in heating occur on spatial and temporal scales that allow effective gravity wave adjustment to occur, a first order balance between apparent heating and large-scale vertical advection of dry static energy (DSE) (i.e. adiabatic cooling) results. This balance is referred to as the WTG balance, and it proves useful in that it allows the large-scale vertical velocity to be diagnosed if both the apparent heating and static stability are known. Given the

vertical moisture gradient, this vertical velocity can then be used to calculate the large-scale vertical moisture advection associated with an apparent heating. Moreover, by considering the individual contributions of various apparent heating processes (i.e. microphysical processes, radiative heating, and SGS eddy transports) to the total apparent heating, the individual contributions of these processes to the total vertical moisture advection can be diagnosed. As highlighted by Chikira (2014), this approach has several advantages when compared to column integrated MSE budget analysis, including the ability to vertically resolve and more accurately assess the effect of various apparent heating processes on moisture. While vertically resolved WTG balance analyses have come to similar conclusions as column MSE analyses regarding the importance of longwave radiative feedbacks, they also highlight important information lost in column integrated analysis. For example, shortwave radiative heating anomalies associated with the MJO have a vertical dipole structure that, when vertically integrated, have a negligible impact on the column MSE budget. However, given the high moisture sensitivity of the lower troposphere to apparent heating (e.g. Chikira (2014)), shortwave radiative heating anomalies in the lower troposphere are associated with sizable moisture tendencies relevant to the moisture budget of the MJO (Ma and Kuang 2011; Wolding and Maloney 2015a; Janiga and Zhang 2016). The importance of such vertical structure to simulated convective aggregation is strongly supported by the results of Muller and Bony (2015), who showed that even when the column integrated radiative heating remained constant, aggregation was highly sensitive to the vertical profile of heating.

Here we present a vertically resolved WTG balance analysis of the MJO in the Superparameterized (Grabowski 2001; Randall et al. 2003) Community Earth System Model (Hurrell et al. 2013) (SP-CESM), where temperature and moisture tendencies resulting from

SGS eddy transports, microphysical processes, and radiative heating are addressed separately from large-scale advective transports. While the MJO is the focus of this paper, we would like to emphasize the applicability of such analysis techniques to more idealized studies of convective aggregation. In this study, we first aim to identify how various apparent heating processes contribute to the destabilization of the MJO. We then assess how the strength of various feedbacks differs between periods of low, moderate, and high MJO amplitude. Finally, a diagnostic approach to scale analysis is used to investigate the cause-effect relationship between apparent heating and large-scale motions at the heart of the WTG balance framework used throughout this study.

The paper is organized as follows. A description of the model and analysis techniques used in this study are provided in section 2. In section 3, composite moisture and moisture variance budgets are used to identify processes affecting large-scale moisture during established MJO events, and WTG balance analysis is used to explore the relationship between various apparent heating processes and large-scale vertical moisture advection. Periods of low, moderate, and high MJO amplitude are compared and contrasted in section 4, and the broader applicability of the WTG balance framework implemented in this study is explored in section 5. A comparison with previous studies is provided in section 6, and additional discussion and our conclusions are presented in section 7.

3.2. Model Description and Experimental Design

Superparameterization (Grabowski 2001; Randall et al. 2003) refers to the use of cloud system-resolving models (CSRMs), embedded within each column of a general circulation model (GCM), to compute tendencies of moisture and temperature resulting from processes occurring on the SGS of the GCM. When compared to conventional parameterizations,

the explicit simulation of deep convection, fractional cloudiness, and cloud overlap that occurs in superparameterization allows for more realistic interactions between radiation, clouds, and the large-scale environment to occur. This may be one reason why models implementing super-parameterization have proved exceptionally adept at producing MJO-like variability (Grabowski 2004; Benedict and Randall 2009; Stan et al. 2010; Andersen and Kuang 2012; Arnold et al. 2015; Arnold and Randall 2015) when compared to conventionally parameterized GCMs (Lin et al. 2006).

Superparameterization couples large-scale dynamics, SGS advective transports (i.e. cloud dynamics and turbulence), microphysics, and radiative transfer in such a way that their individual contributions to large-scale tendencies of moisture and temperature are cleanly separable, providing a unique framework that is ideal for this investigation. In this study, the atmospheric component of the Community Earth System Model (CESM) (Hurrell et al. 2013) version 1.0.2 is the NCAR Community Atmosphere Model (CAM) run at $1.9^\circ \times 2.5^\circ$ horizontal resolution, with 30 vertical levels, CAM4 physics, and a 15 minute timestep. A two-dimensional CSRM, the System for Atmospheric Modeling (SAM) version 6 (Khairoutdinov and Randall 2003), with a single moment bulk microphysics scheme, 32 columns of 4 km width, and 28 vertical levels, is embedded within each CAM column and run with a 20 second timestep. At each model level, a large-scale advective forcing that is calculated at each GCM timestep is applied evenly (both horizontally and temporally) to the CSRM domain as it sub-cycles through a sequence of shorter timesteps spanning the longer GCM timestep. At the end of the CSRM sub-cycling (i.e. the next CAM timestep), domain averaged changes in moisture and temperature resulting from microphysical processes and CSRM scale advection are applied in the host CAM, effectively acting as a parameterization

of sub CAM grid scale processes. As SAM implements period boundary conditions, only vertical advective transports can contribute to changes in domain averaged moisture and temperature at each level. Radiative transfer occurs in each CSRM grid column at each CSRM timestep, although radiative transfer calculations are only done on GCM timesteps using time-averaged SAM fields. The atmospheric components of the SP-CESM are coupled to dynamic ocean (POP2) and sea ice (CICE) models with $1.125^\circ \times 0.63^\circ$ resolution.

We have chosen to analyze the 10-year pre-industrial CO_2 (280 ppm) simulation of Arnold et al. (2015), as this simulation produced a realistic MJO whose basic features are well documented by Arnold et al. (2015), allowing more focus to be placed on the WTG balance analysis in this manuscript. Additionally, this simulation will allow a direct comparison of the vertically resolved WTG balance analysis and the column integrated MSE analysis, which was implemented by Arnold et al. (2015). As sometimes occurs in models that produce vigorous intraseasonal variability (Kim et al. 2011), several mean state biases are present in this simulation. Worth highlighting is that model SST exhibits an approximate 1 K cold bias across the Indian Ocean and west Pacific relative to observations, has mean easterly low level winds across the Indian Ocean and Maritime Continent during boreal winter, and has a boreal winter precipitation maximum shifted too far west in the Indian Ocean. Further details and discussion of the simulation, including mean state biases and the structure of intraseasonal variation produced by this simulation, are provided in Arnold et al. (2015).

The moisture budget analyses of a composite "snapshot" of the MJO are produced from 19 wintertime (October to April) MJO events, selected using an index of $20 - 100$ day bandpass filtered OLR (not limited to eastward propagating wavenumbers), averaged over the area of $10^\circ\text{N} - 10^\circ\text{S}, 110^\circ\text{E} - 130^\circ\text{E}$. Events were defined as index minima separated by

at least 20 days, where anomalously low OLR (i.e. enhanced convection) caused the index to exceed a 1.5 standard deviation threshold. Results of composite "snapshots" will then be generalized using a moisture variance budget.

ERAi reanalysis (Dee et al. 2011), provided by the European Center for Medium-Range Weather Forecasts (ECMWF), will supplement the results of the SP-CESM analysis throughout this manuscript. These data were obtained at 6-hour $1.5^\circ \times 1.5^\circ$ resolution for the years 1979-2012. ERAi moisture budget terms were calculated from the 6-hourly data, vertically integrated from the surface to 100 hPa, and then averaged to daily, unless otherwise indicated. The Filtered MJO OLR (FMO) index (Kiladis et al. 2014) is also used in the analysis of ERAi data. The FMO index and the EOFs used in its calculation can be obtained from http://www.esrl.noaa.gov/psd/mjo/mjoindex/.

An all season OLR based EOF index of the MJO is used in the moisture variance analysis of SP-CESM data. The leading EOFs of latitudinally averaged (15°N-15°S) 20-100 day bandpass filtered OLR were computed following the methodology that Kiladis et al. (2014) used to produce the FMO index. The first two EOFs explain 16.7% and 12.4% percent of the total variance respectively, and are well separated based on the criteria of North et al. (1982). The structure of these EOFs, shown in Figure 4.1, is consistent with the structures of the OLR components of the multivariate EOF derived by Wheeler and Hendon (2004) (See Figure 1 in Wheeler and Hendon (2004)).

In section 5, wavenumber-frequency filtering is used in the estimation of the characteristic magnitude of various terms. To compute spectra, data were divided into 49 overlapping subsets, each with a length of 144 days. The mean and linear trend were removed from each subset, and a Hann window was then applied. Each subset was converted in

wavenumber-frequency space, limited to a single wavenumber-frequency combination, and then transformed back into longitude-time space. The characteristic magnitude of a given variable χ that has been filtered to a specific wavenumber-frequency combination (ω, λ) is estimated by its root mean squared modulus

$$\left[\chi^2\right]^{\frac{1}{2}}(\omega,\lambda) = \left(\frac{1}{\mathrm{L}_x\mathrm{L}_y\mathrm{T}}\int_0^{\mathrm{T}}\int_0^{\mathrm{L}_y}\int_0^{\mathrm{L}_x}\chi^2(x,y,t,\omega,\lambda)\,dx\,dy\,dt\right)^{\frac{1}{2}} \tag{3.1}$$

Each term was squared, and then the average taken over all longitudes, time and all subsets before taking the square root to arrive at a characteristic magnitude of the term for a given wavenumber-frequency combination. This was done for each individual latitude, and results were then averaged over latitudes spanning $3°\mathrm{N} - 3°\mathrm{S}$, where WTG dynamics should be most apparent due to the smallness of the Coriolis force. This process was repeated for each wavenumber-frequency combination. This was done using data at the 525 hPa level, which is taken to be representative of the free troposphere and is near the level of maximum heating anomalies.

3.3. WTG Balance Analysis of Established MJO Events

The aims of this section are to:

(1) motivate the need for understanding intraseasonal variations in large-scale vertical motion

(2) outline a simplified framework for understanding intraseasonal variations in large-scale vertical motion

(3) identify the processes acting to stabilize and destabilize the MJO when it is established

As general characteristics of the mean state and intraseasonal variability of this SP-CESM simulation are well documented in Arnold et al. (2015), a similar analysis will not be repeated here. The reader is encouraged to review section 3 and figures 1 through 5 of Arnold et al. (2015) in order to familiarize themselves with these characteristics. Figure 3.2, which shows total and MJO filtered (following (Wheeler and Kiladis 1999)) precipitation variance, is provided here to facilitate referencing regions used in the moisture and moisture variance budgets.

3.3.1. Motivation From a Traditional Moisture Budget

We begin by considering the moisture budget in the form

$$\frac{\partial \overline{q}}{\partial t} = -\overline{\boldsymbol{V}}_{\boldsymbol{h}} \cdot \boldsymbol{\nabla} \overline{q} - \overline{\omega} \frac{\partial \overline{q}}{\partial p} + \overline{M} - \frac{\partial \overline{\omega' q'}}{\partial p} \tag{3.2}$$

where the overbar and prime indicate the large-scale horizontal area average of a quantity and deviations from the area average respectively, $\boldsymbol{V}_h$ and ω are the horizontal and vertical winds respectively, q is specific humidity, M is the moisture tendency due to microphysical processes, and the term $-\boldsymbol{\nabla} \cdot \overline{q' \boldsymbol{V}_{\boldsymbol{h}}'}$ has been neglected. Note that the moisture tendency was calculated using a centered differences approach. Here "large-scale" refers to the approximately 200 km horizontal resolution of the CAM grid, which is large enough to contain an ensemble of clouds, but small enough to compromise only a small fraction of the MJO. Vertical eddy fluxes of moisture ($-\frac{\overline{\partial \omega' q'}}{\partial p}$) primarily represent the vertical redistribution of moisture by SGS cumulus convection (Yanai and Johnson 1993), and reduce to surface fluxes of moisture when vertically integrated from the surface to tropopause if eddy fluxes of moisture through the tropopause are negligible. Note that the net effect of the last two terms in

equation 4.4, which is calculated at the CRM scale and then applied to the GCM scale, is explicitly output by SP-CESM in this study. We will first present composite "snapshots" of each term in equation 4.4, taken when enhanced convection is centered near 120°E. Please note that the role some terms play (e.g. horizontal advection) is sensitive to the location at which the composites are based. To address this sensitivity, a moisture variance budget will subsequently be used to generalize many of the results obtained from these "snapshot" composites.

Figure 3.3 shows a composite moisture budget of 19 wintertime (October 1 to April 30) MJO events, where each term in equation 4.4 has been bandpass filtered to $20-100$ days (denoted by the subscript $_{\mathrm{MJO}}$ in this and subsequent figures) and averaged from $5°\mathrm{N}-5°\mathrm{S}$. Specific humidity anomalies, given by the contours in each plot, indicate that the entire depth of the free troposphere is anomalously moist from $\sim 110°\mathrm{E}-150°\mathrm{E}$, coincident with enhanced convection and reduced OLR (not shown). A shallow tongue of enhanced moisture extends eastward across the dateline, above which the troposphere remains anomalously dry. The moisture tendency (Fig. 3.3a) indicates further moistening along the low level moisture tongue near and east of the dateline, while moisture anomalies between $\sim 120°\mathrm{E}-170°\mathrm{E}$ appear to be extending upwards while simultaneously being eroded from below. Substantial drying throughout the depth of the troposphere is apparent over the Indian Ocean. Horizontal advective drying (Fig. 3.3b) is enhanced across the entire eastern hemisphere, with the strongest drying centered around 700 hPa. Worth noting is that the largest specific humidity anomalies, occurring near 650 hPa, are coincident with a near zero moisture tendency despite enhanced horizontal advective drying. This indicates that some other process

or set of processes must be acting as an anomalous moisture source in this region. Large-scale vertical moisture advection and the net effect of microphysical processes and SGS eddy moisture fluxes (Figs. 3.3c,d respectively, please note color scale) are large and opposing processes that are strongest in the region of enhanced convection. While these processes result in a large degree of cancellation, anomalous moistening by large-scale vertical moisture advection slightly exceeds the anomalous drying effect of the latter processes (Fig. 3.3e) in many regions. The incomplete cancellation of these processes, which is the focus of the subsequent section and was referred to as the column process in Chikira (2014), results in a net moistening that begins along the shallow tongue of enhanced moisture and then tilts westward with height, and opposes the enhanced advective drying occurring where moisture anomalies are largest. The budget residual (Fig. 3.3f), calculated as the difference between the left and right hand side of equation 4.4, is small relative to the individual budget terms, providing confidence in the assessment provided here.

In summary, it appears that during the enhanced phase, large-scale vertical moisture advection provides more moisture than is removed by process occurring on the SGS (i.e. microphysics and SGS eddy fluxes), resulting in a net moistening which is opposed by horizontal advective drying. But why should it be that large-scale vertical moisture advection exceeds the moisture removed by processes acting on the SGS? A simplified framework for understanding vertical motion in the tropics will be used to address this question.

3.3.2. Vertically Resolved WTG Balance Framework and Analysis

Just as the quasi-geostrophic omega equation provides a useful simplified framework for understanding vertical motion in mid-latitudes, WTG balance may, when applicable, provide a useful simplified framework for understanding vertical motion in the tropics (Sherwood

1999; Sobel et al. 2001; Grabowski and Moncrieff 2004; Chikira 2014; Wolding and Maloney 2015a; Janiga and Zhang 2016). As WTG balance will play a fundamental role in the remainder of this paper, a primary goal of this paper is to be as transparent as possible regarding the physical interpretation of WTG balance in the context of the MJO. This section aims to show the utility of using WTG balance for understanding the MJO. A more detailed discussion of the applicability of WTG balance, and its physical interpretation in the context of the MJO, is provided in section 3.5.

Neglecting $-\boldsymbol{\nabla} \cdot \overline{s' \boldsymbol{V_h'}}$, the DSE budget is given by

$$\frac{\partial \overline{s}}{\partial t} + \overline{\boldsymbol{V}}_{\boldsymbol{h}} \cdot \boldsymbol{\nabla} \overline{s} + \overline{\omega} \frac{\partial \overline{s}}{\partial p} = Q_1 \tag{3.3}$$

where the apparent heat source (Q_1) (Yanai et al. 1973) is

$$Q_1 = \overline{Q}_M + \overline{Q}_R - \frac{\partial \overline{\omega' s'}}{\partial p} \tag{3.4}$$

and Q_M and Q_R are the DSE tendency due to microphysics and radiation respectively. WTG balance refers to a first order balance between large-scale vertical DSE advection and apparent heating, where the DSE tendency and horizontal DSE advection are lower order terms (Sobel et al. 2001). This balance is given by

$$\overline{\omega} \frac{\partial \overline{s}}{\partial p} = Q_1 \tag{3.5}$$

which can be re-arranged to give

$$\overline{\omega} = \frac{Q_1}{\frac{\partial \overline{s}}{\partial p}} \tag{3.6}$$

In the context of the MJO, this paper takes the perspective that intraseasonal variations in large-scale vertical motion are a direct dynamical response to variations in apparent heating. This balance results because effective gravity wave adjustment occurs on temporal scales much shorter than, and spatial scales much larger than, intraseasonal variations in apparent heating. The utility of equation 3.6 is that it can be used to relate large-scale vertical moisture advection to apparent heating, such that

$$-\overline{\omega}\frac{\partial \overline{q}}{\partial p} = \frac{1}{\mathrm{L_v}}\left(\overline{\alpha} Q_1\right) \tag{3.7}$$

where

$$\overline{\alpha} = -\mathrm{L_v}\left(\frac{\frac{\partial \overline{q}}{\partial p}}{\frac{\partial \overline{s}}{\partial p}}\right) \tag{3.8}$$

Note that $\overline{\alpha}$, originally introduced by Chikira (2014), can be thought of as the sensitivity of large-scale vertical moisture advection to apparent heating, where the static stability determines the vertical motion resulting from some apparent heating, and the vertical moisture gradient determines the amount of moistening or drying that results from that vertical motion. This paper takes the perspective that moisture, through convective scale processes such as entrainment, acts as the intermediary through which the dynamical response to apparent heating can, in turn, influence subsequent apparent heating, thereby allowing for potential positive feedbacks to occur. This perspective is summarized in Figure 3.4, and essentially considers the MJO to be a slowly moving Matsuno-Gill pattern maintained by positive feedbacks between moisture, apparent heating, and large-scale dynamics. Note that, from this perspective, processes fundamental to the MJO span from the scale of turbulence (e.g. entrainment) to the planetary scale dynamical response, highlighting the challenges in simulating and understanding the MJO.

Figures 3.5a,b show SP-CESM $\overline{\alpha}$ lowpass filtered (denoted by the subscript $_{\text{LP}}$ in this and subsequent figures) to 20 days, and bandpass filtered to $20-100$, respectively. Moisture sensitivity to apparent heating is largest in the lower troposphere and decreases monotonically with height, largely a result of the sharp decrease in the vertical moisture gradient with height. Intraseasonal moisture variations result in a reduction of $\overline{\alpha}$ at low levels and an increase in $\overline{\alpha}$ at upper levels during the enhanced phase, which will be shown to be important in subsequent sections.

A reasonable "first check" on the WTG balance assumption is to assess the degree to which intraseasonal variations in large-scale vertical motion can actually be diagnosed from apparent heating. Figure 3.6 shows the actual large-scale vertical velocity and vertical moisture advection (Figs. 3.6a,b) , that diagnosed using WTG balance (Figs. 3.6c,d), and the difference between the two (Figs. 3.6e,f). Figure 3.6g is the same as Figure 3.6f, except a different color scale is used to better highlight the structure of errors in the WTG balance diagnosis. Note that, to incorporate the effects of higher frequency variability (i.e. variability occurring on timescales less than 20 days), a 3-day lowpass filter has been used in the WTG diagnosis (Figs. 3.6e,f). This contrasts the 20-day lowpass filter used in the WTG diagnosis of Wolding and Maloney (2015a) (see Figure 6 in Wolding and Maloney (2015a)), and results in an improvement of the WTG estimates of large-scale vertical velocity and vertical moisture advection. The WTG diagnosis of vertical motion and vertical moisture advection is exceptionally accurate throughout the free troposphere. As may be expected, the WTG balance diagnosis does not work as well below 900 hPa. Given this, a conservative limit of 850 hPa is applied to subsequent analyses dependent upon the WTG balance framework, and grey hatching will be applied below 850 hPa in plots which rely on the WTG balance

framework. Now that a simplified framework for understanding intraseasonal variations in vertical motion is in place, the contributions that various apparent heating processes make to vertical moisture advection can be assessed.

Figure 3.7a shows the "direct" effect of SGS processes (i.e. microphysics and SGS eddy fluxes) on large-scale moisture content. This is the same as Figure 3.3d, where only the color scale has been changed to highlight weaker moisture tendencies. The strong drying effect of increased precipitation processes during the enhanced phase is evident. Figure 3.7b shows the large-scale heating that results from these same SGS processes. Please note that this heating does not include the effects of radiation. The similar structures of drying and heating in Figures 3.7a,b respectively highlight the dominant role that microphysical processes play in each, though more subtle differences are evident, owing in part to differences in SGS eddy transports of moisture and DSE (Yanai et al. 1973). The heating in Figure 3.7b, through large-scale adjustment, contributes to large-scale vertical moisture advection, shown in Figure 3.7c. This can be thought of as the "indirect" effect (i.e. WTG balance effect) of SGS processes on large-scale moisture content. The structure of moistening in Figure 3.7c is much more bottom heavy than the structure of heating in Figure 3.7b, reflecting the higher moisture sensitivity of the lower troposphere to apparent heating. When the direct and indirect effects of SGS processes on large-scale moisture content are considered together, shown in Figure 3.7d, their incomplete cancellation results in substantial moistening at low levels to the east of enhanced convection that helps drive the eastward propagation of moisture anomalies in this region. Note that Figure 3.7d is the same as the column process (Fig. 3.3f) without the "indirect" effects of radiative heating on large-scale moisture. Interestingly, while drying is evident at lower and upper levels in the region of enhanced

convection, the incomplete cancellation of the direct and indirect effects of these processes results in a net moistening at mid levels in the region of enhanced convection, where the largest moisture anomalies are observed. Note that the effects of surface flux variations are included in Figure 3.7. The vertical integral of these processes will be considered in the subsequent section, thereby allowing the effects of convection to be separated from the influence of surface latent heat flux (SLHF) feedbacks.

Figure 3.8 shows total, longwave, and shortwave radiative heating anomalies (Figs. 3.8a,c,e respectively), and the large-scale vertical moisture advection (Figs. 3.8b,d,f respectively) they drive under WTG balance. Intraseasonal variations in total radiative heating appear to be sufficient to compensate for the low level drying seen in Figure 3.7d, and contribute to the mid level moistening seen in Figure 3.3e. Total radiative heating anomalies result from opposing changes in longwave and shortwave terms, the latter of which has a distinct vertical dipole structure. In the middle and lower troposphere, the reduction of longwave cooling during the enhanced phase is substantially stronger than the reduction of shortwave heating. Yet it is worth highlighting that the low level moisture tendency associated with variations in shortwave heating is not negligible when compared with other moisture budget terms such as horizontal advection.

In this section, a simplified framework for understanding intraseasonal variations in large-scale vertical motion has been used to highlight the role various apparent heating processes play in driving large-scale vertical moisture advection. It is worth highlighting that composites used in this and previous sections (e.g. Figure 3.3) only provide information about a single phase of the MJO lifecycle at a given geographical location. The next section will

employ an approach that considers the entire lifecycle of the MJO over a broad geographic region.

3.3.3. Moisture Variance Budget of the MJO

In the previous section, intraseasonal variation in large-scale vertical moisture advection in the tropics were shown to be closely related to convective activity under WTG balance. Given this close relationship, subsequent discussion will often focus on the net effect of large-scale vertical moisture advection, microphysical processes, and SGS eddy fluxes. In order to aide discussion of these processes, their net effect will hereafter be referred to as the column process (Chikira 2014). In this section, an intraseasonal moisture variance budget will be used to more objectively assess the role that various moisture budget terms play in the destabilization and propagation of the MJO.

The fractional growth rate of intraseasonal column moisture variance contributed by moisture budget term P is given by

$$G_P(p,t) = \frac{\iint P(p) \langle q \rangle \, dx \, dy}{\iint \langle q \rangle^2 \, dx \, dy} \tag{3.9}$$

where specific humidity has been bandpass filtered to $20-100$ days, and the angled brackets represent vertical integrals from the surface to 100 hPa. Similarly, the fractional contribution of a moisture budget term P to the column moisture tendency is given by

$$T_P(p,t) = \frac{\iint P(p) \left\langle \frac{\partial q}{\partial t} \right\rangle dx \, dy}{\iint \left\langle \frac{\partial q}{\partial t} \right\rangle^2 dx \, dy} \tag{3.10}$$

Here the domain considered is $10°\mathrm{N} - 14.5°\mathrm{S}, 60°\mathrm{E} - 180°\mathrm{E}$, and subsequent figures are averaged over the 30 days preceding and following each of the 19 winter events composited

in Figure 3.3, for a total of 1159 days. The moisture variance tendency was computed by projecting the moisture tendency, calculated using a centered differences approach, onto the column moisture anomalies, as in equation 4.1. Equations 4.1 and 3.10 warrant further discussion. In these equations, the choice was made to project moisture budget term $P(p)$ onto the column integrated terms $\langle q \rangle$ and $\left\langle \frac{\partial q}{\partial t} \right\rangle$. An alternative approach could be to project moisture budget term $P(p)$ onto the anomalous moisture and moisture tendency at each level, $q(p)$ and $\frac{\partial q(p)}{\partial t}$ respectively, and to subsequently consider the vertical integral of the product of those terms. While both methods were investigated in this study, the former was chosen on the basis that the SGS effects of convection can vertically redistribute moisture provided by other processes (e.g. radiative heating), such that their influence is distributed throughout the column.

Figure 3.9a shows vertical profiles of how various moisture budget terms contribute to the growth or reduction of intraseasonal column moisture variance over the entire MJO lifecycle. This can be interpreted as follows. If a term has a positive growth rate at a given level, this indicates that term is moistening that level when the column is anomalously moist, and drying that level when the column is anomalously dry. Each term has been scaled by the mass equivalent of 900 hPa, the depth over which the column moisture anomalies are calculated. This is done in order to obtain a growth rate per unit time (per day), and can be interpreted as the column moisture variance growth rate (i.e. increase or decrease in aggregation) that would result from the moisture budget term at that level acting over the depth of the troposphere. Very little growth exists in domain averaged moisture variance over the period considered here (black solid line), which is the result of an approximate balance between moisture variance growth (i.e. destabilization) by the column process (blue dashed line) and

the reduction of moisture variance (i.e. damping) by horizontal advection (red dashed line). Both of these terms act fairly uniformly between 850 and 500 hPa. Using the WTG balance framework, the column process can be decomposed into contributions from total radiative heating (magenta dot-dashed line) as well as the net effect of microphysical processes and SGS eddy fluxes (green dot-dashed line). Total radiative heating makes large contributions to column moisture variance, acting almost exclusively below 600 hPa. Interpretation of the net effect of microphysical processes and SGS eddy fluxes is more difficult, as SGS eddy fluxes have the ability to redistribute moisture vertically. It is therefore not possible to identify specific levels where column moisture variance is actually being reduced. It seems likely that much of the negative growth rate occurring at low levels in this term represents SGS eddy fluxes vertically redistributing the moisture anomalies provided by radiative heating variations (green dot-dashed line) at low levels to mid and upper levels. Consideration of the mass weighted vertical integral of this term, which will be done shortly, provides much more insight.

Figure 3.9b shows vertical profiles of how various moisture budget terms contribute to the intraseasonal column moisture tendency (i.e. propagation of the MJO) over the entire MJO lifecycle. Again, each term has been scaled by the mass equivalent of 900 hPa, and can be interpreted as the fractional contribution to the column moisture tendency that would result from the moisture budget term at that level acting over the depth of the troposphere. As may be expected, propagation of column moisture anomalies results primarily from processes occurring at low to mid levels, where moisture anomalies are largest (Fig. 3.3). While this results primarily from horizontal advection (red dashed line), the column process (blue dashed line) also plays a significant role. Contributions from the column process are almost

exclusively the result of the net effect of microphysical processes and SGS eddy fluxes (green dot-dashed line), and are weakly opposed by total radiative heating variations (magenta dot-dashed line).

Figures 3.10a,b show the results of taking the mass weighted vertical integral of equations 4.1 and 3.10, and are equivalent to taking the vertical average of each term in Figures 3.9a,b respectively. Given their dependence on WTG balance, terms E, F, and H have only been vertically integrated from 850 to 100 hPa. These levels of vertical integration will be applied to all terms that rely on WTG balance in subsequent figures. Please note that, while a conservative lower limit was applied here, WTG balance may prove to be applicable even lower. Figure 3.10a shows the total growth rate of intraseasonal column moisture variance that results from various moisture budget terms. Again, the column moisture variance growth rate (Term A) is small over the period considered here, a result of the large degree of cancellation between destabilization by the column process (term D) and damping by horizontal advection (Term C).

Terms E and F show the decomposition of the column process (Term D) into contributions from total radiative heating as well as the net effect of microphysical processes and SGS eddy fluxes respectively. It is worth highlighting that term F can be further decomposed into contributions from variations in surface fluxes of moisture (Term G) and SGS convective processes (Term H, i.e. convection in the absence of radiative and surface flux feedbacks). SGS convective processes (Term H) are destabilizing in SP-CESM, and this destabilization is strongly re-enforced by variations in radiative heating (Term E). The results of Arnold and Randall (2015), who found that MJO-like variability persisted when cloud-radiative feedbacks were removed in their global aquaplanet simulation using SP-CESM, support the

finding that SGS convective processes alone (i.e. in the absence of radiative and surface flux feedbacks) have a destabilizing effect in SP-CESM. SLHF feedbacks (Term G) are actually a stabilizing process in SP-CESM, owing to the mean state easterlies that prevail over the Indian Ocean and Maritime Continent. Figure 3.10b re-iterates that the propagation of the MJO is primarily driven by horizontal advection, with the net effect of microphysical processes and SGS eddy fluxes playing a secondary, though still important, role.

In order to highlight similarities and differences between the MJO in SP-CESM and the MJO in the real world, a similar albeit more limited analysis has been produced using ERAi reanalysis data, as shown in Figure 3.11. These terms were calculated over the domain of $10.5°\text{N} - 13.5°\text{S}, 60°\text{E} - 180°\text{E}$, and averaged over every winter (October 1 - April 30) day where the magnitude of the FMO index exceeded a value of 1. Lack of closure of the ERAi moisture budget is thought to be the result of poor estimations of terms associated with the column process (e.g. precipitation, large-scale vertical moisture advection) (Morita et al. 2006; Benedict and Randall 2007; Lau and Wu 2010; Kiranmayi and Maloney 2011; Sobel et al. 2014; Kim et al. 2014b; Wolding and Maloney 2015a). This motivated calculating the ERAi column process as the residual of Eulerian moisture tendency and horizontal advection. As ERAi produces a fairly realistic representation of intraseasonal moisture variations (Tian et al. 2010), this essentially amounts to an assumption that intraseasonal variation in horizontal moisture advection are well represented in ERAi. Comparing Figures 3.10 and 3.11 suggests that the same balance of processes occurs in SP-CESM as in the real world MJO, with the most notable difference being the dramatically higher growth rates occurring in SP-CESM. This suggests that the MJO may be more unstable in SP-CESM than in the real world, and is consistent with the findings of Arnold et al. (2015), who

showed that intraseasonal OLR variance in SP-CESM is substantially larger than that in observations.

3.3.4. The Role of Higher Frequency Variability

Several observational and modeling studies have shown that the intraseasonal modulation of higher frequency convective variability (e.g. convectively coupled equatorial waves and TD-type disturbances) results in substantial horizontal advective diffusion or damping of moisture anomalies (Maloney and Dickinson 2003; Maloney 2009; Maloney et al. 2010; Kiranmayi and Maloney 2011; Andersen and Kuang 2012; Chikira 2014). In this section, the role higher frequency convective variability plays in driving both horizontal advective damping and large-scale vertical moisture advection will be investigated.

As in Chikira (2014), horizontal advection can be decomposed as

$$-\left(\overline{\boldsymbol{V}}_{\boldsymbol{h}}\cdot\boldsymbol{\nabla}\overline{q}\right)_{\mathrm{MJO}}=-\left(\overline{\boldsymbol{V}}_{\boldsymbol{h},\mathrm{LP20}}\cdot\boldsymbol{\nabla}\overline{q}_{\mathrm{LP20}}\right)_{\mathrm{MJO}}-\left(\overline{\boldsymbol{V}}_{\boldsymbol{h}}\cdot\boldsymbol{\nabla}\overline{q}\right)_{\mathrm{HF}} \tag{3.11}$$

where

$$\left(\overline{\boldsymbol{V}}_{\boldsymbol{h}}\cdot\boldsymbol{\nabla}\overline{q}\right)_{\mathrm{HF}}=\left(\overline{\boldsymbol{V}}_{\boldsymbol{h},\mathrm{LP20}}\cdot\boldsymbol{\nabla}\overline{q}_{\mathrm{HP20}}\right)_{\mathrm{MJO}}+\left(\overline{\boldsymbol{V}}_{\boldsymbol{h},\mathrm{HP20}}\cdot\boldsymbol{\nabla}\overline{q}_{\mathrm{LP20}}\right)_{\mathrm{MJO}}+\left(\overline{\boldsymbol{V}}_{\boldsymbol{h},\mathrm{HP20}}\cdot\boldsymbol{\nabla}\overline{q}_{\mathrm{HP20}}\right)_{\mathrm{MJO}} \tag{3.12}$$

and the subscript $_{\mathrm{HP20}}$ indicates the application of 20-day highpass filtering. The first term on the right hand side of equation 4.8 represents horizontal advection resulting from the slowly varying wind field acting on the slowly varying moisture field, while the second term on the right hand side results from the presence of higher frequency variability. These terms will be referred to as horizontal advection by slowly varying fields and higher frequency variability respectively.

Figures 3.12a,b show the decomposition of horizontal moisture advection (Fig. 3.3b) into horizontal advection by slowly varying fields and higher frequency variability respectively. Horizontal advection by slowly varying fields results in drying at the eastern and western periphery of the moisture anomalies, while horizontal advection by higher frequency variability results in considerable drying where the moisture anomalies are largest. Figure 3.13 shows the moisture variance analysis of these terms, which considers their effect throughout the entire lifecycle of the MJO over a broad geographic region. Figures 3.13a,c indicate that horizontal advection damping results solely from presence of higher frequency variability (red dashed line, Term C), and that horizontal advection by slowly varying fields (blue dashed line, Term B) contributes weakly to moisture variance growth. Figures 3.13b,d suggest that horizontal advection by slowly varying fields (blue dashed line, Term B) plays a more dominant role in driving propagation of the MJO than horizontal advection by higher frequency variability (red dashed line, Term C).

Using WTG balance, large-scale vertical moisture advection can be decomposed as

$$-\left(\overline{\omega}\frac{\partial\overline{q}}{\partial p}\right)_{\mathrm{MJO}} = \frac{1}{\mathrm{L_v}}\left(\left(\overline{\alpha}_{\mathrm{LP20}}\, Q_{1,\mathrm{LP20}}\right)_{\mathrm{MJO}} + \left(\overline{\alpha}\, Q_1\right)_{\mathrm{HF}}\right) \tag{3.13}$$

where

$$\left(\overline{\alpha}\, Q_1\right)_{\mathrm{HF}} = \left(\overline{\alpha}_{\mathrm{LP20}}\, Q_{1,\mathrm{BP3-20}}\right)_{\mathrm{MJO}} + \left(\overline{\alpha}_{\mathrm{BP3-20}}\, Q_{1,\mathrm{LP20}}\right)_{\mathrm{MJO}} + \left(\overline{\alpha}_{\mathrm{BP3-20}}\, Q_{1,\mathrm{BP3-20}}\right)_{\mathrm{MJO}} \tag{3.14}$$

and the subscript $_{\mathrm{BP3-20}}$ indicates the application of $3-20$ day bandpass filtering. The first term on the right hand side of equation 4.10 represents large-scale vertical moisture advection resulting from slowly varying heating acting in a moist thermodynamic environment with slowly varying $\overline{\alpha}$, while the second term on the right hand side results from the presence of

higher frequency variability. These terms will be referred to as large-scale vertical moisture advection by slowly varying fields and higher frequency variability respectively.

Figures 3.14a,b show the decomposition of large-scale vertical moisture advection (Fig. 3.3c) into contributions from slowly varying fields and higher frequency variability respectively. While slowly varying fields contribute the majority of the total large-scale vertical moisture advection, the contribution of higher frequency variability is still considerable, being similar in magnitude to horizontal advection and the column process (Figs. 3.3b,e respectively). The last term on the right hand side of equation 4.11, $(\overline{\alpha}_{\mathrm{BP3-20}}\, Q_{1,\mathrm{BP3-20}})_{\mathrm{MJO}}$, is the dominant contributor to $(\overline{\alpha}\, Q_1)_{\mathrm{HF}}$ (not shown). In order to determine how higher frequency variability contributes to large-scale vertical moisture advection, an index of $(\overline{\alpha}_{\mathrm{BP3-20}}\, Q_{1,\mathrm{BP3-20}})_{\mathrm{MJO}}$ integrated from 850 hPa to 100 hPa and averaged over the domain $10°\mathrm{N} - 10°\mathrm{S}, 70°\mathrm{E} - 85°\mathrm{E}$ was used to produce lag-day composites. A total of 81 winter time events, selected by choosing maxima separated by at least 5 days and exceeding 1.5 standard deviations from the time series of domain averaged $(\overline{\alpha}_{\mathrm{BP3-20}}\, Q_{1,\mathrm{BP3-20}})_{\mathrm{MJO}}$, were used to produce Figure 3.15. Figure 3.15a indicates that apparent heating by higher frequency convective variability peaks above the level of the largest moisture anomalies associated with the higher frequency variability. The moisture sensitivity to apparent heating (i.e. $\overline{\alpha}_{\mathrm{BP3-20}}$, Fig. 3.15b) has been increased at this level, a result of the higher frequency moisture anomalies. The covariance of higher frequency variations in apparent heating (Fig. 3.15a) with higher frequency variations in $\overline{\alpha}$ (Fig. 3.15b) result in considerable large-scale vertical advective moistening of the mid and upper troposphere (Fig. 3.15c). Intraseasonal modulation of higher frequency convective activity, as documented by several previous studies (Maloney

and Dickinson 2003; Maloney 2009; Maloney et al. 2010; Kiranmayi and Maloney 2011; Andersen and Kuang 2012; Chikira 2014), can therefore contribute to intraseasonal variations in large-scale vertical moisture advection.

Figure 3.16 shows a moisture variance analysis of the net effect of higher frequency convective variability (black line, Term A) decomposed into contributions from horizontal advection (blue dashed line, Term B) and large-scale vertical moisture advection (red dashed line, Term C). While large-scale vertical moisture advection driven by higher frequency convective variability offsets a considerable portion of the horizontal advective damping effect, the net effect of higher frequency convective variability is still to damp intraseasonal moisture variance.

3.3.5. Detailed Analysis of Large-Scale Vertical Moisture Advection by Slowly Varying Fields

Large-scale vertical moisture advection resulting from slowly varying fields can be decomposed into contributions resulting from intraseasonal variations in apparent heating acting on the background moist thermodynamic profile, background apparent heating rates acting on intraseasonal variations in the moist thermodynamic profile (Fig. 3.5b), and intraseasonal variations in apparent heating acting on intraseasonal variations in the moist thermodynamic profile. This is decomposition is made as follows:

$$\frac{1}{\mathrm{L_v}}\left(\left(\overline{\alpha}_{\mathrm{LP20}}\, Q_{1,\mathrm{LP20}}\right)_{\mathrm{MJO}}\right) = \frac{1}{\mathrm{L_v}}\left(\overline{\alpha}_{\mathrm{LP100}}\, Q_{1,\mathrm{MJO}} + \overline{\alpha}_{\mathrm{MJO}}\, Q_{1,\mathrm{LP100}} + \overline{\alpha}_{\mathrm{MJO}}\, Q_{1,\mathrm{MJO}}\right) \qquad (3.15)$$

where the subscripts LP20, LP100, and MJO indicate application of 20 day lowpass, 100 day lowpass, and $20-100$ day bandpass filtering respectively.

Figure 4.18 shows this decomposition applied to the longwave and shortwave radiative heating terms in the column moisture variance budget, where terms relating to intraseasonal variations in radiative heating acting on intraseasonal variations in the moist thermodynamic profile have been omitted because of their negligible contribution. First consider the column integrated effect of the various terms, as shown in Figure 4.18b. The total radiative heating term (term A) results almost entirely from the longwave radiative heating term (term B), and the shortwave radiative heating term (term C) results in only a small reduction of growth rate. To first order, the total radiative heating term (term A) can be described by the sum of intraseasonal variations in longwave and shortwave heating acting on the background moist thermodynamic profile (terms D and F respectively). Background longwave and shortwave heating rates acting on intraseasonal variations in the moist thermodynamic profile (terms E and G) make relatively small contributions to the total radiative heating term (term A). Inspection of the vertical profiles of how each term contributes to column moisture variance (Fig. 4.18a) provides a more nuanced perspective. Each of the longwave and shortwave terms make important contributions to the vertical structure of the moistening/drying that contributes to moisture variance growth. Throughout most of the column, intraseasonal variations in longwave heating acting on the background moist thermodynamic profile (blue dashed line) contribute to column moisture variance growth. While this profile is bottom heavy to begin with, background longwave heating acting on variations in the moist thermodynamic profile (green dot-dashed line) makes the total longwave heating term (black line) substantially more bottom heavy. Both of the shortwave heating terms (red dashed and magenta dot-dashed lines) act in such a way that their combined effect (grey line) is to

make total radiative heating term (magenta dot-dashed line Fig. 3.10a) substantially more top heavy than would result from the longwave heating term alone (black line).

Do changes in these vertical profiles matter if the column integral stays the same? In other words, does it matter where moistening or drying of the column occurs? As tropical convection is particularly sensitive to dry air entrainment below the freezing level (Lucas et al. 1994; Zipser 2003; Sahany et al. 2012), it would seem that the addition or removal of moisture at low levels (i.e. more bottom heavy profiles) would have a larger influence on convection than that at upper levels (i.e. top heavy profiles). If this is true, longwave radiative feedbacks may be more destabilizing than their column integrated effect (i.e. Term B) would suggest. Similarly, shortwave radiative feedbacks may be more stabilizing than their column integrated effect (i.e. Term C) would suggest. Yet the extent to which SGS eddy fluxes quickly redistribute intraseasonal moisture anomalies in the vertical remains unclear, though it likely varies throughout the MJO lifecycle. This should be a topic of future research.

Figures 3.18a,b shows various microphysical and SGS eddy flux terms of the column moisture variance budget, where the first three terms (black, blue, and red lines and terms A, B, and C) include the effects of both slowly varying fields and higher frequency activity, and the latter two terms (green and magenta lines and terms D and E) result only from slowly varying fields. All terms in 3.18b have been vertically integrated from 850 to 100 hPa. The total effect of microphysical processes and SGS eddy fluxes (black line) results from the sum of their direct effect on column moisture (blue dashed line) and their indirect effect (by producing large-scale vertical moisture advection) on column moisture (red dashed line, Term C). The direct effect of microphysical processes and SGS eddy flux includes the effect of SLHF

variations, and therefore the black and blue dashed terms in Figure 3.18a include this SLHF effect. To address this, the effect of SLHF variations is subtracted from the vertical integral of these terms, as shown in Figure 3.18b. When the effects of SLHF variations are removed, the sum of the direct (Term B) and indirect (Term C) effects of microphysical processes and SGS eddy fluxes, which are large and opposing terms, results in modest growth of column moisture variance (Term A). Recall that this modest growth is strongly re-enforced by the total radiative effect (Fig. 4.18b, term A). As shown in the previous section, the indirect effect of microphysical processes and SGS eddy fluxes (Term C) is the result of slowly varying fields as well as higher frequency convective activity. The indirect effect of the slowly varying fields is primarily the result of intraseasonal variations in heating acting on the background moist thermodynamic profile (green dot-dashed line, term D), but background heating acting on variations in the moist thermodynamic profile (magenta dot-dashed line, term E) results in a substantially more top-heavy profile. Intraseasonal variations in heating acting on intraseasonal variations in the moist thermodynamic profile (not shown) make a negligible contribution.

3.4. Limits to Growth of the MJO

The previous sections indicate that the MJO is destabilized by both SGS convective processes and radiative feedbacks, and that this destabilization is opposed by horizontal advective damping when the MJO is well established. How representative is this characterization of the MJO? Does destabilization by SGS convective processes and radiative feedbacks begin to saturate (i.e. become weaker) as the amplitude of the MJO increases? This section aims to answer these questions by assessing the strength of various feedbacks during periods of low, moderate, and high MJO amplitude.

Figures 3.19a,b shows the results of moisture variance budgets for SP-CESM and ERAi respectively, where budgets for both datasets have been calculated during periods where their MJO indices (FMO-like and FMO respectively, see Section 2 for details) have a magnitude between 0.75 and 1 (dark blue bars), 1 and 1.5 (light blue bars), 1.5 and 2 (green bars), 2 and 2.5 (yellow bars), and greater than 2.5 (red bars). Lower to higher values of these OLR-based MJO indices correspond with periods of time where MJO convective anomalies are weak and geographically limited (dark blue bars) and strong and widespread (red bars) respectively (Wolding and Maloney 2015b). Sample sizes are provided in the figure caption. In both SP-CESM and ERAi, destabilization by the column process (Term D) is greater during periods of high MJO amplitude (red bars) than during periods of low MJO amplitude (blue bars), and this increased destabilization is approximately balanced by an increase in horizontal advective damping (Term C). Figure 3.20 indicates that the increase in horizontal advective damping (Term A) with MJO amplitude results from changes in both horizontal advection by slowly varying fields (Term B) and horizontal advection associated with higher frequency variability (Term C). Figure 3.21 shows that the net damping effect of higher frequency convective variability (Term A) remains unchanged as MJO amplitude increases, a result of opposing changes in the contributions higher frequency variability makes to large-scale vertical moisture advection (Term B) and horizontal advective damping (Term C).

Terms E and F of Figure 3.19a show the decomposition of the column process (Term D) into contributions from total radiative heating as well as the net effect of microphysical processes and SGS eddy fluxes respectively. Greater destabilization via radiative heating (Term E) is evident during periods of high MJO amplitude. Figure 3.22, which shows the decomposition of the slowly varying radiative feedback terms, indicates that the increased

destabilization via radiative is primarily the result of intraseasonal variations of longwave radiative heating acting on the background moist thermodynamic profile (Term D) becoming more destabilizing as MJO amplitude increases. Decomposition of this term (not shown) indicates that this increasing strength results from an increase in the strength of intraseasonal variations in longwave heating, not differences in the background moist thermodynamic profile. This is consistent with the findings of Adames and Kim (2016), who identified a zonal wavenumber dependence of the cloud-radiative feedback that favored growth at larger scales.

Term F of Figure 3.19a can be further decomposed into contributions from variations in surface fluxes of moisture (Term G) and SGS convective processes (Term H). Decreased stabilization by surface flux feedbacks (Term G) is evident during periods of high MJO amplitude. While destabilization by SGS convective processes (Term H) does decrease modestly as MJO amplitude increases, these processes remain a destabilizing force during periods of highest MJO amplitude (red bars).

Figure 3.23 indicates that the modest decrease in destabilization by SGS convective processes (Term A) is the result of rather dramatic changes in the direct (Term B) and indirect (Term C) effects of SGS convective processes. As MJO amplitude increases, damping by precipitation processes (Term B) increases substantially. This increased damping is almost perfectly opposed by the increased large-scale vertical moisture advection (Term C) driven by intraseasonal variations in heating by SGS convective processes (Term D).

Taken together, the results of Figure 3.19 suggest that changes in the vertical structure of apparent heating (Terms E and H) do not play a dominant role in limiting MJO amplitude, at least in SP-CESM. In other words, the column process does not appear to be strongly

"self-limiting" in SP-CESM. While apparent heating may become progressively more top-heavy in regions of enhanced convection as MJO amplitude increases, this appears to play little role in limiting the amplitude of the MJO.

3.5. Diagnostic Investigation and Interpretation of WTG Balance

Throughout this manuscript, WTG balance has been used as a simplified framework for understanding intraseasonal variations in large-scale vertical motion. The physical rationale called upon to justify this simplified framework is that of intraseasonal variations in apparent heating undergoing effective gravity wave adjustment, which results in the observed intraseasonal variations in large-scale vertical motion. Demonstrating the ability to accurately diagnose variations in large-scale vertical motion from variations in apparent heating (Fig. 3.6) has been used to legitimize the application of this framework, but does not directly address the physical rationale behind it. That is the aim of this section.

Atmospheric motions occur across a wide range of spatial and temporal scales, and the dynamics that govern such motions vary across this range of scales. Several approaches exist for gaining an understanding of such governing dynamics. Scale analysis is one such approach that has been used with great success, perhaps most notably in understanding mid-latitude large-scale dynamics (Charney 1948). Unfortunately, scale analysis of large-scale tropical dynamics has proven less fruitful, in part because it is "...hard to make relevant equations that are simple, or simple equations that are relevant" (Vallis 2016) for such motions. Yano and Bonazzola (2009) highlight that results of scale analyses of large-scale tropical motions (Charney 1963) are "inherently inconclusive" because of considerable sensitivities to small changes in the assumed scales of various terms throughout the analysis. In light of these inherent uncertainties, Yano and Bonazzola (2009) employed an alternative approach, whereby

the scale dependence of the magnitude of various dynamical terms was estimated using a diagnostic method applied to observational data from the Tropical Ocean and Global Atmosphere (TOGA) Coupled Ocean-Atmosphere Response Experiment (COARE) field campaign. Briefly, this diagnostic method quantified the scale dependence of a variable through application of spatial and temporal moving averages to the TOGA-COARE data. The characteristic magnitude of a variable for a given spatial and temporal scale was estimated by taking the domain average of the root-mean-square of the smoothed variable. The governing dynamics of the given spatial and temporal scale can then be estimated by comparing the characteristic magnitudes of various thermodynamic terms of interest. The reader is referred to section 7 of Yano and Bonazzola (2009) for further details of this approach.

Here a slightly modified approach is employed, whereby spatial and temporal smoothing is done via wavenumber-frequency filtering instead of application of running means. This modified approach is motivated by knowledge that different governing dynamics may apply to phenomena whose spatial and temporal scales are fairly similar. Here the order of magnitude of a given variable that has been filtered to a specific wavenumber-frequency combination (ω, λ) is estimated using equation 3.1. Further details of the methodology are provided in section 2.

To assist the assessment and interpretation of WTG balance, three terms of interest are defined as follows

$$\mathrm{W} = \frac{\left[\left(\overline{\omega}\frac{\partial \overline{s}}{\partial p}\right)^2\right]^{\frac{1}{2}}}{\left[\left(Q_1\right)^2\right]^{\frac{1}{2}}}(\omega, \lambda) \tag{3.16}$$

$$\mathrm{T} = \frac{\left[\left(\frac{\partial \overline{s}}{\partial t}\right)^2\right]^{\frac{1}{2}}}{\left[\left(Q_1\right)^2\right]^{\frac{1}{2}}}(\omega, \lambda) \tag{3.17}$$

$$\mathrm{H} = \frac{\left[\left(\overline{\boldsymbol{V}}_{\boldsymbol{h}} \cdot \boldsymbol{\nabla}\overline{s}\right)^2\right]^{\frac{1}{2}}}{\left[\left(Q_1\right)^2\right]^{\frac{1}{2}}}(\omega, \lambda) \tag{3.18}$$

As discussed earlier, WTG balance refers to a first order balance between large-scale vertical DSE advection and apparent heating in the DSE budget (see equation 3.3), where the DSE tendency and horizontal DSE advection are lower order terms. Therefore, the degree to which WTG balance applies can be objectively estimated by looking for regions of wavenumber-frequency space where $0.9 < \mathrm{W} < 1.1$, $\mathrm{T} < 0.1$, and $\mathrm{H} < 0.1$. While these values are chosen to provide some objectivity and clarity in the assessment of the subsequent figure, the reader is encouraged not to consider these as firm thresholds delineating clearly different dynamics, but more as being indicative of dynamical transition regions.

The color shading in Figure 3.24 shows the thermodynamic balance W for a range of wavenumber-frequency space. First note that the condition $0.9 < \mathrm{W} < 1.1$, which indicates the characteristic magnitude of large-scale vertical DSE advection and apparent heating are approximately of the same order, is met nearly everywhere in this space. The value $\mathrm{T} = 0.1$ is contoured in red, and red arrows highlight regions where the condition $\mathrm{T} < 0.1$ is met, indicating the characteristic magnitude of DSE tendency is of lower order than that of apparent heating. The value $\mathrm{H} = 0.1$ is contoured in blue, and blue arrows highlight regions where the condition $\mathrm{H} < 0.1$ is met, indicating the characteristic magnitude of horizontal DSE advection is of lower order than that of apparent heating. Taken together, these regions indicate that WTG balance is most applicable in a much narrower region of wavenumber-frequency space than would be implied by assessing the thermodynamic balance W alone. This region is characterized by low frequencies and small wavenumbers.

Another interesting feature of Figure 3.24 is that regions where the thermodynamic balance W exceeds 1 follow dispersion curves (thin black lines) for equatorial Kelvin waves, the eastward component of mixed Rossby gravity (MRG) waves, and the region typically associated with inertio-gravity waves, all strongly divergent phenomena associated with gravity-wave dynamics. As discussed earlier, this paper takes the perspective that intraseasonal variations in large-scale vertical motion are a direct dynamical response to intraseasonal variations in apparent heating, assumed to result from effective gravity wave adjustment occurring on temporal scales much shorter than, and spatial scales much larger than, intraseasonal variations in apparent heating. This perspective portrays local heating as the forcing, the large-scale dynamics as a response, and moisture as the intermediary that couples the two. If this were the case, an upper bound of $W = 1$ may be expected (i.e. large-scale adjustment does not result in adiabatic cooling exceeding apparent heating). But nature is full of examples of large-scale circulations driven, in large part, by processes other than local heating (e.g. mid-latitude baroclinic systems), and these large-scale circulations have the ability to force changes in local heating (e.g. through changes in static stability). Such examples may exist in the tropics in the form of certain convectively coupled equatorial waves (CCEW), whose large-scale dry dynamical counterparts do not rely on coupling with diabatic heating, as evidenced by their analytic counterparts originating from simplified sets of equations that contain no representation of such coupling (e.g. the shallow water equations of Matsuno (1966)). Findings of several recent studies (Yasunaga and Mapes 2012; Fuchs et al. 2014; Herman et al. 2016) suggest that this perspective, which portrays large-scale dynamics as the forcing and changes in local heating as a response, may apply to strongly divergent CCEWs such as Kelvin waves. Using both observations and idealized modeling,

these studies have demonstrated that changes in convective inhibition tend to slightly lead changes in convection in such waves, while changes in moisture tend to lag changes in convection. The finding that $W > 1$ follows the dispersion curves of strongly divergent CCEWs also supports this perspective. Yet the studies of Roundy (2008) and Roundy (2012), who showed that Kelvin waves can contain considerable rotational components and have OLR power spectra that transition fairly continuously into that of the MJO, suggest that the governing dynamics of Kelvin waves may transition as temporal scales approach those of the MJO. While Figure 3.24 offers no definitive diagnosis of cause and effect for the relationship of large-scale circulations to apparent heating with the MJO, it is suggestive that the MJO is governed by different dynamics than those of strongly divergent CCEWs, and that WTG balance dynamics are most relevant in a limited region of wavenumber-frequency space where the MJO occurs.

3.6. Comparison with Previous Studies

This study implements a WTG framework similar to that used in several previous studies, including Chikira (2014), Wolding and Maloney (2015a), and Janiga and Zhang (2016). Differences in these approaches warrants brief discussion. This study, as well as the studies of Wolding and Maloney (2015a) and Janiga and Zhang (2016), diagnose the large-scale vertical motion (equation 3.6) from the apparent heating. The large-scale vertical motion is the difference between the SGS environmental vertical motion and the cumulus induced SGS environmental vertical motion (Yanai et al. 1973), and represents the effect of large-scale horizontal convergence and divergence acting throughout the column. Using moisture and DSE tendencies resulting from detrainment, Chikira (2014) was able to diagnose the SGS environmental vertical motion and cumulus induced SGS environmental vertical motion,

in addition to the large-scale vertical motion. While the approach of Chikira (2014) is more desirable in that it provides a more detailed picture of the physical processes driving moistening or drying, moisture and DSE tendencies resulting from detrainment are often not known, thereby limiting the applicability of this approach to modeling and observational studies. The benefit of diagnosing the large-scale vertical motion is that is can be done with knowledge of only the apparent heat source and apparent moisture sink (Q_1 and Q_2 respectively), both of which are generally available in modeling and observational studies. In any case, these approaches vary only in the level of detail they provide, not in the physical processes they represent, and therefore the results of the aforementioned studies are directly comparable.

Chikira (2014) analyzed a 10 year simulation of the MJO in the Model for Interdisciplinary Research on Climate (MIROC) version 4.1, which implemented the Chikira-Sugiyama cumulus parameterization. Wolding and Maloney (2015a) analyzed 34 years of ERAi data, while Janiga and Zhang (2016) used the SAM to simulate the November MJO event of the Dynamics of the MJO (DYNAMO) field campaign (Yoneyama et al. 2013; Johnson and Ciesielski 2013). While the importance of intraseasonal variations in radiative heating was highlighted in each of these studies, they all exhibited vertical profiles of radiative heating anomalies that appear to be considerably more "top-heavy" than those observed in this study. The relatively bottom-heavy profiles of radiative heating anomalies in SP-CESM, which will drive relatively large moisture tendencies because of the large value of $\overline{\alpha}$ at low levels, may contribute to the apparent excessive instability of the column process noted earlier (Figs. 3.10a and 3.11a). Figures 3.7d and 3.10b support the findings of Wolding and Maloney (2015a) and Janiga and Zhang (2016), who noted the importance of low level heating and

SGS eddy fluxes in moistening low and mid levels during the transition from suppressed to enhanced convection. During the enhanced phase, Janiga and Zhang (2016) emphasize the role of SGS eddy fluxes in maintaining mid-level moisture, while Chikira (2014) finds that radiative heating anomalies play a dominant role. While the results of this study (Figure 3.9a) are, at first glance, more supportive of the findings of Janiga and Zhang (2016), we interpret this as being the vertical redistribution of moisture provided at low levels by the radiative driven anomalous convergence.

A secondary goal of this study was to compare and contrast the WTG balance framework with more traditional column MSE budget analyses of the MJO. While numerous previous studies have used the column MSE budget to investigate the MJO (Maloney 2009; Maloney et al. 2010; Kiranmayi and Maloney 2011; Andersen and Kuang 2012; Wu and Deng 2013; Kim et al. 2014a; Sobel et al. 2014; Arnold et al. 2015), this discussion will focus on the results of Arnold et al. (2015), who analyzed the same simulation used in this study. Figures 10 and 12 in Arnold et al. (2015) can be compared to Figures 3.10a,b from this study for reference during the following discussion. Using a column MSE variance budget, Arnold et al. (2015) concluded that the MJO was a radiative driven instability damped by horizontal advection, largely consistent with the findings of previous sections. Direct comparison of assessments made using the column MSE and WTG balance frameworks shows that, in most cases, both frameworks come to very similar conclusions regarding the contributions that individual processes (e.g. longwave radiative heating and SLHF) make to the growth and propagation of moisture/MSE anomalies. Yet these two frameworks come to opposite conclusions regarding the role of variations in SW radiative heating, which the column MSE

framework deems to be a destabilizing process (Figure 10 of Arnold et al. (2015)), and which the WTG framework deems to be a stabilizing process (Fig. 4.18b).

Inspection of Figures 4.18e,f provides some insight as to why these two approaches differ, and highlights the importance of quantitatively partitioning the vertical advection term of the MSE budget. During the enhanced phase, anomalous SW radiative heating in the upper troposphere exceeds anomalous SW cooling in the lower troposphere, such that the column integrated effect (not shown) is a net heating. As this is associated with a positive MSE tendency, this net heating appears as to act as a positive feedback (see Figure 10 of Arnold et al. (2015)) when assessed using a column MSE approach. Yet Figure 4.18f highlights that, because of the high moisture sensitivity of the lower troposphere, the anomalous SW radiative cooling at low and mid levels produces considerable drying, and results in a net drying of the column. This net drying of the column, which gets lumped into the vertical advection term of the MSE budget, is a negative feedback and is accurately assessed using the WTG balance framework (Fig. 4.18b). The results of Muller and Held (2012), who found that interactive SW radiation opposed aggregation, support the conclusion that variations in SW radiative heating act as a negative feedback for the MJO.

The differing assessments of the SW radiative feedback underscore a fundamental distinction that must be made between column integrated MSE and column integrated moisture, which are sometimes given a false equivalence on intraseasonal timescales. While it is true that, under WTG balance, column MSE anomalies are approximately equal to column moisture anomalies, processes that drive changes in MSE do not necessarily drive equivalent changes in moisture, as evidenced by variations in SW radiative heating. In the case of SW radiative heating, the column MSE framework measures its direct effect on column

DSE, while its effect on moisture (by driving large-scale vertical moisture advection) ends up lumped in with the vertical MSE advection term. This distinction can be the source of misinterpretation of results based on the column MSE framework, and metrics derived from column MSE (e.g. gross moist stability), if such tools do not evoke a clear and tangible connection to the physical processes at work in the minds of their users. The authors of this study believe that the WTG balance framework provides a more accurate and easily understood assessment of the relationship between heating, large-scale vertical motion, and moisture.

3.7. Conclusions

The superparameterized Community Earth System Model (SP-CESM) was used to investigate the MJO, with a primary focus on understanding the relationship between moisture, apparent heating, and large-scale vertical motion. In this study, the MJO is viewed as a slowly moving Matsuno-Gill pattern maintained by positive feedbacks between moisture, apparent heating, and large-scale dynamics. Intraseasonal variations in large-scale vertical motion are viewed as the result of effective gravity wave adjustment of intraseasonal variations in apparent heating. This dynamical response alters the large-scale distribution of moisture which, through convective scale processes such as entrainment, influences subsequent apparent heating and results in the aforementioned positive feedback. This perspective of the MJO is outlined in Figure 3.4.

WTG theory provides a useful framework for understanding the relationship between moisture, apparent heating, and large-scale vertical motion, allowing intraseasonal variations in large-scale vertical motion to be accurately diagnosed from apparent heating. Large-scale

vertical moisture advection can therefore be decomposed into contributions from various apparent heating processes, including microphysical processes, SGS eddy fluxes, and radiative heating. In this study, the WTG framework has been used to arrive at the following main conclusions:

(1) the MJO is strongly supported by radiative feedbacks and damped by horizontal advection, consistent with the findings of previous studies

(2) higher frequency convective variability contributes to damping by horizontal advection as well as destabilization by large-scale vertical moisture advection

(3) the evolution of the vertical structure of apparent heating does not play a dominant role in limiting the strength of MJO convection in SP-CESM

Each of these conclusions will now be discussed in turn.

While results from SP-CESM moisture and moisture variance budgets clearly support the conclusion that the MJO is strongly supported by radiative feedbacks, they suggest that such feedbacks may not be essential to the MJO, at least in SP-CESM. This is consistent with the findings of Arnold and Randall (2015), who showed that MJO-like activity persisted in a rotating global aqua-planet SP-CESM simulation when longwave radiative feedbacks were removed. Comparison of SP-CESM and ERAi moisture variance budgets suggests the former may have an unrealistically unstable column process, likely a result of excessive destabilization by radiative feedbacks or SGS convective processes. Discussion provided below may offer more insight to this issue.

Destabilization of the MJO is primarily limited by horizontal advective damping, which is accomplished through the modulation of higher frequency convective variability (Maloney and Dickinson 2003; Maloney 2009; Maloney et al. 2010; Kiranmayi and Maloney 2011;

Andersen and Kuang 2012; Chikira 2014). This study has shown that the modulation of higher frequency convective variability also enhances anomalous large-scale vertical moisture advection, which helps to destabilize the MJO. While the net effect of higher frequency convective variability remains a damping one, higher frequency variability may not play as important a role in limiting the strength of the MJO as once perceived by considering its horizontal advective damping effects alone.

Moisture variance budgets were used to assess how the strength of various feedbacks change as MJO amplitude increases. It was found that destabilization by radiative feedbacks actually increased as MJO amplitude increased. Perhaps more interesting is that the destabilizing effect of SGS convective processes showed only a modest decrease as MJO amplitude increased, and remained a destabilizing force even during periods of highest MJO amplitude. This occurs despite a dramatic increase in the damping effect of precipitation, and results from the near perfect compensation by large-scale vertical moisture advection driven by convective heating. To state this another way, heating released by increased precipitation drives enough large-scale vertical moisture advection to replace the moisture directly removed by increased precipitation, or $\Delta \left\langle \overline{\alpha} \left(Q_1 - \overline{Q}_R \right) \right\rangle \approx \Delta \left\langle \left(Q_1 - \overline{Q}_R \right) \right\rangle$, where Δ is change associated with a change in MJO amplitude. Taken together with the increasing strength of the radiative feedback, this leads to the conclusion that changes in the vertical structure of apparent heating structure play little role in limiting MJO amplitude, at least in SP-CESM. This is important because it implies that MJO amplitude ceases to increase when horizontal advective damping has become sufficiently strong, not when destabilization by the column process has become sufficiently weak. While apparent heating may become progressively more top-heavy in regions of enhanced convection as MJO amplitude increases,

this appears to play little role in limiting the amplitude of the MJO. Destabilization by the column process does not appear to be strongly "self-limiting".

But how is it that, as MJO convective anomalies increase in magnitude, and the convective heating profile becomes progressively more top-heavy, heating can continue to drive sufficient large-scale vertical moisture advection to result in destabilization? Inspection of Figure 3.5a, which shows the moisture sensitivity to apparent heating, offers a suggestion. The large moisture sensitivity of the lower troposphere means that a small increase in heating at lower levels can drive comparably large amounts of large-scale vertical moisture advection. Therefore, as long as sufficient increases in low level heating occur coincidentally with increased heating at upper levels, the heating profile may become progressively more top heavy but still drive sufficient large-scale vertical moisture advection to remain unstable. This idea is consistent with the findings of Riley et al. (2011), who used CloudSat observations to show that increased occurrence of all cloud types occur during the enhanced phase of the MJO. This idea would also suggest that convective schemes lacking the ability to simulate the coincidental enhancement of both shallow and deep convection may have difficulties simulating instabilities driven by SGS convective processes.

The findings of this study suggest the following physical picture of the MJO in SP-CESM. The enhanced phase of the MJO is characterized by a considerable increase in convective activity over a large geographic region. Phrases such as "convective moistening" are often used to describe convective processes occurring on the SGS (i.e. microphysical processes and SGS eddy fluxes). While these processes can act to moisten the atmosphere at certain levels by vertically redistributing moisture throughout the column, this vertical redistribution often comes at a cost to column moisture, which is removed by precipitation processes. The

net effect is such that, during the enhanced phase when precipitation increases, convective processes occurring on the SGS act to warm and dry the column on the large-scale. When such processes occur over several days or more in the tropics, very little of the aforementioned warming is realized, as effective gravity wave adjustment results in low level mass convergence, large-scale ascent, and adiabatic cooling that balances the warming. This low level mass convergence represents the drawing in of moist air from distant regions, which is returned at upper levels in a much drier condition. During the enhanced phase, the increased large-scale convergence resulting from warming by SGS convective processes alone (i.e. without variations in radiative heating) brings with it more than enough moisture to offset the increased drying by SGS convective processes. The enhanced phase is also accompanied by a reduction in longwave radiative cooling, which drives additional low level moisture convergence. The result is that the enhancement of convection over a large geographic region converges more moisture than it removes via precipitation, allowing enhanced precipitation to be sustained (or even amplified), despite reduced surface fluxes of moisture, which are suppressed in the enhanced phase of the MJO in SP-CESM. The ability of convection to acquire moisture from remote sources is what permits the coexistence of minima in surface fluxes of moisture and maxima in precipitation observed over the warm pool (Sobel 2003). A similar coexistence of minima in surface fluxes of moisture and maxima in precipitation is observed during the enhanced phase of the MJO in SP-CESM, suggesting that understanding the mechanisms whereby convection acquires moisture from remote sources is crucial to understanding the moisture-convection feedback thought to drive the MJO.

Examination of Figure 3.4 highlights the numerous difficulties faced when trying to understand and simulate the MJO. First note the incredible range of scales encompassed by

the processes that appear to be crucial to the MJO, which span from small scale processes such as entrainment and microphysics to the global scale dynamical response. While GCMs are able to span the global scale dynamical response, many do not exhibit an appropriate sensitivity of convection to free tropospheric humidity (Thayer-Calder and Randall 2009), emblematic of the poor representation of small scale processes (bottom left arrows) such as entrainment (Hannah and Maloney 2014). Yet CSRMs, while able to represent small scale process more realistically, are often computationally limited to domains which only encompass a fraction of the large-scale dynamical response. Only recent generations of models have begun to effectively span the range of scales necessary to produce realistic intraseasonal variability (Randall et al. 2003; Raymond and Zeng 2005; Sessions et al. 2010; Bretherton and Khairoutdinov 2015; Arnold and Randall 2015). Even when a model is able to realistically represent processes across this range of scales, a model's climate may produce unrealistic feedbacks between these various processes. The dynamical response to apparent heating (top arrow) will be scaled by a model's static stability, while the resulting moisture convergence (bottom right arrow) will be closely related to a model's $\overline{\alpha}$. Such factors may help to explain not only why some models produce insufficient intraseasonal variability, but also why some models produce intraseasonal variability with characteristics different from that of the real world.

Phenomena are often distinguished by their organizing forces, a custom borne more from understanding than from the desire to categorize. Advancing understanding of both the MJO and convective aggregation may be accelerated by continuing to seek out and apply meaningful process oriented diagnostics to these phenomena. Given the weak destabilizing effect of convection alone (i.e. in the absence of radiative and surface flux feedbacks), it seems

reasonable to expect that a positive feedback between moisture, heating, and large-scale dynamics could be achieved through a different combination of processes than those that occur in SP-CESM. Process oriented diagnostics should assess not only if a model is simulating sufficiently strong feedbacks between moisture, heating, and large-scale dynamics, but also that such feedbacks are driven by the "correct" combination of stabilizing and destabilizing processes. Successful implementation of such diagnostics will require the "correct" combination of stabilizing and destabilizing processes of the real world MJO be better constrained. In particular, more work must be done to constrain the vertical profile of radiative heating (Lin et al. 2004; Ma and Kuang 2011; Jiang et al. 2011), and how this profile relates to destabilization by the column process.

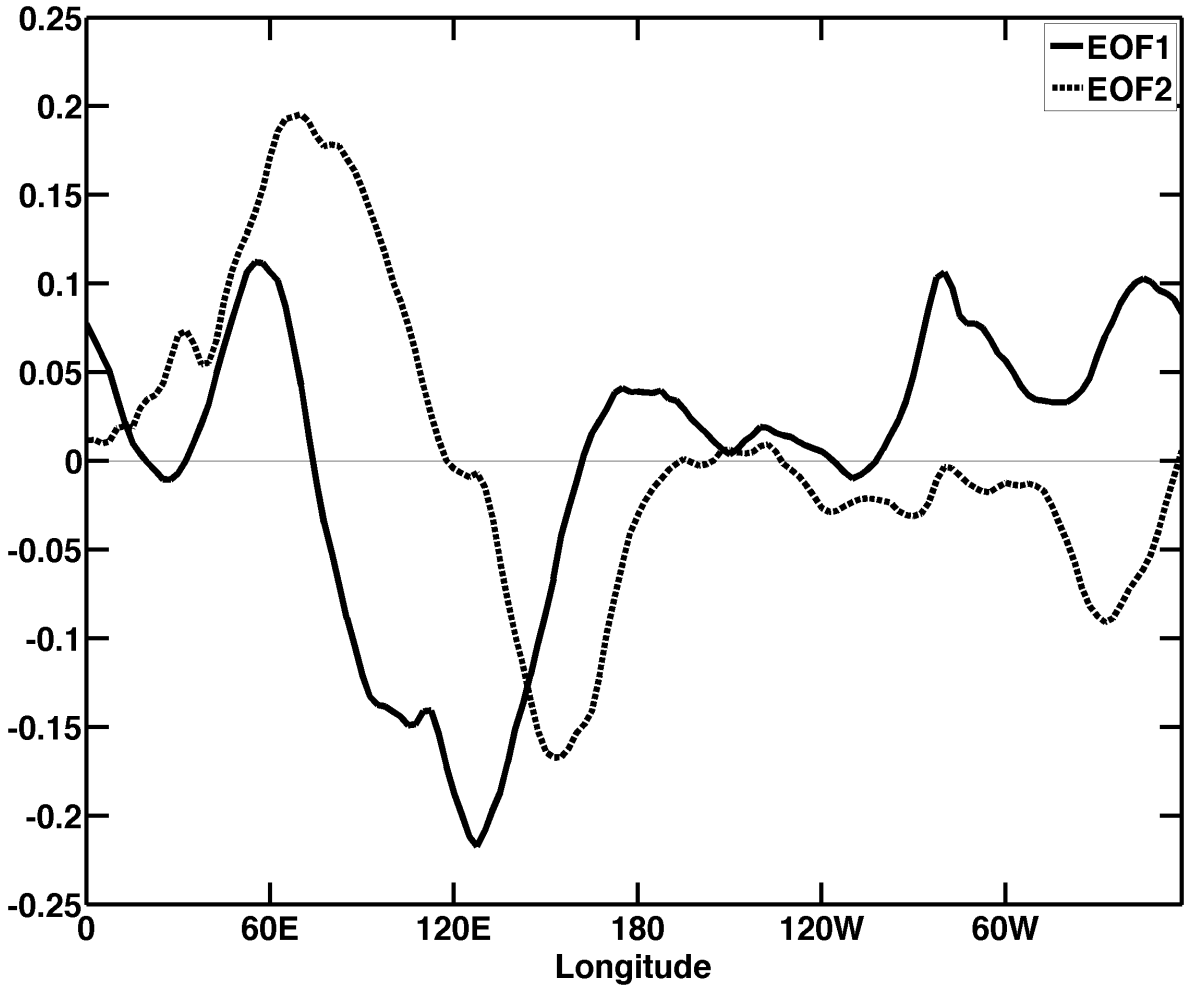

FIG. 3.1. The two leading EOF structures of latitudinally averaged (15°N-15°S) 20-100 day bandpass filtered OLR for SP-CESM. The first two EOFs explain 16.7% and 12.4% percent of the total variance respectively.

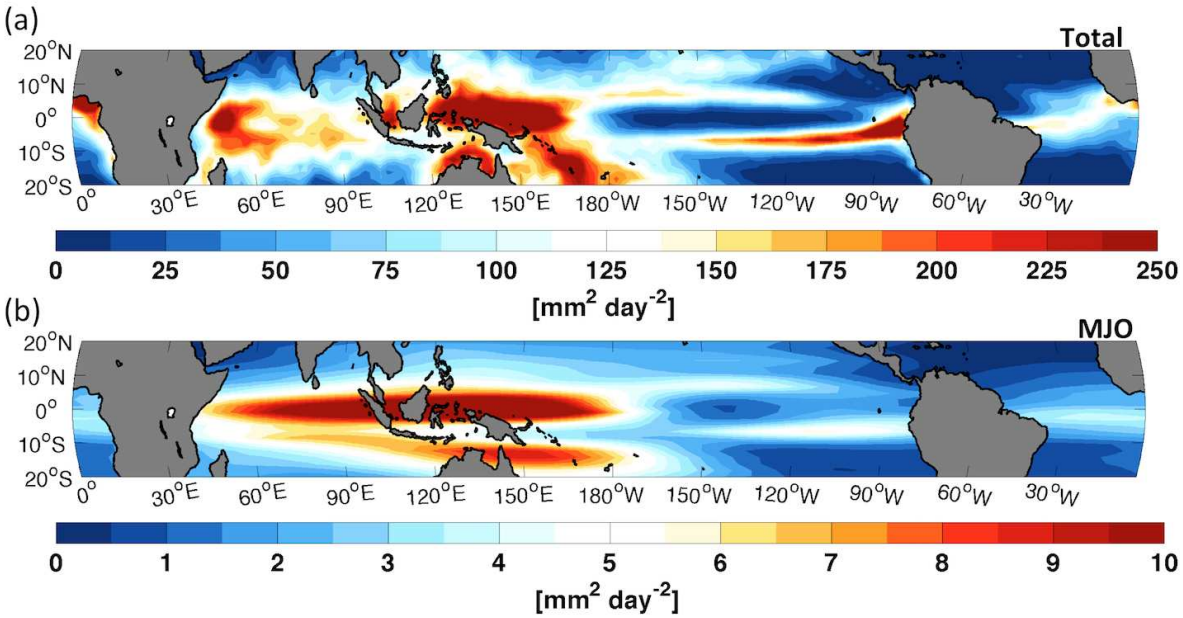

FIG. 3.2. Variance of (a) unfiltered precipitation and (b) precipitation filtered to eastward wavenumbers 0 to 5 and frequencies corresponding to 20-100 days in SP-CESM.

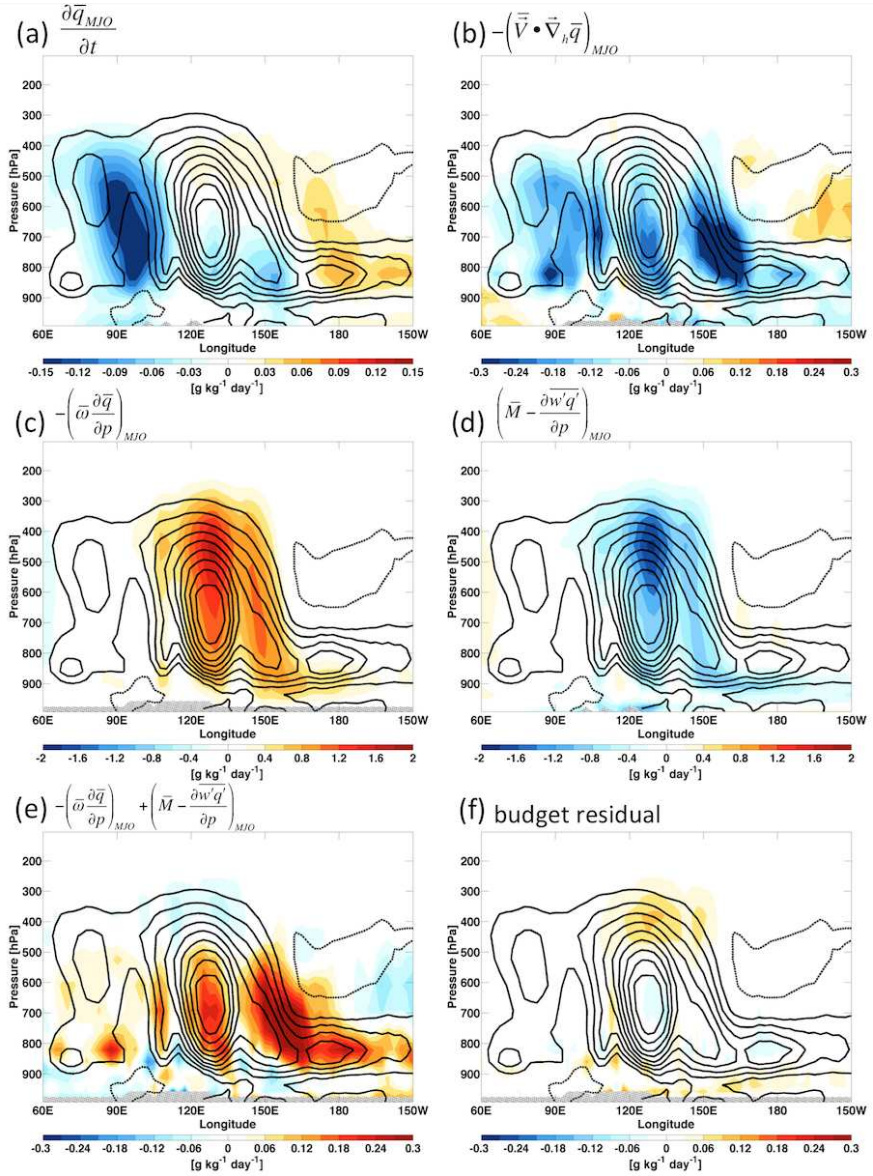

FIG. 3.3. Longitude-height sections of latitudinally averaged (5°N−5°S) composite intraseasonal moisture budget terms (shading). These terms are the (a) Eulerian moisture tendency, (b) horizontal moisture advection, (c) vertical moisture advection, (d) the net effect of the microphysical moisture tendency and sub-grid scale vertical eddy moisture flux convergence, (e) the column process (i.e. the sum of plots (c) and (d)), and (f) the moisture budget residual. Solid and dashed contours indicate positive and negative specific humidity anomalies respectively, with contour intervals of 0.1 g kg^{-1}. Composites are produced from 19 independent wintertime (October 1 to April 30) events. Grey hatching indicates regions where data has been lost as a result of proximity to the surface. The subscript MJO indicates application of 20-100 day bandpass filtering. Please note the color scale differs between plots.

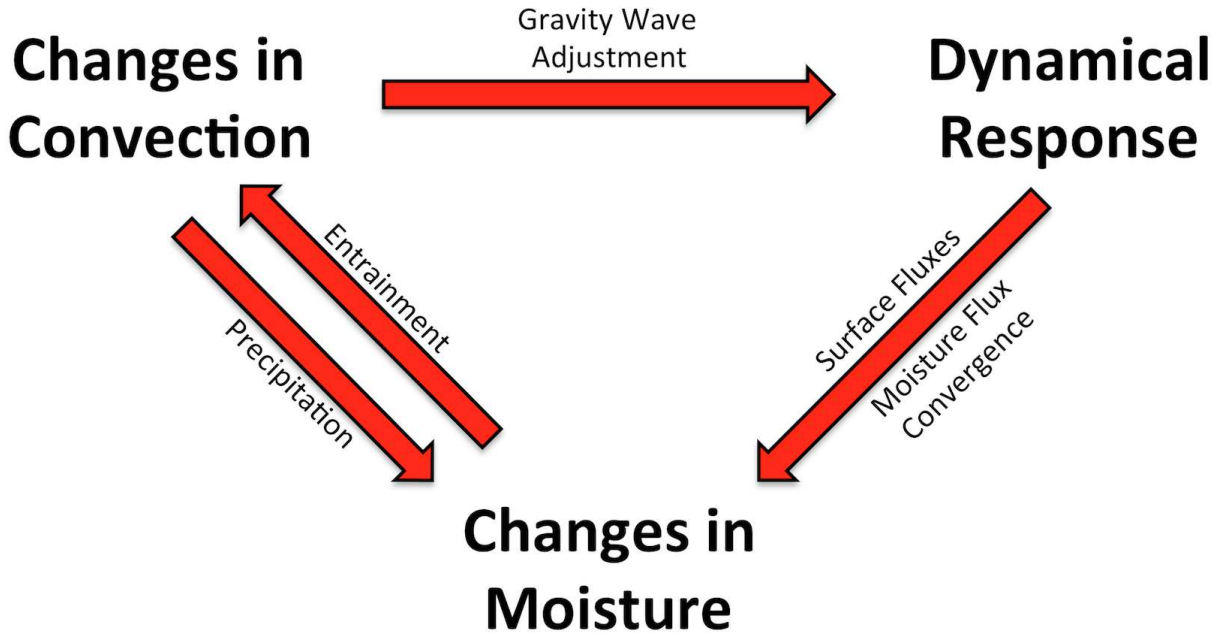

FIG. 3.4. A simplified schematic illustrating the relationship between various processes as viewed from the idealized weak temperature gradient balance framework adopted in this study.

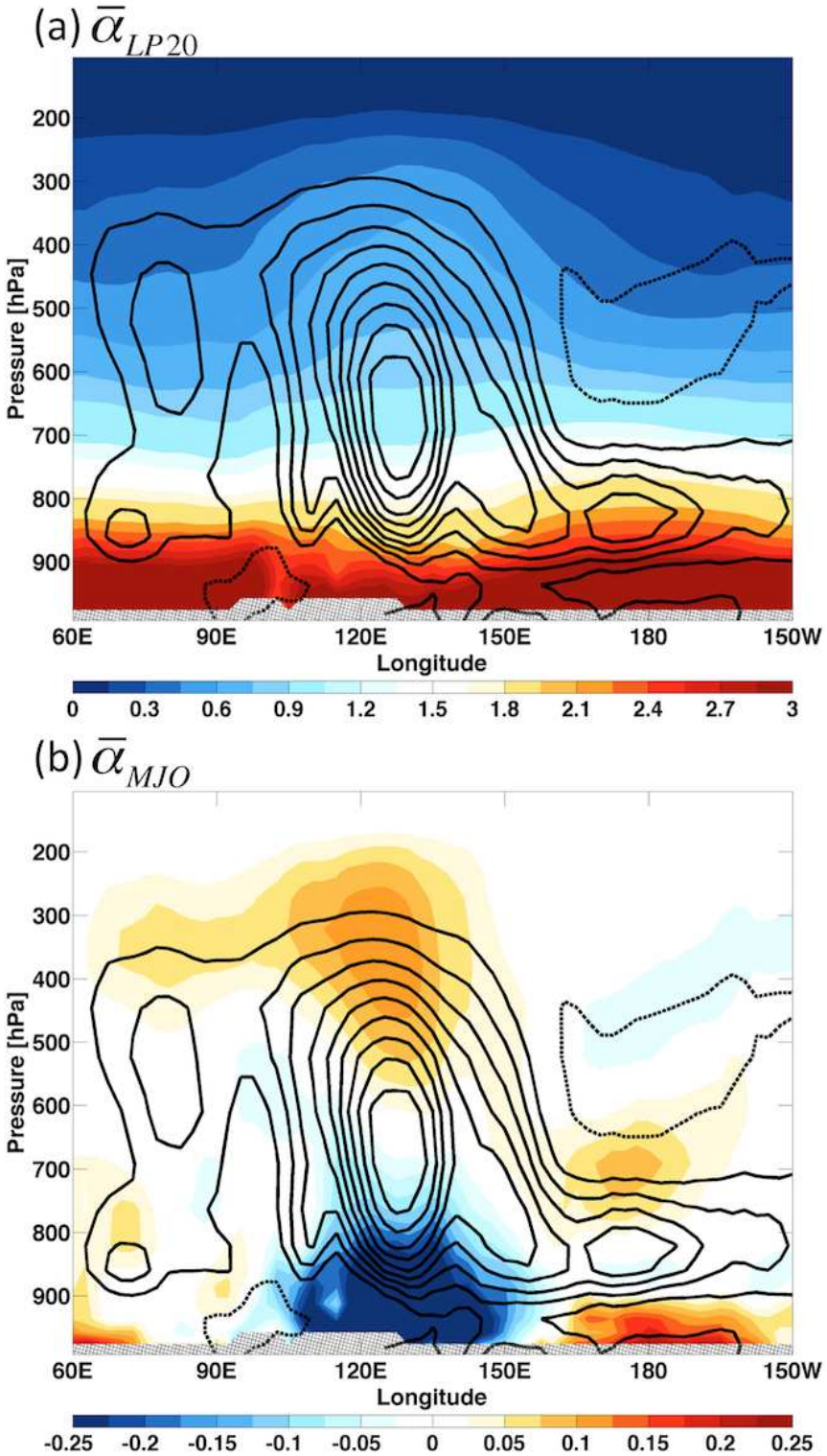

FIG. 3.5. As in Figure 3.3, except the color shading indicates alpha, where alpha has been (a) lowpass filtered to 20 days and (b) bandpass filtered to 20-100 days. The subscripts LP20 and MJO indicate application of 20 day lowpass and 20-100 day bandpass filtering respectively. Please note the color scale differs between plots.

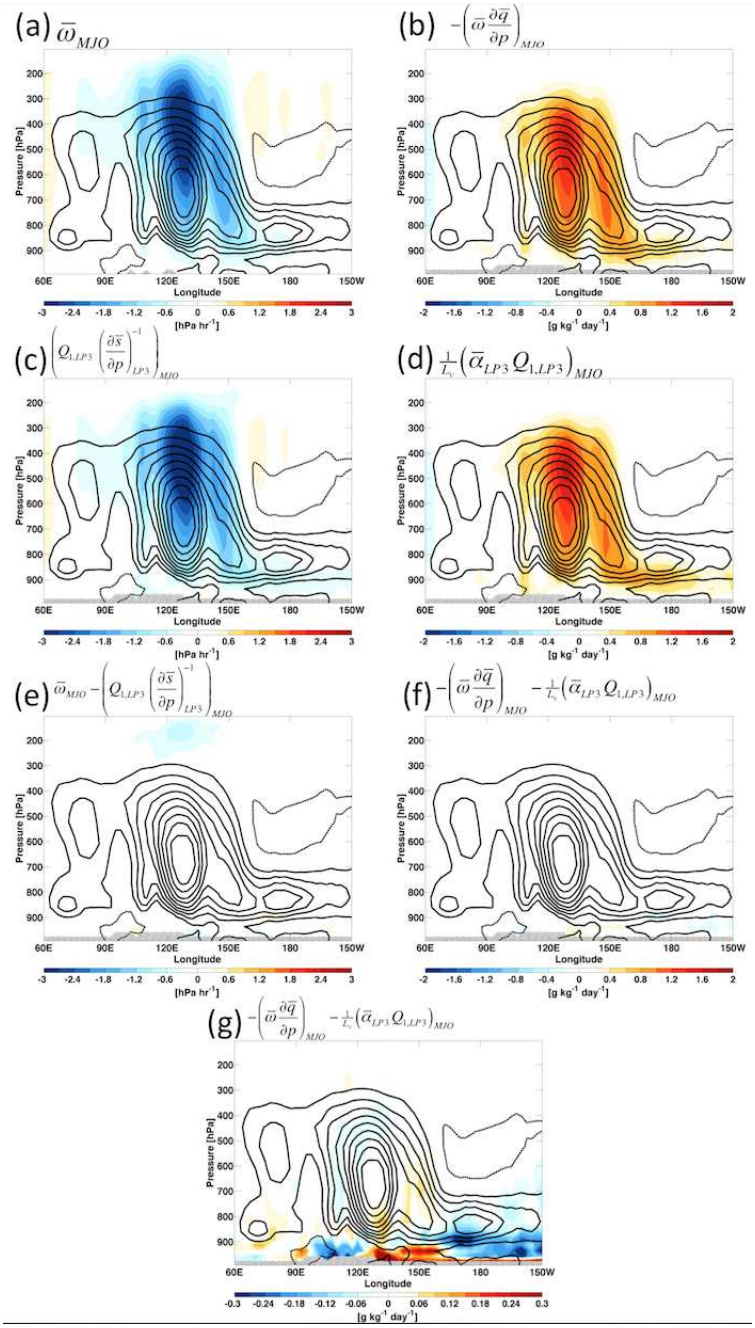

FIG. 3.6. As in Figure 3.3, except the color shading indicates the anomalous (a) large-scale vertical velocity and (b) vertical moisture advection in SP-CESM, the anomalous (c) large-scale vertical velocity and (d) vertical moisture advection diagnosed using weak temperature gradient balance assumptions, and the difference between the actual and diagnosed (e) large-scale vertical velocity and (f,g) vertical moisture advection. The subscripts LP3 and MJO indicate application of 3 day lowpass and 20-100 day bandpass filtering respectively. Please note the color scale of plot (g) differs from that of plots (b), (d), and (f).

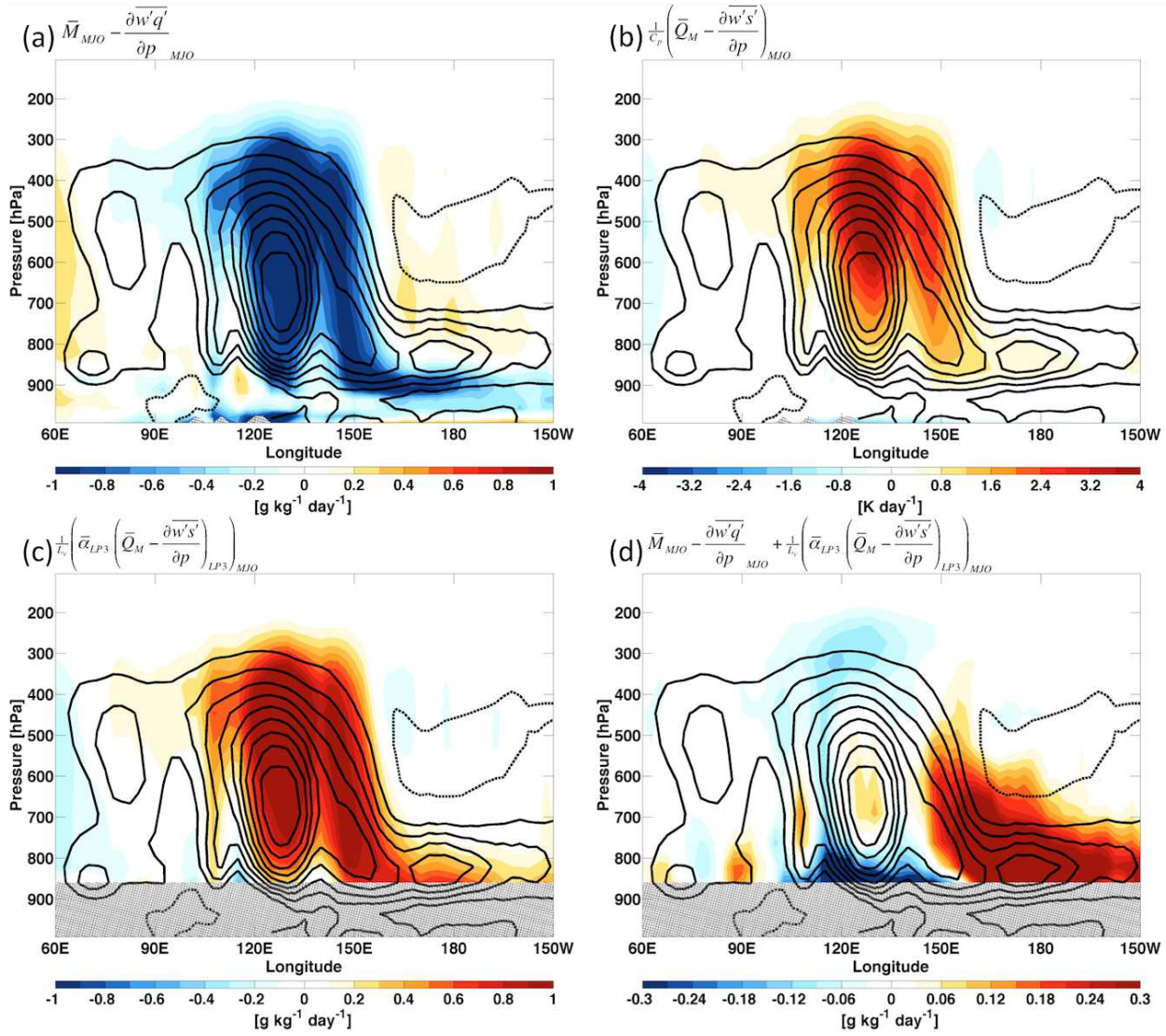

FIG. 3.7. As in Figure 3.3, except the color shading indicates (a) the net effect of the microphysical moisture tendency and sub-grid scale (SGS) vertical eddy moisture flux convergence, (b) the net effect of microphysical heating and SGS vertical eddy heat flux convergence, (c) the large-scale vertical moisture advection associated with the aforementioned heating (i.e. plot (b)) under weak temperature gradient balance, and (d) the sum of the direct and weak temperature gradient balance moisture tendencies associated with microphysical processes and SGS vertical eddy flux convergence (i.e. the sum of plots (a) and (c) respectively). Grey hatching has been applied below 850 hPa in plots (c),(d), as weak temperature gradient balance in not applicable in the boundary layer. The subscripts LP3 and MJO indicate application of 3 day lowpass and 20-100 day bandpass filtering respectively. Please note the color scale differs between plots.

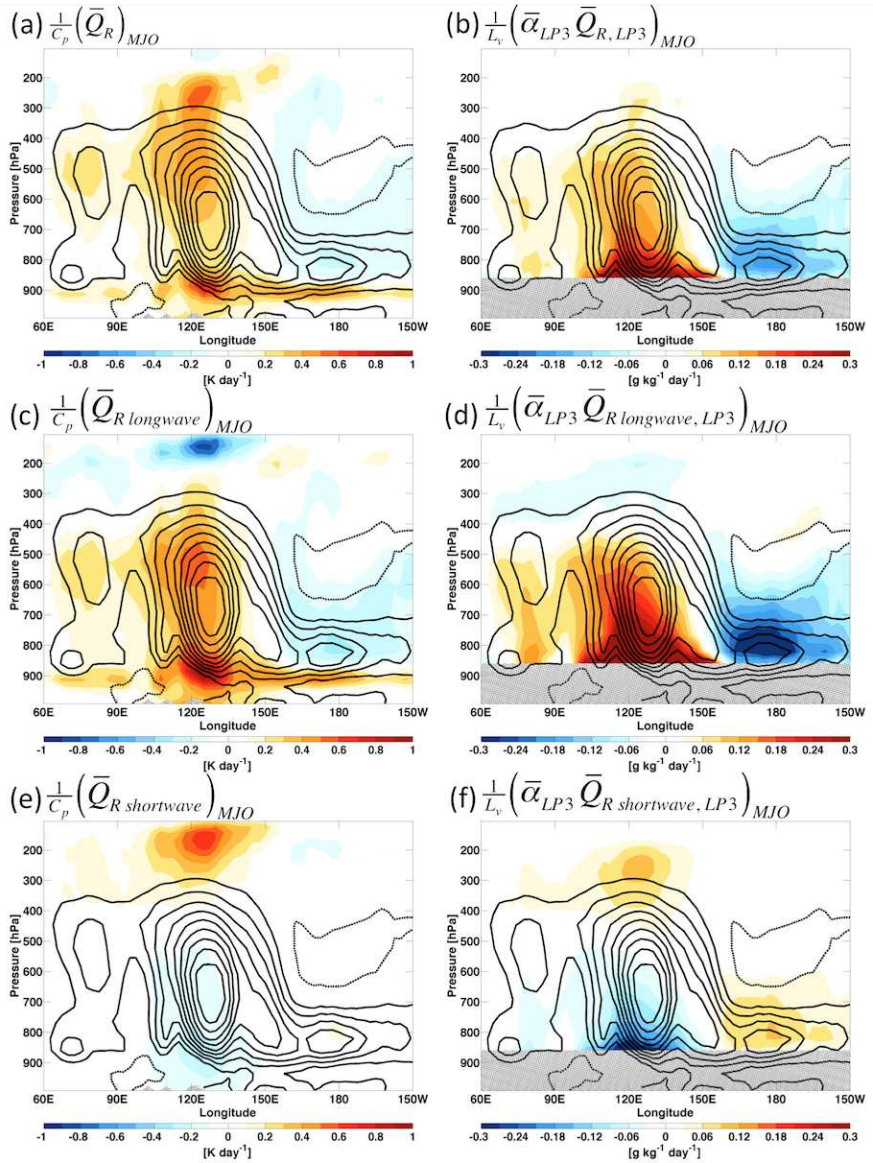

FIG. 3.8. As in Figure 3.3, except the color shading indicates anomalous (a) total, (c) longwave, and (e) shortwave radiative heating, and the corresponding (b),(d),(f) large-scale vertical moisture advection diagnosed using weak temperature gradient balance. Grey hatching has been applied below 850 hPa in plots (b),(d),(f), as weak temperature gradient balance in not applicable in the boundary layer. The subscripts LP3 and MJO indicate application of 3 day lowpass and 20-100 day bandpass filtering respectively.

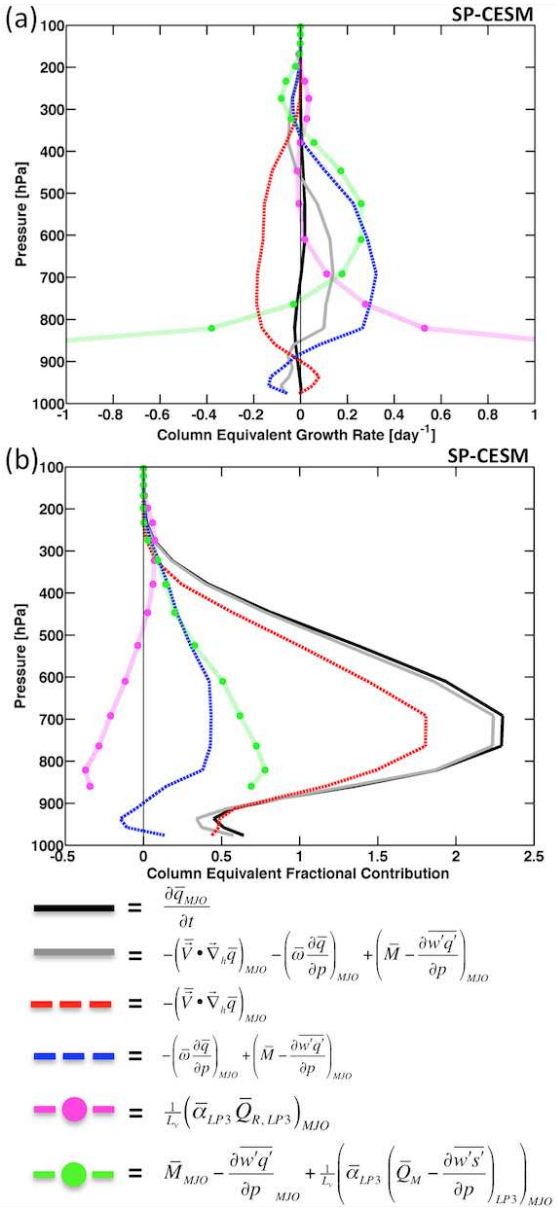

FIG. 3.9. Vertical profiles of contributions various budget terms make to the (a) column moisture variance growth rate and (b) column moisture tendency in SP-CESM, corresponding to equations 4.1 and 3.10 respectively. Column moisture was calculated by vertically integrating from the surface to 100 hPa. The area weighted integral has been taken from 10.5°N-14.5°S, 60°E-180°E, and averaged from day -30 to day +30 for each of the 19 independent winter events composited. In order to ease interpretation, each term has been scaled by the mass equivalent of 900 hPa at each level. The subscripts LP3 and MJO indicate application of 3 day lowpass and 20-100 day bandpass filtering respectively.

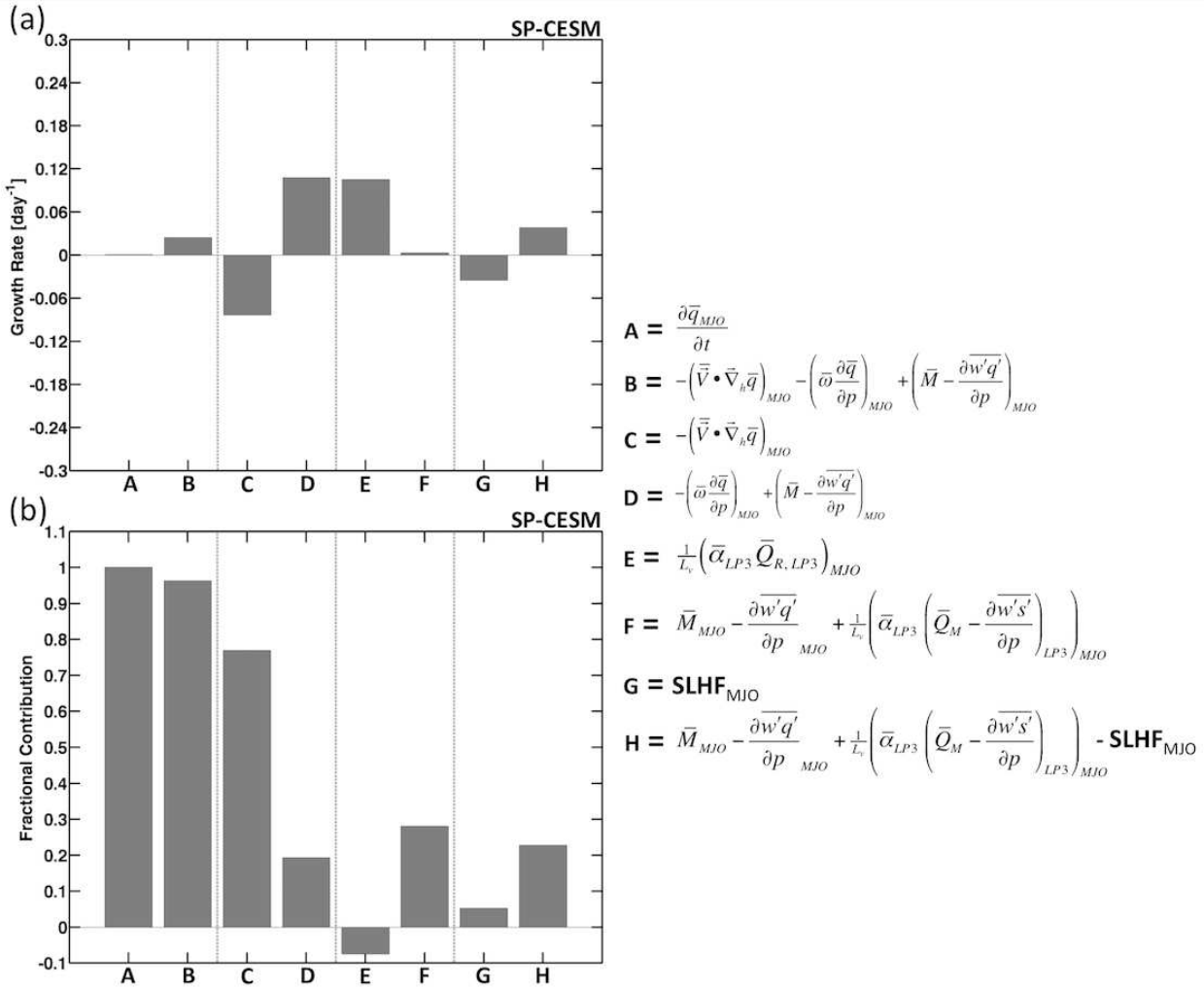

FIG. 3.10. Vertically integrated contributions various budget terms make to the (a) column moisture variance growth rate and (b) column moisture tendency in SP-CESM, corresponding to the vertical integral of equations 4.1 and 3.10 respectively. Column moisture was calculated by vertically integrating from the surface to 100 hPa, as were terms A through D. Terms E, F, and H were vertically integrated from 850 to 100 hPa, as they depend on the weak temperature gradient approximation. The area weighted integral has been taken from 10.5°N-14.5°S, 60°E-180°E, and averaged from day -30 to day +30 for each of the 19 independent winter events composited. The subscripts LP3 and MJO indicate application of 3 day lowpass and 20-100 day bandpass filtering respectively.

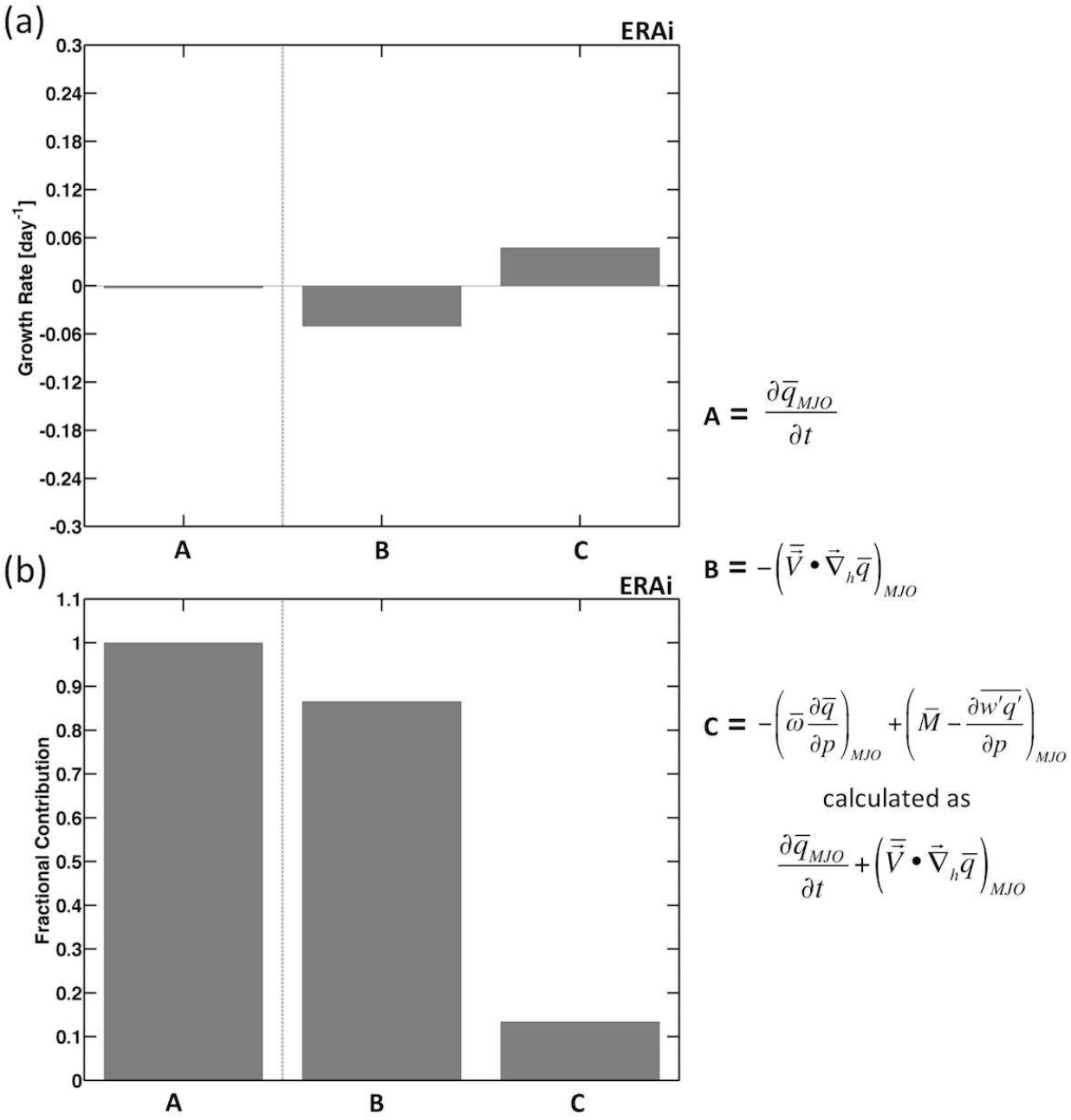

FIG. 3.11. As in Figure 3.10, except for ERA-interim reanalysis data. The area weighted integral has been taken from 10.5°N-13.5°S, 60°E-180°E, and averaged over every winter (October 1 - April 30) day where the magnitude of the FMO index exceeded a value of 1. The subscript MJO indicates application of 20-100 day bandpass filtering.

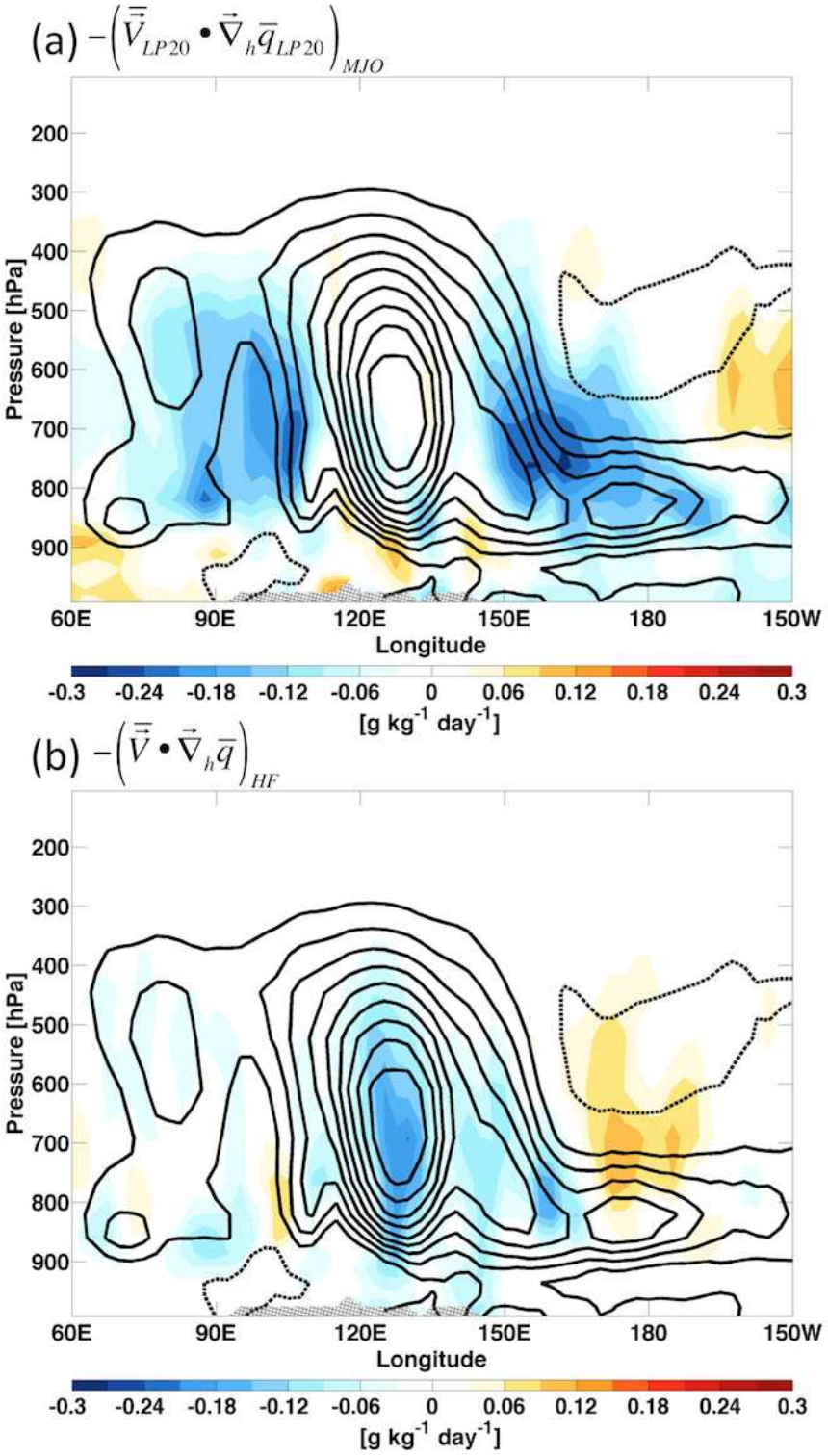

FIG. 3.12. As in Figure 3.3, except the color shading indicates horizontal moisture advection due to (a) slow variations and (b) higher frequency variability (as indicated by the subscript HF) calculated following equation 4.9. The subscripts LP20 and MJO indicate application of 20 day lowpass and 20-100 day bandpass filtering respectively.

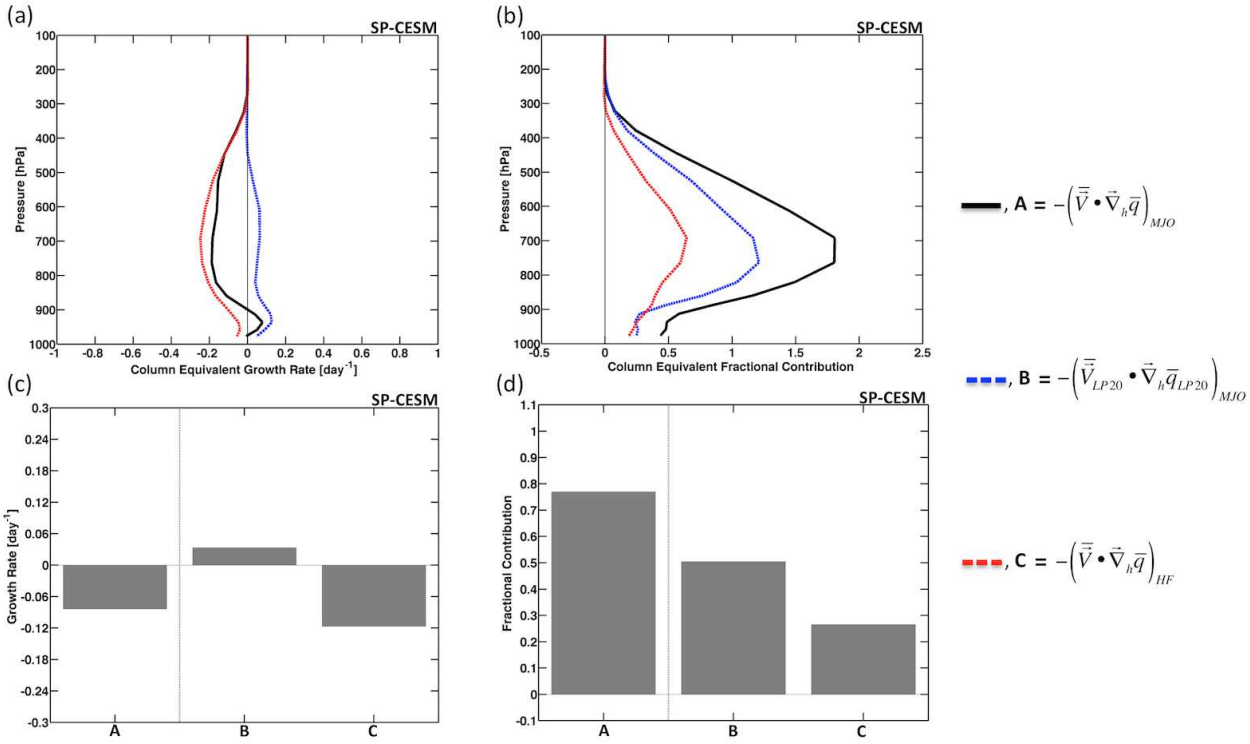

FIG. 3.13. (a,b) as in Figure 3.9a, and (c,d) as in Figure 3.10a, except for various horizontal advective terms. The subscripts LP20 and MJO indicate application of 20 day lowpass and 20-100 day bandpass filtering respectively. The subscript HF indicates terms related to higher frequency variability, calculated following equation 4.9.

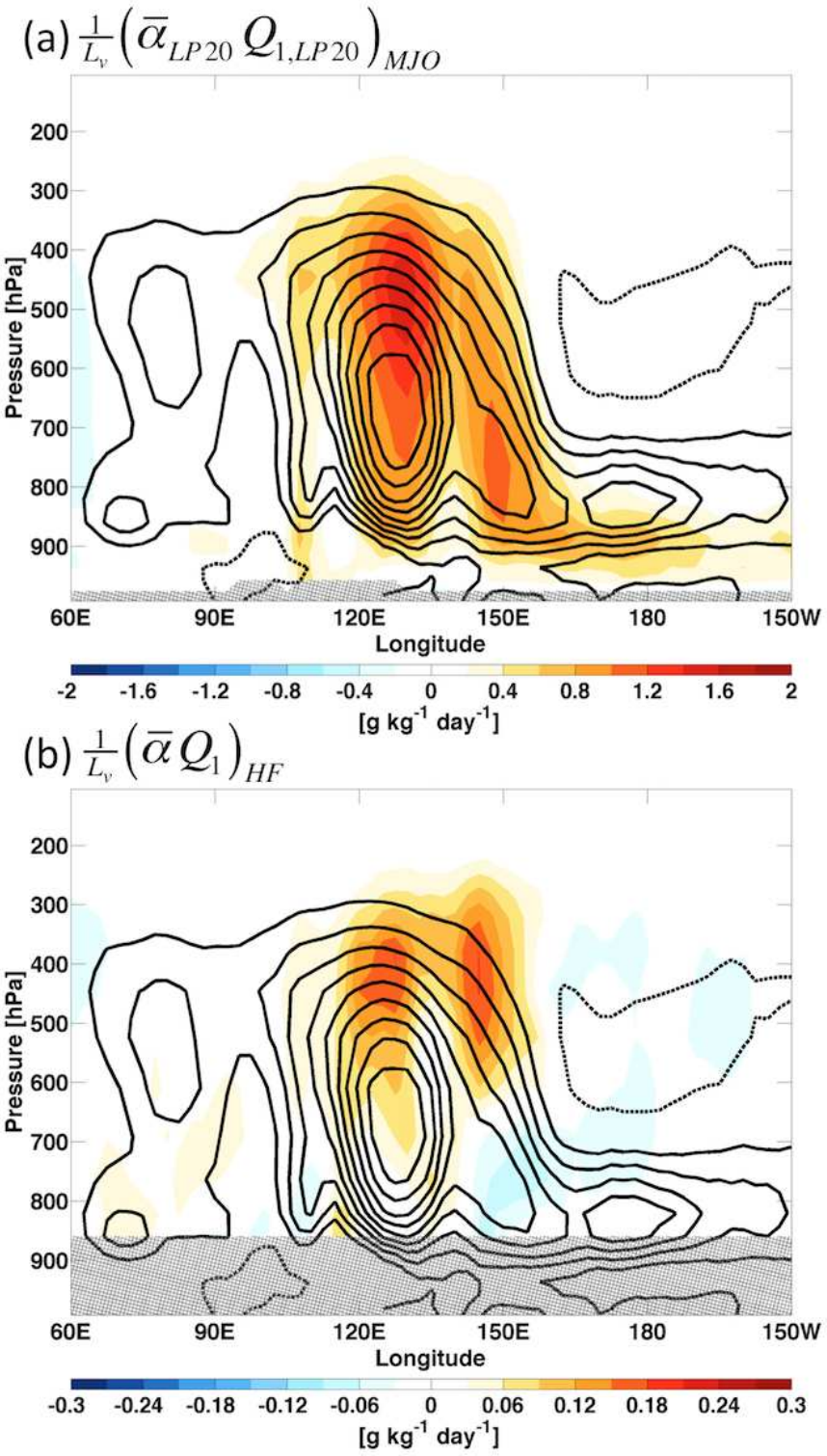

FIG. 3.14. As in Figure 3.3, except the color shading indicates large-scale vertical moisture advection due to (a) slow variations and (b) higher frequency variability (as indicated by the subscript HF) calculated following equation 4.11. The subscripts LP20 and MJO indicate application of 20 day lowpass and 20-100 day bandpass filtering respectively.

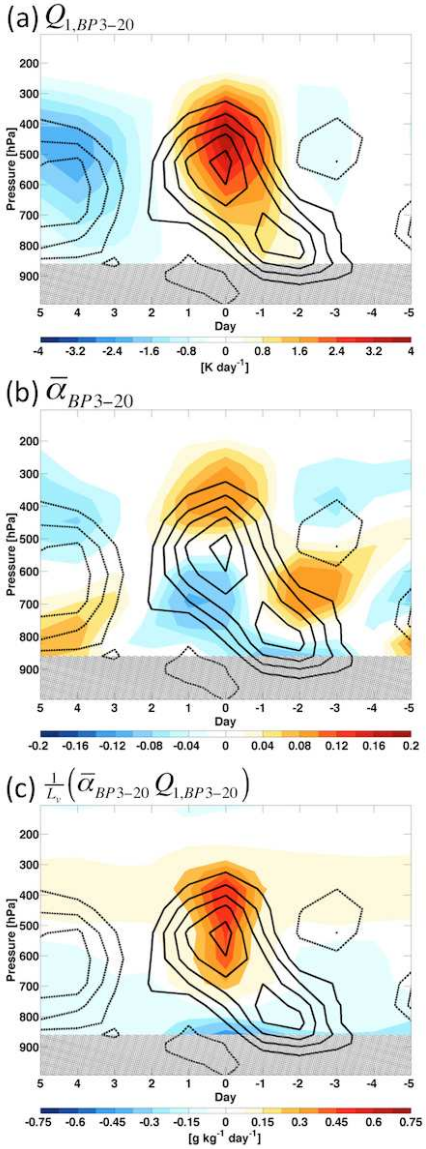

FIG. 3.15. Vertical profiles of various terms relating to higher frequency convective activity (shading) as a function of lag-day. Solid and dashed contours indicate positive and negative specific humidity anomalies respectively, with contour intervals of 0.1 g kg^{-1}. Composites are produced from 81 independent wintertime (October 1 to April 30) events, and averaged over the domain 10°N−10°S, 75°E−85°E. See text for more details on the compositing method. Grey hatching has been applied below 850 hPa, as weak temperature gradient balance in not applicable in the boundary layer. The subscript BP3-20 indicates application of 3-20 bandpass filtering.

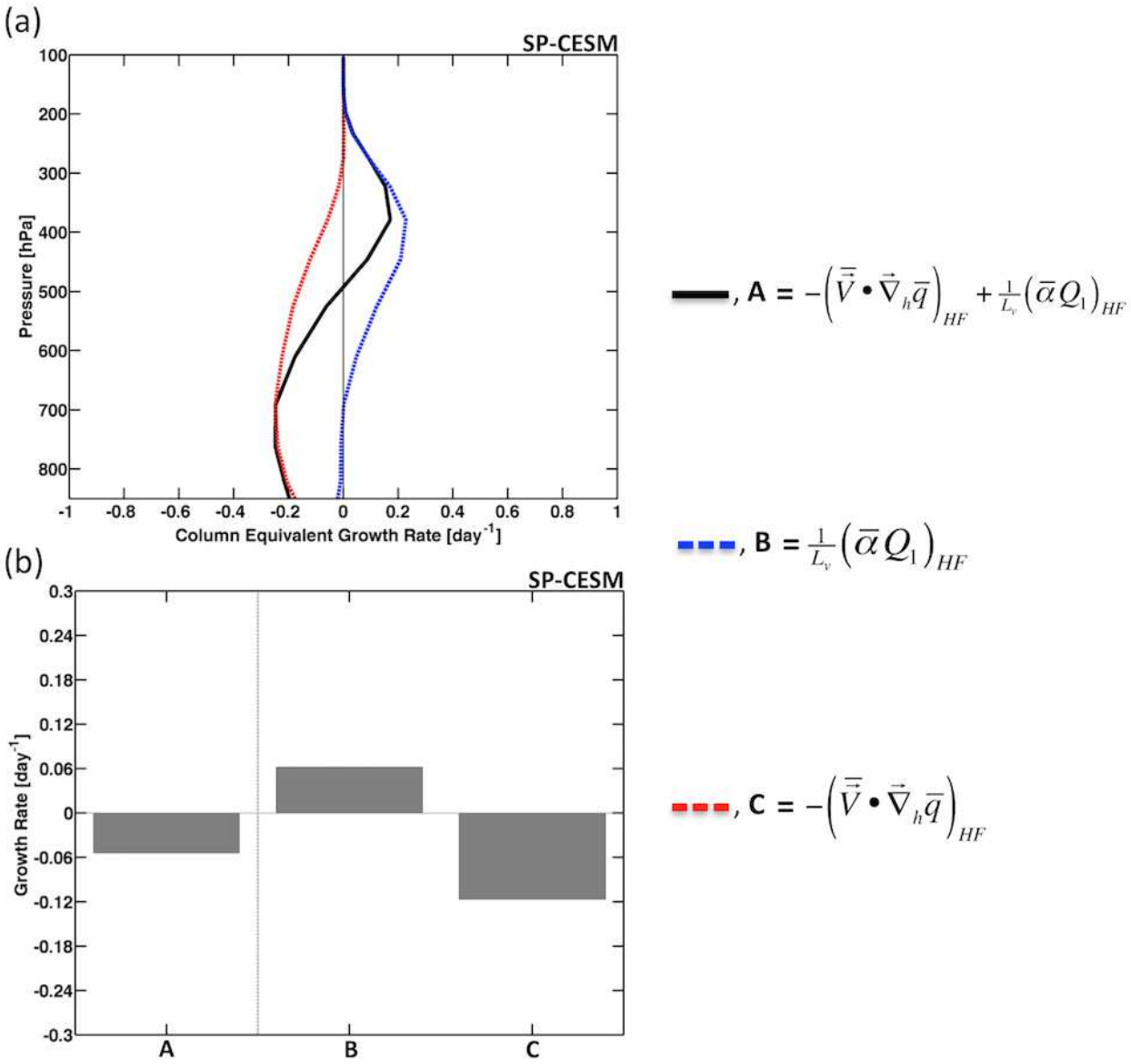

FIG. 3.16. (a) as in Figure 3.9a, and (b) as in Figure 3.10a, except for terms related to higher frequency convective variability. The subscript HF indicates terms related to higher frequency variability, calculated following equations 4.9 and 4.11.

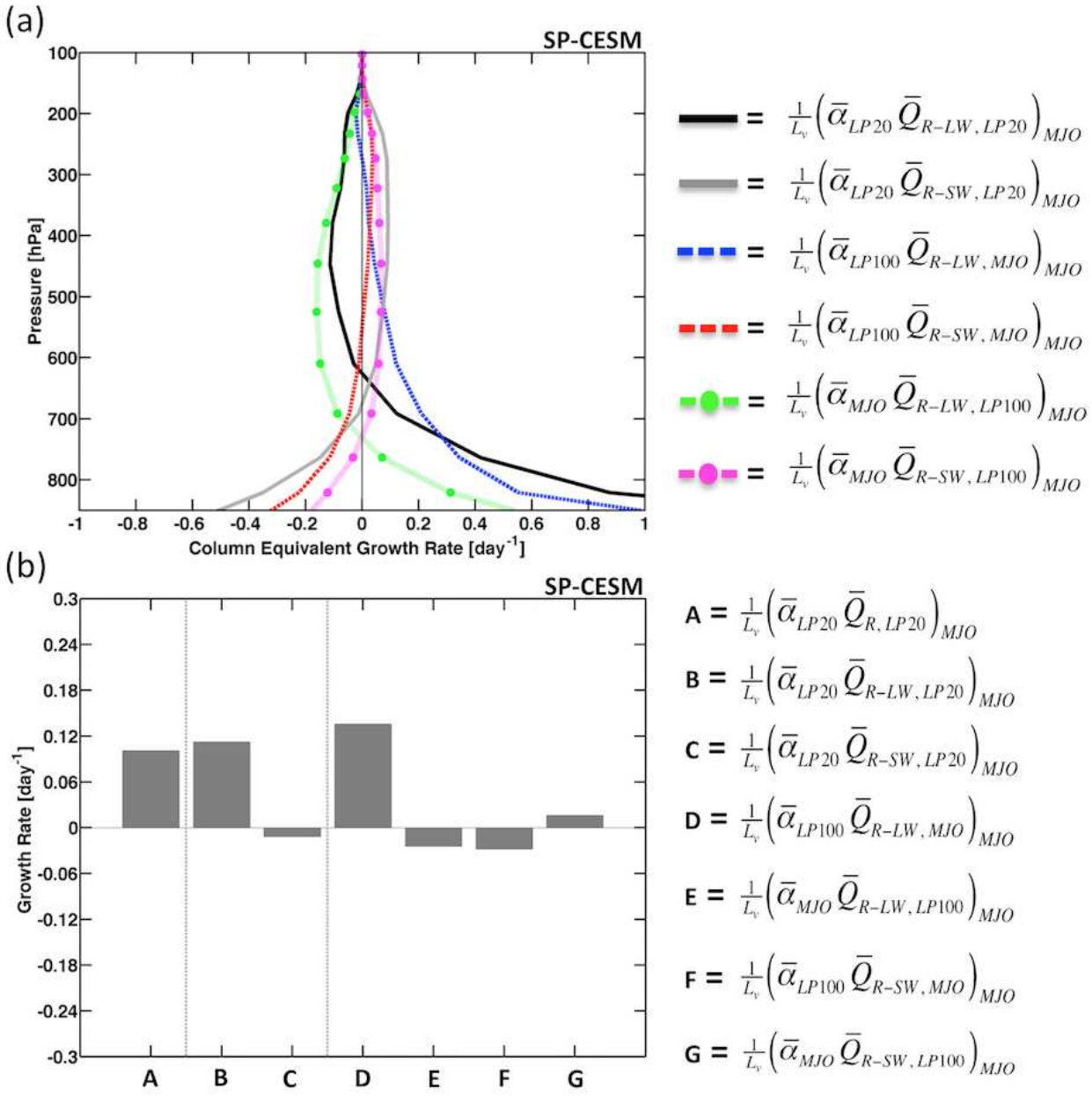

FIG. 3.17. (a) as in Figure 3.9a, and (b) as in Figure 3.10a, except for various radiative heating terms. Each term in (b) was vertically integrated from 850 to 100 hPa, as they depend on the weak temperature gradient approximation. The subscripts LP20, LP100, and MJO indicate application of 20 day lowpass, 100 day lowpass, and 20-100 day bandpass filtering respectively.

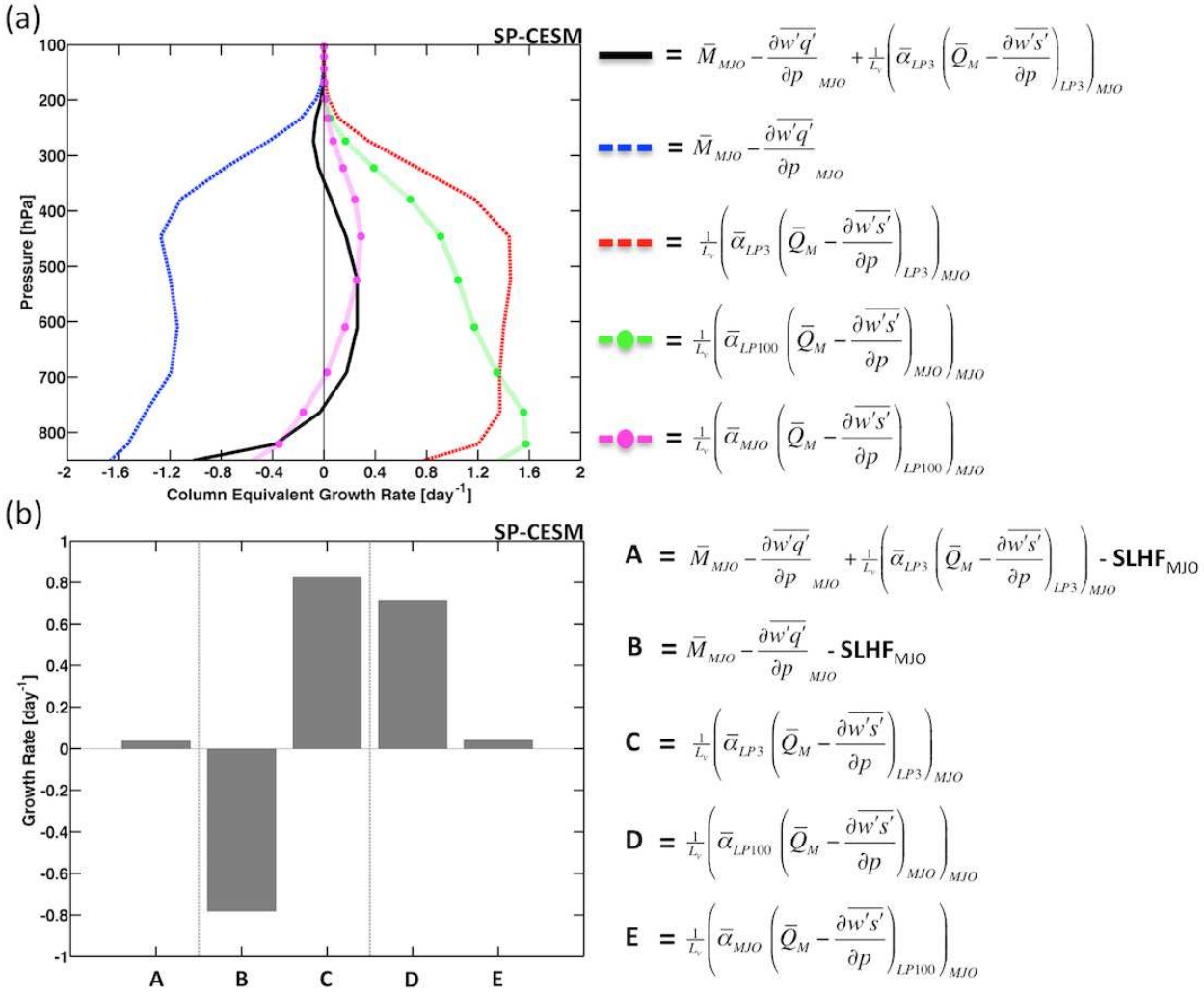

FIG. 3.18. (a) as in Figure 3.9a, and (b) as in Figure 3.10a, except for various terms relating to microphysical processes and sub-grid scale vertical eddy flux convergence. Each term in (b) was vertically integrated from 850 to 100 hPa. The subscripts LP3, LP100, and MJO indicate application of 3 day lowpass, 100 day lowpass, and 20-100 day bandpass filtering respectively.

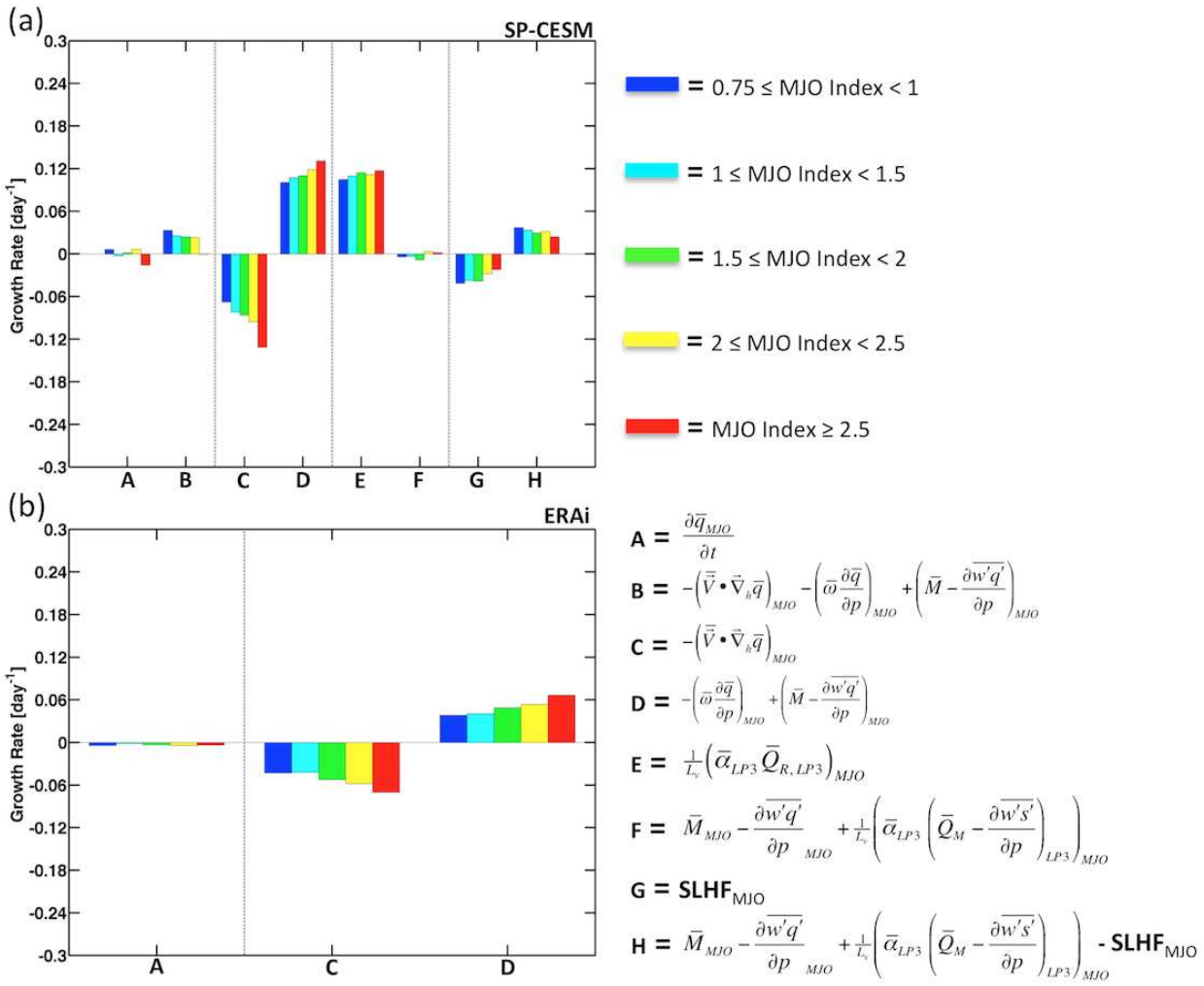

FIG. 3.19. As in Figure 3.10a, except composited over wintertime periods when the magnitude of the MJO index was between 0.75 and 1 (dark blue bars), 1 and 1.5 (light blue bars), 1.5 and 2 (green bars), 2 and 2.5 (yellow bars) and greater than 2.5 (red bars). Moisture variance budgets were calculated for both SP-CESM (a) and ERAi (b), where an FMO-like and FMO index was used respectively (see Section 2 for details of the indices). The corresponding sample sizes are (a) dark blue = 273, light blue = 489, green = 343, yellow = 159, red = 90 and (b) dark blue = 887, light blue = 1730, green = 1193, yellow = 593, red = 387. The subscripts LP3 and MJO indicate application of 3 day lowpass and 20-100 day bandpass filtering respectively. Please note that term D, the column process, was calculate as the residual of Eulerian moisture tendency and horizontal advection for ERAi (plot (b)).

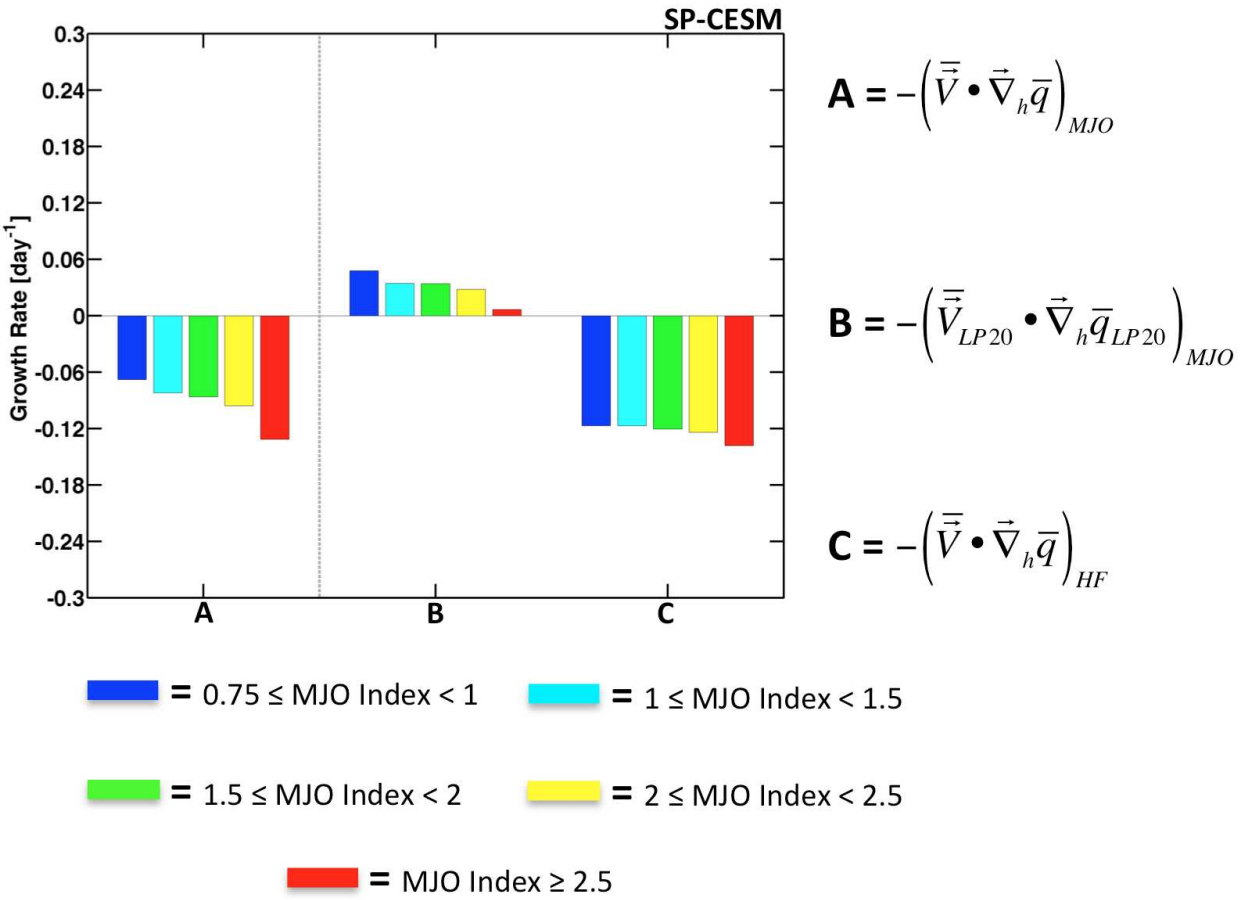

FIG. 3.20. As in Figure 3.19a, except for various horizontal advective terms. The subscripts LP20 and MJO indicate application of 20 day lowpass and 20-100 day bandpass filtering respectively. The subscript HF indicates terms related to higher frequency variability, calculated following equation 4.9.

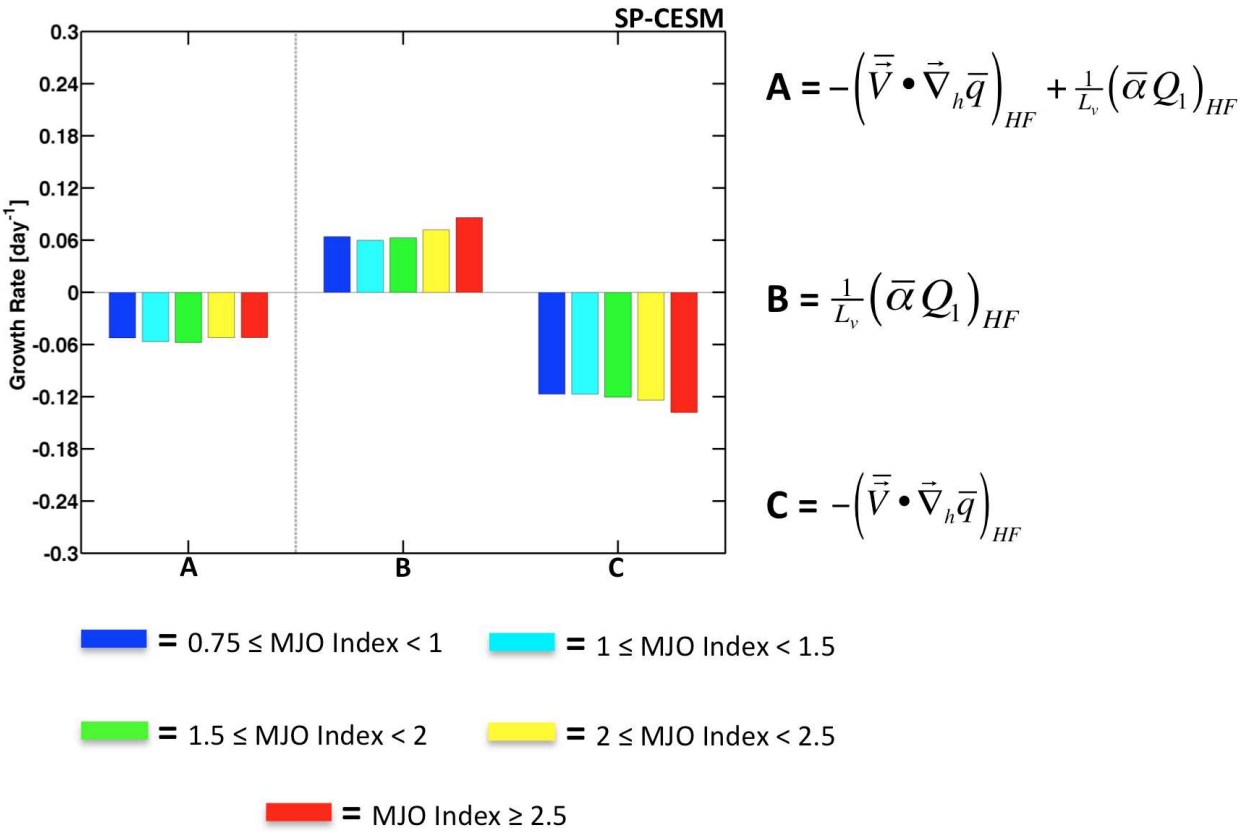

FIG. 3.21. As in Figure 3.19a, except for terms related to higher frequency convective variability. The subscript HF indicates terms related to higher frequency variability, calculated following equations 4.9 and 4.11.

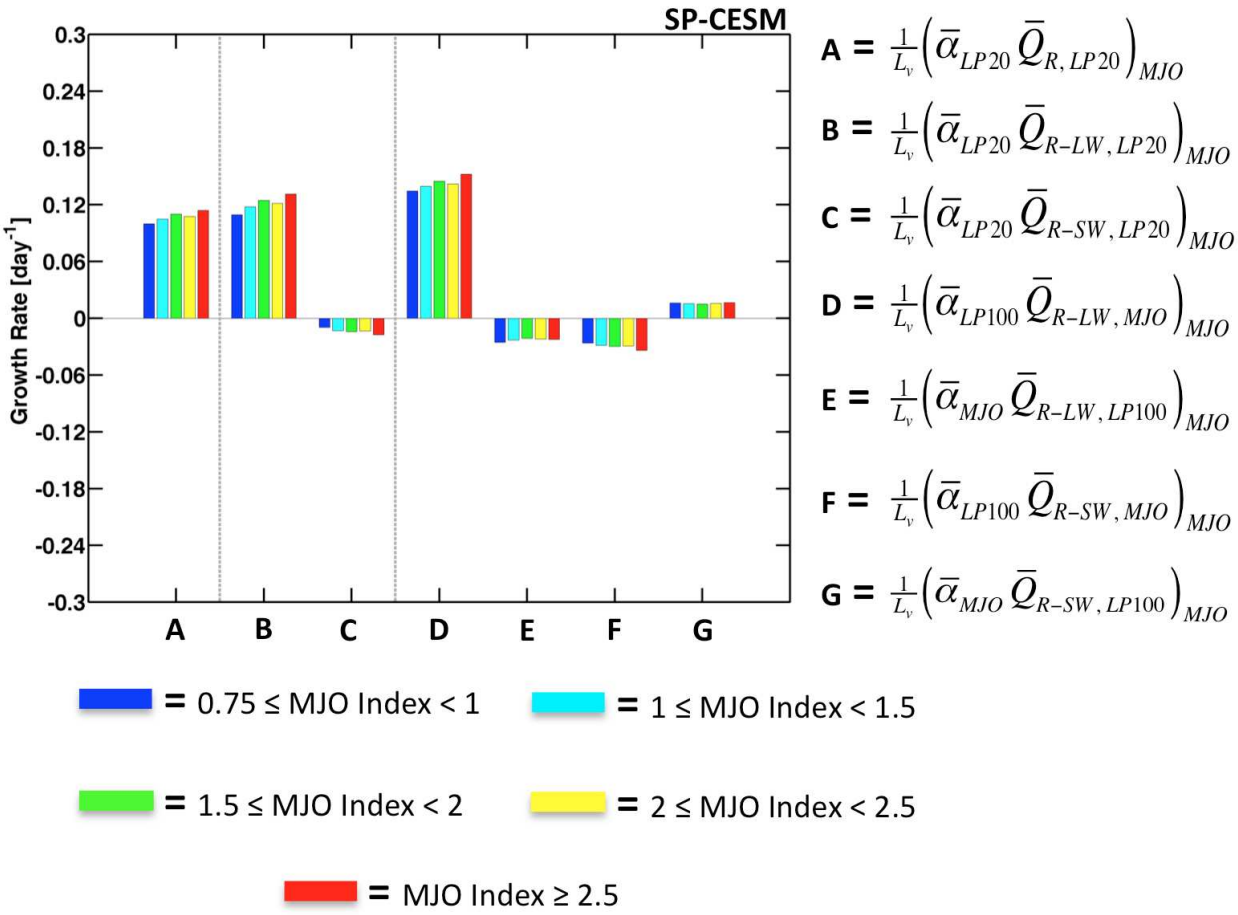

FIG. 3.22. As in Figure 3.19a, except for various radiative heating terms. Each term was vertically integrated from 850 to 100 hPa, as they depend on the weak temperature gradient approximation. The subscripts LP20, LP100, and MJO indicate application of 20 day lowpass, 100 day lowpass, and 20-100 day bandpass filtering respectively.

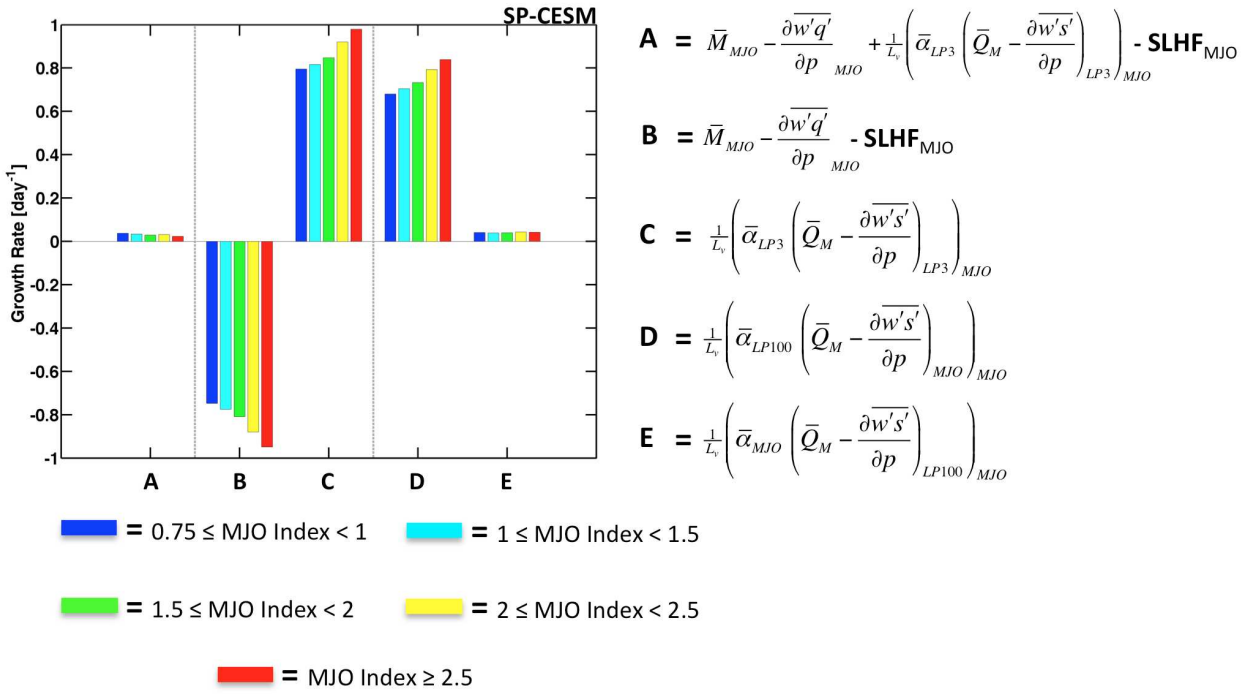

FIG. 3.23. As in Figure 3.19a, except for various terms relating to sub-grid scale convective processes. Each term was vertically integrated from 850 to 100 hPa. The subscripts LP3, LP100, and MJO indicate application of 3 day lowpass, 100 day lowpass, and 20-100 day bandpass filtering respectively.

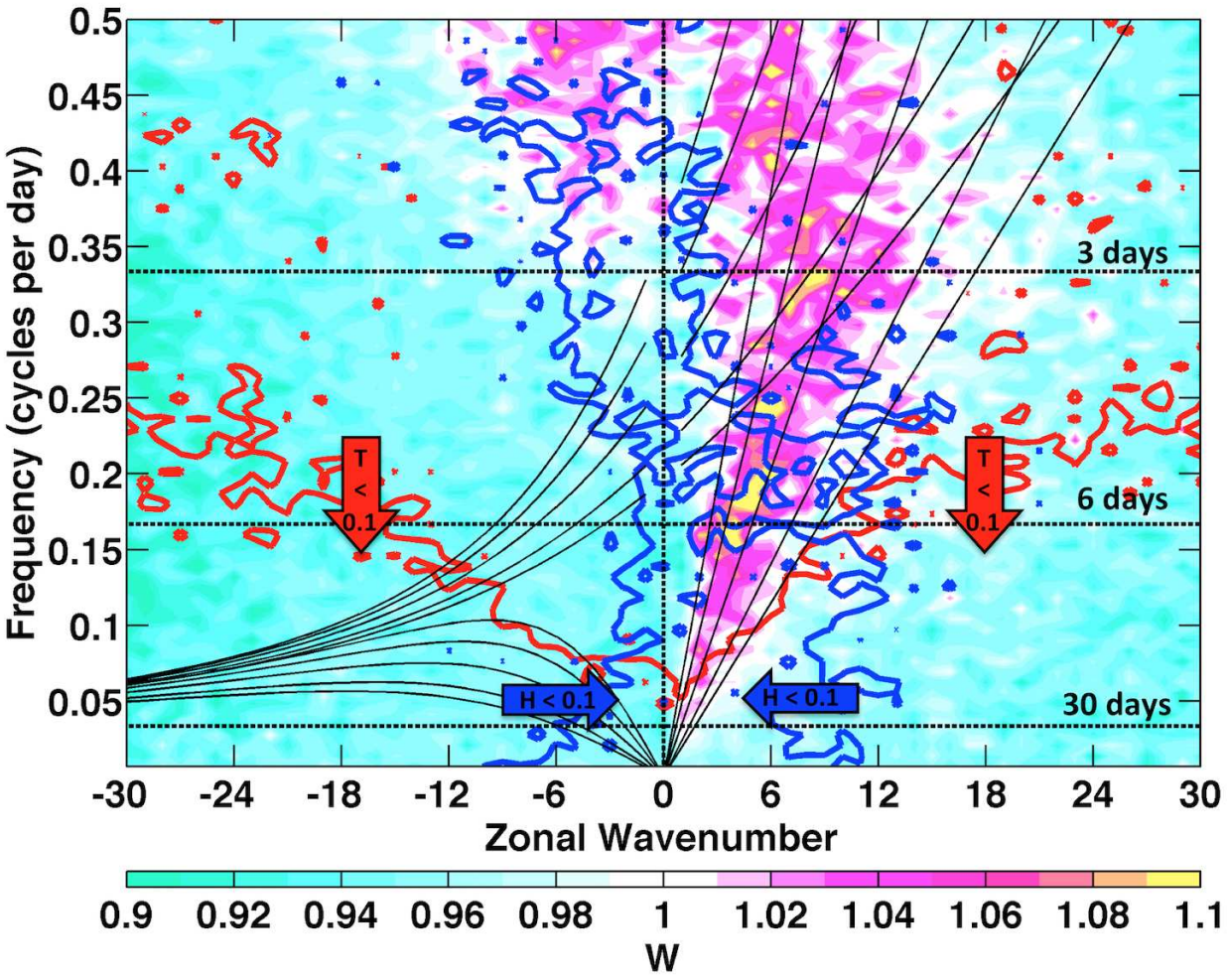

FIG. 3.24. Wavenumber-frequency space of W (shading), the ratio of the characteristic magnitude of large-scale adiabatic cooling to that of apparent heating. Red contours indicate a value of 0.1 for T, the ratio of the characteristic magnitude of the Eulerian dry static energy tendency to that of apparent heating, and red arrows indicate regions where T is less than 0.1. Blue contours indicate a value of 0.1 for H, the ratio of the characteristic magnitude of horizontal dry static energy advection to that of apparent heating, and blue arrows indicate regions where T is less than 0.1. Dispersion curves for equatorial waves of equivalent depths ranging from 8 to 90 meters are superimposed in thin black lines. For each term, the characteristic magnitude of the numerator and denominator were calculated separately by filtering each to a single wavenumber-frequency combination. Each term was calculated from fields at 525 hPa. More details of the methodology are provided in Section 2.

CHAPTER 4

Climate Change and the Madden-Julian Oscillation: A Vertically Resolved Weak Temperature Gradient Analysis

In this chapter, SP-CESM is used to examine how the MJO, and its global influence, may be impacted by the changing moist thermodynamic structure of the tropics as the climate system warms. This chapter is published in the Journal of Advances in Modeling Earth Systems as Wolding et al. (2017).

4.1. Introduction

Two fundamental features of the tropics, the large Rossby radius of deformation and the strong influence of free tropospheric humidity on convection (Bretherton et al. 2004; Peters and Neelin 2006; Neelin et al. 2009; Sahany et al. 2012), help promote interactions between convection and large-scale circulations. Moisture mode theory (Sobel et al. 2001; Raymond 2001; Fuchs and Raymond 2005; Raymond and Fuchs 2009; Sobel and Maloney 2012; Arnold and Randall 2015; Adames and Kim 2016) posits that such interactions play an important role in organizing the Madden-Julian Oscillation (MJO), an intraseasonal phenomena characterized by broad envelopes of enhanced and suppressed convection coupled to large-scale circulations that propagate slowly eastward from the Indian to west Pacific Oceans (Madden and Julian 1971, 1972; Zhang 2005). The MJO dominates tropical variability on weekly to monthly timescales, and has such a profound influence on tropical precipitation and wind that its signal can often be visually discerned in raw data (Zhang 2005). In addition to its direct impacts on tropical rainfall and winds, the MJO strongly modulates tropical cyclone

This chapter is published in the Journal of Advances in Modeling Earth Systems as Wolding et al. (2017).

activity in all basins (Maloney and Hartmann 2000a,b; Hall et al. 2001; Slade and Maloney 2013) and interacts with ENSO (McPhaden 1999; Takayabu et al. 1999).

The influence of the MJO extends well beyond the tropics. It has long been recognized that tropical convective variability has the ability to influence the extratropics (Bjerknes 1966) by exciting stationary Rossby wave trains (Hoskins and Karoly 1981; Sardeshmukh and Hoskins 1988; Hoskins and Ambrizzi 1993; Jin and Hoskins 1995; Trenberth et al. 1998), and the MJO is a well documented example of this (see review in Lau et al. (2012)). Briefly, the MJO has been shown to influence extratropical modes of variability including the North Atlantic Oscillation (NAO) (Cassou 2008; Lin et al. 2009), Northern Annular Mode (NAM) (Zhou and Miller 2005; L'Heureux and Higgins 2008), Southern Annular Mode (SAM) (Carvalho et al. 2005), and the Pacific-North-America Pattern (PNA) (Mori and Watanabe 2008; Johnson and Feldstein 2010), and significantly impact regional surface temperature in North America (Vecchi and Bond 2004; Zhou et al. 2012), violent tornado outbreaks in North America (Thompson and Roundy 2013), Northern Hemisphere winter blocking (Hamill and Kiladis 2014; Henderson et al. 2016), and atmospheric rivers impacting the west coast of North America (Mundhenk et al. 2016). While the MJO subjects the extratropics to variability they would not otherwise experience, it also helps "anchor" capricious extratropical weather, providing an important source of predictability on weekly to monthly timescales (Lau and Waliser 2012; Zhang 2013). Even though medium range forecasting still poses significant challenges to the development of seamless prediction suites aimed at bridging the gap between weather and climate, continual advancement in our understanding of the MJO and its teleconnections (Roundy et al. 2010) offers prospects of progress in the years to come (Zhang 2013).

The findings of a growing number of studies, both observational and numerical simulation based, indicate that MJO activity may increase as the climate system warms, suggesting a potential boon for medium range forecasting (Hand 2015). The findings of Slingo et al. (1999); Jones and Carvalho (2006); Oliver and Thompson (2012), who used reanalaysis products to examine historical changes in MJO activity, suggest that increases in MJO activity on decadal or longer timescales may be related to increases in tropical SST. Numerical simulations, ranging from idealized aquaplanet studies (Lee 1999; Caballero and Huber 2010; Maloney and Xie 2013; Arnold et al. 2013; Carlson and Caballero 2016) to more realistic simulations (Schubert et al. 2013; Arnold et al. 2015), have found robust increases in MJO convective activity with increasing SST, though Maloney and Xie (2013) highlight that any future changes in the MJO are likely to be sensitive to the spatial pattern of warming. The findings of Arnold et al. (2015) are particularly relevant to this study, as the same simulations analyzed in that study will be investigated here. Arnold et al. (2015) analyzed MJO activity in two 10-year simulations of the superparameterized NCAR Community Earth System Model (SP-CESM), one at pre-industrial levels of CO_2 (280 ppm, hereafter PI) and one where CO_2 levels have been quadrupled (1120 ppm, hereafter 4xCO2). MJO activity was found to increase considerably in both frequency and strength from the PI to 4xCO2 simulation. A column moist static energy (MSE) budget was used to identify the steepening of the mean MSE profile, a robust thermodynamic consequence of warming, as the most likely cause of enhancement in MJO activity. A steepened mean MSE profile makes the export of column MSE by the anomalous circulation less efficient, thereby reducing the stabilizing effect variations in convection have on column MSE. This mechanisms for MJO intensification with warming is supported by the findings of Carlson and Caballero (2016), as well as

more idealized studies of convective aggregation (Arnold and Randall 2015). Yet Pritchard and Yang (2016) found no significant changes in the effect of vertical MSE advection on the MJO across the temperature range of 25°C-35°C in their climate sensitivity study of the MJO, affirming the need for further work on this topic. It is also worth emphasizing that only one convection permitting GCM framework (various super-parameterized versions of the Community Atmosphere Model) has been used to demonstrate amplification of the MJO with warming to this point, again highlighting the need for further research on this topic.

An alternative framework for understanding the interactions between moisture, convection, and large-scale circulations in the tropics, which provides a more detailed perspective than that provided by the column MSE budget, has been implemented in recent studies of the MJO (Chikira 2014; Wolding and Maloney 2015a; Janiga and Zhang 2016; Wolding et al. 2016). Briefly, these studies use weak temperature gradient (WTG) balance to diagnose large-scale vertical motion from apparent heating (Sobel et al. 2001; Raymond 2001), allowing large-scale vertical moisture advection to be decomposed into contributions from various apparent heating processes (e.g. radiative heating, microphysical processes, etc.). This vertically resolved WTG framework is consistent with the column MSE budget framework, and is akin to quantitatively partitioning the vertical advection term of the column MSE budget into contributions from radiative heating, microphysical processes, and sub-grid scale (SGS) eddy transports. A detailed discussion of the physical underpinnings of this framework is provided in Wolding et al. (2016). In addition to providing a more detailed perspective on interactions between moisture, heating, and large-scale circulations, the vertically resolved WTG analysis provides a clear framework for assessing how these interactions are impacted

by changes in the mean state static stability and vertical moisture gradient of the tropics, making it an ideal framework for investigating the MJO in a warming climate.

Here we have chosen perform a vertically resolved WTG analysis of the PI and 4xCO2 simulations investigated by Arnold et al. (2015). As these simulations, and the associated changes in the MJO, are well documented in Arnold et al. (2015), this allows more focus to be placed on the analysis of unique findings in this study. In addition, this allows the findings of the vertically resolved WTG balance analysis to be directly compared to the findings of the column MSE analysis implemented by Arnold et al. (2015). This study will focus on the impacts of increased static stability and a steepened vertical moisture gradient, as these features are robust moist thermodynamic responses to warming. The impacts these changes have on the MJO itself, as well as how they impact the MJO's global influence, will be assessed using WTG theory.

This paper is organized as follows. A description of the model, experimental setup, and analysis techniques is provided in section 2. Basic features of both simulations, and changes in the moist thermodynamic structure of the tropics, are presented in section 3. Section 4 will focus on the impacts of changes in static stability. Moisture variance budgets of the PI and 4xCO2 simulations will be compared in section 5, with a focus on the impacts of changes in the moist thermodynamic structure of the tropics. Discussion and conclusions will be provided in section 6.

4.2. Model Description, Experimental Design, and Method of Analysis

Superparameterization (Grabowski 2001; Randall et al. 2003), whereby cloud system-resolving models (CSRMs) are embedded within each column of a general circulation model (GCM) and used to compute tendencies of moisture and temperature resulting from processes

occurring on the SGS of the GCM, has several advantages when compared to conventional parameterizations of convection. Deep convection, fractional cloudiness, and cloud overlap are explicitly simulated, allowing for more realistic interactions between radiation, clouds, and the large-scale environment. Additionally, processes occurring on the SGS are coupled to the large-scale in such a way that their individual contributions to large-scale tendencies of moisture and temperature are cleanly separable.

The 10 year PI and 4xCO2 simulations of SP-CESM used in this study are the same used by Arnold et al. (2015). Briefly, this version of SP-CESM implements a two-dimensional version of the System for Atmospheric Modeling (SAM) 6 (Khairoutdinov and Randall 2003), with a single moment bulk microphysics scheme, 32 columns of 4 km width, and 28 vertical levels as the CSRM embedded within each column of the CESM version 1.0.2 (Hurrell et al. 2013). The NCAR Community Atmosphere Model (CAM), run with $1.9^\circ \times 2.5^\circ$ horizontal resolution, with 30 vertical levels, CAM4 physics, and a 15 minute timestep, serves as the atmospheric component of the CESM, and is coupled to dynamic ocean (POP2) and sea ice (CICE) models with $1.125^\circ \times 0.63^\circ$ resolution. Section 2 of Arnold et al. (2015) provides details of model spin up, as well as several mean state biases present in the PI simulation.

All season OLR based EOF indices of the MJO, calculated for both the PI and 4xCO2 simulations, are used to produce composite life-cycles of the MJO. Leading EOFs of latitudinally averaged (15°N-15°S) 20-100 day bandpass filtered OLR were computed following the methodology that Kiladis et al. (2014) used to produce the FMO index. These "FMO-like" indices will hereafter be referred to as FMO indices. The first two EOFs explain 16.7% and 12.4% percent of the total variance respectively for the PI simulation, and 17.6% and 16.3% percent of the total variance respectively for the 4xCO2 simulation. The leading EOFs are

well separated based on the criteria of North et al. (1982) for both the PI and 4xCO2 simulations. The structures of these EOFs, shown in Figure 4.1, are consistent with the structures of the OLR components of the multivariate EOF derived by Wheeler and Hendon (2004) (See Figure 1 in Wheeler and Hendon (2004)).

Analysis techniques and plotting convections similar to those used by Wolding et al. (2016), who provide a detailed analysis of the MJO in the PI simulation, will be implemented when possible to facilitate direct comparison with the results of that study. Moisture budget composite "snapshots" of the 4xCO2 MJO are produced from 19 wintertime (October to April) MJO events, selected using an index of $20-100$ day bandpass filtered OLR, averaged over the area of $10°\text{N}-10°\text{S}, 110°\text{E}-130°\text{E}$. Following the methodology of Wolding et al. (2016), events were defined as index minima separated by at least 20 days, where anomalously low OLR (i.e. enhanced convection) caused the index to exceed a 1.5 standard deviation threshold.

As in Wolding et al. (2016), intraseasonal moisture variance budgets are used to compare the role that various moisture budget terms play in the destabilization of the MJO in the PI and 4xCO2 simulations. The fractional growth rate of intraseasonal column moisture variance contributed by moisture budget term P is given by

$$G_P(p,t) = \frac{\iint P(p)\,\langle q\rangle\,dx\,dy}{\iint \langle q\rangle^2\,dx\,dy} \tag{4.1}$$

where q is specific humidity that has been bandpass filtered to $20-100$ days, and the angled brackets represent vertical integrals from the surface to 100 hPa. This equation will be vertically integrated over different levels throughout this paper, and the levels of integration will be noted in respective figure captions. As in Wolding et al. (2016), the choice was made

to project moisture budget term $P(p)$ onto the column integrated specific humidity $\langle q \rangle$. An alternative approach could be to project moisture budget term $P(p)$ onto the anomalous moisture at each level, $q(p)$, and to subsequently consider the vertical integral of the product of those terms. Although both methods were investigated in this study, the former was chosen on the basis that the SGS effects of convection can vertically redistribute moisture provided by other processes (e.g. radiative heating), such that their influence is distributed throughout the column. Moisture variance budgets for both PI and 4xCO2 simulations are calculated over the domain of $15°\text{N} - 15°\text{S}, 60°\text{E} - 180°\text{E}$ for all days when their respective FMO indices exceed a magnitude of 1. Conclusions drawn from this analysis are not sensitive to reasonable changes in the domain or magnitude threshold considered.

MJO phase composites in section 4.4.1.1 were produced, and their statistical significance assessed, in the following manner. For each phase of the MJO, dates where the magnitude of the FMO index exceeded 1 were selected. These dates were then limited to the months of DJF, when the northern hemisphere extratropical response to MJO heating is particularly strong. Various anomalous fields were composited together for the selected dates for each respective phase, meant to represent anomalous conditions associated with the MJO. Moving-block bootstrap analysis (e.g. Henderson et al. (2016)) was used to assess the statistical significance of the composites for each MJO phase, as well as the significance of the average of all eight phase composites. Specifically, the goal was to assess if the root mean square (RMS) of an anomalous field (e.g. column averaged Q_1) over a given domain (e.g. $15°\text{N} - 15°\text{S}$) was significantly larger for a given composite than for randomly sampled days. In other words, the goal was to determine if there was a significant signal associated with the MJO being captured in the composite. A second goal was to test if there was a significant

difference between the RMS anomalies of the PI and 4xCO2 simulations. In other words, the goal was to determine if there are significant changes in the strength of some signal associated with the MJO from the PI to 4xCO2 simulation. As in traditional bootstrap analysis, samples were taken with replacement to approximate the distribution and characteristics of the data being used in the composites. As MJO events often spend several consecutive days in a single MJO phase, moving-block bootstrap imposes the additional requirement that samples be chosen in consecutive blocks of length l such that the effect of data autocorrelation is preserved. A bootstrap sample of size N was produced by joining N/l randomly sampled blocks, where N is the number of days used in the composite being assessed, and an l of 5 was used, corresponding to an average persistence of 5 days in each MJO phase, and an average period of 40 days for the entire eight phase MJO lifecycle. This process was repeated 2000 times to obtain bootstrap samples sufficient to represent the distribution and characteristics of the data being used. The size of N for the eight MJO phases composited in the both PI and 4xCO2 simulations is given in the captions of Figures 4.6 and 4.7.

4.3. Changes from PI to 4xCO2

This section will introduce differences between the PI and 4xCO2 simulations that are most relevant to the subsequent sections. As the basic state and intraseasonal variability of both simulations are well documented in section 3 and figures 1 through 5 of Arnold et al. (2015), a limited analysis is presented here. Figures 4.2a,c show mean SST and total precipitation variance in the PI simulation. As discussed in Arnold et al. (2015), the PI simulation has a $\sim$ 1K SST cold bias relative to observations (not shown), a pronounced double ITCZ over the Pacific Ocean, and precipitation variance that is too large over the western Indian Ocean relative to observations (not shown). SST cold biases are a common

symptom of models that produce vigorous intraseasonal variability (Kim et al. 2011). The enhanced precipitation variance in the western Indian Ocean contributes to unrealistic mean state low level easterlies in the Indian Ocean, which affects surface latent heat flux (SLHF) feedbacks to the MJO (Arnold et al. 2015; Wolding et al. 2016). Figures 4.2b,d show changes in SST and total precipitation variance from the PI to 4xCO2 simulations. SST increases everywhere, but exhibits an El-Nino like pattern of warming. Total precipitation variance increases most dramatically over the Pacific Ocean, and has a pattern indicative of an equatorward shift of the northern ITCZ. Figures 4.2e,f show that PI MJO precipitation variance is largest over the Indian and west Pacific Oceans, and that MJO precipitation variance more than doubles in most regions in the 4xCO2 simulation. MJO precipitation variance increases most dramatically over the Pacific Ocean, consistent with the increase in total precipitation variance. Figure 4.2g shows PI intraseasonal zonal wind variance at 850 hPa, which has a longitudinal distribution similar to that of MJO precipitation variance. Interestingly, despite the considerable increase in MJO precipitation variance in the 4xCO2 simulation (Fig 4.2f), zonal wind variance actually decreases in most areas (Fig 4.2h). This remarkable change was noted by Arnold et al. (2015), and Maloney and Xie (2013) used WTG balance to show that similar changes in their aquaplanet simulations were the result of increased tropical static stability with warming. Consequences of this change, and of increasing static stability with warming, will be a primary focus of the next section.

Figure 4.3a shows vertical profiles of static stability (dashed lines) and the vertical moisture gradient (solid lines) for the PI (blue lines) and 4xCO2 (blue lines) simulations, averaged from $10°\mathrm{N}-10°\mathrm{S}, 60°\mathrm{E}-180°\mathrm{E}$. Both static stability and the vertical moisture gradient have increased throughout the depth of the troposphere in the 4xCO2 simulation. Figure 4.3b

shows that static stability (dashed line) increases by around 10% in the lower troposphere, and by as much as 50% in the upper troposphere. Similarly, the vertical moisture gradient (solid line) shows the largest percentage increase in the upper troposphere. Subsequent sections will use WTG to investigate how these changes in static stability and the vertical moisture gradient will impact the MJO and its global influence.

4.4. Implications of Increased Static Stability

The tropics are characterized by weak horizontal gradients of temperature and pressure, a result of effective gravity wave adjustment given the large Rossby radius of deformation. On intraseasonal timescales, the leading order balance in the dry static energy (DSE, s) budget is between apparent heating and adiabatic cooling. This balance is widely referred to as WTG balance, and is given by

$$\overline{\omega}\frac{\partial \overline{s}}{\partial p} = Q_1 \tag{4.2}$$

which can be re-arranged to give

$$\overline{\omega} = \frac{Q_1}{\frac{\partial \overline{s}}{\partial p}} \tag{4.3}$$

where the overbar indicates the large-scale average of a quantity and Q_1 is the apparent heat source (Yanai et al. 1973). In the context of the MJO, this paper takes the perspective that intraseasonal variations in large-scale vertical motion are the result of effective gravity wave adjustment occurring on temporal scales much shorter than, and spatial scales much larger than, intraseasonal variations in apparent heating. Inspection of equation 4.3 indicates that static stability serves as a measure of dynamic sensitivity to apparent heating, determining the large-scale vertical velocity required for adiabatic cooling to balance apparent heating.

This relationship holds to a high degree of accuracy in both the PI (see Figure 6 of Wolding et al. (2016)) and 4xCO2 (see Appendix Figure 4.16) simulations. As static stability increases, the large-scale velocity required to balance a given amount of apparent heating decreases (Knutson and Manabe 1995; Held and Soden 2006). Given that large-scale vertical velocity results from horizontal convergence and divergence acting throughout the column, it follows that the horizontal wind response to apparent heating may also decrease as static stability increases (Maloney and Xie 2013).

Figure 4.4a shows a box and whisker plot of the RMS of 850 hPa zonal wind anomalies for the domain $10°\text{N} - 10°\text{S}, 60°\text{E} - 180°\text{E}$, binned by the RMS of column averaged Q_1 anomalies for the same domain. The central mark of each box indicates the median, the bottom and top edges of each box indicate the 25th and 75th percentiles respectively, the whiskers extend to the most extreme data points not considered outliers, and red markers indicate outliers that are more than 1.5 times beyond the interquartile range of the lower and upper quartiles. Medians differ with 95% statistical significance if their notched intervals do not overlap. Figure 4.4a indicates that the same amount of heating consistently produces a weaker zonal wind response in the 4xCO2 simulation (red boxes) than the PI simulation (blue boxes), with the median values of the former being less than the latter with 95% statistical significance for each bin considered. Figure 4.4b, which shows a vertical profile of the domain RMS zonal wind anomalies for the 1.75 to 2.00 $\text{K}\,\text{day}^{-1}$ bin, indicates that the zonal wind response to a given amount of heating is weaker at all levels in the 4xCO2 simulation (red line) than in the PI simulation (blue line). This suggests that changes in zonal wind variance at 850 hPa (Fig 4.2h) are not simply a result of changes in the vertical structure of Q_1, and that the dynamical response to intraseasonal variations in heating

is consistently weaker throughout the column in the 4xCO2 simulation. This is consistent with the findings of Pritchard and Bretherton (2014), who noted a weakening of the dynamic anomalies associated with the MJO despite the amplification of its convective signature in a simulation where static stability had been inadvertently increased. It is worth noting that the increased MJO activity in the 4xCO2 simulation is accompanied by an increase in column averaged Q_1 anomalies, partially counteracting the weakened dynamical response to variations in heating. As will be shown in subsequent sections, a reduced dynamical response to variations in apparent heating has implications for the MJO itself, as well as implication for how the MJO forces the extratropics.

4.4.1. Communication breakdown: implications for MJO forcing of the extratropics

The ability of variations in tropical heating to force the extratropics through the excitation of stationary Rossby wave trains (Hoskins and Karoly 1981; Sardeshmukh and Hoskins 1988; Hoskins and Ambrizzi 1993; Jin and Hoskins 1995; Trenberth et al. 1998) is closely related to anomalous divergence occurring in the presence of mean state absolute vorticity, as well as the advection of mean state absolute vorticity by the divergent part of the anomalous wind (Sardeshmukh and Hoskins 1988). As increased tropical static stability results in a decreased horizontal wind response to intraseasonal variations of apparent heating, it follows that the MJO's ability to excite an extratropical response may also decrease in a warming climate. Investigating this issue posses significant challenges, as mean state changes (e.g. changes in jet strength and location) and changes in the structure of anomalous heating will influence the ability of variations in tropical heating to force the extratropics. Two different approaches are employed in this section in an attempt to address this issue.

4.4.1.1. Composite analysis of SP-CESM simulations

To aid understanding of subsequent analysis, begin by considering Figure 4.5, which shows DJF phase 4 MJO composites of column averaged Q_1 anomalies (contours) for the tropics and 525 hPa geopotential height (Z525) anomalies (shading) for the extratropics in the PI (top) and 4xCO2 simulations (bottom). The red lines located at 15°N and 15°S are used to indicate regions used for averaging in the subsequent analysis, where tropical averaging occurs equatorward of the lines and extratropical averaging occurs poleward of the lines. The months of DJF were chosen because of the strong northern hemisphere (NH) extratropical response to MJO heating at this time, and the 525 hPa level was chosen to facilitate comparison with previous studies of the MJO teleconnection patterns (Lin et al. 2009; Henderson et al. 2016), which is commonly defined at this level. First note that anomalous heating near the maritime continent is much greater in the 4xCO2 simulation than the PI simulation. This is consistent with the increased strength of the MJO in the 4xCO2 simulation which Arnold et al. (2015) documented. The RMS of phase 4 column averaged Q_1 anomalies in the tropics has increased by 0.18 K day^{-1}, a 50% increase from the PI simulation. Now consider the NH extratropical response to the anomalous tropical heating, which appears to have both shifted and weakened in the 4xCO2 simulation, despite the aforementioned increase in anomalous heating. The RMS of phase 4 NH extratropical Z525 anomalies has decreased by 3.8 m, a 23% decrease from the PI simulation.

Similar calculations were done for each of the eight phase composites of the MJO, as well as the average across the eight phase composites. Figure 4.6 shows the RMS of column averaged Q_1 anomalies for the tropics (top) and the RMS of NH extratropical Z525 anomalies (bottom) for the PI (blue) and 4xCO2 (red) simulations. Dark brackets indicate the 95%

confidence bounds, calculated using the bootstrapping methodology detailed in section 2. Composite values that exceed the upper bracket are significantly larger than values obtained by compositing together randomly sampled days, indicating that there is a significant signal associated with the MJO being captured in the composite. First note that, for all eight phases of both simulations, tropical Q_1 anomalies exceed the upper bracket of the 95% bounds. This provides confidence that we are sampling heating associated with the MJO, and not simply background intraseasonal Q_1 anomalies. For seven of the eight phases, tropical Q_1 anomalies are greater in the 4xCO2 simulation than in the PI simulation, consistent with the strengthening of the MJO in the 4xCO2 simulation. The RMS of NH extratropical Z525 anomalies (bottom) exceeds the 95% bounds for each of the eight phases for the PI simulation (blue bars), but does so only in phases 2 and 3 of the 4xCO2 simulation. This indicates the extratropical response to MJO heating anomalies is only strong enough to exceed background Z525 anomalies in phases 2 and 3 in the 4xCO2 simulation. In other words, MJO forcing of the extratropics is clearly discernible in the PI simulation, but is much less discernible in the 4xCO2 simulation. This comes as a result of the reduction in extratropical Z525 anomalies from the PI to the 4xCO2 simulation, which occurs in each of the eight phases. Considering the average across all eight phases, extratropical Z525 anomalies are significant in both the PI and 4xCO2 simulation.

To test the significance of the changes in tropical Q_1 and extratropical Z525 anomalies, a bootstrap analysis was performed on both the absolute changes and fractional changes, shown in Figure 4.7. Composite values exceeding the upper or lower brackets indicate that changes between the PI and 4xCO2 simulation are significantly larger than changes obtained by compositing randomly sampled days for each simulation. In other words, absolute and/or

fractional changes associated with the MJO are greater than those occurring in background intraseasonal anomalies. Of the individual phases, only phases 2 and 4 show statistically significant absolute increases in tropical Q_1 anomalies (Fig. 4.7a), but the average absolute increase across all eight phases is statistically significant, consistent with the documented increases in the MJO strength (Arnold et al. 2015). The tendency for the brackets to be centered above the zero value indicates that background intraseasonal Q_1 anomalies increase from the PI to 4xCO2 simulation. As a percentage increase (Fig. 4.7b), composite changes are not significant for any individual phase, nor are they significant for the average across all eight phases. In other words, while a statistically significant increase in MJO Q_1 anomalies occurs, the fractional increase (i.e. rate of increase) in MJO Q_1 anomalies is not significantly greater than that of background intraseasonal Q_1 anomalies. Pritchard and Yang (2016) similarly found that MJO precipitation variability remained an approximately invariant fraction of tropical mean precipitation variability across a wide range of climates. Of the individual phases, phases 1, 5, and 7 show statistically significant absolute decreases in extratropical Z525 anomalies (Fig. 4.7c). Considering the average change across all eight phases, both the absolute decrease (Fig. 4.7c) and fractional decrease (Fig. 4.7d) in extratropical Z525 anomalies are significant. Similar decreases in extratropical geopotential height anomalies occur at all levels throughout the column (not shown), though it is worth noting that the level of maximum geopotential height anomalies shifts slightly upwards by around 50 hPa in the 4xCO2 simulation. When considering changes in anomalous extratropical Z525 per tropical Q_1 anomaly (Fig. 4.7e,f) (i.e. extratropical response per unit MJO heating), significant absolute and fractional decreases occur in the average across all eight phases, with the latter showing a 40% decrease. In other words, over a complete MJO lifecycle, the ability

for anomalous MJO heating to force an extratropical response decreases by 40% from the PI to 4xCO2 simulation.

4.4.1.2. Mechanism denial with a linear baroclinic model

As an alternative approach to the composite analysis above, the dry linear baroclinic model (LBM) of Watanabe and Kimoto (2000) was used to help isolate the effects of changes in static stability on MJO forcing of the extratropics. This model linearizes the hydrostatic primitive equations on a sphere around a user provided basic state that includes profiles of DSE and horizontal winds, and calculates a steady linear response to a user prescribed steady heating. Four initial simulations were performed, all using the PI phase 3 DJF composite anomalous apparent heating, limited to $15°\mathrm{N} - 15°\mathrm{S}$, as the prescribed heating. The control simulation uses the full PI DJF basic state. The second simulation, which seeks to isolate the effect of changes in horizontal winds, uses the PI DJF basic state with the exception of horizontal winds, which were from the 4xCO2 simulation. The third simulation, which seeks to isolate the effect of changes in DSE (i.e. changes in static stability), uses the PI DJF basic state with the exception of DSE, which is from the 4xCO2 simulation. The fourth simulation uses the full 4xCO2 DJF basic state. Each simulation was run for 34 days, and the 500 hPa geopotential height anomaly response was calculated as the average from days 20 to 34. Each simulation was performed at T42 horizontal resolution, with 20 vertical sigma levels. An e-folding timescale of 2 hours was used for horizontal diffusion at the largest wavenumbers, and a Newtonian damping timescale of $(20\,\mathrm{days})^{-1}$ was used for all levels except the lowest and highest, which used a $(0.5\,\mathrm{day})^{-1}$ damping timescale.

The control simulation (Fig 4.8a), which uses the PI basic state, produces NH extratropical Z525 anomalies that have pattern similar to the phase 4 composites of the PI simulation

(Fig 4.5a), though of lesser magnitude. The LBM response to phase 3 heating most closely matches PI phase 4 composites because the former is an approximate steady-state response to stationary heating anomalies, while the latter reflects an evolving response to an eastward moving anomalous heat source (i.e. the eastward propagating MJO). In the second simulation, which seeks to isolate the effects of changes in basic state winds (Fig 4.8b), the resulting pattern of NH extratropical Z525 anomalies shifts, but the Z525 anomalies show relatively little change in strength. In the third simulation, which seeks to isolate the effects of changes in basic state DSE (i.e. changes in static stability) (Fig 4.8c), the resulting pattern of NH extratropical Z525 anomalies matches that of the control run, but the Z525 anomalies are considerably weakened. In other words, only the strength of the extratropical response changes. In the fourth simulation, which uses the 4xCO2 basic state are used (i.e. winds and static stability change) (Fig 4.8d), the pattern of NH extratropical Z525 anomalies both shifts and weakens.

Comparing the two simulations that used the PI basic state winds (i.e. left set of panels, Fig 4.8a,c), the RMS of NH extratropical Z525 anomalies decreased by 35% from the PI to 4xCO2 basic state DSE (i.e. from top left to bottom left, Fig 4.8a to c). In other words, the strength of the extratropical response decreased by 35% when the static stability increased. Comparing the two simulations that used the 4xCO2 basic state winds (i.e. right set of panels, Fig 4.8b,d), the RMS of NH extratropical Z525 anomalies decreased by 36% from the PI to 4xCO2 basic state DSE (i.e. from top right to bottom right, Fig 4.8b to d). In other words, the strength of the extratropical response decreased by 36% when the static stability increased. These reductions are very close to the 40% reduction in the DJF extratropical response per unit MJO heating observed in SP-CESM.

The same analysis was performed on a second set of four simulations, where each used JJA phase 3 composite Q_1 anomalies and JJA basic state fields (not shown). Comparing the two JJA simulations that used the PI basic state winds, the RMS of SH extratropical Z525 anomalies decreased by 27% from the PI to 4xCO2 basic state DSE. Comparing the two JJA simulations that used the 4xCO2 basic state winds, the RMS of SH extratropical Z525 anomalies decreased by 32% from the PI to 4xCO2 basic state DSE. Equation 4.3 suggests that a 40% increase in static stability, roughly that which occurs near the levels of peak anomalous heating in SP-CESM (Fig 4.3b), would reduce the anomalous large-scale vertical velocity produced by a given amount of heating by roughly 30%. The pattern of static stability increase (Fig 4.3b), which is largest near levels of peak anomalous heating and anomalous vertical velocity, would also contribute to weakening anomalous divergence associated with MJO convective heating. While not conclusive, the results of this section support the idea that increasing static stability reduces the ability of anomalous tropical heating to induce an extratropical Rossby wave response.

4.5. Implications of Increased Sensitivity of Large-Scale Vertical Moisture Advection to Apparent Heating

Detailed moisture and moisture variance budget analyses were performed as part of this study, and the moisture variance budget has been included in the Appendix for the interested reader. Results of these analyses indicate that the balance of processes acting to destabilize the MJO undergoes relatively small changes from the PI to 4xCO2 simulation, consistent with the findings of Arnold et al. (2015). This section will not address these changes, but will instead focus on how changes in the mean state moist thermodynamic structure of the tropics help support enhanced MJO activity in the 4xCO2 simulation.

Consider the moisture budget, given by

$$\frac{\partial \overline{q}}{\partial t} = -\overline{\boldsymbol{V}}_{\boldsymbol{h}} \cdot \boldsymbol{\nabla} \overline{q} - \overline{\omega} \frac{\partial \overline{q}}{\partial p} + \overline{M} - \frac{\partial \overline{\omega' q'}}{\partial p} \tag{4.4}$$

where the overbar and prime indicate the large-scale average of a quantity and deviations from the area average respectively, $\boldsymbol{V}_h$ and ω are the horizontal and vertical winds respectively, q is specific humidity, and M is the moisture tendency due to microphysical processes. Following the vertically resolved WTG framework developed in recent studies (Chikira 2014; Wolding and Maloney 2015a; Janiga and Zhang 2016; Wolding et al. 2016), equation 4.3 can be used to relate large-scale vertical moisture advection to apparent heating, such that

$$-\overline{\omega} \frac{\partial \overline{q}}{\partial p} = \overline{\alpha} Q_1 \tag{4.5}$$

where

$$\overline{\alpha} = -\mathrm{L_v} \left(\frac{\frac{\partial \overline{q}}{\partial p}}{\frac{\partial \overline{s}}{\partial p}} \right) \tag{4.6}$$

and

$$Q_1 = \overline{Q}_M + \overline{Q}_R - \frac{\partial \overline{\omega' s'}}{\partial p} \tag{4.7}$$

Q_M and Q_R are the DSE tendency due to microphysics and radiation respectively. Inspection of equation 4.5 indicates that apparent heating will drive more large-scale vertical moisture advection in a moist thermodynamic environment with a larger $\overline{\alpha}$ (Chikira 2014). In that sense, $\overline{\alpha}$ serves as a measure of the sensitivity of large-scale vertical moisture advection to apparent heating (see Wolding et al. (2016) for more discussion of $\overline{\alpha}$). Given that variations in large-scale vertical moisture advection plays a crucial role in destabilizing the MJO, changes in $\overline{\alpha}$ caused by a warming climate are of considerable interest.

Increases in static stability and the vertical moisture gradient in the 4xCO2 simulation (Fig. 4.3) have opposing effects on $\overline{\alpha}$ (equation 4.6). Increased static stability reduces the large-scale vertical velocity produced per unit apparent heating (equation 4.3), but the steepened vertical moisture gradient increases the moisture advected by that vertical velocity. The effect of the increased vertical moisture gradient wins out in the 4xCO2 simulation, resulting in an increase in $\overline{\alpha}$ throughout the troposphere (Fig. 4.9). In other words, at a given level, variations in apparent heating will drive stronger variations in large-scale vertical moisture advection in the 4xCO2 simulation. Absolute changes in $\overline{\alpha}$ are largest in the middle troposphere (Fig. 4.9a), while fractional changes in $\overline{\alpha}$ are smallest in the lower troposphere and increase with height (Fig. 4.9b). Column averaged $\overline{\alpha}$ increases across most of the tropics in the 4xCO2 simulation (Fig. 4.10), with the largest increases occurring in regions where precipitation variance has increased the most (Fig. 4.2d).

To illustrate why this increase in $\overline{\alpha}$ may play a crucial role in supporting the increased strength of the MJO, consider the composite moisture budget of the MJO in the 4xCO2 simulation, shown in figure 4.11. To facilitate comparison of PI and 4xCO2 moisture budgets, figure 4.11 was produced following the same methodology and plotting conventions that Wolding et al. (2016) used to analyze the PI moisture budget (their Figure 3). Specific humidity anomalies (contours) indicate that much of the free troposphere is anomalously moist from $\sim 110°\text{E} - 160°\text{E}$, consistent with the enhanced phase of the MJO. As in the PI simulation (Wolding et al. 2016), anomalous moistening (color shading) by large-scale vertical moisture advection (Fig. 4.11c) opposes anomalous drying by microphysical processes and SGS eddy fluxes (Fig. 4.11d). The net effect of these large and opposing processes (Fig. 4.11e), hereafter referred to as the column process (Chikira 2014), results in further

moistening of regions that are already moist. This moistening by the column process is crucial to the destabilization of the MJO, and is opposed by horizontal advective drying during the enhanced phase (Fig. 4.11b). Comparing moisture budgets of the PI (figure 3 of Wolding et al. (2016)) and 4xCO2 simulations shows that moistening by the column process has increased considerably in the latter (Fig. 4.11e), helping support larger specific humidity anomalies in that simulation. Equation 4.5 indicates that the increased mean state $\overline{\alpha}$ in the 4xCO2 simulation allows MJO convective heating to drive more large-scale vertical moisture advection, helping support this increased moistening by the column process.

Figure 4.12a shows the contribution that the increase in mean state $\overline{\alpha}$ makes to the amount of large-scale vertical moisture advection MJO convective heating is able to drive in the 4xCO2 simulation. As a result of the increased mean state $\overline{\alpha}$, MJO convective heating in the 4xCO2 simulation produces considerable additional moistening via large-scale vertical moisture advection, particularly from 700 to 300 hPa. The importance of this additional moistening is evident when it is removed from the column process, as shown in Figure 4.12b. Figure 4.12b is equivalent to subtracting Figure 4.12a from Figure 4.11e. Without the increased mean state $\overline{\alpha}$, moistening by the column process would become anemic, and would be unable to maintain specific humidity against the increased horizontal advective drying (Fig. 4.11b) in the 4xCO2 simulation.

In order to assess if this result can be generalized over the entire MJO lifecycle for a much broader geographic area, moisture variance budgets were calculated for the PI and 4xCO2 simulations. Figure 4.13 shows the column process (term D) is acting to increase moisture variance in both the PI and 4xCO2 simulations, and that horizontal advection (term C) is acting to damp moisture variance. Remember that each term in the moisture

variance budget is normalized by domain averaged moisture variance (see equation 4.1), which increases considerably in the 4xCO2 simulation (not shown). Therefore, even though individual moisture budgets terms are much larger in the 4xCO2 simulation (Fig. 4.11), they result in moisture variance growth rates similar to those of the PI simulation. Interestingly, despite the increased mean state $\overline{\alpha}$ in the 4xCO2 simulation, destabilization by the column process is weaker in the 4xCO2 simulation than in the PI simulation (Fig. 4.13, term D). This will be examined further below. For now, consider figure 4.14, which shows how MJO moisture variance is affected by the contribution that increased mean state $\overline{\alpha}$ makes to the large-scale vertical moisture advection resulting from total apparent heating (term A), radiative heating (term B), and heating by microphysical processes and SGS eddy fluxes (term C) in the 4xCO2 simulation. Without the additional large-scale vertical moisture advection resulting from the increased $\overline{\alpha}$ (Fig. 4.14, term A), the column process in the 4xCO2 simulation (Fig. 4.13, term D) would only be weakly destabilizing, and would not be able to maintain the elevated levels of moisture variance (not shown) against horizontal advective damping (Fig. 4.13, term C). In other words, without the increased mean state $\overline{\alpha}$, MJO convective heating in the 4xCO2 simulation would not drive sufficient large-scale vertical moisture advection to maintain itself at such elevated levels.

Enhanced MJO convective heating in the 4xCO2 simulation is accompanied by an increasingly top-heavy heating profile. Figure 4.15a shows profiles of the RMS of apparent heating anomalies over the entire PI and 4xCO2 simulations, for the domain $15°\text{N} - 15°\text{S}, 60°\text{E} - 180°\text{E}$. Almost all of the additional heating variability in the 4xCO2 simulation occurs above 500 hPa, and the level of peak heating shifts notably upwards. This upward shift may result from a strengthening of the convective anomalies, as well as from more basic energetic

and thermodynamic properties of the warmer climate (Bony et al. 2016). Profiles of RMS radiative heating anomalies (Fig. 4.15b) become more top heavy, yet the upward shift in total apparent heating (Fig. 4.15a) results from change in convective heating to first order. Remember that $\overline{\alpha}$ decreases with height (Fig. 4.9), so this upward shift in peak heating counteracts some of the effect of increased $\overline{\alpha}$. This may help explain why the column process drives slightly weaker moisture variance growth in the 4xCO2 simulation. In short, MJO convective heating occurring in a moist thermodynamic environment with increased $\overline{\alpha}$ is able to more efficiently re-supply itself with moisture, supporting enhanced levels of convection. The enhancement of convection is accompanied by a transition to a more top-heavy heating profile, driving down the efficiency with which MJO convection re-supplies itself with moisture until its growth is once again limited by horizontal advective damping.

4.5.1. Comparison with previous studies

As previously stated, the vertically resolved WTG framework is consistent with the column integrated MSE framework used by previous studies of the MJO and climate change (Arnold et al. 2013, 2015; Carlson and Caballero 2016; Pritchard and Yang 2016). The results of this section support one of the primary conclusions reached by several of these studies, namely that the increase in the mean state vertical MSE gradient in the lower troposphere, and the elevation of the mid-tropospheric minimum in MSE, help support MJO activity by increasing up-gradient MSE transport via vertical MSE advection (Arnold et al. 2013, 2015; Carlson and Caballero 2016). The consistency of these results can be highlighted by using the vertically resolved WTG balance framework (see equation 4.3) to express large-scale vertical advection of MSE in terms of $\overline{\alpha}$ and Q_1, giving $-\left\langle \overline{\omega}\frac{\partial \overline{h}}{\partial p} \right\rangle = \langle Q_1 \left(\overline{\alpha} - 1\right) \rangle$. This study has provided some additional insight to this mechanism, highlighting that increasing

$\overline{\alpha}$ in the middle and upper troposphere (Fig. 4.9), where heating variations are large, plays an important role in driving additional large-scale vertical moisture advection in a warming climate. Yet the results of Pritchard and Yang (2016), who assessed the climate sensitivity of the MJO across temperatures spanning 1°C-35°C and found MJO-like variability in even the coldest climates, challenges the notion of a critical temperature threshold for destabilization of the MJO.

Carlson and Caballero (2016) proposed a second mechanisms for MJO intensification, whereby a transition to super-rotation in a warming climate allows extratropical eddies to more easily penetrate the tropics, weakening the mean state meridional moisture gradient and reducing the impact of horizontal advective damping of MJO moisture variance by higher frequency convective variability. This mechanism does not appear to play a role in the 4xCO2 simulation, as no transition towards super-rotation is evident in the near equatorial profile of zonal wind (not shown). Additionally, moisture and moisture variance budgets, provided in the appendix, show no indication of changes in horizontal advective damping by higher frequency convective variability in the 4xCO2 simulation.

It is also worth highlighting that destabilization by radiative feedbacks, presented in more detail in the Appendix and in Figure 4.18, weaken slightly in the 4xCO2 simulation. This is consistent with the findings of Pritchard and Yang (2016), who found the strength of the radiative feedback decreased considerably with warming in their simulations spanning 1°C-35°C. While the more top-heavy profile of radiative heating anomalies (Fig. 4.15b) in the 4xCO2 simulation suggests the weakening radiative feedback may be related to changes in the vertical structure of the radiative heating anomalies, the results of Adames and Kim (2016) and Bony et al. (2016) may provide some additional insight. Bony et al. (2016) showed that

increased static stability results in the decreased spreading of convective anvils at upper levels in a warming climate, and Adames and Kim (2016) demonstrated a scale dependence of the radiative feedback. Further work should be done to identify the mechanism(s) responsible for weakening radiative feedbacks with warming.

4.6. Discussion

Interactions between convection, large-scale circulations, and moisture are strongly influenced by the moist thermodynamic structure of the environment in which they occur, and such interactions are thought to play an important role in destabilizing the MJO. In this study, the vertically resolved WTG framework has been used to examine how the MJO may be affected by the changing moist thermodynamic structure of the tropics as the climate system warms. Analysis of two SP-CESM simulations, one at pre-industrial levels of CO_2 (280 ppm, hereafter PI) and one where CO_2 levels have been quadrupled (1120 ppm, hereafter 4xCO2), support the following main conclusions:

(1) intraseasonal variations in tropical convective heating will become more efficient at driving variations in large-scale vertical moisture advection as the climate system warms, aiding destabilization of the MJO

(2) increasing static stability will reduce the dynamical response to intraseasonal variations in tropical convective heating as the climate system warms

(3) the weakening dynamical response to intraseasonal variations in tropical convective heating will reduce the MJO's ability to influence the extratropics as the climate system warms

Each of these conclusions will now be discussed in turn.

WTG balance provides a useful framework for understanding how changes in static stability and the vertical moisture gradient will alter interactions between convection, large-scale circulations, and moisture as the climate system warms. Increasing static stability and a steepening vertical moisture gradient have opposing effects on the ability of convection to drive large-scale vertical moisture advection. In the 4xCO2 simulation, the effect of the steepened vertical moisture gradient surpasses the effect of increased static stability, allowing variations in convection to drive greater variations in large-scale vertical moisture advection in the warmer climate. This is true throughout the troposphere, with the largest fractional changes occurring in the middle and upper troposphere. The increased variations in large-scale vertical moisture advection promote moisture variance, aiding in the destabilization of the MJO. In other words, the moist thermodynamic environment in the 4xCO2 simulation allows MJO convective heating to more efficiently re-supply itself with moisture, supporting elevated levels of convection. This conclusion is consistent with the findings of several previous studies that used the column MSE budget approach (Arnold et al. 2013, 2015; Carlson and Caballero 2016). The balance of processes acting to destabilize the MJO underwent relatively small changes from the PI to 4xCO2 simulation (see Appendix), lending credence to the notion that increased MJO activity may be a robust response to a warming climate.

Increasing static stability reduces the large-scale vertical velocity required for adiabatic cooling to balance diabatic heating, resulting in a weaker dynamical response to intraseasonal variations in convection in the 4xCO2 simulation. This occurs throughout the troposphere, but is largest in the middle and upper troposphere. As large-scale vertical motion is associated with horizontal convergence/divergence acting throughout the column, a decrease in

horizontal wind variance occurs at all levels in the 4xCO2 simulation, consistent with the findings of Maloney and Xie (2013).

The reduced dynamical response to MJO convective variability has implications for SLHF feedbacks to the MJO. Surface flux feedbacks to the MJO depend on background low-level winds, to which intraseasonal wind anomalies add constructively or destructively (Shinoda et al. 1998; Riley Dellaripa and Maloney 2015). Additionally, SLHF feedbacks depend on the absolute air-sea moisture deficit, and the covariance between SLHF anomalies and column moisture anomalies. These dependences present significant challenges to assessing how SLHF feedbacks may change in a warming climate, as realistic assessment of such changes depends not only on accurately simulating these relationships in the current climate, but also on accurately simulating how these relationships will change as the climate system warms. Arnold et al. (2015) found that a reduced air-sea moisture deficit contributed to weakened SLHF feedbacks in the 4xCO2 simulation. The results of this study suggest that a weakened dynamical response to MJO convective variability may also contribute to weakened SLHF feedbacks as the climate system warms.

The reduced dynamical response to MJO convective variability also impacts the MJO's ability to influence the extratropics. The excitation of Rossby wave trains by tropical convective variability is closely related to anomalous divergence driven by such variability (Sardeshmukh and Hoskins 1988). Northern hemisphere (NH) extratropical 525 hPa geopotential height (Z525) anomalies associated with the MJO were shown to be significantly weaker in the 4xCO2 simulation, despite a significant increase in MJO heating anomalies. The ratio of the root mean square (RMS) of NH extratropical Z525 anomalies to RMS anomalous MJO heating was reduced by 40% in the 4xCO2 simulation. In other words, the ability of

MJO convective heating to force the extratropics was reduced by roughly 40% in the 4xCO2 simulation. The linear baroclinic model (LBM) of Watanabe and Kimoto (2000) was used to isolate the effect of changing static stability on MJO forcing of the extratropics from the effects of changes in climatological winds and changes in the structure of MJO heating anomalies. Results of the LBM analysis show decreases in the ability of MJO convective heating to force the extratropics that are comparable to those seen in SP-CESM. While not conclusive, the LBM results support the idea that decreases in the ability of MJO convective heating to force the extratropics result from increased tropical static stability.

The MJO drives changes in both means and extremes across the globe, and serves as the primary source of predictability on weekly to monthly timescales. Given the MJO's prominent role in "bridging weather and climate" (Zhang 2005), it is tempting to suppose that, as the climate system warms, increased MJO activity may help ameliorating the medium-range forecasting woes faced by seamless weather prediction efforts. Results of this study suggest that, even though MJO convective heating is likely to increase in a warming climate, the MJO's influence on the extratropics may not. The authors of this study would like to emphasize that the WTG balance relationships discussed here are applicable to phenomena besides the MJO (e.g. ENSO). The WTG balance framework may provide insight to how other phenomena, and their impacts (e.g. ENSO teleconnections), may change as the climate system warms.

4.7. Additional Analysis

4.7.1. Moisture variance budget analysis

Before examining the moisture variance budget, consider Figure 4.16, which highlights the exceptional accuracy of the vertically resolved WTG framework. Both the anomalous large-scale vertical velocity and anomalous large-scale vertical moisture advection (Fig. 4.16a,b) are well diagnosed using WTG balance (Fig. 4.16c,d), with very little error (Fig. 4.16e,f,g) being evident throughout the free troposphere. WTG diagnosis of large-scale vertical moisture advection does not work as well in the boundary layer. Therefore a conservative limit of 850 hPa has been adopted for the vertical integration of terms in the moisture variance budget which depend upon WTG balance.

Figure 4.17 shows more comprehensive decomposition of the moisture variance budget presented in Figure 4.13. Remember that moisture variance budget terms are normalized by domain averaged moisture variance (see equation 4.1). Therefore, even though individual moisture budgets terms are much larger in the 4xCO2 simulation (Fig. 4.11), they may result in similar growth rates as those in the PI simulation. Comparing the PI and 4xCO2 moisture variance budgets highlights any changes (or lack thereof) in the balance of processes acting to destabilize the MJO. As discussed in section 4.5, the column process (term D) promotes the growth of moisture variance while horizontal advective damping (term C) limits moisture variance growth, and both terms weaken slightly in the 4xCO2 simulation (red). The column process (term D) can be decomposed in contributions from total radiative heating (term E) and the net effect of microphysical processes and SGS eddy fluxes (term F). The latter (term F) can be further decomposed into contributions from SLHF feedbacks (term G) and SGS convective processes (term H, i.e. convection in the absence of radiative and surface

flux feedbacks). Destabilization by both radiative feedbacks (term E) and SGS convective processes (term G) weakens in the 4xCO2 simulation, consistent with the progression to more top-heavy heating profiles discussed in Figure 4.15 of section 4.5, and helping explain the modest weakening of destabilization by the column process (term D). Figure 4.18 shows the decomposition of the total radiative feedback (term A) into contributions from longwave (term B) and shortwave (term C) components. The modest weakening in destabilization by total radiative feedbacks in the 4xCO2 simulation primarily results from the longwave component (Term B), again consistent with the more top-heavy heating profiles discussed in Figure 4.15 of section 4.5. Again, it is worth emphasizing that the weakening radiative feedback may also be related to the mechanisms described by Bony et al. (2016), whereby increased static stability results in a decreased spreading of convective anvils at upper levels, or to the scale dependence of the radiative feedback described by Adames and Kim (2016). Taken as a whole, Figure 4.17 suggests that no large change in the balance of processes acting to destabilize the MJO occurs.

In order to ensure that no large compensating changes occur in the balance of processes acting to destabilize the MJO, horizontal advection and large-scale vertical moisture advection are further decomposed. As in Chikira (2014) and Wolding et al. (2016), horizontal advection can be decomposed as

$$-\left(\overline{\boldsymbol{V}}_{\boldsymbol{h}} \cdot \boldsymbol{\nabla}\overline{q}\right)_{\mathrm{MJO}} = -\left(\overline{\boldsymbol{V}}_{\boldsymbol{h},\mathrm{LP20}} \cdot \boldsymbol{\nabla}\overline{q}_{\mathrm{LP20}}\right)_{\mathrm{MJO}} - \left(\overline{\boldsymbol{V}}_{\boldsymbol{h}} \cdot \boldsymbol{\nabla}\overline{q}\right)_{\mathrm{HF}} \tag{4.8}$$

where

$$\left(\overline{\boldsymbol{V}}_{\boldsymbol{h}} \cdot \boldsymbol{\nabla}\overline{q}\right)_{\mathrm{HF}} = \left(\overline{\boldsymbol{V}}_{\boldsymbol{h},\mathrm{LP20}} \cdot \boldsymbol{\nabla}\overline{q}_{\mathrm{HP20}}\right)_{\mathrm{MJO}} + \left(\overline{\boldsymbol{V}}_{\boldsymbol{h},\mathrm{HP20}} \cdot \boldsymbol{\nabla}\overline{q}_{\mathrm{LP20}}\right)_{\mathrm{MJO}} + \left(\overline{\boldsymbol{V}}_{\boldsymbol{h},\mathrm{HP20}} \cdot \boldsymbol{\nabla}\overline{q}_{\mathrm{HP20}}\right)_{\mathrm{MJO}} \tag{4.9}$$

and the subscript $_{\mathrm{HP20}}$ indicates the application of 20-day highpass filtering. Similarly, using WTG balance, large-scale vertical moisture advection can be decomposed as

$$-\left(\overline{\omega}\frac{\partial\overline{q}}{\partial p}\right)_{\mathrm{MJO}} = \frac{1}{\mathrm{L_v}}\left(\left(\overline{\alpha}_{\mathrm{LP20}}\, Q_{1,\mathrm{LP20}}\right)_{\mathrm{MJO}} + \left(\overline{\alpha}\, Q_1\right)_{\mathrm{HF}}\right) \tag{4.10}$$

where

$$\left(\overline{\alpha}\, Q_1\right)_{\mathrm{HF}} = \left(\overline{\alpha}_{\mathrm{LP20}}\, Q_{1,\mathrm{BP3-20}}\right)_{\mathrm{MJO}} + \left(\overline{\alpha}_{\mathrm{BP3-20}}\, Q_{1,\mathrm{LP20}}\right)_{\mathrm{MJO}} + \left(\overline{\alpha}_{\mathrm{BP3-20}}\, Q_{1,\mathrm{BP3-20}}\right)_{\mathrm{MJO}} \tag{4.11}$$

and the subscript $_{\mathrm{BP3-20}}$ indicates the application of $3-20$ day bandpass filtering. The first term on the right hand side of equations 4.8 and 4.10 result from slowly varying fields, while the second term on the right hand side of both equations results from the presence of higher frequency variability. These terms will be referred to as the horizontal advection and large-scale vertical moisture advection resulting from slowly varying fields and higher frequency variability respectively. Figure 4.19 shows total horizontal advection (term A) decomposed into contributions by slowly varying fields (term b) and higher frequency variability (term C) respectively. In both simulations, horizontal advective damping (term A) results from the modulation of higher frequency variability on intraseasonal timescales (term C), and the efficacy of this damping of moisture variance shows no change from the PI to 4xCO2 simulation. As discussed in Wolding et al. (2016), modulation of higher frequency convective variability also contributes to destabilization by large-scale vertical moisture advection,

offsetting some of the horizontal advective damping effect. Figure 4.20 shows the total effect of higher frequency convective variability, broken down into contributions from horizontal advection (term B) and large-scale vertical moisture advection (term C). Almost no change occurs in the effect of higher frequency variability between the PI and 4xCO2 simulations. These results further support the conclusion that no large changes occur in the balance of processes acting to destabilize the MJO.

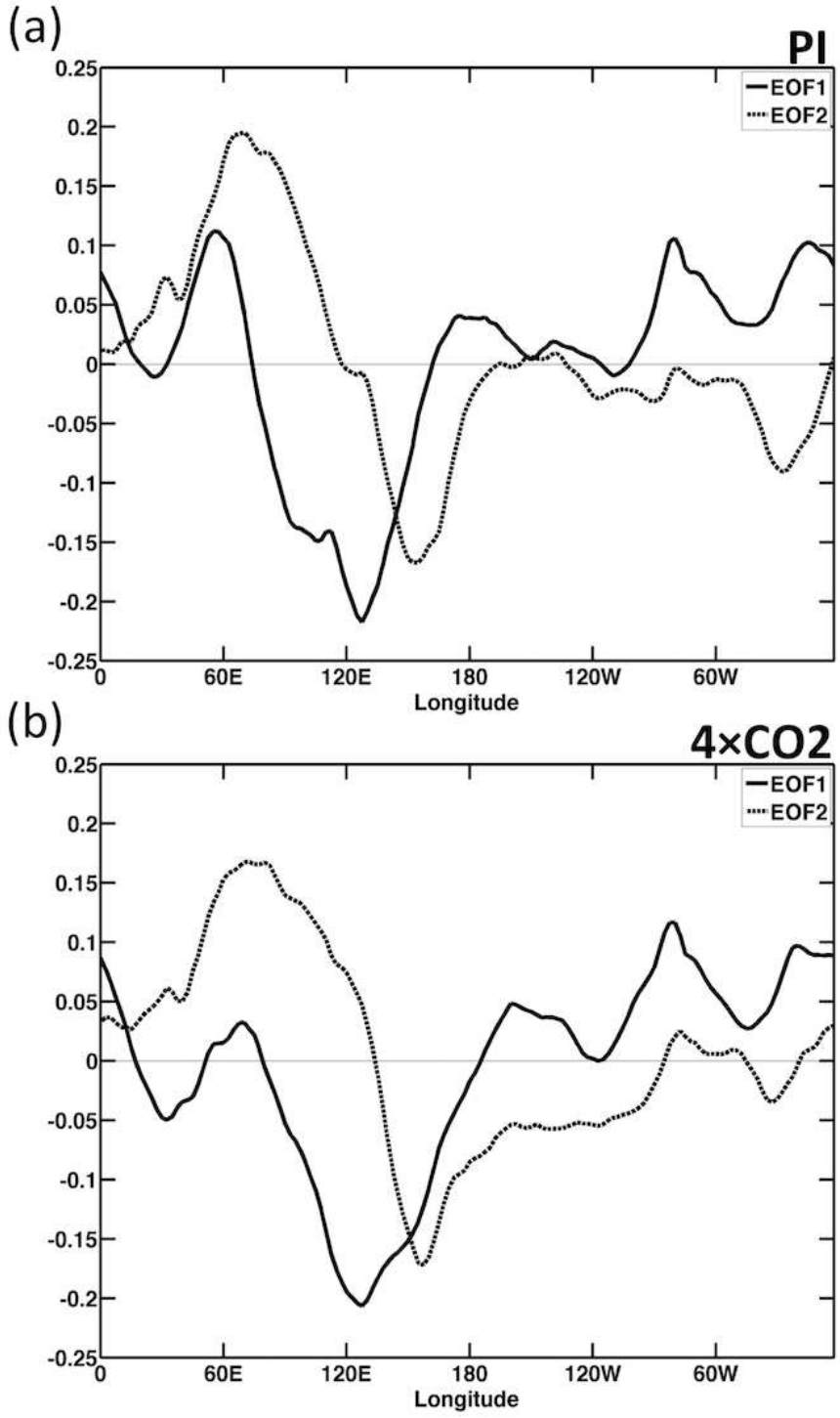

FIG. 4.1. The two leading EOF structures of latitudinally averaged (15°N-15°S) 20-100 day bandpass filtered OLR for the (a) PI and (b) 4xCO2 SP-CESM simulations. The first two EOFs explain 16.7% and 12.4% percent of the total variance respectively for the PI simulation, and 17.6% and 16.3% percent of the total variance respectively for the 4xCO2 simulation.

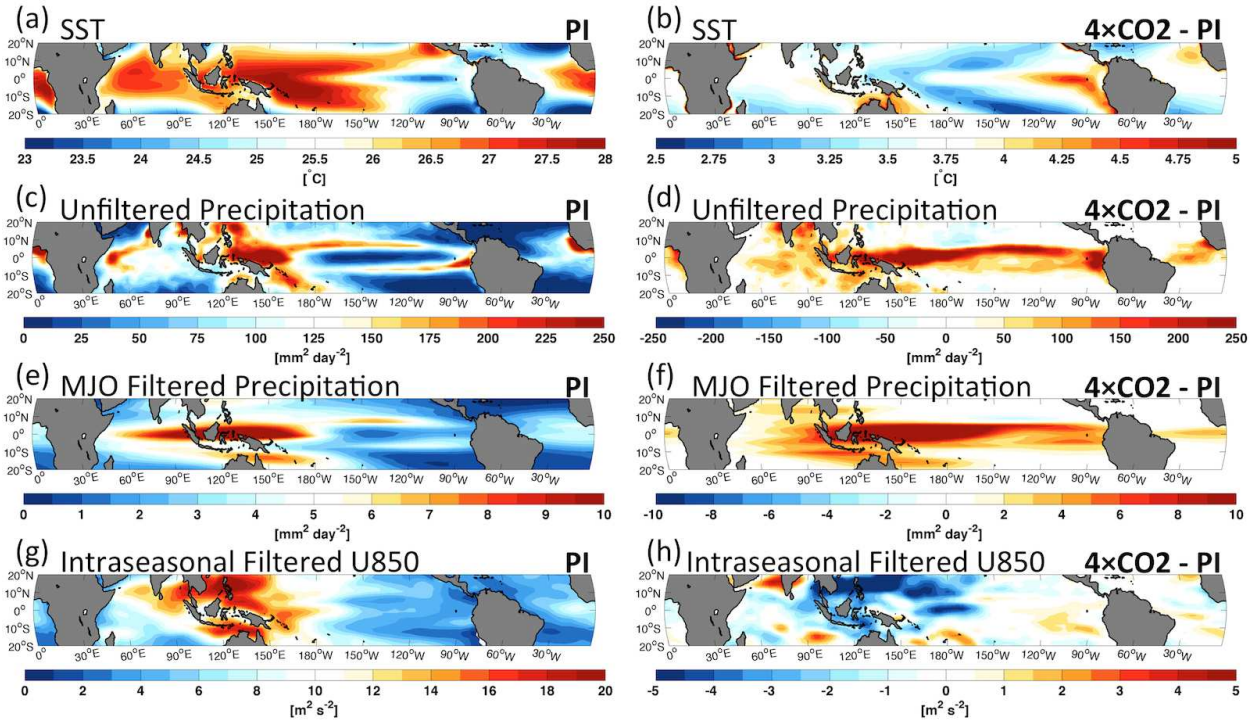

FIG. 4.2. (a,b) Time mean SST, (c,d) variance of unfiltered precipitation variance, (e,f) variance of precipitation filtered to eastward wavenumbers 0 to 5 and frequencies corresponding to 20-100 days, and (g,h) variance of 20-100 day bandpass filtered 850 hPa zonal wind for the PI simulation, and difference between the 4xCO2 and PI simulations respectively.

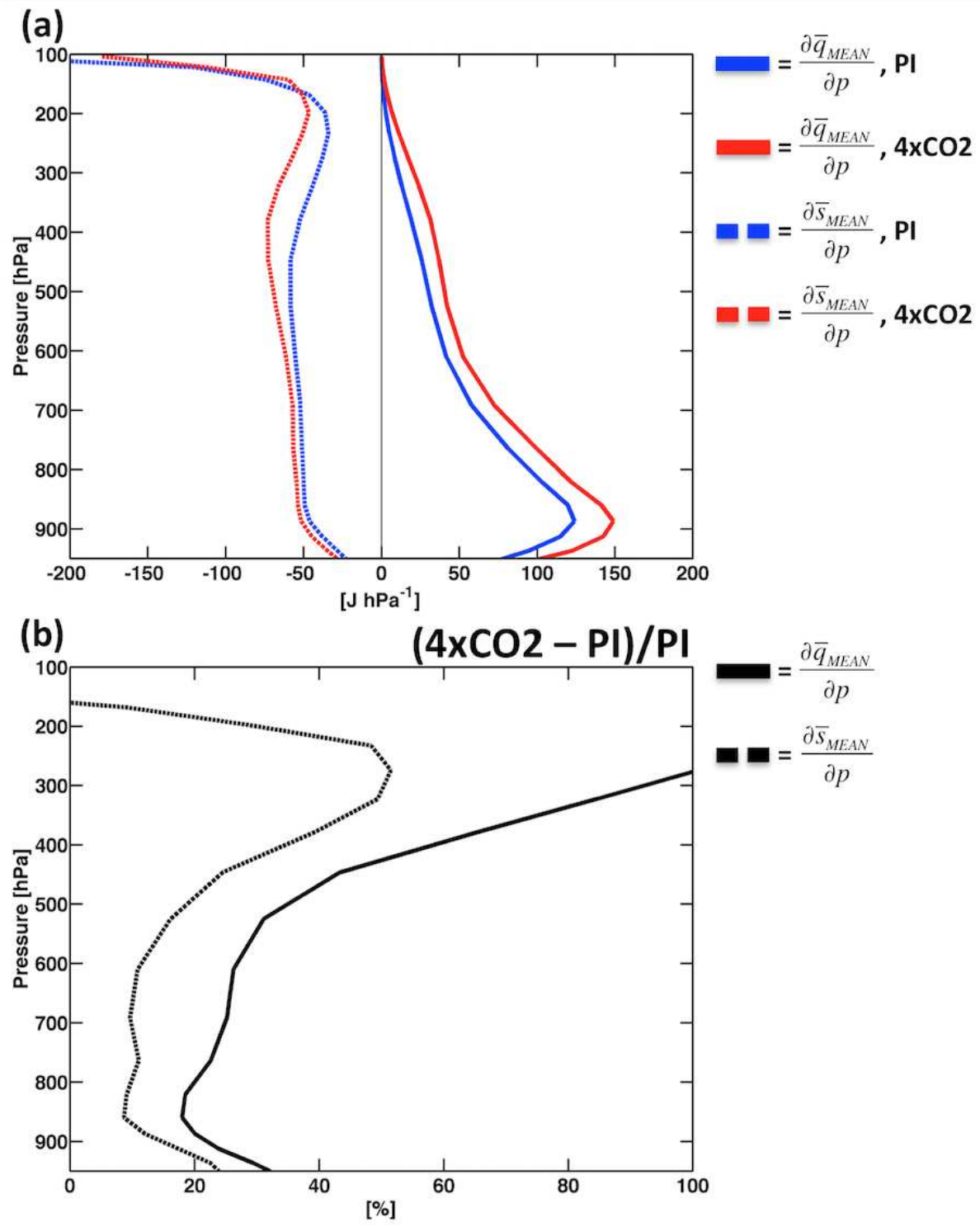

FIG. 4.3. (a) Time mean profiles of the vertical moisture gradient (solid lines) and vertical dry static energy gradient (dashed lines) averaged over the domain $10°\text{N} - 10°\text{S}, 60°\text{E} - 180°\text{E}$ for the PI (blue) and 4xCO2 (red) simulations, and (b) fractional change between the 4xCO2 and PI simulations.

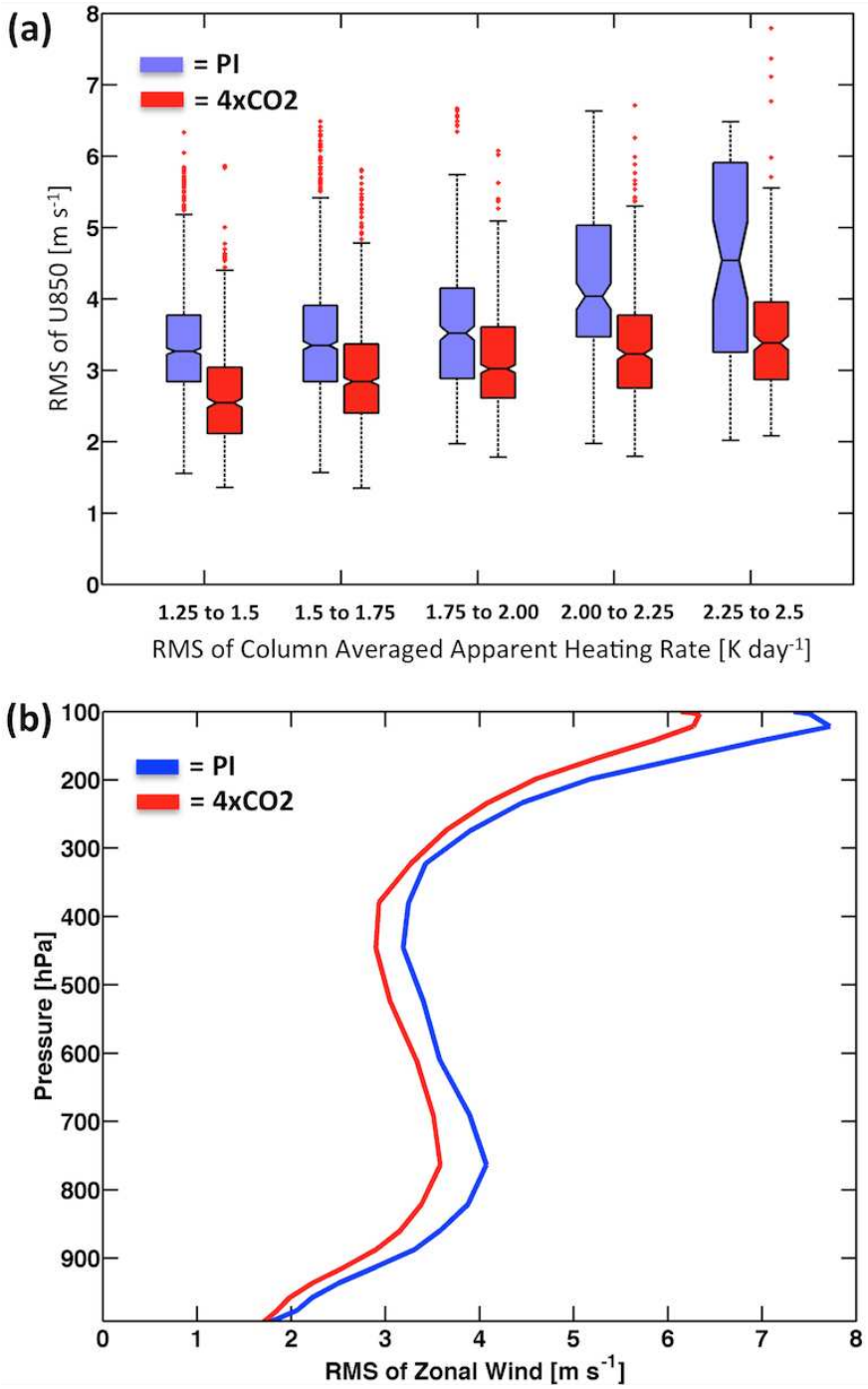

FIG. 4.4. (a) Box and whisker plots of the root mean square (RMS) of 20-100 day bandpass filtered 850 hPa zonal wind for the domain $10°\mathrm{N} - 10°\mathrm{S}, 60°\mathrm{E} - 180°\mathrm{E}$, binned by the RMS of 20-100 day bandpass filtered column averaged apparent heating rate over the same domain, for the PI (blue) and 4xCO2 (red) simulations. Medians differ with 95% statistical significance if their notched intervals do not overlap. (b) Vertical profile of the RMS 20-100 day bandpass filtered zonal wind for the 1.75 to 2.00 $\mathrm{K\,day^{-1}}$ bin in (a).

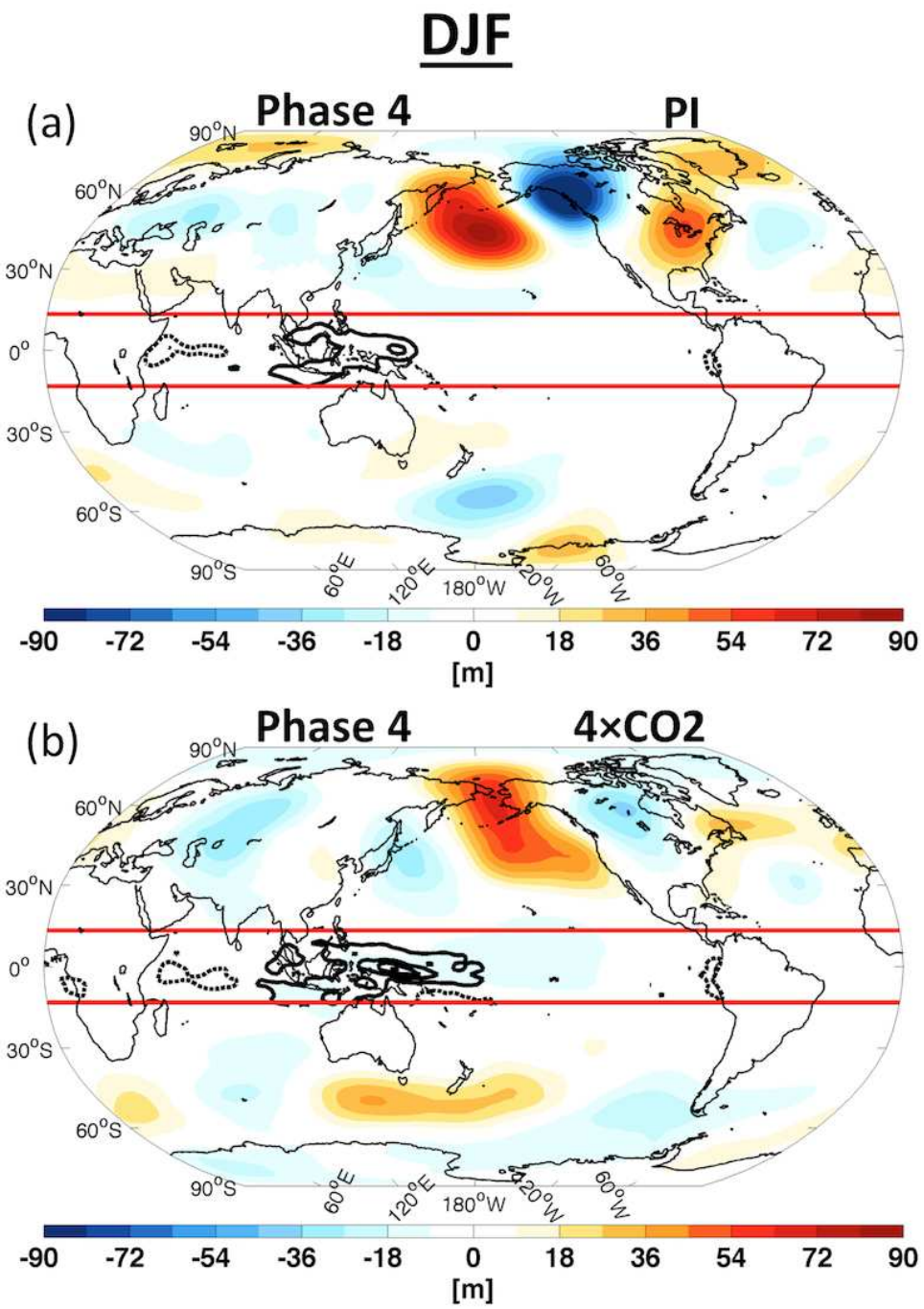

FIG. 4.5. DJF phase 4 composites of 20-100 day bandpass filtered column averaged apparent heating anomalies (contours) in the tropics, and 20-100 day bandpass filtered 525 hPa geopotential height anomalies (color shading) in the extratropics for the (a) PI and (b) 4xCO2 simulations. Red lines at 15°N and 15°S denote the boundaries used for tropical and extratropical averaging in the corresponding analysis. Solid and dashed contours correspond to positive and negative heating rates respectively, contoured every 2 K day^{-1} starting at ± 1 K day^{-1}, with the 0 K day^{-1} contour ommitted.

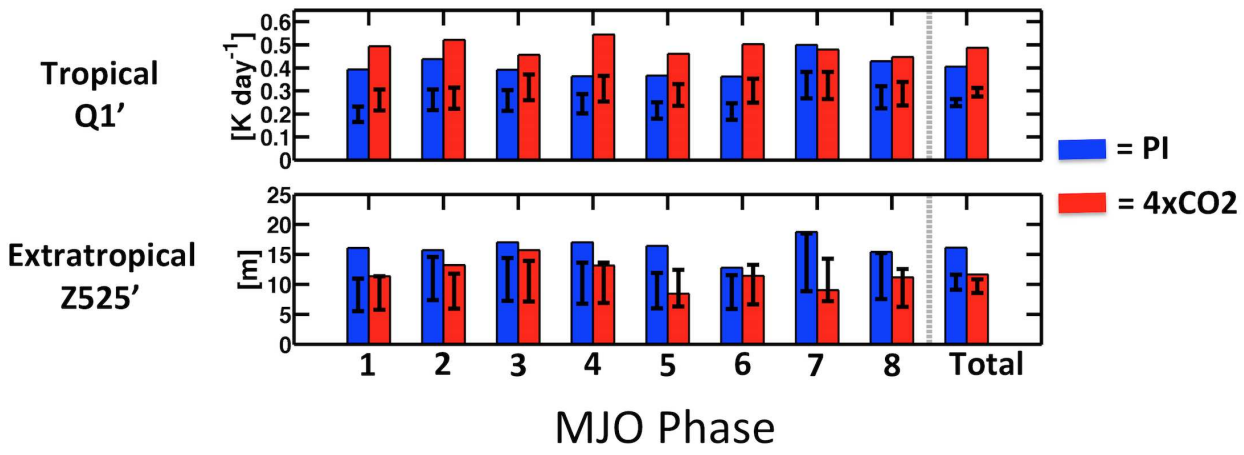

FIG. 4.6. Root mean square (RMS) of tropical 20-100 day bandpass filtered column averaged apparent heating anomalies (top) and northern hemisphere extratropical 20-100 day bandpass filtered 525 hPa geopotential height anomalies (bottom) for composites of each MJO phase, and the average across all eight phase composites for the PI (blue) and 4xCO2 (red) simulations. Tropical and extratropical averaging occurs equatorward and poleward of 15°N and 15°S respectively. Brackets indicate the 95% confidence intervals, determined using the moving block bootstrapping analysis described in section 4.2. Bootstrap sample size N, corresponding to the number of days in each phase composite, is equal to 101, 57, 59, 66, 86, 89, 36, and 52 for phases 1 through 8 of the PI simulation. Bootstrap sample size N is equal to 84, 78, 56, 58, 71, 62, 54, and 69 for phases 1 through 8 of the 4xCO2 simulation.

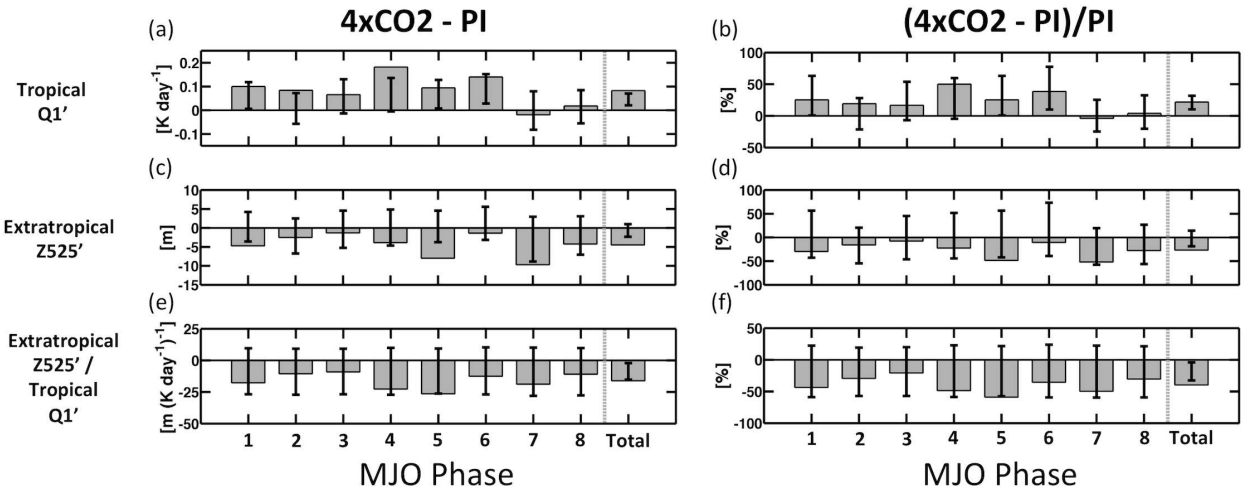

FIG. 4.7. Absolute (left) and fractional (right) changes in the root mean square (RMS) of tropical 20-100 day bandpass filtered column averaged apparent heating anomalies (top), RMS of northern hemisphere extratropical 20-100 day bandpass filtered 525 hPa geopotential height anomalies (middle), and the ratio of the two (bottom) for composites of each MJO phase, and the average across all eight phase composites. Tropical and extratropical averaging occurs equatorward and poleward of 15°N and 15°S respectively. Brackets indicate the 95% confidence intervals, determined using the moving block bootstrapping analysis described in section 4.2. Bootstrap sample size N, corresponding to the number of days in each phase composite, is equal to 101, 57, 59, 66, 86, 89, 36, and 52 for phases 1 through 8 of the PI simulation. Bootstrap sample size N is equal to 84, 78, 56, 58, 71, 62, 54, and 69 for phases 1 through 8 of the 4xCO2 simulation.

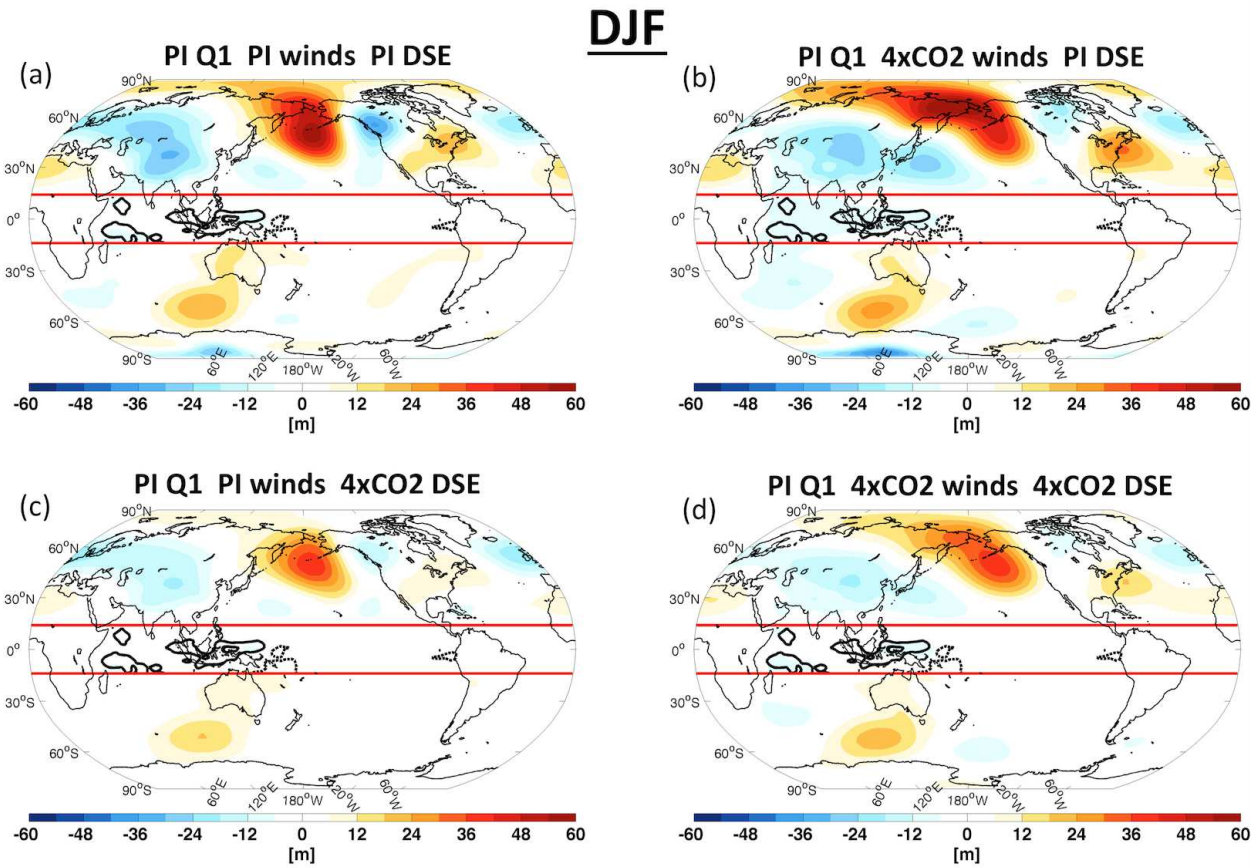

FIG. 4.8. 500 hPa geopotential height anomaly (shading) response of the dry linear baroclinic model (LBM) of Watanabe and Kimoto (2000), averaged from days 20 to 34, for four simulations. Each simulation was forced with DJF phase 3 composite column averaged apparent heating anomalies (contours) within the domain of 15°N and 15°S, denoted by the red lines. Basic state fields required by the model include horizontal winds and dry static energy (DSE). (a) Simulation using full PI DJF basic state. (b) Simulation using the PI DJF basic state, with the exception of horizontal winds, which were from the 4xCO2 simulation. (c) Simulation using the PI DJF basic state, with the exception of DSE, which was from the 4xCO2 simulation. (d) Simulation using the 4xCO2 DJF basic state. More details of the LBM and the simulations are provided in section 4.4.1.2. Solid and dashed contours correspond to positive and negative heating rates respectively, contoured every 2 K day^{-1} starting at ± 1 K day^{-1}, with the 0 K day^{-1} contour ommitted.

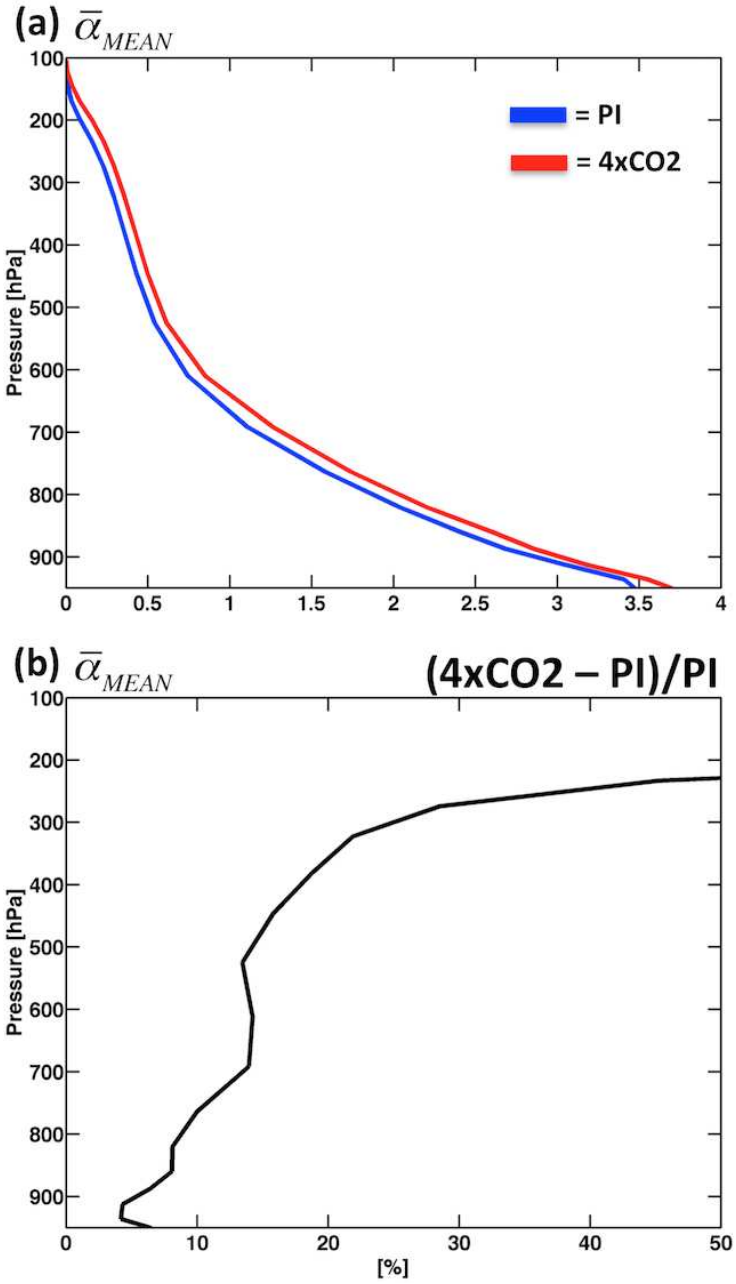

FIG. 4.9. (a) Time mean profiles of $\overline{\alpha}$ (see equation 4.6) averaged over the domain $10°\text{N} - 10°\text{S}, 60°\text{E} - 180°\text{E}$ for the PI (blue) and 4xCO2 (red) simulations, and (b) fractional change between the 4xCO2 and PI simulations.

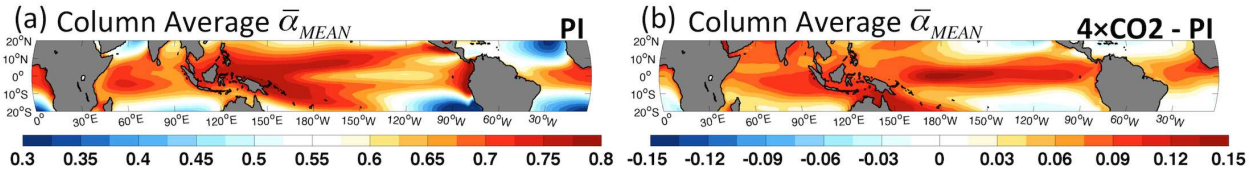

FIG. 4.10. Time mean $\overline{\alpha}$, averaged from 850 to 100 hPa, for the (a) PI simulation, and (b) difference between the 4xCO2 and PI simulations.

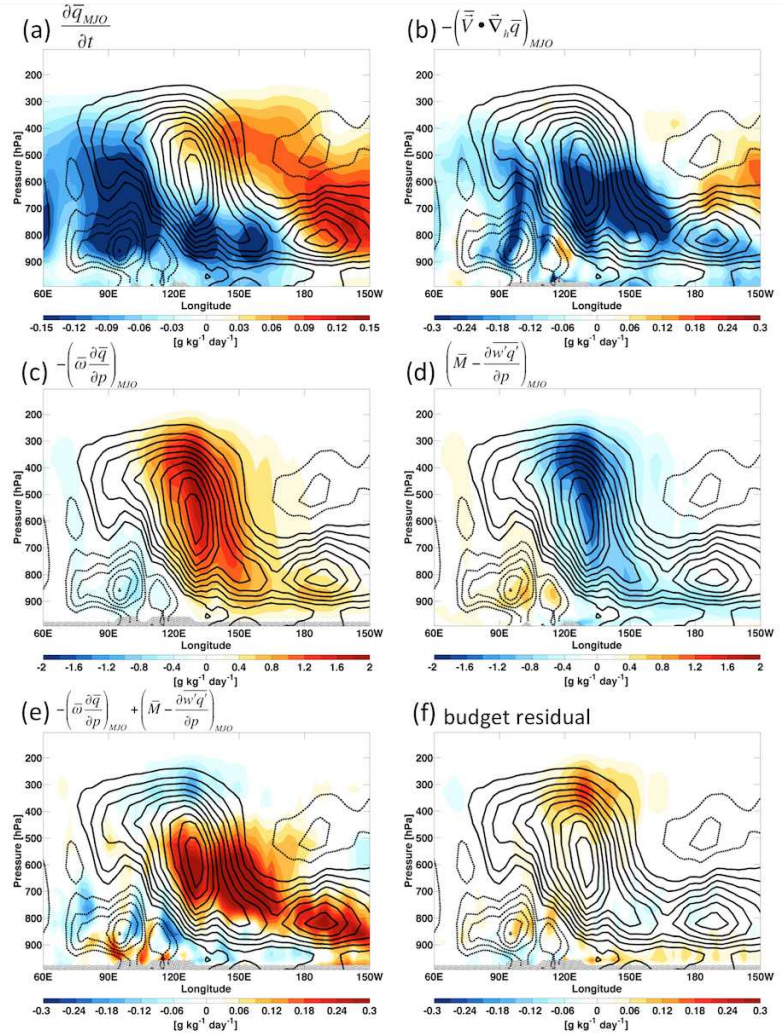

FIG. 4.11. Longitude-height sections of latitudinally averaged (5°N−5°S) composite intraseasonal moisture budget terms (shading) for the 4xCO2 simulation. These terms are the (a) Eulerian moisture tendency, (b) horizontal moisture advection, (c) vertical moisture advection, (d) the net effect of the microphysical moisture tendency and sub-grid scale vertical eddy moisture flux convergence, (e) the column process (i.e. the sum of plots (c) and (d)), and (f) the moisture budget residual. Solid and dashed contours indicate positive and negative specific humidity anomalies respectively, with contour intervals of 0.1 g kg^{-1}. Composites are produced from 19 independent wintertime (October 1 to April 30) events. Grey hatching indicates regions where data has been lost as a result of proximity to the surface. The subscript MJO indicates application of 20-100 day bandpass filtering. Please note the color scale differs between plots. See figure 3 of Wolding et al. (2016) for results of the PI moisture budget, produced following the same methodology and plotting convections used here.

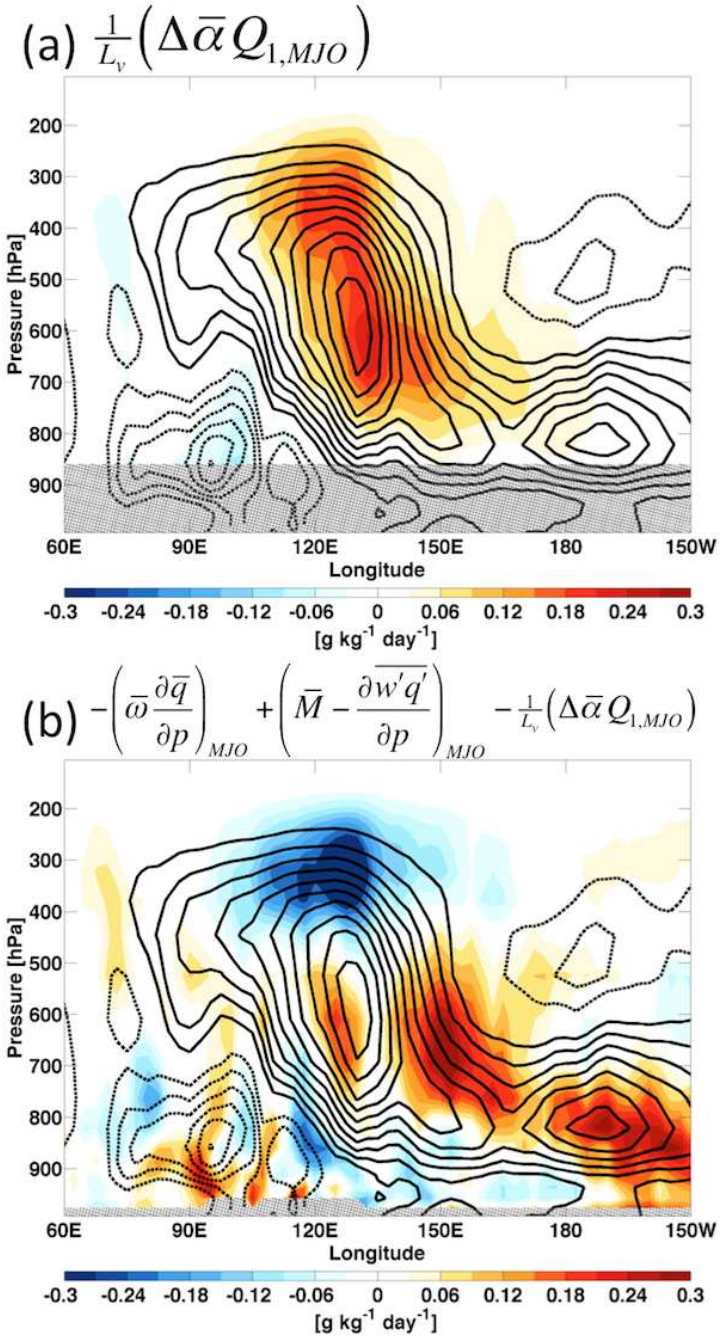

FIG. 4.12. As in Figure 4.11, except the color shading shows (a) the contribution that changes in time mean $\overline{\alpha}$ between the PI and 4xCO2 simulation make to large-scale vertical moisture advection in the 4xCO2 simulation, and (b) the column process without the contribution changes in $\overline{\alpha}$ make to large-scale vertical moisture advection. Plot (b) is equivalent to subtracting plot (a) from Figure 4.11e. The subscript MJO indicates application of 20-100 day bandpass filtering.

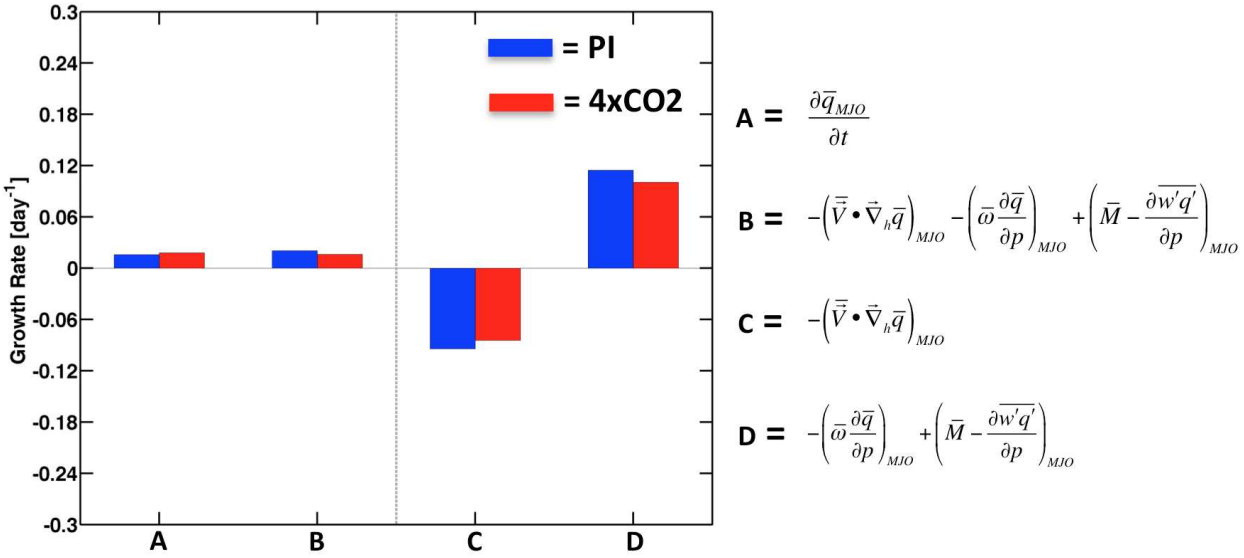

FIG. 4.13. Vertically integrated contributions various budget terms make to the column moisture variance growth rate in the PI (blue) and 4xCO2 (red) simulations, corresponding to the vertical integral of equation 4.1. Column moisture was calculated by vertically integrating from the surface to 100 hPa, as were terms A through D. The area weighted integral has been taken from 15°N-15°S, 60°E-180°E, averaged for every day where the magnitude FMO index exceeded a value of 1 for the respective simulations. The subscript MJO indicates application of 20-100 day bandpass filtering.

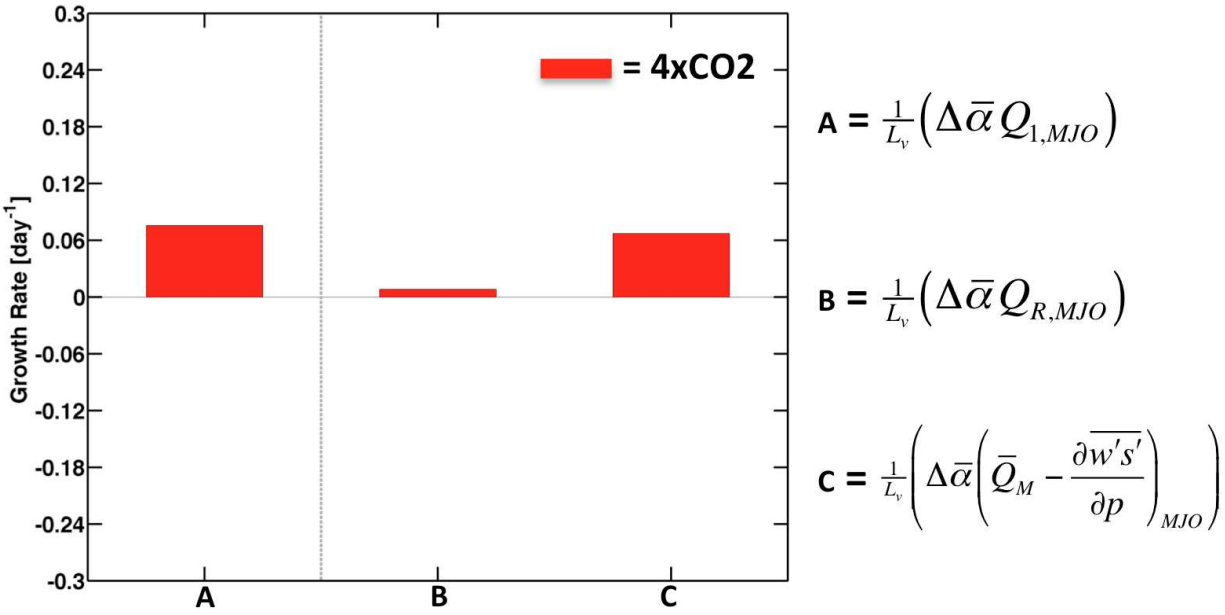

FIG. 4.14. As in Figure 4.13, except for the contribution that changes in time mean $\overline{\alpha}$ between the PI and 4xCO2 simulation make to large-scale vertical moisture advection resulting from variations in (a) apparent heating, (b) radiative heating, and (c) heating by microphysical processes and SGS eddy fluxes of DSE in the 4xCO2 simulation. All terms were vertically integrated from 850 to 100 hPa, as they depend on the weak temperature gradient approximation.

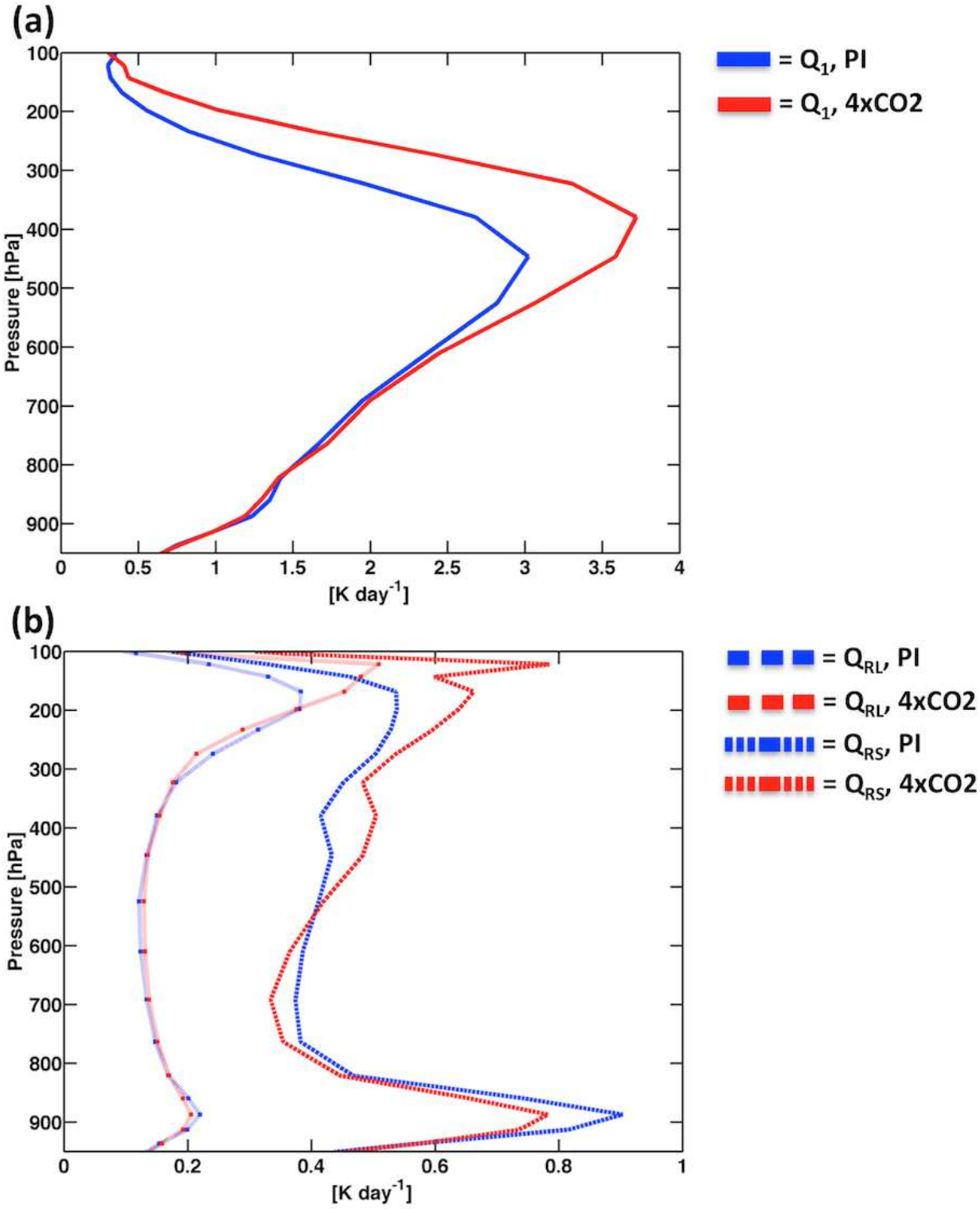

FIG. 4.15. (a) Profiles of the RMS of 20-100 day bandpass filtered apparent heating anomalies, calculated over the entire PI (blue) and 4xCO2 (red) simulations for the domain $15°\text{N} - 15°\text{S}, 60°\text{E} - 180°\text{E}$. (b), as in (a), except for longwave (dashed) and shortwave (dot-dashed) radiative heating anomalies.

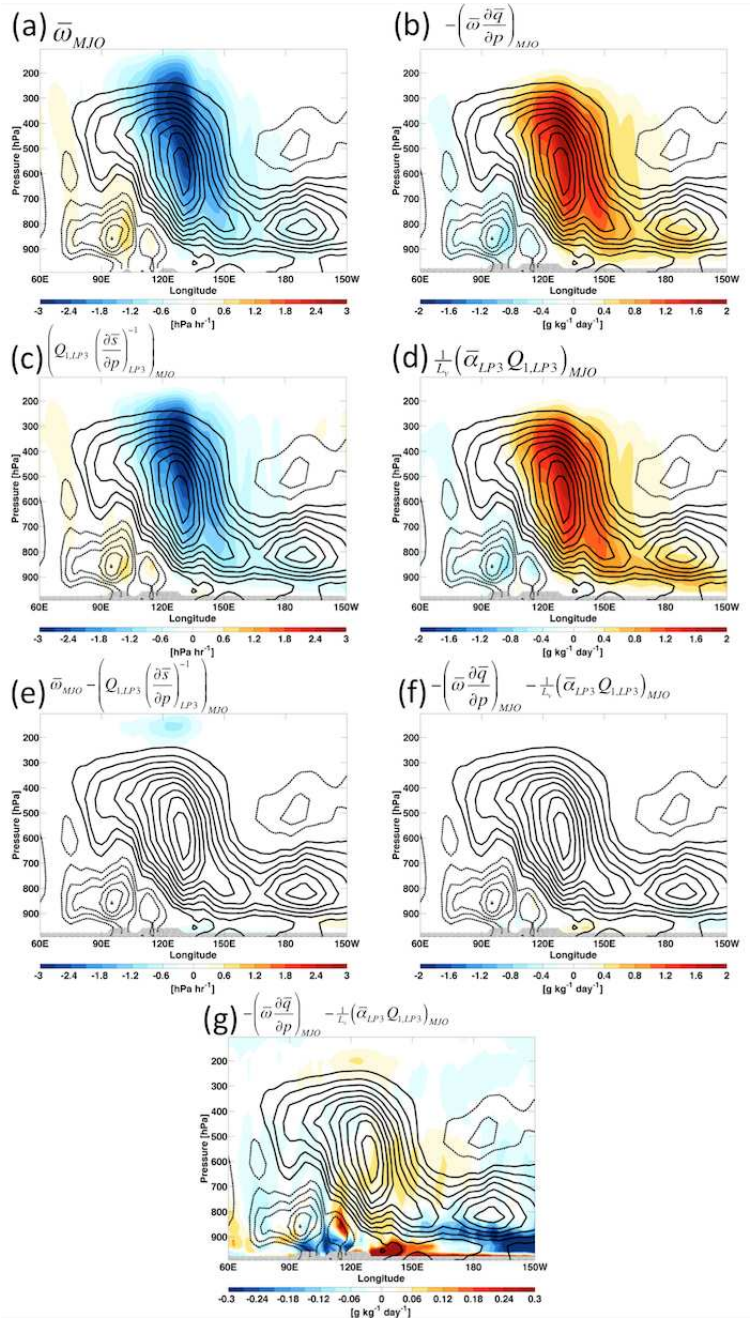

FIG. 4.16. As in Figure 4.11, except the color shading indicates the anomalous (a) large-scale vertical velocity and (b) vertical moisture advection in the 4xCO2 simulation, the anomalous (c) large-scale vertical velocity and (d) vertical moisture advection diagnosed using weak temperature gradient balance assumptions, and the difference between the actual and diagnosed (e) large-scale vertical velocity and (f,g) vertical moisture advection. The subscripts LP3 and MJO indicate application of 3 day lowpass and 20-100 day bandpass filtering respectively. Please note the color scale of plot (g) differs from that of plots (b), (d), and (f).

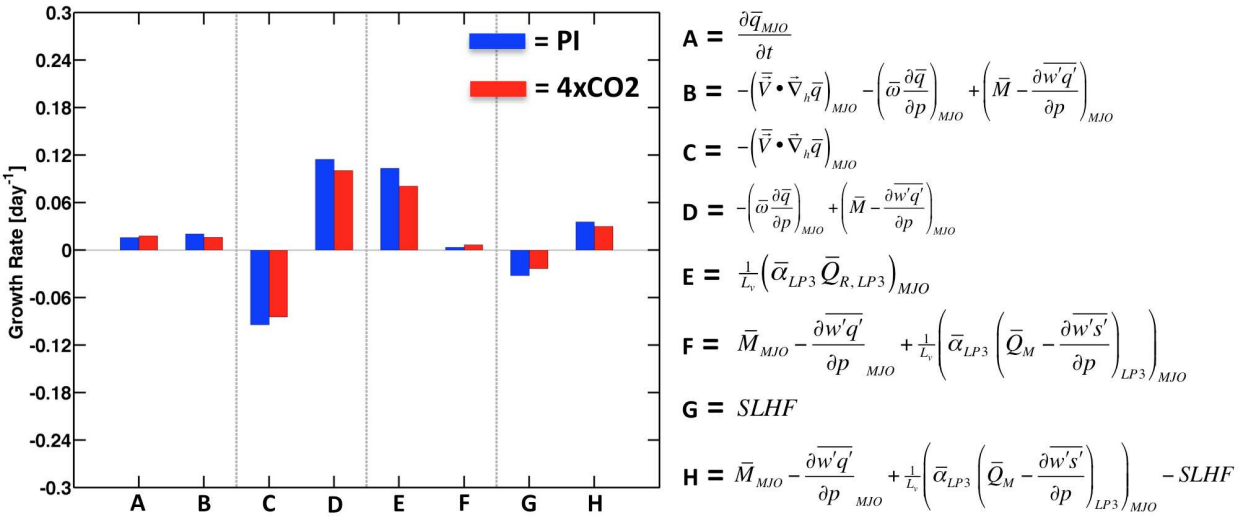

FIG. 4.17. As in Figure 4.13, except expanded to include additional terms. The subscripts LP3 and MJO indicate application of 3 day lowpass and 20-100 day bandpass filtering respectively. Terms E, F, and H were vertically integrated from 850 to 100 hPa, as they depend on the weak temperature gradient approximation.

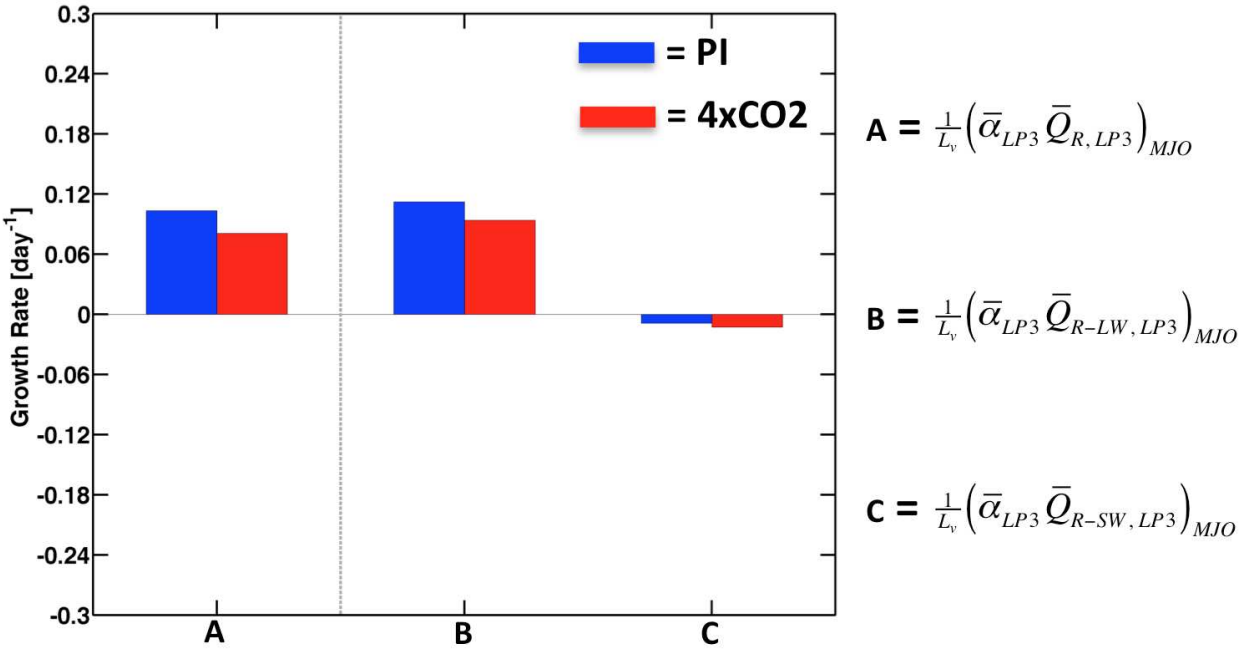

FIG. 4.18. As in Figure 4.13, except for various radiative heating terms. The subscripts LP3 and MJO indicate application of 3 day lowpass and 20-100 day bandpass filtering respectively. Each term was vertically integrated from 850 to 100 hPa, as they depend on the weak temperature gradient approximation.

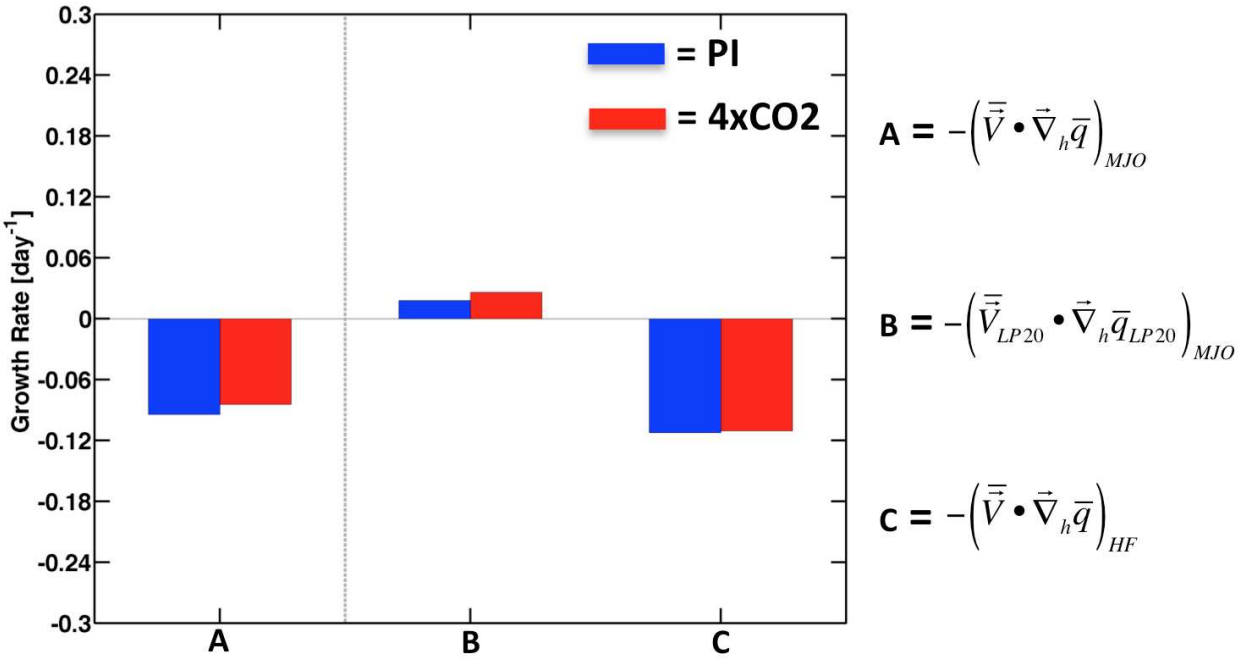

FIG. 4.19. As in Figure 4.13, except for various horizontal advective terms. The subscripts LP20 and MJO indicate application of 20 day lowpass and 20-100 day bandpass filtering respectively. The subscript HF indicates terms related to higher frequency variability, calculated following equation 4.9.

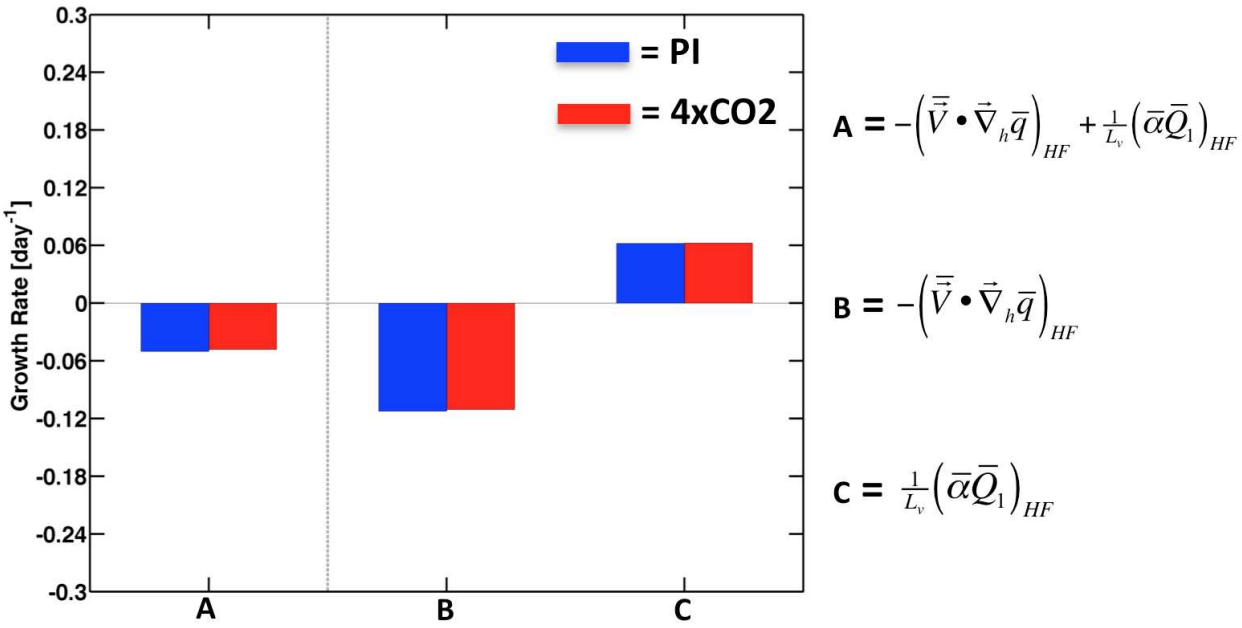

FIG. 4.20. As in Figure 4.13, except for terms related to higher frequency convective variability. The subscript HF indicates terms related to higher frequency variability, calculated following equations 4.9 and 4.11. Term C was vertically integrated from 850 to 100 hPa, as it depends on the weak temperature gradient approximation.

CHAPTER 5

Conclusions

The purpose of this study is to better understand interactions between moisture, convection, and large-scale circulations thought to be important to the MJO. This study contributes to the development of a simplified framework for understanding such interactions, improves the understanding of the role various apparent heating processes play in destabilizing and propagating the MJO, and provides insight to how the MJO, and its global influence, may change as the climate system warms.

The main contributions this study makes to the development of a simplified framework for understanding interactions between moisture, convection, and large-scale circulations can be summarized by the following points:

(1) Intraseasonal variations in large-scale vertical motion can be accurately diagnosed from variations in apparent heating, allowing variations in large-scale vertical moisture advection to be decomposed into contributions from various apparent heating processes.

(2) The WTG framework allows the vertical advection term of the column MSE budget to be quantitatively partitioned into contributions from various apparent heating processes. This study has shown that the vertical structure of apparent heating processes must be considered to accurately assess the effect of those processes on the MJO.

(3) Applicability of the WTG balance framework is not solely a function of the spatial and temporal scale, and the governing dynamics of phenomena in question must also be considered. A diagnostic approach to scale analysis suggests that the governing

dynamics of the MJO differ from those of convectively coupled Kelvin waves, and indicates that the WTG balance framework is more applicable to the former than the later.

The WTG balance framework was used to examine the processes destabilizing and propagating the MJO in both ERAi reanalysis and SPCESM. The main findings of this analysis can be summarized in the following points:

(1) The MJO is strongly supported by radiative feedbacks and is damped by the intraseasonal modulation of higher frequency convective variability. This finding is consistent with the findings of several previous studies.

(2) The modulation of higher frequency convective variability on intraseasonal timescales makes an important contribution to intraseasonal variations in large-scale vertical moisture advection.

(3) The evolution of the vertical structure of apparent heating does not play a dominant role in limiting the amplitude of the MJO in the current climate, at least in SPCESM. Analysis of ERAi suggests that this may also be true for the real world MJO.

(4) Positive feedbacks between moisture, convection, and large-scale circulations can arise through different combinations of processes. Process oriented diagnostics are needed to determine if models are producing MJO-like variability through the "correct" combination of processes.

The WTG balance framework was also used to examine how changes in the moist thermodynamic structure of the tropics may impact the MJO, and its global influence, as the

climate system warms. The main findings of this analysis can be summarized in the following points:

(1) As the climate system warms, increasing static stability will reduce the dynamical response to MJO convective variability.

(2) As the climate system warms, increasing static stability and a steepening vertical moisture gradient will have opposing effects on the ability of MJO convective variability to drive variations in large-scale vertical moisture advection. The effect of the steepening vertical moisture gradient wins out in SP-CESM, allowing variations in tropical convective heating to drive stronger variations in large-scale vertical moisture advection, thereby supporting increased MJO convective variability.

(3) As the climate system warms, the ability of MJO convective variability to influence the extratropics will decrease as a result of the weakened dynamical response to such convective variability.

There are numerous limitations of this study that may be addressed in future work. These limitations include:

(1) The role that various microphysical processes (e.g. net condensation, net freezing, net deposition) play in destabilizing the MJO was not examined, nor were potential sensitivities to the representation of these processes in SP-CESM. Model representation of microphysical processes influences the vertical structure of both latent and radiative heating produced by a simulated ensemble of clouds, and this study has highlighted how important the vertical structure of heating is to the MJO. Given their explicit representation of convection, clear scale separation, and optional two moment microphysics scheme, superparameterized versions of the CAM provide a

particularly amenable framework for this assessment that may be leveraged by future studies.

(2) This study did not investigate what role aerosols, which can similarly affect the vertical structure of diabatic heating, may potentially play in influencing the MJO.

(3) Additional SGS processes whose representation in SP-CESM is either missing or inadequate may play an important role in influencing the MJO. For example, surface flux feedbacks driven by SGS gustiness are not included in the version of SP-CESM used in this study. Sensitivities to such processes should be examined in future work.

(4) Shortcomings of data products used in this study provide important limitations to some of the conclusions of this study, most notable the conclusions that the MJO is unrealistically unstable in SP-CESM.

(5) Several of the analysis techniques used in this study (e.g. moisture variance budget) give equal weighting to moisture sources/sinks, regardless of the vertical level at which they occur. This is a shortcoming of these analysis techniques, as the ability of environmental moisture to influence convection depends on the vertical level in question.

(6) A myriad of uncertainties are introduced by the potential misrepresentation of the changing characteristics of convection as the climate system warms. For example, given a fixed relative humidity, the environmental saturation deficit will increase in a warming climate, increasing the impacts of entrainment on convection and driving the environmental thermodynamic profile away from that of a moist adiabat (Singh and O'Gorman 2015). The course resolution of SAM used in this study brings into

question the representation of entrainment, and thereby the representation of the changing characteristics of convection in a warming climate.

This study focuses on understanding the balance of processes maintaining the MJO when it is well established. Future work may consider using the WTG balance framework to understand how this balance of processes changes (i.e. becomes un-balanced) during periods of MJO initiation, intensification, and cessation. Preliminary results suggest that changes in horizontal advective damping may play a more important role during these periods than changes in the column process. Along similar lines of thinking, as different "flavors" of MJO events (i.e. MJO events of different character) are currently the topic du jour, future work may consider using the WTG balance framework to better understand the difference between these "flavors". The decreasing dynamical sensitivity to variations in tropical convective heating has wide ranging implications that should be examined further. For example, a weakened dynamical response to interannual variations in convective heating may affect ENSO by altering the Bjerknes feedback, discharge of warm water volume, and forcing of oceanic equatorial waves. In future work, I hope to explore feedbacks between moisture, convection, and large-scale circulations at play in other tropical phenomena.

REFERENCES

Adames, Á. F. and D. Kim, 2016: The mjo as a dispersive, convectively coupled moisture wave: Theory and observations. *Journal of the Atmospheric Sciences*, **73 (3)**, 913–941.

Andersen, J. A. and Z. Kuang, 2012: Moist static energy budget of mjo-like disturbances in the atmosphere of a zonally symmetric aquaplanet. *Journal of Climate*, **25 (8)**, 2782–2804.

Arnold, N. P., M. Branson, Z. Kuang, D. A. Randall, and E. Tziperman, 2015: Mjo intensification with warming in the superparameterized cesm. *Journal of Climate*, **28 (7)**, 2706–2724.

Arnold, N. P., Z. Kuang, and E. Tziperman, 2013: Enhanced mjo-like variability at high sst. *Journal of Climate*, **26 (3)**, 988–1001.

Arnold, N. P. and D. A. Randall, 2015: Global-scale convective aggregation: Implications for the madden-julian oscillation. *Journal of Advances in Modeling Earth Systems*.

Benedict, J. J. and D. A. Randall, 2007: Observed characteristics of the mjo relative to maximum rainfall. *Journal of the atmospheric sciences*, **64 (7)**, 2332–2354.

Benedict, J. J. and D. A. Randall, 2009: Structure of the madden-julian oscillation in the superparameterized cam. *Journal of the Atmospheric Sciences*, **66 (11)**, 3277–3296.

Bjerknes, J., 1966: A possible response of the atmospheric hadley circulation to equatorial anomalies of ocean temperature. *Tellus*, **18 (4)**, 820–829.

Bladé, I. and D. L. Hartmann, 1993: Tropical intraseasonal oscillations in a simple nonlinear model. *Journal of the atmospheric sciences*, **50 (17)**, 2922–2939.

Bony, S., B. Stevens, D. Coppin, T. Becker, K. A. Reed, A. Voigt, and B. Medeiros, 2016: Thermodynamic control of anvil cloud amount. *Proceedings of the National Academy of*

Sciences, 201601472.

Bony, S., et al., 2015: Clouds, circulation and climate sensitivity. *Nature Geoscience*, **8 (4)**, 261–268.

Bretherton, C. S., P. N. Blossey, and M. Khairoutdinov, 2005: An energy-balance analysis of deep convective self-aggregation above uniform sst. *Journal of the atmospheric sciences*, **62 (12)**, 4273–4292.

Bretherton, C. S. and M. F. Khairoutdinov, 2015: Convective self-aggregation feedbacks in near-global cloud-resolving simulations of an aquaplanet. *Journal of Advances in Modeling Earth Systems*.

Bretherton, C. S., M. E. Peters, and L. E. Back, 2004: Relationships between water vapor path and precipitation over the tropical oceans. *Journal of climate*, **17 (7)**, 1517–1528.

Caballero, R. and M. Huber, 2010: Spontaneous transition to superrotation in warm climates simulated by cam3. *Geophysical Research Letters*, **37 (11)**.

Carlson, H. and R. Caballero, 2016: Enhanced mjo and transition to superrotation in warm climates. *Journal of Advances in Modeling Earth Systems*.

Carvalho, L. M., C. Jones, and T. Ambrizzi, 2005: Opposite phases of the antarctic oscillation and relationships with intraseasonal to interannual activity in the tropics during the austral summer. *Journal of climate*, **18 (5)**, 702–718.

Cassou, C., 2008: Intraseasonal interaction between the madden–julian oscillation and the north atlantic oscillation. *Nature*, **455 (7212)**, 523–527.

Charney, J., 1948: On the scale of atmospheric motions. *Geofysiske Publikasjoner*, **17**, 1–17.

Charney, J. G., 1963: A note on large-scale motions in the tropics. *Journal of the Atmospheric Sciences*, **20 (6)**, 607–609.

Chikira, M., 2014: Eastward-propagating intraseasonal oscillation represented by chikira–sugiyama cumulus parameterization. part ii: Understanding moisture variation under weak temperature gradient balance. *Journal of the Atmospheric Sciences*, **71 (2)**, 615–639, doi: 10.1175/JAS-D-13-038.1, URL `http://dx.doi.org/10.1175/JAS-D-13-038.1`.

Dee, D., et al., 2011: The era-interim reanalysis: Configuration and performance of the data assimilation system. *Quarterly Journal of the Royal Meteorological Society*, **137 (656)**, 553–597.

Del Genio, A. D. and Y. Chen, 2015: Cloud-radiative driving of the madden-julian oscillation as seen by the a-train. *Journal of Geophysical Research: Atmospheres*.

DeMott, C. A., C. Stan, D. A. Randall, and M. D. Branson, 2014: Intraseasonal variability in coupled gcms: The roles of ocean feedbacks and model physics. *Journal of Climate*, **(2014)**.

Fuchs, Z. and D. J. Raymond, 2005: Large-scale modes in a rotating atmosphere with radiative-convective instability and wishe. *Journal of the atmospheric sciences*, **62 (11)**, 4084–4094.

Fuchs, Ž., S. L. Sessions, and D. J. Raymond, 2014: Mechanisms controlling the onset of simulated convectively coupled kelvin waves. *Tellus A*, **66**.

Grabowski, W. W., 2001: Coupling cloud processes with the large-scale dynamics using the cloud-resolving convection parameterization (crcp). *Journal of the Atmospheric Sciences*, **58 (9)**, 978–997.

Grabowski, W. W., 2004: An improved framework for superparameterization. *Journal of the atmospheric sciences*, **61 (15)**, 1940–1952.

Grabowski, W. W. and M. Moncrieff, 2004: Moisture–convection feedback in the tropics. *Quarterly Journal of the Royal Meteorological Society*, **130 (604)**, 3081–3104.

Hall, J. D., A. J. Matthews, and D. J. Karoly, 2001: The modulation of tropical cyclone activity in the australian region by the madden-julian oscillation. *Monthly weather review*, **129 (12)**, 2970–2982.

Hamill, T. M. and G. N. Kiladis, 2014: Skill of the mjo and northern hemisphere blocking in gefs medium-range reforecasts. *Monthly Weather Review*, **142 (2)**, 868–885.

Hand, E., 2015: The storm king. *Science*, **350 (6256)**, 22–25.

Hannah, W. M. and E. D. Maloney, 2014: The moist static energy budget in ncar cam5 hindcasts during dynamo. *Journal of Advances in Modeling Earth Systems*, **6 (2)**, 420–440.

Held, I. M. and B. J. Soden, 2006: Robust responses of the hydrological cycle to global warming. *Journal of Climate*, **19 (21)**, 5686–5699.

Henderson, S. A., E. D. Maloney, and E. A. Barnes, 2016: The influence of the madden-julian oscillation on northern hemisphere winter blocking. *Journal of Climate*, **(2016)**.

Herman, M. J., Z. Fuchs, D. J. Raymond, and P. Bechtold, 2016: Convectively coupled kelvin waves: From linear theory to global models. *Journal of the Atmospheric Sciences*, **73 (1)**, 407–428.

Hoskins, B. J. and T. Ambrizzi, 1993: Rossby wave propagation on a realistic longitudinally varying flow. *Journal of the Atmospheric Sciences*, **50 (12)**, 1661–1671.

Hoskins, B. J. and D. J. Karoly, 1981: The steady linear response of a spherical atmosphere to thermal and orographic forcing. *Journal of the Atmospheric Sciences*, **38 (6)**, 1179–1196.

Hu, Q. and D. A. Randall, 1994: Low-frequency oscillations in radiative-convective systems. *Journal of the atmospheric sciences*, **51 (8)**, 1089–1099.

Hurrell, J. W., et al., 2013: The community earth system model: a framework for collaborative research. *Bulletin of the American Meteorological Society*, **94 (9)**, 1339–1360.

Janiga, M. A. and C. Zhang, 2016: Mjo moisture budget during dynamo in a cloud-resolving model. *Journal of the Atmospheric Sciences*, **73 (6)**, 2257–2278.

Jiang, X., et al., 2011: Vertical diabatic heating structure of the mjo: Intercomparison between recent reanalyses and trmm estimates. *Monthly Weather Review*, **139 (10)**, 3208–3223.

Jin, F. and B. J. Hoskins, 1995: The direct response to tropical heating in a baroclinic atmosphere. *Journal of the atmospheric sciences*, **52 (3)**, 307–319.

Johnson, N. C. and S. B. Feldstein, 2010: The continuum of north pacific sea level pressure patterns: Intraseasonal, interannual, and interdecadal variability. *Journal of Climate*, **23 (4)**, 851–867.

Johnson, R. and P. Ciesielski, 2013: Evolution of mjo convection during dynamo deduced from the atmospheric sounding network. *EGU General Assembly Conference Abstracts*, Vol. 15, 2115.

Jones, C. and L. M. Carvalho, 2006: Changes in the activity of the madden-julian oscillation during 1958-2004. *Journal of Climate*, **19 (24)**, 6353–6370.

Kemball-Cook, S. R. and B. C. Weare, 2001: The onset of convection in the madden-julian oscillation. *Journal of climate*, **14 (5)**, 780–793.

Khairoutdinov, M. F. and D. A. Randall, 2003: Cloud resolving modeling of the arm summer 1997 iop: Model formulation, results, uncertainties, and sensitivities. *Journal of the*

Atmospheric Sciences, **60 (4)**, 607–625.

Kiladis, G. N., J. Dias, K. H. Straub, M. C. Wheeler, S. N. Tulich, K. Kikuchi, K. M. Weickmann, and M. J. Ventrice, 2014: A comparison of olr and circulation-based indices for tracking the mjo. *Monthly Weather Review*, **142 (5)**, 1697–1715.

Kiladis, G. N., K. H. Straub, and P. T. Haertel, 2005: Zonal and vertical structure of the madden-julian oscillation. *Journal of the atmospheric sciences*, **62 (8)**, 2790–2809.

Kim, D., J.-S. Kug, and A. H. Sobel, 2014a: Propagating versus nonpropagating madden–julian oscillation events. *Journal of Climate*, **27 (1)**, 111–125.

Kim, D., M.-I. Lee, D. Kim, S. D. Schubert, D. E. Waliser, and B. Tian, 2014b: Representation of tropical subseasonal variability of precipitation in global reanalyses. *Climate dynamics*, **43 (1-2)**, 517–534.

Kim, D., A. H. Sobel, and I.-S. Kang, 2011: A mechanism denial study on the madden-julian oscillation. *Journal of Advances in Modeling Earth Systems*, **3 (4)**.

Kiranmayi, L. and E. D. Maloney, 2011: Intraseasonal moist static energy budget in reanalysis data. *Journal of Geophysical Research: Atmospheres (1984–2012)*, **116 (D21)**.

Knutson, T. R. and S. Manabe, 1995: Time-mean response over the tropical pacific to increased c02 in a coupled ocean-atmosphere model. *Journal of Climate*, **8 (9)**, 2181–2199.

Lau, K. and H. Wu, 2010: Characteristics of precipitation, cloud, and latent heating associated with the madden-julian oscillation. *Journal of Climate*, **23 (3)**, 504–518.

Lau, W. K. and D. Waliser, (Eds.), 2012: *Intraseasonal Variability in the Atmosphere-Ocean Climate System*, chap. Predictability and forecasting. Springer.

Lau, W. K., D. E. Waliser, and P. E. Roundy, 2012: Tropical–extratropical interactions. *Intraseasonal Variability in the Atmosphere-Ocean Climate System*, Springer, 497–512.

Lee, S., 1999: Why are the climatological zonal winds easterly in the equatorialupper troposphere? *Journal of the atmospheric sciences*, **56 (10)**, 1353–1363.

L'Heureux, M. L. and R. W. Higgins, 2008: Boreal winter links between the madden-julian oscillation and the arctic oscillation. *Journal of Climate*, **21 (12)**, 3040–3050.

Liebmann, B. and C. Smith, 1996: Description of a complete (interpolated) outgoing longwave radiation dataset. *Bulletin of the American Meteorological Society*, **77**, 1275–1277.

Lin, H., G. Brunet, and J. Derome, 2009: An observed connection between the north atlantic oscillation and the madden-julian oscillation. *Journal of Climate*, **22 (2)**, 364–380.

Lin, J., B. Mapes, M. Zhang, and M. Newman, 2004: Stratiform precipitation, vertical heating profiles, and the madden-julian oscillation. *Journal of the Atmospheric Sciences*, **61 (3)**, 296–309.

Lin, J.-L., et al., 2006: Tropical intraseasonal variability in 14 ipcc ar4 climate models. part i: Convective signals. *Journal of climate*, **19 (12)**, 2665–2690.

Ling, J., C. Zhang, and P. Bechtold, 2013: Large-scale distinctions between mjo and non-mjo convective initiation over the tropical indian ocean. *Journal of the Atmospheric Sciences*, **70 (9)**, 2696–2712.

Lucas, C., E. J. Zipser, and M. A. Lemone, 1994: Vertical velocity in oceanic convection off tropical australia. *Journal of the atmospheric sciences*, **51 (21)**, 3183–3193.

Ma, D. and Z. Kuang, 2011: Modulation of radiative heating by the madden-julian oscillation and convectively coupled kelvin waves as observed by cloudsat. *Geophysical Research Letters*, **38 (21)**.

Madden, R. A. and P. R. Julian, 1971: Detection of a 40-50 day oscillation in the zonal wind in the tropical pacific. *Journal of the Atmospheric Sciences*, **28 (5)**, 702–708.

Madden, R. A. and P. R. Julian, 1972: Description of global-scale circulation cells in the tropics with a 40-50 day period. *Journal of the Atmospheric Sciences*, **29 (6)**, 1109–1123.

Majda, A. J. and S. N. Stechmann, 2009: The skeleton of tropical intraseasonal oscillations. *Proceedings of the National Academy of Sciences*, **106 (21)**, 8417–8422.

Majda, A. J. and S. N. Stechmann, 2011: Nonlinear dynamics and regional variations in the mjo skeleton. *Journal of the Atmospheric Sciences*, **68 (12)**, 3053–3071.

Maloney, E. D., 2009: The moist static energy budget of a composite tropical intraseasonal oscillation in a climate model. *Journal of Climate*, **22 (3)**, 711–729.

Maloney, E. D. and M. J. Dickinson, 2003: The intraseasonal oscillation and the energetics of summertime tropical western north pacific synoptic-scale disturbances. *Journal of the atmospheric sciences*, **60 (17)**, 2153–2168.

Maloney, E. D. and D. L. Hartmann, 2000a: Modulation of eastern north pacific hurricanes by the madden-julian oscillation. *Journal of climate*, **13 (9)**, 1451–1460.

Maloney, E. D. and D. L. Hartmann, 2000b: Modulation of hurricane activity in the gulf of mexico by the madden-julian oscillation. *Science*, **287 (5460)**, 2002–2004.

Maloney, E. D. and A. H. Sobel, 2007: Idealized hot spot experiments with a general circulation model. *Journal of climate*, **20 (5)**, 908–925.

Maloney, E. D., A. H. Sobel, and W. M. Hannah, 2010: Intraseasonal variability in an aquaplanet general circulation model. *Journal of Advances in Modeling Earth Systems*, **2 (2)**.

Maloney, E. D. and S.-P. Xie, 2013: Sensitivity of tropical intraseasonal variability to the pattern of climate warming. *Journal of Advances in Modeling Earth Systems*, **5 (1)**, 32–47.

Matsuno, T., 1966: Quasi-geostrophic motions in the equatorial area. *J. Meteor. Soc. Japan*, **44 (1)**, 25–43.

Matthews, A. J., 2008: Primary and successive events in the madden–julian oscillation. *Quarterly Journal of the Royal Meteorological Society*, **134 (631)**, 439–453.

McPhaden, M. J., 1999: Genesis and evolution of the 1997-98 el niño. *Science*, **283 (5404)**, 950–954.

Mori, M. and M. Watanabe, 2008: The growth and triggering mechanisms of the pna: A mjo-pna coherence. *Journal of the Meteorological Society of Japan*, **86 (1)**, 213–236.

Morita, J., Y. N. Takayabu, S. Shige, and Y. Kodama, 2006: Analysis of rainfall characteristics of the madden–julian oscillation using trmm satellite data. *Dynamics of atmospheres and oceans*, **42 (1)**, 107–126.

Muller, C. and S. Bony, 2015: What favors convective aggregation and why? *Geophysical Research Letters*, **42 (13)**, 5626–5634.

Muller, C. J. and I. M. Held, 2012: Detailed investigation of the self-aggregation of convection in cloud-resolving simulations. *Journal of the Atmospheric Sciences*, **69 (8)**, 2551–2565.

Mundhenk, B. D., E. A. Barnes, and E. D. Maloney, 2016: All-season climatology and variability of atmospheric river frequencies over the north pacific. *Journal of Climate*, **(2016)**.

Neelin, J. D., O. Peters, and K. Hales, 2009: The transition to strong convection. *Journal of the Atmospheric Sciences*, **66 (8)**, 2367–2384.

North, G. R., T. L. Bell, R. F. Cahalan, and F. J. Moeng, 1982: Sampling errors in the estimation of empirical orthogonal functions. *Monthly Weather Review*, **110 (7)**, 699–706.

Oliver, E. C. and K. R. Thompson, 2012: A reconstruction of madden-julian oscillation variability from 1905 to 2008. *Journal of Climate*, **25 (6)**, 1996–2019.

Peters, O. and J. D. Neelin, 2006: Critical phenomena in atmospheric precipitation. *Nature Physics*, **2 (6)**, 393–396.

Pritchard, M. S. and C. S. Bretherton, 2014: Causal evidence that rotational moisture advection is critical to the superparameterized madden–julian oscillation. *Journal of the Atmospheric Sciences*, **71 (2)**, 800–815.

Pritchard, M. S. and D. Yang, 2016: Response of the superparameterized madden-julian oscillation to extreme climate and basic state variation challenges a moisture mode view. *Journal of Climate*, **(2016)**.

Randall, D., M. Khairoutdinov, A. Arakawa, and W. Grabowski, 2003: Breaking the cloud parameterization deadlock. *Bulletin of the American Meteorological Society*, **84 (11)**, 1547–1564.

Raymond, D. J., 1995: Regulation of moist convection over the west pacific warm pool. *Journal of the atmospheric sciences*, **52 (22)**, 3945–3959.

Raymond, D. J., 2001: A new model of the madden-julian oscillation. *Journal of the atmospheric sciences*, **58 (18)**, 2807–2819.

Raymond, D. J. and Ž. Fuchs, 2009: Moisture modes and the madden-julian oscillation. *Journal of Climate*, **22 (11)**, 3031–3046.

Raymond, D. J. and X. Zeng, 2005: Modelling tropical atmospheric convection in the context of the weak temperature gradient approximation. *Quarterly Journal of the Royal Meteorological Society*, **131 (608)**, 1301–1320.

Riley, E. M., B. E. Mapes, and S. N. Tulich, 2011: Clouds associated with the madden-julian oscillation: A new perspective from cloudsat. *Journal of the Atmospheric Sciences*, **68 (12)**.

Riley Dellaripa, E. M. and E. D. Maloney, 2015: Analysis of mjo wind-flux feedbacks in the indian ocean using rama buoy observations. *Journal of the Meteorological Society of Japan*, **93 (0)**, 1–20.

Roundy, P. E., 2008: Analysis of convectively coupled kelvin waves in the indian ocean mjo. *Journal of the Atmospheric Sciences*, **65 (4)**, 1342–1359.

Roundy, P. E., 2012: Tracking and prediction of large-scale organized tropical convection by spectrally focused two-step space–time eof analysis. *Quarterly Journal of the Royal Meteorological Society*, **138 (665)**, 919–931.

Roundy, P. E., K. MacRitchie, J. Asuma, and T. Melino, 2010: Modulation of the global atmospheric circulation by combined activity in the madden-julian oscillation and the el niño-southern oscillation during boreal winter. *Journal of Climate*, **23 (15)**, 4045–4059.

Sahany, S., J. D. Neelin, K. Hales, and R. B. Neale, 2012: Temperature-moisture dependence of the deep convective transition as a constraint on entrainment in climate models. *Journal of the Atmospheric Sciences*, **69 (4)**, 1340–1358.

Sardeshmukh, P. D. and B. J. Hoskins, 1988: The generation of global rotational flow by steady idealized tropical divergence. *Journal of the Atmospheric Sciences*, **45 (7)**, 1228–1251.

Schubert, J. J., B. Stevens, and T. Crueger, 2013: Madden-julian oscillation as simulated by the mpi earth system model: Over the last and into the next millennium. *Journal of Advances in Modeling Earth Systems*, **5 (1)**, 71–84.

Sessions, S. L., S. Sugaya, D. J. Raymond, and A. H. Sobel, 2010: Multiple equilibria in a cloud-resolving model using the weak temperature gradient approximation. *Journal of Geophysical Research: Atmospheres*, **115 (D12)**.

Sherwood, S. C., 1999: On moistening of the tropical troposphere by cirrus clouds. *Journal of Geophysical Research: Atmospheres (1984–2012)*, **104 (D10)**, 11 949–11 960.

Shinoda, T., H. H. Hendon, and J. Glick, 1998: Intraseasonal variability of surface fluxes and sea surface temperature in the tropical western pacific and indian oceans. *Journal of climate*, **11 (7)**, 1685–1702.

Singh, M. S. and P. A. O'Gorman, 2015: Increases in moist-convective updraught velocities with warming in radiative-convective equilibrium. *Quarterly Journal of the Royal Meteorological Society*, **141 (692)**, 2828–2838.

Slade, S. A. and E. D. Maloney, 2013: An intraseasonal prediction model of atlantic and east pacific tropical cyclone genesis. *Monthly Weather Review*, **141 (6)**, 1925–1942.

Slingo, J., D. Rowell, K. Sperber, and F. Nortley, 1999: On the predictability of the interannual behaviour of the madden-julian oscillation and its relationship with el niño. *Quarterly Journal of the Royal Meteorological Society*, **125 (554)**, 583–609.

Sobel, A. and E. Maloney, 2012: An idealized semi-empirical framework for modeling the madden-julian oscillation. *Journal of the Atmospheric Sciences*, **69 (5)**, 1691–1705.

Sobel, A. and E. Maloney, 2013: Moisture modes and the eastward propagation of the mjo. *Journal of the Atmospheric Sciences*, **70 (1)**, 187–192.

Sobel, A., S. Wang, and D. Kim, 2014: Moist static energy budget of the mjo during dynamo. *Journal of the Atmospheric Sciences*, **71 (11)**, 4276–4291, doi:10.1175/JAS-D-14-0052.1, URL `http://dx.doi.org/10.1175/JAS-D-14-0052.1`.

Sobel, A. H., 2003: On the coexistence of an evaporation minimum and precipitation maximum in the warm pool. *Journal of climate*, **16 (6)**, 1003–1009.

Sobel, A. H., J. Nilsson, and L. M. Polvani, 2001: The weak temperature gradient approximation and balanced tropical moisture waves. *Journal of the atmospheric sciences*, **58 (23)**, 3650–3665.

Stan, C., M. Khairoutdinov, C. A. DeMott, V. Krishnamurthy, D. M. Straus, D. A. Randall, J. L. Kinter, and J. Shukla, 2010: An ocean-atmosphere climate simulation with an embedded cloud resolving model. *Geophysical Research Letters*, **37 (1)**.

Stocker, T., et al., 2014: *Climate change 2013: The physical science basis*. Cambridge University Press Cambridge, UK, and New York.

Takayabu, Y. N., T. Iguchi, M. Kachi, A. Shibata, and H. Kanzawa, 1999: Abrupt termination of the 1997–98 el niño in response to a madden–julian oscillation. *Nature*, **402 (6759)**, 279–282.

Thayer-Calder, K. and D. A. Randall, 2009: The role of convective moistening in the madden-julian oscillation. *Journal of the Atmospheric Sciences*, **66 (11)**, 3297–3312.

Thompson, D. B. and P. E. Roundy, 2013: The relationship between the madden-julian oscillation and us violent tornado outbreaks in the spring. *Monthly Weather Review*, **141 (6)**, 2087–2095.

Tian, B., D. E. Waliser, E. J. Fetzer, and Y. L. Yung, 2010: Vertical moist thermodynamic structure of the madden-julian oscillation in atmospheric infrared sounder retrievals: An update and a comparison to ecmwf interim re-analysis. *Monthly Weather Review*, **138 (12)**, 4576–4582.

Tompkins, A. M., 2001: Organization of tropical convection in low vertical wind shears: The role of water vapor. *Journal of the atmospheric sciences*, **58 (6)**, 529–545.

Trenberth, K. E., G. W. Branstator, D. Karoly, A. Kumar, N.-C. Lau, and C. Ropelewski, 1998: Progress during toga in understanding and modeling global teleconnections associated with tropical sea surface temperatures. *Journal of Geophysical Research: Oceans*, **103 (C7)**, 14 291–14 324.

Vallis, G. K., 2016: *Atmospheric and oceanic fluid dynamics: fundamentals and large-scale circulation. Second edition*. Cambridge University Press.

Vecchi, G. A. and N. A. Bond, 2004: The madden-julian oscillation (mjo) and northern high latitude wintertime surface air temperatures. *Geophysical research letters*, **31 (4)**.

Wang, B., 2012: Theory. *Intraseasonal Variability in the Atmosphere-Ocean Climate System*, Springer, 335–398.

Watanabe, M. and M. Kimoto, 2000: Atmosphere-ocean thermal coupling in the north atlantic: A positive feedback. *Quarterly Journal of the Royal Meteorological Society*, **126 (570)**, 3343–3369.

Wheeler, M. and G. N. Kiladis, 1999: Convectively coupled equatorial waves: Analysis of clouds and temperature in the wavenumber–frequency domain. *Journal of the Atmospheric Sciences*, **56 (3)**, 374–399, doi:10.1175/1520-0469(1999)056⟨0374:CCEWAO⟩2.0.CO;2, URL `http://dx.doi.org/10.1175/1520-0469(1999)056<0374:CCEWAO>2.0.CO;2`.

Wheeler, M. C. and H. H. Hendon, 2004: An all-season real-time multivariate mjo index: Development of an index for monitoring and prediction. *Monthly Weather Review*, **132 (8)**, 1917–1932.

Wing, A. A. and K. A. Emanuel, 2014: Physical mechanisms controlling self-aggregation of convection in idealized numerical modeling simulations. *Journal of Advances in Modeling Earth Systems*, **6 (1)**, 59–74.

Wolding, B. O. and E. D. Maloney, 2015a: Objective diagnostics and the madden–julian oscillation. part ii: Application to moist static energy and moisture budgets. *Journal of Climate*, **28 (19)**, 7786–7808.

Wolding, B. O. and E. D. Maloney, 2015b: Objective diagnostics and the madden-julian oscillation. part i: Methodology. *Journal of Climate*, doi:10.1175/JCLI-D-14-00688.1, URL `http://dx.doi.org/10.1175/JCLI-D-14-00688.1`.

Wolding, B. O., E. D. Maloney, and M. Branson, 2016: Vertically resolved weak temperature gradient analysis of the madden-julian oscillation in sp-cesm. *Journal of Advances in Modeling Earth Systems*, In press.

Wolding, B. O., E. D. Maloney, S. Henderson, and M. Branson, 2017: Climate change and the madden-julian oscillation: A vertically resolved weak temperature gradient analysis. *Journal of Advances in Modeling Earth Systems*.

Wu, X. and L. Deng, 2013: Comparison of moist static energy and budget between the gcm-simulated madden-julian oscillation and observations over the indian ocean and western pacific. *Journal of Climate*, **26 (14)**, 4981–4993.

Yanai, M., S. Esbensen, and J.-H. Chu, 1973: Determination of bulk properties of tropical cloud clusters from large-scale heat and moisture budgets. *Journal of the Atmospheric Sciences*, **30 (4)**, 611–627.

Yanai, M. and R. Johnson, 1993: Impacts of cumulus convection on thermodynamic fields. *Met. Monogr*, **24**, 39–62.

Yano, J.-I. and M. Bonazzola, 2009: Scale analysis for large-scale tropical atmospheric dynamics. *Journal of the Atmospheric Sciences*, **66 (1)**, 159–172.

Yasunaga, K. and B. Mapes, 2012: Differences between more divergent and more rotational types of convectively coupled equatorial waves. part i: Space-time spectral analyses. *Journal of the Atmospheric Sciences*, **69 (1)**, 3–16.

Yokoi, S., 2015: Multireanalysis comparison of variability in column water vapor and its analysis increment associated with the madden–julian oscillation. *Journal of Climate*, **28 (2)**, 793–808, doi:10.1175/JCLI-D-14-00465.1, URL `http://dx.doi.org/10.1175/JCLI-D-14-00465.1`.

Yoneyama, K., C. Zhang, and C. N. Long, 2013: Tracking pulses of the madden-julian oscillation. *Bulletin of the American Meteorological Society*, **94 (12)**.

Zhang, C., 2005: Madden-julian oscillation. *Reviews of Geophysics*, **43 (2)**.

Zhang, C., 2013: Madden-julian oscillation: Bridging weather and climate. *Bulletin of the American Meteorological Society*, **94 (12)**, 1849–1870.

Zhou, S., M. L'Heureux, S. Weaver, and A. Kumar, 2012: A composite study of the mjo influence on the surface air temperature and precipitation over the continental united states. *Climate dynamics*, **38 (7-8)**, 1459–1471.

Zhou, S. and A. J. Miller, 2005: The interaction of the madden-julian oscillation and the arctic oscillation. *Journal of climate*, **18 (1)**, 143–159.

Zipser, E. J., 2003: Some views on "hot towers" after 50 years of tropical field programs and two years of trmm data. *Meteorological Monographs*, **29 (51)**, 49–58.